Genetic and molecular characterization of *Arabidopsis* cysteine protease RD19 and its role in plant immunity



Doctoral thesis

for

the award of the doctoral degree

of the Faculty of Mathematics and Natural Sciences

of the University of Cologne

Submitted by

Giuliana Cornelia Heßler

2024

Abstract

In plant immune responses, two types of immune receptors are essential for pathogen recognition: cell surface receptors detect pathogen-associated molecular patterns (PAMPs) to initiate pattern-triggered immunity (PTI), while intracellular nucleotide-binding/leucine-rich repeat (NLR) receptors recognize effector molecules to activate effector-triggered immunity (ETI). In *Arabidopsis thaliana*, ETI signaling requires the ENHANCED DISEASE SUSCEPTIBILITY 1 (EDS1)-family as a downstream signaling platform. EDS1 forms exclusive heterodimers with either PHYTOALEXIN DEFICIENT 4 (PAD4) or SENESCENCE-ASSOCIATED GENE 101 (SAG101). Interestingly, EDS1-PAD4 is essential not only for ETI but also for PTI signaling mediated by the surface receptor RECEPTOR-LIKE PROTEIN 23 (RLP23) upon recognition of the peptide nlp20. This branch of immunity is therefore a convergence point between surface and intracellular immune signaling. In search for additional immune components that support this role of EDS1-PAD4 in both PTI and ETI, we identified the papain-like cysteine protease RESPONSIVE TO DEHYDRATION 19 (RD19) as a specific interaction partner of PAD4.

The work presented here provides both genetic and proteomic analyses to elucidate the molecular mechanisms underlying the role of RD19 in plant immunity. This study revealed that RD19 is only required for ETI responses to certain types of pathogens, contrasting with the broad function of PAD4 in immunity. Investigation of the function of RD19 in PTI responses identified a potential role of the protease in balancing the production of reactive oxygen species (ROS) following nlp20 treatment. Therefore, a putative substrate of RD19 may be involved in regulating ROS production, such as RESPIRATORY BURST OXIDASE HOMOLOGUE D (RBOHD) or one of its many regulators. In parallel, this study found that RD19 is required for stimulating increased responsiveness of plant cells, as loss of RD19 leads to a loss of nlp20-induced priming responses to different types of pathogens. Proteomic approaches revealed specific cleavage patterns of RD19 and uncovered potential substrates, including immunity components.

Based on the results presented in this thesis, it was hypothesized, that RD19, through its protease activity, is involved in the regulation of different types of PAD4-dependent and -independent immune responses, activated by both surface- and intracellular immune receptors.

Table of contents

Abstract I
Table of contents II
Abbreviations V
1 Introduction 1
1.1 The plant immune system – the role of surface and intracellular immune receptors 1
1.2 The EDS1 protein family – an essential signaling platform for activation of cell death and pathogen restriction 3
1.3 Establishing spatiotemporal immune responses 6
1.4 ROS signaling in plant-pathogen interactions 9
1.5 The role of proteases in plant immunity 10
1.6 The papain-like cysteine protease RD19 in plant immunity 13
1.7 Aims of the thesis 15
2 Results 16
2.1 RD19 is not required to establish ETI triggered by oomycete *Hyaloperonospora arabidopsidis* (*Hpa*) Emwa1 16
2.2 RD19 is dispensable for establishing basal resistance responses to biotrophic and necrotrophic pathogens 19
2.3 RD19 is required for nlp20-triggered ROS burst regulation 22
2.4 Increased ROS burst in *rd19ac* is dependent on RBOHD 26
2.5 RD19 is essential for nlp20-triggered priming against biotrophic and necrotrophic virulent pathogens 29
2.6 *RD19* is expressed in guard cells but increased ROS burst in *rd19ac* does not lead to increased stomatal closure 31
2.7 Overexpression of *RD19A* leads to nuclear and apoplastic localization 34
2.8 Activity-based protein profiling does not confirm RD19A activity in overexpressing $RD19A^{WT}$ lines 41
2.9 Generation of pRD19A::gRD19A stable transgenic lines in *rd19ac* mutant background 44
2.10 Proteomic Identification of Cleavage Sites (PICS) of RD19A reveals cleavage preference for non-polar amino acids 46
2.11 Proteomic analyses reveal potential RD19 substrates following nlp20-treatment 49
2.11.1 Shotgun proteomics verify increased presence of RBOHD in *rd19ac* mutants after nlp20 treatment 49
2.11.2 N-terminomics method (HUNTER) allows identification of potential RD19 substrates 54
3 Discussion 60
3.1 The role of RD19 in PAD4-dependent immune responses 60

3.1.1 RD19 is not as broadly required for TNL-ETI and basal immune responses as PAD4 60

3.1.2 RD19 fulfills a distinct role in PTI responses by potentially regulating nlp20-triggered ROS burst 61

3.1.3 RD19 is indispensable for nlp20-triggered priming in response to two distinct pathogens 62

3.1.4 RD19 shows increased expression at stomata and stomatal closure of *rd19ac* mutants is less responsive to elicitors....63

3.2 Localization and activity of RD19 and its link to PAD4 65

3.2.1 Subcellular localization of RD19A extends to all tested compartments in overexpression lines....65

3.2.2 Activity-based protein profiling did not confirm RD19A protease activity in overexpression lines....67

3.3 Potential substrates of RD19 and their link to RD19 function in immunity....69

3.3.1 The loss of RD19 is interfering with RBOHD protein levels....69

3.3.2 Indicative overview of RD19-mediated proteomic changes by shotgun proteomics....70

3.3.3 N-terminomic profiling using HUNTER revealed GRP3, CA2, GAPB and AQI as potential RD19 substrates 72

3.4 Future perspectives....76

4 Material and methods....78

4.1 Material 78

4.1.1 Oligonucleotides....78

4.1.2 Vectors....80

4.1.3 Plant material 83

4.1.4 Bacterial strains....83

4.1.5 Antibiotics....84

4.1.6 Antibodies 84

4.1.7 Media 84

4.1.8 Public RNAseq datasets....85

4.2 Methods 85

4.2.1 Biochemical methods 85

4.2.1.1 Total leaf protein extraction 85

4.2.1.2 Measurement of protein concentration using Pierce 660 nm 85

4.2.1.3 Protein enrichment via immunoprecipitation (IP) 86

4.2.1.4 SDS-PAGE 86

4.2.1.5 Immunoblot analysis 86

4.2.2 Molecular Biological Methods....87

4.2.2.1 Plant gDNA extractions 87

4.2.2.2 Polymerase chain reaction (PCR) 87

4.2.2.3 Agarose gel electrophoresis 88
4.2.2.4 DNA purification from agarose gels 89
4.2.2.5 Generation of In-Fusion expression vectors 89
4.2.2.6 Plasmid isolation and restriction enzyme digests 90
4.2.2.7 Sanger sequencing 90
4.2.2.8 Site-directed mutagenesis (SDM) 90
4.2.2.9 In silico sequence generation 91
4.2.2.10 RNA extraction and cDNA synthesis 91
4.2.2.11 RT-qPCR 91
4.2.2.12 Measurement of ROS production 92
4.2.2.13 MAPK activity assay 92
4.2.2.14 Isolation of apoplastic fluids from *N. benthamiana* and *A. thaliana* 93
4.2.2.15 Isolation of nuclei from *A. thaliana* 93
4.2.2.16 Guard cell aperature assay 94
4.2.3 Plant protease assays 94
4.2.3.1 Activity-based protein profiling 94
4.2.3.2 PICS assay 96
4.2.3.3 N-terminomic profiling using High-efficiency Undecanal-based N-Termini EnRichment 97
4.2.3.4 Shotgun proteomics 98
4.2.4 Bacterial Methods 99
4.2.4.1 *E. coli* cultivation and transformation 99
4.2.4.2 *A. tumefaciens* cultivation and transformation 99
4.2.4.3 *P. syringae* cultivation 100
4.2.4.4 *B. cinerea* cultivation 100
4.2.4.5 *H. arabidopsidis* (*Hpa*) cultivation 100
4.2.5 Plant Methods 100
4.2.5.1 Plant cultivation 100
4.2.5.2 Stable transformation of *A. thaliana* (floral dip) 101
4.2.5.3 Transient protein expression in *N. benthamiana* 101
4.2.5.4 *B. cinerea* growth assay in *A. thaliana* 101
4.2.5.5 *Pst* growth assay in *A. thaliana* 102
4.2.5.6 *Hpa* Emwa1 and Noco2 growth assays in *A. thaliana* 102
4.2.6 Microscopy 103
5 Supplementary data 104
5.1 Supplementary figures 104
5.2 Supplementary tables 112
6 References 131

Abbreviations

%	percent
°C	degree Celsius
A. thaliana	*Arabidopsis thaliana*
aa	amino acid(s)
ABA	abscisic acid
ADP	adenosine diphosphate
ADPR	adenosine diphosphate ribose
ADPr-ATP	ADP-ribosylated ATP
ADR1	ACTIVATED DISEASE RESISTANCE 1
AF	apoplastic fluid
AQI	AQUAPORIN INTERACTOR
ATP	adenosine triphosphate
ATR1	A. THALIANA RECOGNIZED 1
AUC	area under curve
B. cinerea	*Botrytis cinerea*
BAK1	BRI1-ASSOCIATED RECEPTOR KINASE 1
BIK1	BOTRYTIS-INDUCED KINASE 1
BLAST	Basic Local Alignment Search Tool
bp	base pair(s)
BSK1	BRASSINOSTEROID-SIGNALING KINASE 1
C-terminus	carboxyl terminus
CA2	BETA CARBONIC ANHYDRASE 2
Ca^{2+}	calcium
CAPE9	CYSTEINE-RICH SECRETORY PROTEIN, ANTIGEN 5, AND PATHOGENESIS-RELATED 1 PROTEIN (CAP)-DERIVED PEPTIDE 9
CAT2	CATALASE 2
CC	coiled-coil domain
CC9	CORN CYSTATIN 9
cDNA	complementary DNA
CDPK	calcium-dependent protein kinase
CDS	coding sequence
CFU	colony forming unit(s)
cm	centimeter(s)
CNL	CC-domain NLR
Col-0	*Arabidopsis thaliana* accession “Columbia 0”

CP1/2	CORN CYSTEINE PROTEASE ½
CPK	calcium protein kinase
CRK	Cysteine-rich RLK
cROS	Chloroplast-derived ROS
CYS	CYSTATIN
DAMP	damage-associated molecular pattern(s)
ddH_2O	double-distilled water
DEG	differentially expressed genes
Desi3A	DeSUMOylating isopeptidase 3A
di-ADPr	ADR-ribosylated ADPR
DMSO	dimethyl sulfoxide
DNA	deoxyribonucleic acid
dpi	day(s) post infection
DTT	dithiothreitol
e.g.,	„exempli gratia“ – for example
ECD	Extracellular domain
EDS1	ENHANCED DISEASE SUSCEPTIBILITY 1
EDTA	ethylenediaminetetraacetic acid
EF	elongation factor
EGF	epidermal growth factor
ELP5	ELONGATOR COMPLEX PROTEIN
EP-domain	EDS1-PAD4 C-terminal domain
ER	endoplasmatic reticulum
ETI	effector-triggered immunity
EV	empty vector
flg22	22 amino acid epitope of flagellin
FLS2	FLAGELLIN SENSING 2
FRK1	FLG22-INDUCED RECEPTOR-LIKE KINASE 1
fw	forward
GAPB	GLYCERALDEHYDE-3-PHOSPHATE DEHYDROGENASE B SUBUNIT
GAPDH	glyceraldehyde 3-phosphate dehydrogenase
GC	guard cells
gDNA	genomic DNA
GO	Gene ontology
GPA	green peach aphid
GRP3	GLYCINE RICH PROTEIN 3
h	hour(s)

H_2O_2	hydrogen peroxide
HA	human influenza hemagglutinin
HMGB2	HIGH MOBILITY GROUP B2
Hpa	*Hyaloperonospora arabidopsidis*
hpi	hour(s) post infection
HR	hypersensitive response
HRP	horse radish peroxidase
Hz	Hertz
i.e.,	“id est” – that is
IgG	immunoglobulin G
IP	immunoprecipitation
IP-MS/MS	immunoprecipitation tandem mass spectrometry
JA	jasmonic acid
kb	kilobase(s)
kDa	kilo Dalton
kV	kilo Volt
l	liter(s)
LAR	local acquired resistance
LLD	lipase-like domain
LRR	leucine-rich repeat domain
LysM	lysine motif
M	molar
MAMP	microbe-associated molecular pattern(s)
MAPK	mitogen-activated protein kinase
MC	metacaspase
mg	milligram(s)
MIK2	MDIS1-INTERACTING RECEPTOR LIKE KINASE2
min	minute(s)
ml	milliliter(s)
mm	millimeter(s)
mM	millimolar
ms	millisecond(s)
MS	mass spectrometry
mYFP	monomeric yellow-fluorescent protein
N-terminus	amino terminus
N. benthamiana	*Nicotiana benthamiana*
NaCl	sodium chloride

NAD	nicotinamide adenine dinucleotide
NADP	nicotinamide adenine dinucleotide phosphate
NB	nucleotide-binding domain
NB-ARC	nucleotide-binding, shared by Apaf-1, R-proteins and CED-4
Nep1	necrosis and ethylene-inducing peptide 1
NES	nuclear export signal
ng	nanogram(s)
NHP	N-Hydroxypipecolic Acid
nlp20	20 amino acid epitope of fungal necrosis and ethylene-inducing peptide 1-like
NLPs	Nep1-like proteins
NLR	nucleotide-binding and leucine-rich repeat
NLS	nuclear localization signal
nm	nanometer(s)
nM	nanomolar
NOD	nucleotide-binding-oligomerization domain
NPC	no probe control
NPR1	NON-EXPRESSOR OF PR GENES1
NRG1	N REQUIREMENT GENE 1
nt	nucleotide(s)
O_2	singlet oxygen
O_{2^-}	superoxide anion
OD_{600}	optical density at 600 nm
OE	overexpressing
PAD3	PHYTOALEXIN DEFICIENT 3
PAD4	PHYTOALEXIN-DEFICIENT 4
PAGE	polyacrylamide gel electrophoresis
PAMP	pathogen-associated molecular pattern
PB1CP	PHAGOCYTOSIS OXIDASE/BEM1P (PB1) DOMAIN-CONTAINING PROTEIN
PBL	PBS1-LIKE
PCR	polymerase chain reaction
PEP	PLANT ELICITOR PEPTIDE
PEPR1/2	PEP1 RECEPTOR ½
Pip	pipecolic acid
PIP1;4	PLASMA MEMBRANE INTRINSIC PROTEIN 1;4
PIRE	PBL13 INTERACTING RING DOMAIN E3 LIGASE

PLCP	papain-like cysteine protease
PM	plasma membrane
PopP2	Pseudomonas outer protein P2
PORC	PROTOCHLOROPHYLLIDE OXIDOREDUCTASE C
PPC2	PHOSPHOENOLPYRUVATE CARBOXYLASE 2
PR1	PATHOGENESIS RELATED 1
pRib-ADP	2′-(5″-phosphoribosyl)-5′-adenosine diphosphate
pRib-AMP	2′-(5″-phosphoribosyl)-5′-adenosine monophosphate
PRR	pattern-recognition receptor
Pst	*Pseudomonas syringae* pv. *tomato*
Pst ΔCor	*Pseudomonas syringae* pv. *tomato* strain lacking Coronatine
PTI	pattern-triggered immunity
pv.	pathovar
RBA1	RECOGNITION OF HOPBA1
RBOHD	RESPIRATORY BURST OXIDASE HOMOLOGUE D
RD19	RESPONSIVE TO DEHYDRATION 19
RD21A	RESPONSIVE TO DEHYDRATION 21A
RK	receptor kinase
RLK	receptor-like kinase
RLP	receptor-like protein
RLP23	RECEPTOR-LIKE PROTEIN 23
RNA	ribonucleic acid
RNAseq	RNA-sequencing
RNL	RPW8-like CNL
ROQ1	RECOGNITION OF XOPQ 1
ROS	reactive oxygen species
rpm	rounds per minute
RPP1	RECOGNITION OF PERONOSPORA PARASITICA 1
RPS2	RESISTANT TO P. SYRINGAE 2
RPS4	RESISTANT TO P. SYRINGAE 4
RPW8	RESISTANCE TO POWDERY MILDEW 8
RRS1	RESISTANT TO RALSTONIA SOLANACEARUM 1
RT	room temperature
RT-PCR	reverse-transcriptase PCR
rv	reverse
SA	salicylic acid
SADR1	TNL SUPPRESSOR OF ADR1-L2 1

SAG101	SENESCENCE-ASSOCIATED GENE 101
SAI	stomata aperture index
SAP1/2	SECRETED ASPARTIC PROTEASE ½
SAR	systemic acquired resistance
SCOOP	SERINE-RICH ENDOGENOUS PEPTIDE
SDM	site-directed mutagenesis
SDS	sodium dodecyl sulfate
sec	second(s)
SOBIR1	SUPPRESSOR OF BIR1 1
SP	signal peptide
SRA	Sequence Read Archive
SUMO	SMALL UBIQUITIN-LIKE MODIFIER
T-DNA	Transfer DNA from *Agrobacterium tumefaciens*
TBS	TRIS-buffered salines
TIC56	TRANSLOCON AT THE INNER ENVELOPE MEMBRANE OF CHLOROPLASTS 56
TIP2-1	DELTA TONOPLAST INTEGRAL PROTEIN
TIR	Toll/interleukin-1 receptor
TM	Transmembrane domain
TN	TIR-NB protein
TRIS	tris(hydroxymethyl)aminomethane
V	Volt(s)
v/v	volume per volume
VPE	vacuolar processing enzymes
VSP2	VEGETATIVE STORAGE PROTEIN 2
w/v	weight per volume
WAK1	WALL-ASSOCIATED KINASE 1
Ws-2	*A. thaliana* accession “Wassilewskija”
WT	wild type
x	times
XCP1	XYLEM CYSTEINE PEPTIDASE 1
xg	relative centrifugal force
ZAR1	HOPZ-ACTIVATED RESISTANCE 1
Zip1	*Z. mays* immune signaling peptide 1
µl	microliter(s)
µm	micrometer(s)
µM	micromolar

1 Introduction

1.1 The plant immune system – the role of surface and intracellular immune receptors

In their environment, plants are constantly exposed to a variety of biotic and abiotic stresses. In response to biotic stresses, they evolved a cell-autonomous, two-tiered immune system. At the surface of the plant cell, sensing of pathogen-/microbe-associated molecular patterns (PAMPs/MAMPs) or of endogenous damage-associated molecular patterns (e.g. endogenous fragments and/or fragments of plant cell walls; DAMPs) leads to activation of the first layer of plant defense, referred to as pattern-triggered immunity (PTI) (Dangl and Jones 2001). Sensing of these conserved patterns is achieved by the plasma-membrane anchored pattern-recognition receptors (PRRs), namely receptor kinases (RKs) or receptor-like proteins (RLPs) (Couto and Zipfel 2016). RKs consist of an extracellular domain (ECD), a single-pass transmembrane (TM) domain, and an intracellular kinase domain, while RLPs consist of an ECD and a TM but lack the intracellular signaling domain and therefore require RKs as co-receptors for functional signal transduction (Monaghan and Zipfel 2012). RKs and RLPs both possess a set of different ECDs, such as leucine-rich repeats (LRR), lysin motif (LysM) or epidermal growth factor (EGF)-like domains, allowing recognition of a broad range of microbial or endogenous patterns (Couto and Zipfel 2016). For example, LysM ECDs recognize microbial carbohydrate molecules, such as chitin or peptidoglycan (Couto and Zipfel 2016). LRR domains are the most common form of ECDs and have been demonstrated to perceive different peptide sequences, such as flagellin, elongation factor Tu (EF-Tu) or necrosis and ethylene-inducing peptide 1 (Nep1)-like proteins (NLPs) (Böhm et al. 2014; Couto and Zipfel 2016; Zipfel et al. 2004, 2006).

A well-studied LRR-RK is FLAGELLIN-SENSING 2 (FLS2), which recognizes the peptide flg22 (a 22 amino acid epitope of flagellin) (Zipfel et al. 2004). Upon binding of flg22, FLS2 forms a complex with its co-receptor BRI-ASSOCIATED RECEPTOR KINASE 1 (BAK1), stabilizing the binding of flg22 and leading to activation of the cytoplasmic kinase BOTRYTIS-INDUCED KINASE 1 (BIK1) (Chinchilla et al. 2007; Sun et al. 2013). In non-immune elicited plants, BIK1 associates with FLS2 but upon stimulation with flg22, BAK1 phosphorylates BIK1, causing the activation of BIK1 and its disassociation from the complex (Zhang et al. 2010). BAK1 has been described as a co-receptor of several known RKs, as well as RLPs, while BIK1 is only known to act downstream of RKs but not RLPs, suggesting multiple levels of signal regulation (Chinchilla et al. 2007; Couto and Zipfel 2016; Heese et al. 2007; Mühlenbeck et al. 2023). Upon activation, BIK1 interacts with and phosphorylates the NADPH oxidase RESPIRATORY BURST OXIDASE HOMOLOGUE D (RBOHD), leading to the production of extracellular reactive oxygen species (ROS) (Kadota et al. 2014; Kadota, Shirasu, and Zipfel 2015; L. Li et

al. 2014). Simultaneously, BIK1 activates Ca^{2+}-influx into the cell which, together with ROS production, represents one of the first immune outputs occurring after pathogen perception (Boller and Felix 2009; Couto and Zipfel 2016). Furthermore, phosphorylation of mitogen-activated protein kinases (MAPKs), together with Ca^{2+}-influx, trigger transcriptional reprogramming to establish PTI (Lee et al. 2015; Seybold et al. 2014) (Figure 1).

An example of an RLP in PTI-signaling is RLP23, which recognizes the peptides nlp20 or nlp24 (a 20- or 24-amino acid pattern of NLP) and constitutively associates with RK SUPPRESSOR OF BIR1 1 (SOBIR1) due to the lack of an intracellular kinase domain (Albert et al. 2015; Böhm et al. 2014). As for FLS2, upon elicitor binding, BAK1 is recruited to the RLP23-SOBIR1 complex but requires the receptor-like cytoplasmic kinase (RLCK) PBS1-LIKE 31 (PBL31) for downstream signaling (Albert et al. 2015; Pruitt et al. 2021). Interestingly, BIK1, which positively regulates RK-mediated PTI, suppresses RLP-mediated immune signaling, suggesting high elicitor-dependent flexibility in the regulation of immune signaling (W. L. Wan, Zhang, et al. 2019). Consequently, RK- and RLP-signaling leads to different immune outputs. For instance, ligand-triggered RKs typically induce quicker, shorter and stronger responses (such as higher ROS burst) compared to RLPs. On the other hand, RLP activation leads to an ethylene (ET) and salicylic acid (SA) burst. as well as camalexin production, which is lacking in RK-triggered immunity (W. L. Wan, Zhang, et al. 2019). In summary, PRRs recognize a variety of pathogens, leading to induction of robust immune responses with a tight regulation of signaling pathways.

Host-adapted pathogens employ a variety of mechanisms to suppress, exploit or manipulate immune responses of their plant host. This is mainly achieved by secretion of effector molecules, which are different types of small molecules, proteins or metabolites that interfere with various host processes to support pathogen colonization (Jones and Dangl 2006) (Figure 1). In order to respond to these adapted pathogens, plants have evolved a second type of immune receptor, the intracellular nucleotide-binding LRR receptors (NLRs) (Dangl and Jones 2001; Jones, Staskawicz, and Dangl 2024; Ngou, Ding, and Jones 2022). NLRs typically contain a central nucleotide-binding (NB-ARC) domain, a C-terminal LRR domain and are classified based on their variable N-terminal domain: CNLs with an N-terminal coiled-coiled domain and TNLs with an N-terminal Toll and Interleukin-1 Receptor (TIR)-like domain (Jones, Vance, and Dangl 2016). Recognition of effector molecules by CNLs and TNLs initiates a signaling cascade that leads to enhanced resistance or cell death (also termed hypersensitive response, HR) at the site of infection and is termed effector-triggered immunity (ETI) (Lapin, Bhandari, and Parker 2020).

Over the past decades a variety of receptor-effector pairs have been identified, such as the *Arabidopsis thaliana* receptor RECOGNITION OF PERONOSPORA PARASITICA 1 (RPP1),

which recognizes the *Hyaloperonospora arabidopsidis* effector A. THALIANA RECOGNIZED 1 (ATR1^{Emoy2}) or the *Nicotiana benthamina* RECOGNITION OF XOPQ 1 (ROQ1), recognizing the *Xanthomonas campestris* pv. *vesicatoria* (*Xcv*) effector XopQ (Krasileva, Dahlbeck, and Staskawicz 2010; Schultink et al. 2017). Cryo-EM resolved structure of both activated RPP1 and ROQ1 revealed a tetrameric oligomerization of both TNL receptors bound to the respective effector molecule (Figure 1) (Ma et al. 2020; Martin et al. 2020). Interestingly, plants not only possess TNL receptors but also receptors lacking the LRR domain (TIR-NB) or TIR-only proteins (Johanndrees et al. 2023). Many of the tested plant TIR domains have a NADase activity that is dependent on a conserved glutamate residue in their catalytic site (Essuman et al. 2022; Horsefield et al. 2019; L. Wan et al. 2019). The cryo-EM structures of RPP1 and ROQ1 revealed that the NADase active site is formed in the effector-induced TNL tetramer by two asymmetrically aligned TIR domain pairs (Ma et al. 2020; Martin et al. n.d.), highlighting why the TIR domain alone is sufficient for NADase activity (Essuman et al. 2022; Horsefield et al. 2019; L. Wan et al. 2019). While TIR-domain proteins are therefore a class of NAD+ hydrolyzing enzymes to activate downstream immune responses, plant CNLs act differently. The CNLs *A. thaliana* HOPZ-ACTIVATED RESISTANCE 1 (ZAR1) or the wheat Sr35 form pentameric structures following indirect/direct effector recognition, which creates an autonomous calcium permeable channel by inserting into the plasma membrane, directly inducing cell death (Förderer et al. 2022; J. Wang, Hu, et al. 2019; J. Wang, Wang, et al. 2019).

1.2 The EDS1 protein family – an essential signaling platform for activation of cell death and pathogen restriction

The use of cryo-EM guided structural biology over the last years led to major advances in our understanding of TNL activation and their enzymatic functions. Prior to this, genetic approaches have been extensively used to understand signaling downstream of TNLs. All studied TNLs signal via the conserved ENHANCED DISEASE SUSCEPTIBILITY 1 (EDS1) protein family. EDS1 forms exclusive heterodimers with either PHYTOALEXIN-DEFICIENT 4 (PAD4) or SENESCENCE-ASSOCIATED GENE 101 (SAG101) (Wagner et al. 2013) (Figure 1). All three proteins contain an N-terminal lipase-like domain (LLD), essential for the heterodimer interaction, and a C-terminal EDS1-PAD4 (EP) domain, essential for signaling function (Dongus et al. 2022; Gantner et al. 2019; Lapin et al. 2019).

In comparison to CNLs, TNLs are solely functioning as sensor NLRs and signaling via the EDS1 family requires downstream so-called helper NLRs with an N-terminal RESISTANCE TO POWDERY MILDEW 8 (RPW8)-domain (RNLs) (Castel et al. 2019; Feehan et al. 2020; Jones et al. 2024; Monteiro and Nishimura 2018; Tamborski and Krasileva 2020). EDS1-PAD4 and EDS1-SAG101 require the RNLs (also called “helper NLRs”) ACTIVATED DISEASE

RESISTANCE 1 (ADR1) and N REQUIREMENT GENE 1 (NRG1), respectively, for immunity signaling (Lapin et al. 2019; Sun et al. 2021; Wu et al. 2019) (Figure 1).

Previous studies identified differences in the requirement of the EDS1-PAD4-ADR1 and the EDS1-SAG101-NRG1 branches in TNL-ETI immune responses. The *Pseudomonas syringae* pv. *tomato* strain carrying the effector AvrRps4 is recognized in *A. thaliana* by the TNL pair RESISTANT TO P. SYRINGAE 4 (RPS4) and RESISTANT TO RALSTONIA SOLANACEARUM 1 (RRS1) (Hinsch and Staskawicz 1996). Using AvrRps4 as TNL-ETI activator, a series of experiments demonstrated a predominant role of EDS1-PAD4-ADR1 in limiting pathogen growth by inducing transcriptional reprogramming without cell death in *A. thaliana* (the so-called "basal immunity") (Parker, Hessler, and Cui 2021), while EDS1-SAG101-NRG1 mainly acts as a mediator of cell death (Bonardi et al. 2011; Castel et al. 2019; Lapin et al. 2019; Saile et al. 2020; Sun et al. 2021; Wu et al. 2019) (Figure 1). Differently from *A. thaliana*, in *N. benthamiana*, all tested activations of TNL-ETI are dependent on EDS1-SAG101-NRG1 for both pathogen restriction and cell death (Gantner et al. 2019; Qi et al. 2018). It was only recently established that EDS1-PAD4-ADR1 is required for stomatal closure in response to flg22 in both *N. benthamiana* and *A. thaliana* (Wang et al. 2024).

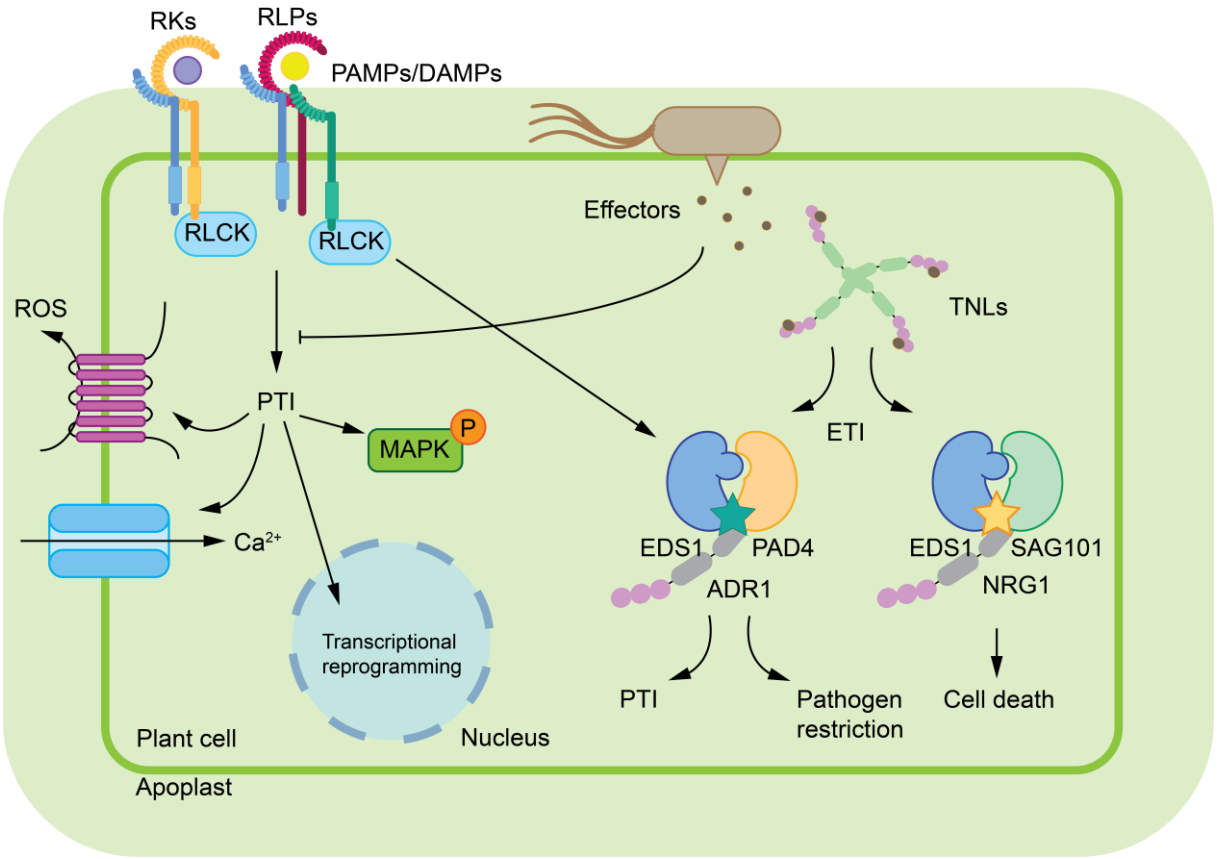


Figure 1: Schematic representation of the *A. thaliana* plant immune system. Recognition of PAMPs or DAMPs by RK or RLP surface receptors leads to activation of PTI. PTI is defined by hallmark outputs, such as generation of ROS, Ca^{2+} influx into the cell, transcriptional reprogramming and activation of MAP kinases. PTI can be inhibited by effector molecules,

secreted by adapted pathogens. Intracellular TNL receptors oligomerize upon recognition of effectors and activate ETI signaling. ETI signals via the EDS1-PAD4-ADR1 or EDS1-SAG101-NRG1 immune branch, to activate pathogen restriction or cell death, respectively. EDS1-PAD4-ADR1 is furthermore required for PTI signaling activated by an RLP. Stars bound to EP domains indicate different small molecules.

Despite the identification of different roles of the two EDS1 signaling branches by genetic studies, some questions remained unanswered. One question is how the two branches are selectively activated by TNLs. Biochemical analyses both *in vitro* and *in vivo* revealed that NAD^+ (oxidized form of nicotinamide adenine dinucleotide) or $NADP^+$ (oxidized form of nicotinamide adenine dinucleotide phosphate) are used by TNLs as substrates to produce ADPR (adenosine diphosphate ribose), cADPR (cyclic ADPR) and 2'cADPR (Bayless and Nishimura 2020; Horsefield et al. 2019; Locci, Wang, and Parker 2023). Nevertheless, neither of these molecules were sufficient to induce cell death *in planta* (Duxbury et al. 2020). A significant advance in studying this question came from resolving the structure of activated EDS1-PAD4 heterodimers from *A. thaliana*, using the insect cell expression system, followed by cryo-EM (Huang et al. 2022; Jia et al. 2022). The crystal structure and following mass spectrometry (MS) analysis revealed that the small molecules, 2'-(5''-phosphoribosyl)-5′-adenosine diphosphate (pRib-ADP) and 2'-(5''-phosphoribosyl)-5′-adenosine monophosphate (pRib-AMP), bind specifically to a conserved pocket in the EP domain of EDS1 and PAD4. Binding of the molecule induced a 10° conformational change of the PAD4 EP domain, allowing association of EDS1-PAD4 to ADR1 but not NRG1 (Huang et al. 2022). On the contrary, the TIR catalytic metabolites ADP-ribosylated ATP (ADPr-ATP) and ADP-ribosylated ADPR (di-ADPR) bind to the EDS1-SAG101 heterodimer, leading to a 15° conformational change and inducing binding of NRG1 (Jia et al. 2022) (Figure 1). Likely, in an initial step, ADPr-ATP and di-ADPR are produced due to the ADPR transferase activity of TIR domain proteins, which catalyzes transfer of the ADPR moiety from NAD^+ to ADPR or ATP (Huang et al. 2023; Jia et al. 2022). Hydrolysis of di-ADPR or ADPr-ATP might then result in pRib-ADP and pRib-AMP (Huang et al. 2022, 2023; Jia et al. 2022). It remains to be elucidated whether the signal specificity depends on the type of molecule that is produced or on the availability of EDS1-PAD4 or EDS1-SAG101 heterodimers.

While these findings provide the long-missing link between TNL/TIR enzymatic activity and downstream signaling, it is unclear how RNLs function after binding to the heterodimers and therefore, how the two signaling branches lead to different immune outputs. An auto-active form of NRG1 was proposed to oligomerize and form a Ca^{2+}-channel at the plasma membrane (PM), while evidence of ADR1 Ca^{2+}-channel formation is restricted to an ADR1 association to the PM but not evidently in an oligomeric state (Feehan et al. 2023; Jacob et al. n.d.; Saile et al. 2021; Wang et al. 2023). It is not clear if the EDS1 family binds the oligomeric RNL to alter or enhance its channel activity, or if the binding to the EDS1 family is only a transient but

necessary step, to release a mature oligomeric RNL to function alone at the PM (Jacob et al. n.d.; Parker et al. 2021; Saile et al. 2021). Nevertheless, this suggests that both RNL families function similarly to CNL receptors while it remains to be answered how their function relates to that of other Ca^{2+} channels in PTI and ETI responses.

Despite perception of distinct ligands and therefore their previous description as two distinct pathways, PTI and ETI signaling share a plethora of downstream signaling events. These include production of ROS, Ca^{2+} influx, MAPK activation and transcriptional reprogramming, though differing in both amplitude and time scales (Bjornson and Zipfel 2021; Yuan, Ngou, et al. 2021). For example, while PTI and ETI both require RBOHD to produce ROS, PTI induces a fast and strong ROS burst and ETI induces a biphasic burst, with the second peak stronger and more sustained than the first one (Kadota et al. 2014; L. Li et al. 2014). Recent studies have verified a crosstalk between PTI and ETI, suggesting ETI as an amplification mechanism that relies on the PTI machinery (Ngou et al. 2021; Yuan, Jiang, et al. 2021). Immune components traditionally described as ETI components, such as TIR proteins, are upregulated in PTI responses, suggesting a mutual amplification of both pathways (Tian et al. 2021). Furthermore, the EDS1-PAD4-ADR1 branch is required for PTI-signaling triggered by recognition of nlp20 by RLP23, placing the EDS1-PAD4-ADR1 branch as a convergence point of both intracellular and surface triggered immune responses (Pruitt et al. 2021). Taken together, these studies show that the EDS1 family represents a central node in TNL-ETI signaling, that extends to PTI signaling for EDS1-PAD4-ADR1 (Figure 1).

1.3 Establishing spatiotemporal immune responses

While plant immunity studies have primarily focused on cell-autonomous signaling responses, little is known about the coordination of cell-to-cell signaling and establishment of a spatiotemporal immune response to various pathogens. An important factor might be the activity or availability of different types of immune components in diverse cell types or areas of the infection. The two phytohormones salicylic acid (SA) and jasmonic acid (JA), which are antagonizing each other in immune responses, are activated in spatially distinct regions around an infection site during ETI (Betsuyaku et al. 2018; Spoel and Dong 2008). While SA is found in regions adjacent to the hypersensitive response (HR), JA dominates over SA distally from the infection site (Betsuyaku et al. 2018). Interestingly, JA pathways are repressed by activity of EDS1-PAD4, therefore promoting SA accumulation around infection sites (Bhandari et al. 2019; Cui et al. 2018). Since cell death in TNL triggered tissues is mediated by the EDS1-SAG101-NRG1 module, activities of EDS1-SAG101-NRG1 and EDS1-PAD4-ADR1 might be spatially distinct, allowing for a local activation of cell death and a suppression of pathogen growth in bystander cells (Lapin et al. 2020; Locci and Parker 2024). How EDS1-PAD4-ADR1 could be activated in local/bystander cells, is not yet understood.

Cell-to-cell communication in plants is possible via the apoplast (the extracellular space outside of cell membranes) or the symplast via plasmodesmata (a cytoplasmic continuum between the cells) (Cheval and Faulkner 2018; Darino, Kanyuka, and Hammond-Kosack 2022). The significance of both routes has been described in immune signaling contexts, transmitting both immune and damage signals from infection sites to systemic tissues (Cheval and Faulkner 2018; Rzemieniewski and Stegmann 2022). For example, the host apoplastic phytocytokines PLANT ELICITOR PEPTIDES (PEPs) and SERINE-RICH ENDOGENOUS PEPTIDES (SCOOPs) are generated upon stresses such as wounding, abiotic stress or pathogenic attack and apoplastically transmitted and recognized at membranes of neighboring cells by their PRRs PEP1 RECEPTOR 1/2 (PEPR1/2) and MDIS1-INTERACTING RECEPTOR LIKE KINASE2 (MIK2), respectively (Hander et al. 2019; Krol et al. 2010; Rhodes et al. 2021; Yamaguchi et al. 2010). On the other hand, hormones such as SA or N-Hydroxypipecolic Acid (NHP) and its precursor pipecolic acid (Pip), are transduced to neighboring cells via plasmodesmata and are essential for establishment of systemic acquired resistance (SAR) (Chen et al. 2023; Hartmann et al. 2018).

The role of SAR extends beyond signaling to local cells, since SAR is far-reaching into distal cells and tissues (Zeier 2021). NHP and SA accumulate both at infection sites of *A. thaliana* inoculated with a compatible *Pseudomonas syringae* strain, as well as in the distal leaf of the inoculated plant (Bernsdorff et al. 2016; Návarová et al. 2012; Yildiz et al. 2021; Zeier 2021). Here, the interplay of SA and NHP is essential for establishing SAR (Hartmann and Zeier 2019). Interestingly, EDS1-PAD4 are required for regulation of both NHP and SA, by promoting transcriptional activation of genes involved in their biosynthesis (Bhandari et al. 2019; Hartmann et al. 2018). In distal leaves, SAR induces transcriptional changes and other responses, such as camalexin accumulation, which improves the plant defense readiness and systemically primes leaves for a potential second pathogenic exposure (Bernsdorff et al. 2016; Návarová et al. 2012). This systemic priming response mainly requires NHP, while SA amplifies NHP triggered responses (Bernsdorff et al. 2016; Yildiz et al. 2021). Both hormones require the SA receptor NON-EXPRESSOR OF PR GENES 1 (NPR1) for signal transduction in SAR (Fu and Dong 2013; Yildiz et al. 2021; Zavaliev and Dong 2024). After local accumulation, NHP functions as a mobile defense hormone and might be transported to systemic tissues by vasculature movement, while it might also activate other processes required for distal signaling (Hartmann et al. 2018; Schnake et al. 2020). In wounding for example, Ca^{2+}- or ROS-mediated electrical signals are rapidly spread through the vasculature, but whether similar mechanisms exist for SAR remains to be assessed (Farmer et al. 2020).

The role of TNL/TIR proteins in propagation of both local and systemic defense has gained increasingly more interest in the field over the last years. A single-cell RNAseq dataset

revealed that upon fungal infection with *Colletotrichum higginsianum*, a set of TNL genes was significantly upregulated in vasculature cells, suggesting a role in long distance defense propagation, such as SAR (Tang et al. 2023). On the other hand, the TNL SUPPRESSOR OF ADR1-L2 1 (SADR1) is required for the so-called local acquired resistance (LAR), a process involved in restricting pathogen growth in cells surrounding infection sites (Jacob, Hige, and Dangl 2023). SADR1 NADase activity appears to be required for its function, accompanied by induction of *PATHOGENESIS RELATED 1* (*PR1*) gene expression (Jacob et al. 2023). Surprisingly, SADR1 is dispensable for the tested ETI responses and partially signals in an EDS1-independent manner (Jacob et al. 2023). Mutants of the ADR1 family are fully defective in both local and distal responses, supporting a broader function of ADR1 (Jacob et al. 2023).

The study of SADR1 is in line with the above-mentioned model claiming that the availability or activity of immune components in different cell types around infection sites most likely determines the success of pathogen growth restriction, however how TNLs such as SADR1 are activated in bystander cells remains unclear. An important contributor might be the availability of cytoplasmic Ca^{2+}, since NLR activation induces Ca^{2+}-influx but conversely Ca^{2+} ions also stimulate TNL NADase activity *in vitro*, which could establish a cell-to-cell signal amplification (Lee and Romeis 2022; Ma et al. 2020; Wang and Luan 2024). Ca^{2+}-influx can furthermore dictate the maturation of the DAMP Pep1 from its vacuolar-bound precursor PROPEP1, initiating Pep1 diffusion to neighboring cells, where it is recognized by PEPR1/2 to activate immune responses (Hander et al. 2019). Furthermore, ROS may play an important role in LAR, since ROS has been described to directly inhibit pathogen growth, acting as a barrier to pathogen spread (Torres and Dangl 2005; Torres, Dangl, and Jones 2002; Torres, Jones, and Dangl 2005). Also, systemic responses require ROS production, designating ROS as a major regulator of both local and systemic defense signaling (Alvarez et al. 1998; Miller et al. 2009). This dual role of ROS is dependent on their accumulation level, since low levels of ROS serve signal transduction and high levels cause oxidative stress to the pathogen and restrict their spread (Wu, Qi, and Liang 2023).

1.4 ROS signaling in plant-pathogen interactions

Due to its multifaceted role, production of ROS must be tightly regulated. ROS are produced in different plant subcellular compartments, such as the PM, cell wall, mitochondria, chloroplasts, and peroxisomes (Qi et al. 2017). ROS are singlet oxygen ($^1O_2$), superoxide anion (O_{2-}), hydrogen peroxide (H_2O_2), and hydroxyl radicals, with H_2O_2 being the most stable and acting in inter- and intracellular signaling (Baxter, Mittler, and Suzuki 2014; Kadota et al. 2015). During biotic stress responses, the apoplast is the major site of ROS production, with RBOHs residing at the plasma membrane and generating ROS by transferring electrons from cytoplasmic NADPH or FAD to apoplastic oxygen, generating O_{2-}, which is then converted to H_2O_2 (Suzuki et al. 2011). In *A. thaliana*, the RBOH family consists of 10 members, with RBOHD, and to a lesser extent RBOHF, being the known major producers of apoplastic ROS in plant-pathogen interactions (Nühse et al. 2007; Qi et al. 2017; Torres and Dangl 2005; Torres et al. 2002). Apoplastic ROS is, for example, regulating stomatal movement during biotic stress responses, causing the stomata closure under pathogenic attack since they represent easy entry points for pathogens (Dou and Zhou 2012; Melotto et al. 2006; Qi et al. 2017; Singh et al. 2019).

RBOHD contains multiple regulatory sites or motifs, such as different phosphorylation sites, helix-loop-helix (EF) hand and phosphatic-acid binding motifs, allowing a wide regulatory range to this crucial enzyme (Kadota et al. 2015). In the past, the interplay of Ca^{2+} and ROS has been widely studied and while increase of intracellular calcium is essential for the activation of RBOHD, not all regulatory mechanisms of RBOHD require calcium (Ogasawara et al. 2008). Ca^{2+} ions can bind the EF hand of RBOHD and calcium burst activates several CALCIUM-DEPENDENT PROTEIN KINASEs (CPKs) necessary for RBOHD activation (Oda et al. 2010; Ogasawara et al. 2008). CPK5, for example, N-terminally phosphorylates RBOHD for activation (Dubiella et al. 2013). On the other hand, BIK1 N-terminally phosphorylates RBOHD in a Ca^{2+}-independent manner, though this phosphorylation is most likely only priming RBOHD for further regulation (in a CPK-dependent manner), since BIK1 phosphorylation alone is not sufficient for RBOHD activation (Kadota et al. 2014, 2015; L. Li et al. 2014). Importantly, BIK1 and CPK5 require different RBOHD phosphorylation sites, confirming a multilevel regulation of RBOHD (Dubiella et al. 2013; Kadota et al. 2014; L. Li et al. 2014). Conversely, ROS can increase intracellular Ca^{2+} levels, suggesting a mutual regulation of the two immune outputs (Mazars et al. 2010). RBOHD is furthermore regulated by heterotrimeric G proteins, which directly interact with FLS2 in a resting state and allow for production of sufficient amounts of BIK1 (Liang et al. 2016). Following flg22 perception, the heterotrimeric G proteins are phosphorylated by BIK1 to further enhance ROS production, likely through interaction with RBOHD (Liang et al. 2016). Moreover, cysteine-rich RLK 2 (CRK2) interacts with and C-terminally phosphorylates RBOHD at resting state conditions, which is enhanced upon flg22

perception (Kimura et al. 2020). These examples highlight multiple mechanisms involved in the activation of RBOHD, while the inactivation of RBOHD, and therefore the inhibition of ROS production before and after pathogen infection, is far less studied.

In recent years, three major studies shed light on the inhibitory regulation of RBOHD. After identifying the RLCK PBL13 as a negative regulator of RBOHD (Lin et al. 2015), the E3 ubiquitin ligase PIRE (PBL13 INTERACTING RING DOMAIN E3 LIGASE) was identified as interaction partner of both PBL13 and RBOHD (Lee et al. 2020). Both PIRE and PBL13 *A. thaliana* knockout lines displayed increased level of RBOHD protein accumulation (Lee et al. 2020). The study identified that PIRE constitutively associates with RBOHD in a resting state, ubiquitinating RBOHD C-terminally and leading to its vacuolar degradation (Lee et al. 2020). Upon flg22 perception, PIRE is N-terminally phosphorylated by PBL13, inactivating PIRE and therefore preventing RBOHD degradation (Lee et al. 2020). Fascinatingly, a different study identified that the papain-like cysteine protease (PLCP) XYLEM CYSTEINE PEPTIDASE 1 (XCP1) is the protease that destabilizes RBOHD by vacuolar degradation in resting state (Liu et al. 2023). Upon pathogen infection, XCP1 is inhibited by CYSTATIN 6 (CYS6), preventing RBOHD degradation and allowing its accumulation in response to the pathogen (Liu et al. 2023). XCP1 protease activity is required to balance RBOHD protein abundance and therefore ROS production.

1.5 The role of proteases in plant immunity

Tight control of immune responses is of utmost importance for plants, as activation of immunity often comes at the cost of growth and development (He, Webster, and He 2022; Monson et al. 2022). Proteolysis, the process of breaking down proteins to peptides or amino acids via ubiquitination or protease activity, is the essential mechanism in regulating protein abundance and activity (Liu et al. 2024). Therefore, the role of proteases in plant immunity extends to almost all subcellular compartments and the apoplastic space. This allows a fast protein turnover and precise spatial regulation, quickly controlling plant immune responses (Liu et al. 2024). Accordingly, some proteases are required for the degradation of proteins, which are either dysfunctional or not needed, and recycle their amino acids, while others cleave proteins to contribute to their maturation and activation (Van Der Hoorn 2008).

Plants possess a plethora of different proteases, which can be classified by their catalytic properties, depending on the nucleophile they employ for the peptide bond cleavage. The four main classes are cysteine, serine, aspartic, or metalloproteases (Liu et al. 2024). Proteases are furthermore categorized in different clans by the MEROPS database (Rawlings et al. 2018). PLCPs, for example are categorized as C1A proteases, while metacaspases, another type of cysteine protease, belongs to the C14 family (Rawlings et al. 2018). Most proteases, independent of their catalytic site, contain an N-terminal signal peptide (SP) for the protein's

secretion, a pro-domain, inhibiting unwanted functions or degradation, and lastly, the actual protease domain with catalytic active sites (Misas-Villamil, van der Hoorn, and Doehlemann 2016; Richau et al. 2012). Some proteases additionally possess a C-terminal domain, such as a granulin domain, which function remains uncharacterized (Misas-Villamil et al. 2016; Richau et al. 2012). Both SP and pro-domain are cleaved off in the protease maturation process, either by self-cleavage or by cleavage through other enzymes (Misas-Villamil et al. 2016; Richau et al. 2012).

Independent of their category, many proteases contribute to plant defense through different mechanisms (Figure 2). For instance, some proteases target pathogenic proteins, such as the *A. thaliana* SECRETED ASPARTIC PROTEASE 1 and 2 (SAP1 and SAP2) (Y. Wang et al. 2019). SAP1 and SAP2 are apoplastically secreted during infection with *P. syringae*, cleaving the bacterial MucD protein and thereby mediating resistance to the bacterium (Y. Wang et al. 2019).

Proteases are furthermore able to release host immunogenic peptides, which are activating immune responses upon infection (Figure 2). The aforementioned Ca^{2+}-mediated maturation of the DAMP Pep1 from the vacuolar-bound precursor PROPEP1 is mediated by cleavage of the metacaspase MC4 (Hander et al. 2019). In undisturbed tissues, MC4 exists in its inactive zymogen form (zMC4), which still contains the N-terminal pro-domain. Damage at the *A. thaliana* root epidermal cells induce an influx of Ca^{2+}, which activates MC4 and cleavage of PROPEP1 to release Pep1 (Hander et al. 2019) (Figure 2). In the apoplast, subtilases of the SBT3 family cleave different types of PROSCOOP peptides, releasing their mature SCOOP form (Yang et al. 2023). SBT3.5, for example, is cleaving PROSCOOP12, while PROSCOOP20 is cleaved by SBT3.6, SBT3.8 and SBT3.9 (Yang et al. 2023) (Figure 2). While high specificity is achieved at the level of peptide processing, all known SCOOP peptides are recognized by the PRR MIK2 (Hou et al. 2021; Rhodes et al. 2021; Yang et al. 2023). In the maize apoplast, *Z. mays* immune signaling peptide 1 (Zip1) is released from its precursor PROZIP1 by SA-activated PLCPs, such as CORN CYSTEINE PROTEASE 1 (CP1) and CP2, and conversely promotes accumulation of SA and protease activity (Ziemann et al. 2018) (Figure 2). A similar positive feedback loop for SA biosynthesis was described in *A. thaliana*. SA treatment leads to activity of XCP1, which cleaves part of a caspase-like motif of PR1 to release CAPE9 (CYSTEINE-RICH SECRETORY PROTEIN, ANTIGEN 5, AND PATHOGENESIS-RELATED 1 PROTEIN (CAP)-DERIVED PEPTIDE 9) (Chen et al. 2023) (Figure 2). CAPE9 is then required for activating SA biosynthesis and systemic immunity (Chen et al. 2023). Since XCP1 is furthermore required for degradation of RBOHD in resting state tissue, XCP1 has a dual role and multiple sites of action in regulating plant immunity (Chen et al. 2023; Liu et al. 2023).

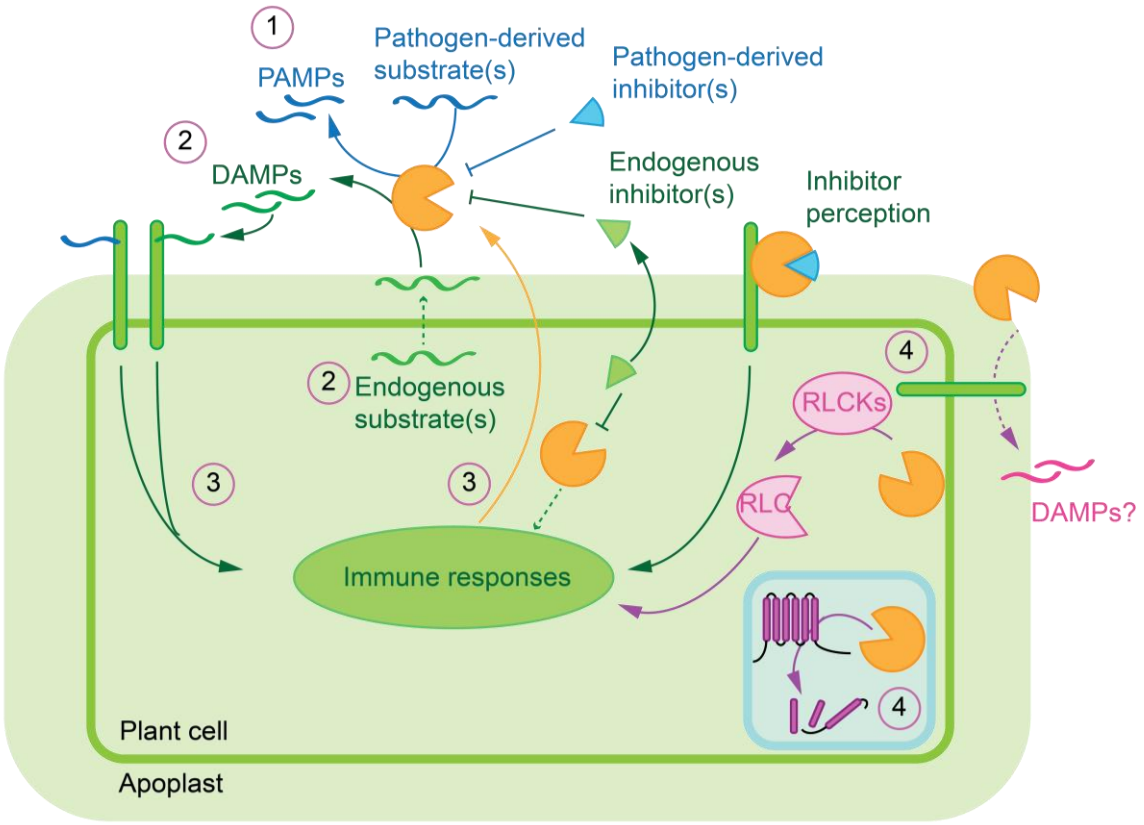


Figure 2: Overview of proteases acting in plant immunity. Proteases can cleave (1) pathogen-associated molecular patterns (PAMPs) and (2) damage-associated molecular patterns (DAMPs) which are further recognized by plasma-membrane receptors. (3) Secretion of proteases to the apoplast leads to cleavage of substrates in the apoplast which then induces immune responses, establishing a positive feedback loop. (4) Proteases target plant components for regulation of immune activation or inactivation. Examples numbered and indicating are described in the text. The model is partially based on Misas-Villamil et al., 2016.

Another important role of proteases in plant immunity is their contribution to the activity regulation of host immune components (Figure 2). Most studied proteases activate themselves by self-cleavage, induced for example by a change of pH, such as for MC9, or the presence of Ca^{2+}, as for MC4 (Fernández-Fernández, Stael, and Van Breusegem 2023; Hander et al. 2019; Vercammen et al. 2004). Other proteases may require cleavage by distinct proteases, though identification of proteolytic signaling cascades remains a challenge (Paulus and Van der Hoorn 2019). One identified example of such a cascade is the regulation of tomato PLCP Rcr3 (Paulus et al. 2020). The apoplastically localized protease is not relying on its catalytic active site for maturation but is processed by secreted subtilase P69B, that activates Rcr3 by cleavage between the inhibitory pro-domain and the protease domain (Paulus et al. 2020).

The co-receptor BAK1, required for a plethora of immune signaling responses, is a proteolytic target in a process named receptor shedding (Zhou et al. 2019). Treatment with flg22 induces a Ca^{2+}-dependent cleavage of BAK1 specifically at the Asparagine 287 residue ($BAK1^{D287}$), which lies between the TM and ECD (Zhou et al. 2019). Mutation of the proteolytic cleavage

site inhibits immune signaling by preventing BAK1 PM localization and phosphorylation of BIK1 (Zhou et al. 2019). Though this cleavage site is conserved in *A. thaliana*, *N. benthamiana* and *Saccharomyces cerevisiae*, the protease(s) responsible for BAK1 cleavage have not yet been identified and the precise role of cleaved BAK1 in immunity remains to be understood (Zhou et al. 2019) (Figure 2). Another intriguing role of a protease in surface-triggered immunity is that of MC4 cleaving the plasma membrane-anchored RLCK PBL19 to a truncated form (ntPBL19) which interacts with and phosphorylates EDS1 (Li et al. 2022). While a nuclear pool of EDS1 is important for ETI signaling, PBL19-mediated EDS1 phosphorylation may facilitate a cytoplasmic accumulation of EDS1 under chitin elicitation (García et al. 2010; Li et al. 2022) (Figure 2). These findings suggest that the localization of EDS1 is important for executing different types of immune signaling and that this is potentially mediated by protease activity.

While BAK1 and PBL19 cleavage is an activation mechanism mediated by proteases, other proteases are required to inactivate immune components. The DeSUMOylating isopeptidase 3A (Desi3A) (SUMO; SMALL UBIQUITIN-LIKE MODIFIER) for example, is deSUMOylating FLS2 in a resting state to inactivate immune signaling (Orosa et al. 2018). Upon flg22 recognition, Desi3A is degraded, promoting SUMOylation of FLS2 and release of BIK1, to activate intracellular immune signaling (Orosa et al. 2018). On the other hand, as mentioned above, ROS production is regulated by RBOHD vacuolar degradation, mediated by the PLCP XCP1 (Liu et al. 2023) (Figure 2). Overall, the function of proteases is far-reaching both in their mechanisms and localizations, reinforcing their essential role in establishing a well-operating immune system (Figure 2).

1.6 The papain-like cysteine protease RD19 in plant immunity

While a variety of different classes and clans of proteases have been studied in context of immunity, increasing evidence places PLCPs as central hubs in plant immune signaling (Misas-Villamil et al. 2016). Mechanisms of some PLCPs, like XCP1, are well studied (Chen et al. 2023; Liu et al. 2023), whereas for others, an involvement in immunity could be demonstrated but the precise mechanisms of activation and function are not well understood. For example, the PLCP RD19A was previously identified to carry a role in resistance to *Ralstonia solanacearum* (Bernoux et al. 2008). While RD19A localized to mobile vacuole-associated vesicles and the vacuole in non-immune elicited conditions, presence of the *R. solanacearum* effector PopP2 (Pseudomonas outer protein P2) led to co-localization of RD19A and PopP2 to the nucleus (Bernoux et al. 2008). Since an *A. thaliana* knockout mutant of *rd19a* was more susceptible to *R. solanacearum*, the authors proposed that RD19A is needed for PopP2-triggered RRS1-R–mediated resistance and that the RD19A-PopP2 nuclear complex is required for the resistance response (Bernoux et al. 2008). Nevertheless, it was not

shown whether localization to the nucleus requires active RD19A and therefore, whether resistance truly requires the PLCP activity.

Furthermore, RD19A was identified in an IP-MS/MS experiment as interacting more strongly with PAD4-YFP than with SAG101-YFP six hours after activating TNL-ETI using *Pst* DC3000 AvrRps4 (Sun et al. 2021). Different experiments, such as co-immunoprecipitation or a split-luciferase assay, verified a specific interaction of RD19A with PAD4 but not EDS1 and SAG101 (Zeng et al. 2024). Similarly, transient assays in *A. thaliana* protoplasts or in *N. benthamiana* showed that RD19A co-localizes to the nucleus with PAD4 in its zymogen form (proRD19) (Zeng et al. 2024; Figure 3). Here, PAD4 appears to promote the nuclear localization and the maturation of RD19A as shown by protein blots of nuclear fractions (Zeng et al. 2024). Even though PAD4 interacts most strongly with proRD19A and the fully mature form (Figure 3), interaction with full length RD19A was still detected (Zeng et al. 2024). Nevertheless, since this was determined in transient assays without any immune activation, a constitutive interaction of PAD4 with RD19A at all maturation stages cannot be concluded.

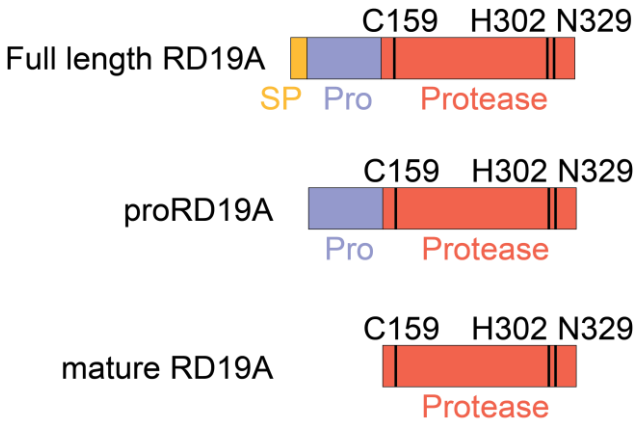


Figure 3: Three maturation forms of RD19A. RD19A consists of an N-terminal signal peptide (SP), which is cleaved off in the first maturation step, resulting in the zymogen proRD19A form. In a second step, the N-terminal pro-domain (Pro) is cleaved off, resulting in mature RD19A with three catalytic active sites: C159 (cysteine 159), H302 (histidine 302) and N329 (asparagine 329).

Interestingly, presence of EDS1 reduces the RD19A-PAD4 interaction, while mutation in the PAD4 MLF motif, which reduces interaction with EDS1, increases interaction with RD19A (Zeng et al. 2024). This suggests a competitive binding of EDS1 and RD19A to PAD4 (Zeng et al. 2024). Indeed, a possibility would be that RD19A is part of a PAD4 function independent of the EDS1-PAD4 heterodimer, such as previously described for the N-terminal PAD4 LLD domain in resistance to green peach aphid (GPA) (Dongus et al. 2020). Overexpression of *RD19A* in a Col-0 background induces strong symptoms of autoimmunity, such as stunted growth, increased resistance to *Pst* DC3000, increased immune gene expression, and cell

death, which was dependent on the two tested protease active sites C159 and N329, and on EDS1 and PAD4 but not SAG101 (Zeng et al. 2024).

In conclusion, recent publications established a role of RD19 in both ETI and basal immune responses and link this PLCP to the immune signaling hub of the EDS1 family. However, the molecular mechanisms under which RD19 is activated in these immune responses and which substrates RD19 is targeting, remains to be investigated.

1.7 Aims of the thesis

While our understanding of the role of the EDS1 family in immune signaling was considerably furthered in the recent years, it remains to be understood how the two different signaling branches, EDS1-PAD4-ADR1 and EDS1-SAG101-NRG1, are selectively activated, or are simultaneously activated but have distinct functions in the plant immune response. Specific interaction partners of the two branches might therefore shed light on their independent functions. This study aimed to gain better understanding of the role of EDS1-PAD4-ADR1 by deciphering a novel, specific interaction partner of PAD4, the PLCP RD19. We hypothesized that RD19 and PAD4 interaction has an important function in plant immunity. Since EDS1-PAD4-ADR1 is a convergence point of intracellular and surface immune receptor signaling, a first aim was to investigate the role of RD19 in ETI and PTI responses. A second aim was to characterize the localization and protease activity of RD19. To fully understand the role of RD19 in immune responses and how this role links to the role of PAD4, identifying substrates of RD19 in immune activated conditions was the last aim.

2 Results

The initial part of this study (chapter 2.1 and 2.2) was conducted in a collaboration with the group of Prof. Dr. Haitao Cui, Agricultural University of Shangdong, China. Results presented in these parts of the thesis were partially published in Zeng et al. 2024. Any data previously published is indicated in the corresponding figure legend and text. If not mentioned otherwise, experiments shown in this thesis were not previously published.

2.1 RD19 is not required to establish ETI triggered by oomycete *Hyaloperonospora arabidopsidis* (*Hpa*) Emwa1

A. thaliana possesses four homologues of the PLCP RD19: RD19A, RD19B, RD19C, and RD19D (Richau et al. 2012). RD19A and RD19C have previously been described to be involved in *A. thaliana* immune processes (Bernoux et al. 2008; Zeng et al. 2024). Following the establishment of the specific interaction between RD19A and PAD4, the software Genevestigator was used to get an overview of the expression patterns of *RD19A*, *RD19C*, and *PAD4* in response to different biotic and abiotic stresses, and PTI (Figure 4A). Inspecting the overall patterns of up- and downregulations, *RD19A* and *RD19C* clearly share a very similar expression pattern throughout the various stresses, while their expression is very distinct, in some cases even opposite to *PAD4* (Figure 4A). This gene expression overview showed that even though RD19 and PAD4 interact, their roles in immunity might be (partially) distinct or potentially antagonistic. Nevertheless, a closer look at a specific RNAseq dataset, where the well-studied pathogen *Pst* AvrRps4 was used as a trigger, revealed also similarities in their expressions (Figure 4B; Zeng et al. 2024). Expression analysis of this RNAseq dataset was extended to *RD19B* and *RD19D*, but their expression was not induced by the TNL-ETI trigger (Figure 4B). On the other hand, *RD19A* and *RD19C* expression was upregulated, peaking at 8 hpi for *RD19A* and slightly weaker at 24 hpi for *RD19C* (Figure 4B). Gene expression analysis of *PAD4* also showed an increase at 8 hpi, with a peak of expression at 24 hpi, suggesting a longer requirement for presence of *PAD4* in immune responses. Alike the phenotype observed in *pad4* mutant lines (Feys et al. 2001), T-DNA insertion lines of *rd19a*, *rd19c* and the double mutant *rd19ac* showed increased susceptibility to *Pst* DC3000 AvrRps4, with an additive effect in the double mutant line (Zeng et al. 2024). This phenotype raised the question, whether the role of RD19 in TNL-ETI extends to other types of pathogens, which also require PAD4 for full immune responses of the plant. Therefore, plants were treated with the *A. thaliana* pathogen *Hyaloperonospora arabidopsidis* (*Hpa*) isolate Emwa1, which is recognized by the TNL RPP4 (van der Biezen et al. 2002) (Figure 4C). Spray inoculation was performed on 4.5-week-old plants and infection phenotypes were visualized 4 dpi using trypan blue staining, which stains both the host plant cell death and the oomycete growth (Keogh, Deverall, and McLeod 1980). Col-0 wild-type plants were used as the resistant control, showing

cell death at infection sites (round blue staining of cells) and trailing necrosis (elongation of dying cells) on the leaf (Figure 4C, black arrows). The mutant lines *eds1-12* and *pad4-1* (hereafter *eds1* and *pad4*) were used as susceptible controls and growth of *Hpa* Emwa1 on these lines could be observed by the trypan blue staining (Figure 4C, red arrows). All knockout lines of *RD19* showed a comparable phenotype as the Col-0 control, with clear cell death spots and some trailing necrosis, indicating that these lines were not impaired in resistance against *Hpa* Emwa1 and therefore in RPP4-dependent ETI (Figure 4C, black arrows). Indeed, analysis of sporulation at 7 dpi verified that *Hpa* Emwa1 was not growing on either of the *rd19* mutant lines, while *eds1* and *pad4* were highly susceptible (Figure 4D).

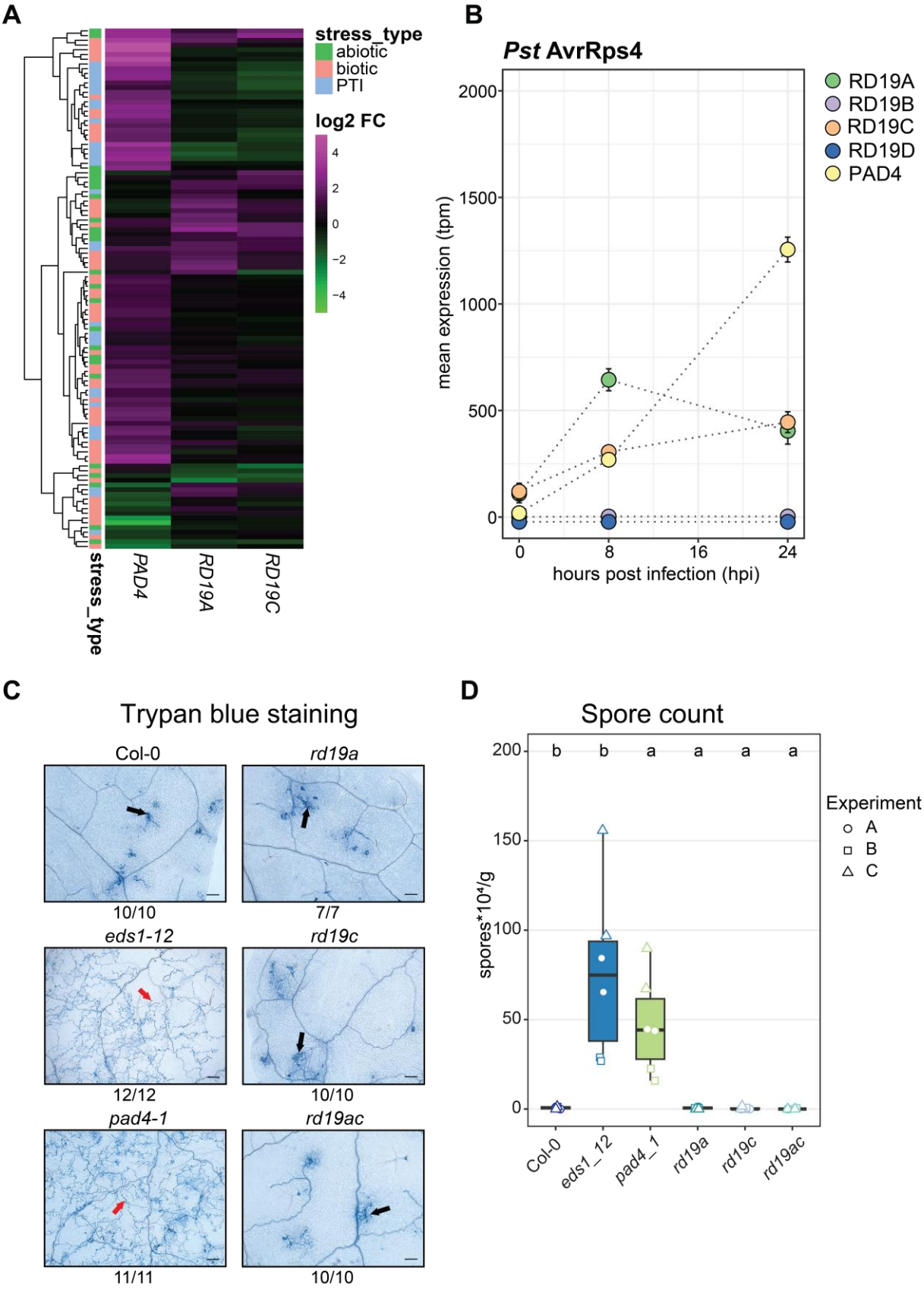


Figure 4: Requirement of RD19 in a subset of TNL-ETI responses. (**A**) Heatmap of *PAD4*, *RD19A* and *RD19C* gene expression during abiotic, biotic and PTI stress types. Dataset from Genevestigator Affymetrix Arabidopsis ATH1 genome array, filtered for WT genetic background and clustered using Euclidean distance. (**B**) Expression analysis of *RD19A*,

RD19B, *RD19C*, *RD19D* and *PAD4* from publicly available RNA-seq data set PRJNA477936; GEO: GSE116269, downloaded from the NCBI SRA data bank. Expressions of genes in Col-0 are shown hours post infection (hpi) with *Pst* AvrRps4. (**C** and **D**) *Hyaloperonospora arabidopsidis* (*Hpa*) Emwa1 spray inoculation of 4.5-week-old *A. thaliana* Col-0, *eds1-12*, *pad4-1*, *rd19a*, *rd19c* and *rd19ac*. (**C**) Trypan blue staining of leaves at 4 dpi, visualized by light microscopy. Black arrows indicate cell death, red arrows indicate oomycete growth. Similar colonization and cell death patterns were observed on 7-12 plants in 3 biological replicates. Scale bars: 200 µm. (**D**) Spore count of *Hpa* Emwa1 at 7 dpi. Graphs represent three biological replicates with two technical replicates (pool of 4-6 plants). Quadratic root transformation was used to reach normal distribution. Genotypes sharing letters above boxplots do not show statistically significant differences (ANOVA and Tukey HSD test, $p < 0.05$).

These results suggest that while RD19 and PAD4 interact and share certain phenotypes in TNL-ETI responses, general gene expression patterns in response to different stresses are distinct and PAD4 is more broadly required for immune responses than RD19.

2.2 RD19 is dispensable for establishing basal resistance responses to biotrophic and necrotrophic pathogens

The EDS1-PAD4-ADR1 immune signaling branch is unique for its requirement in basal immunity, an immune response leading to pathogen restriction without the activation of cell death (Cui et al. 2017; Lapin et al. 2019; Rietz et al. 2011). Following only a certain requirement in TNL-ETI, it was next investigated whether RD19 is required for basal immune responses. The mutant lines *rd19a*, *rd19c* and *rd19ac* showed increased susceptibility to the fungal pathogen *Golovinomyces cichoracearum* (Zeng et al. 2024). Furthermore, the *Hpa* isolate Noco2 was used as an oomycete activating basal immunity. Plants were spray inoculated and sporulation was measured by spore counts 5 dpi (Figure 5A). In comparison to *Hpa* Emwa1, the isolate Noco2 grew on the susceptible Col-0 plants, while the wild-type accession Wassilewskija (Ws-2) was used as resistant control (Figure 5A). For simplicity, due to the comparable phenotypes of *rd19a* and *rd19c* mutants and the additive effect observed in *rd19ac* double mutants treated with *Pst* DC3000 AvrRps4, exclusively the double mutant line was included in the following experiments. While *eds1* mutants were, as previously shown, hypersusceptible to *Hpa* Noco2 (Parker et al. 1996; Figure 5A), *rd19ac* mutant susceptibility was comparable to Col-0, indicating that loss of *RD19A* and *RD19C* did not influence plant resistance against *Hpa* Noco2 (Figure 5A). Furthermore, resistance to the avirulent bacterial strain *Pst* DC3000 was tested. Plants were infiltrated with bacterial solutions and resistance was analyzed at 3 dpi by calculating the colony forming units (CFUs) (Figure 5B). As previously described, *pad4* mutants displayed enhanced susceptibility to *Pst* DC3000 (Feys et al. 2001), while the *rd19ac* knockout line showed CFUs comparable to Col-0 (Figure 5B). A cross of *rd19ac* and *pad4* was as susceptible to *Pst* DC3000 as the *pad4* single mutant, phenocopying the effect of loss of only *PAD4* (Figure 5B).

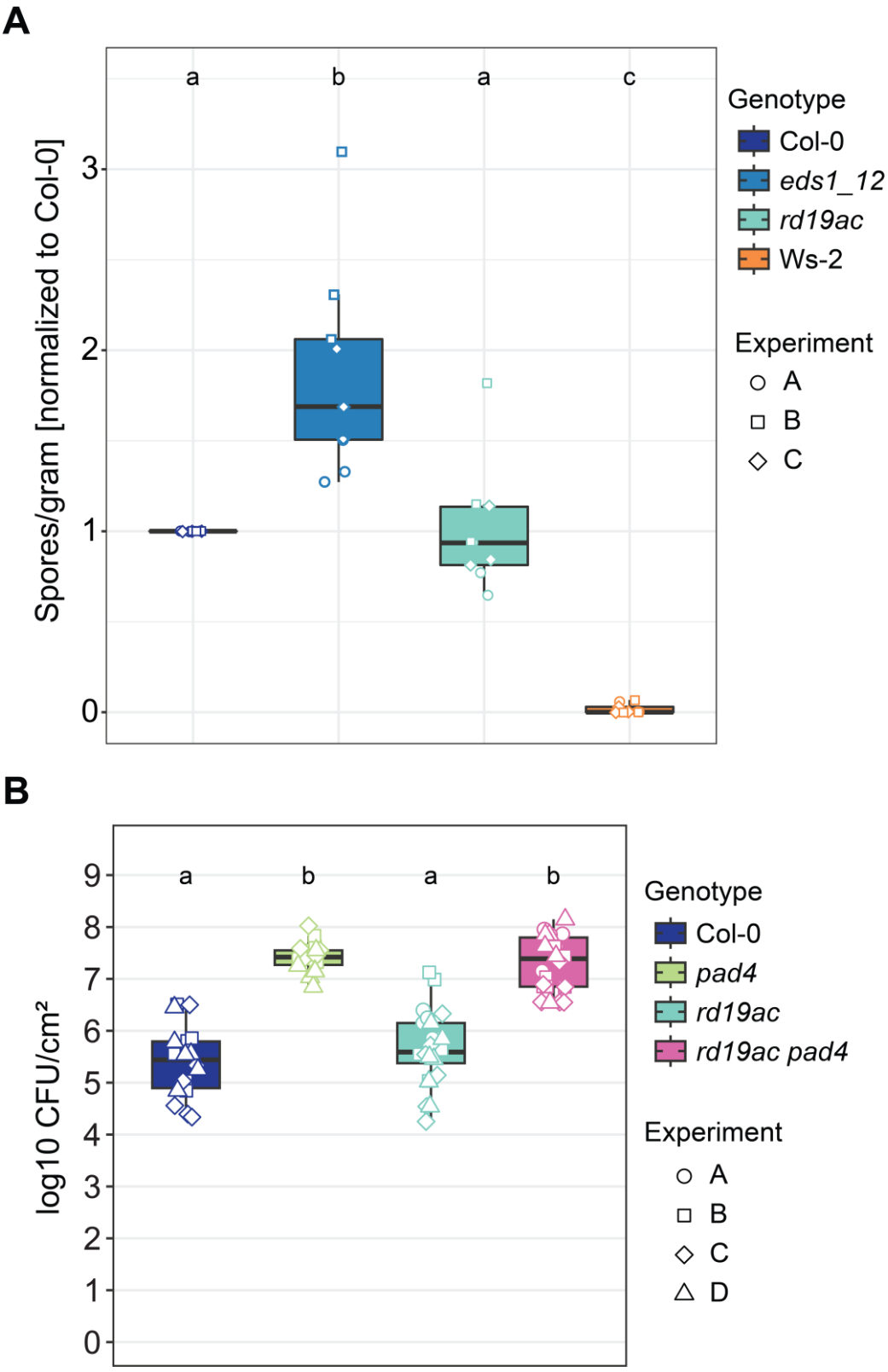


Figure 5: Testing the role of RD19 in basal resistance responses. (**A**) *Hpa* Noco2 spray inoculation of 4.5-week-old *A. thaliana* Col-0, *eds1-12*, *rd19ac* and Ws-2. Spore count per plant weight was normalized to Col-0. Graphs represent three biological replicates, each represented by their own shape, with two technical replicates (pool of 4-6 plants each). Genotypes sharing letters above boxplots do not show statistically significant differences (Kruskal-Wallis and pairwise Wilcox-test, $p < 0.05$). (**B**) *Pst* DC3000 growth assay in *A. thaliana* Col-0, *pad4*, *rd19ac* and *rd19ac pad4* at three days post syringe infiltration. Boxplots show

colony forming units (CFU)/cm^2 with each shape representing one biological replicate. Genotypes sharing letters above boxplots do not show statistically significant differences (ANOVA and Tukey HSD test, $p < 0.05$, n=24).

Finally, the necrotrophic fungus *Botrytis cinerea* was used for infection assays. Even though infection with a necrotrophic pathogen does not activate basal immunity per se, *B. cinerea* infection causes strong cell wall damage, releasing DAMPs which when recognized, activate a response similar to basal immunity in the plant (Yamada et al. 2016). Infection was carried out by placing drops of fungal inoculum on the plant leaves and measuring the lesion area of infection at 2 dpi. As a susceptible control, the receptor mutant *rlp23* was included in the assay (Ono, Mise, and Takano 2020). Though variation in lesion area was high throughout the experiments, *rlp23* mutants showed significantly higher susceptibility to *B. cinerea* than Col-0 (belowFigure 6). On the contrary, *rd19ac* showed a similar phenotype to Col-0, indicating that RD19 was not required in *B. cinerea* immune responses (belowFigure 6).

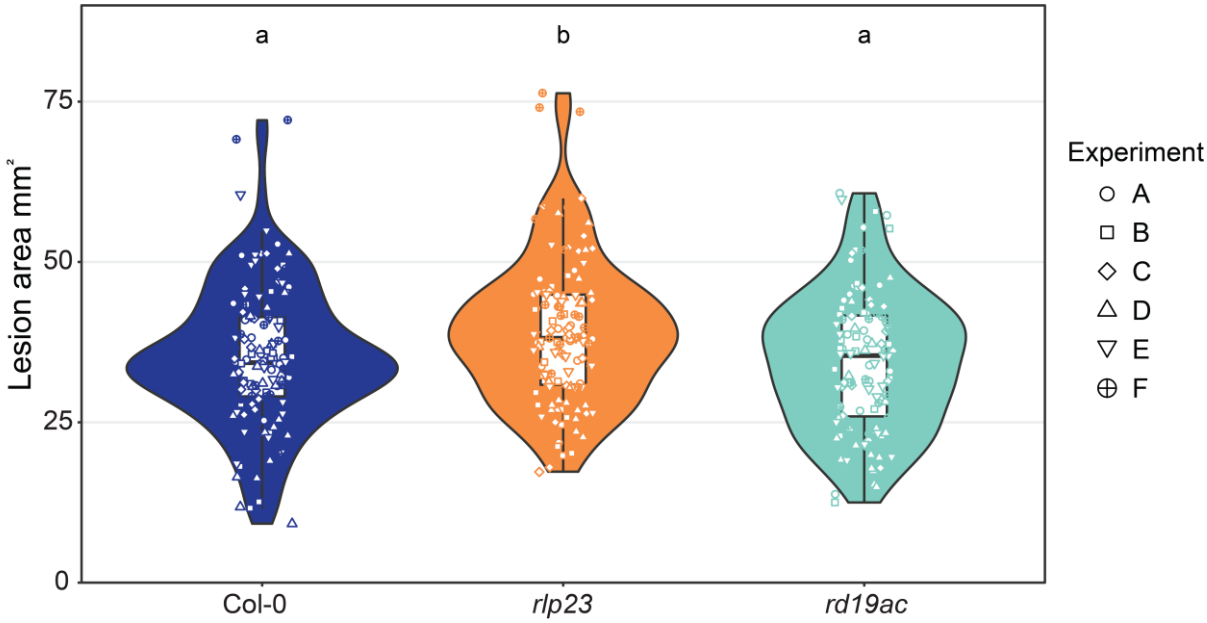


Figure 6: Requirement of RD19 for resistance to necrotrophic fungus *Botrytis cinerea*. *B. cinerea* spores were drop inoculated on leaves of 4.5-week-old *A. thaliana* Col-0, *rlp23* and *rd19ac,* and as a proxy of pathogen growth, lesion areas were measured at 2 dpi using ImageJ. Violin blots show lesion areas in mm^2, with dots of the same shape representing one biological replicate. Genotypes sharing letters above boxplots do not show statistically significant differences (Kruskal-Wallis and pairwise Wilcox-test, $p < 0.05$, n=90).

While RD19 was indispensable for resistance to *Golovinomyces cichoracearum* (Zeng et al. 2024), resistance to pathogens tested in this thesis did not require RD19 to activate basal immunity. Comparable to responses in TNL-ETI, requirement of RD19 in basal immunity might be restricted to certain types of pathogens.

2.3 RD19 is required for nlp20-triggered ROS burst regulation

One of the latest identifications of an EDS1-PAD4-ADR1 specific requirement in immune responses is the role of this branch in a certain type of PTI (Pruitt et al. 2021). The peptide nlp20 recognized by the receptor RLP23 triggers EDS1-PAD4-ADR1 dependent immune responses, while flg22 recognition by the RK FLS2 activates immune responses independent of this branch (Pruitt et al. 2021). Initial analysis of two publicly available RNAseq datasets revealed continuous expression of *RD19A* and *RD19C* during the first two hours following flg22 treatment (Figure 7). *RD19B* and *RD19D* were not expressed during either treatment (Figure 7). Treatment with nlp20 induced strong upregulation of especially *RD19A* but also *RD19C* expression 8 hpi, decreasing over the course of 24 hpi for *RD19A* but slightly increasing for *RD19C* (Figure 7). Therefore, both nlp20 and flg22 were used to investigate a potential role of RD19 in PTI responses, that are either EDS1-PAD4-ADR1 dependent or independent. PTI is defined by several hallmark outputs, such as transcriptional reprogramming, MAPK activation, ROS burst, or Ca^{2+}-influx (Bjornson and Zipfel 2021). In this study, the first three outputs were chosen to investigate the role of RD19 in PTI.

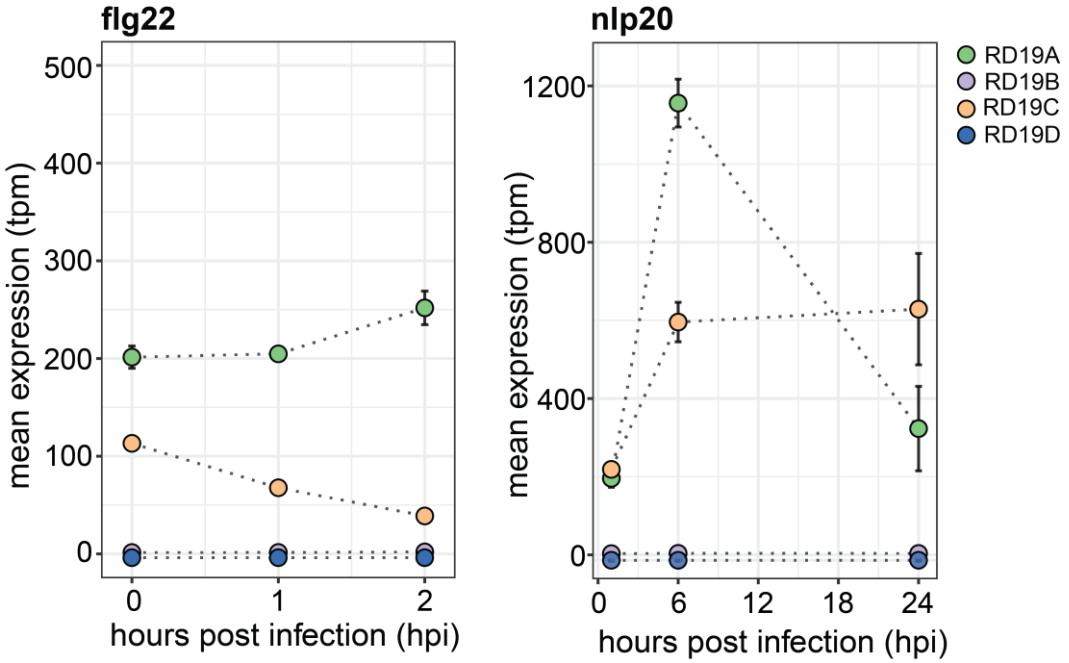


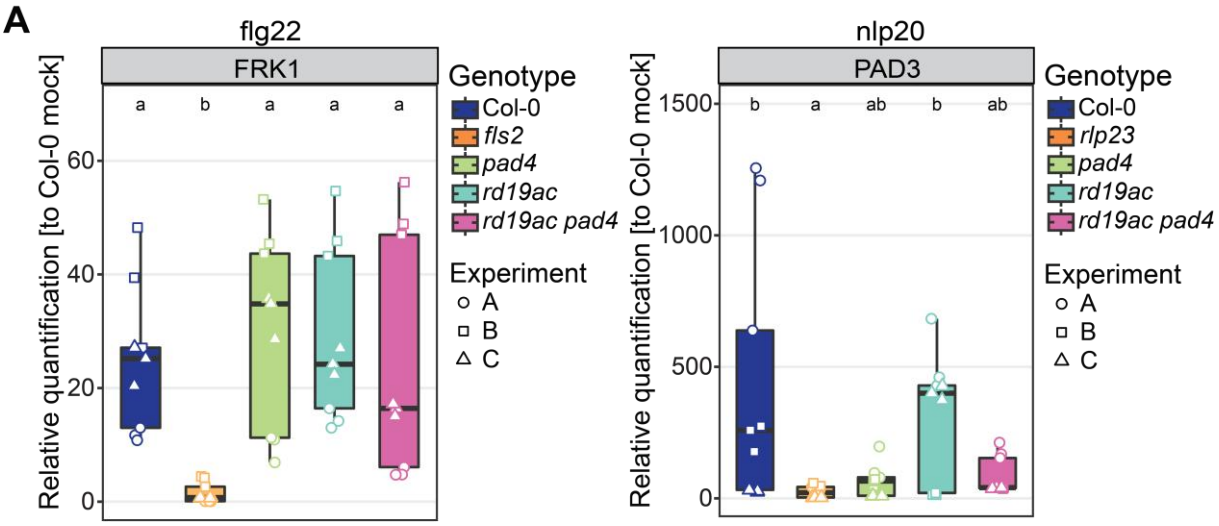
Figure 7: *RD19* expression analysis of publicly available RNA-seq data sets following flg22 and nlp20 treatment. RNA-seq data sets were downloaded from the NCBI SRA data bank (flg22: PRJNA339762; GEO: GSE85923, nlp20: PRJNA549850; GEO: GSE133053). Expression of *RD19A*, *RD19B*, *RD19C* and *RD19D* are shown hours post infection (hpi) with flg22 and nlp20. The treatment was performed on 12- and 10-day old Col-0 seedlings, respectively.

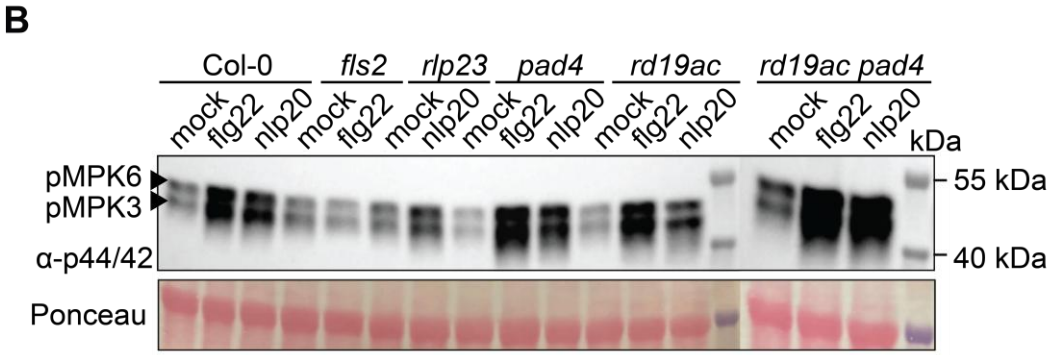
Plants were syringe infiltrated with elicitor solutions containing flg22 or nlp20, and a mock solution and samples for gene expression analysis were harvested at 3 hpi. Successful flg22 treatment induced expression of flg22 marker gene *FLG22-INDUCED RECEPTOR-LIKE*

KINASE 1 (*FRK1*) in Col-0 plants, while the non-responsive *fls2* mutant did not induce *FRK1* expression upon treatment (Figure 8A). The tested mutant lines *pad4*, *rd19ac*, and *rd19ac pad4* all exhibited induction of *FRK1* gene expression comparable to Col-0 (Figure 8A). *PHYTOALEXIN DEFICIENT 3* (*PAD3*), encoding an enzyme required for biosynthesis of the phytoalexin camalexin, has been previously established as an important gene in the nlp20-triggered pathway and was therefore used to test for transcriptional changes following nlp20 treatment (Pruitt et al. 2021). Col-0 plants showed induced expression of *PAD3*, while this was lost in the *rlp23* receptor mutant (Figure 8A). The *pad4* mutants displayed partial loss of PAD3 expression, as PAD4 is required for full functional transcriptional reprogramming (Figure 8A; Pruitt et al. 2021). The *rd19ac pad4* mutant phenocopied the *pad4* mutant, while *rd19ac* mutants induced *PAD3* expression comparable to Col-0 (Figure 8A). While *PAD4* is required only for nlp20-triggered transcriptional reprogramming, loss of RD19 did not lead to an effect in both tested gene expressions, suggesting that *RD19* is not required for flg22- or nlp20-induced transcriptional reprogramming.

Next, MAPK activation in Col-0, *fls2*, *rlp23*, *pad4*, *rd19ac*, and *rd19ac pad4* treated with flg22 and nlp20 was analyzed by immunoblot assay, 15 min after the treatment. The p44/42 antibody was used for visualization of phosphorylated MPK3 and MPK6 in protein samples (Figure 8B). Treatment with both flg22 and nlp20 induced activation of MAPK in Col-0 samples, while *fls2* and *rlp23* mutants did not respond to the flg22 and nlp20 treatment, respectively, and exhibited weaker MPK3 and MPK6 accumulation (Figure 8B). As previously reported, *pad4* mutants were not affected in MAPK activation after both elicitor treatments and neither were *rd19ac* and *rd19ac pad4* mutants (Figure 8B; Pruitt et al. 2021).

As a last PTI output, production of ROS was visualized by measuring relative light units (RLUs) following flg22 and nlp20 treatment. Flg22 treatment induced production of ROS with a peak around 10 min after adding the elicitor to leaf discs in Col-0, *pad4*, *rd19ac*, and *rd19ac pad4* plants, but not in the *fls2* mutants (Figure 8C). Comparable induction of ROS burst was reflected in statistical analysis performed on the area under curve (AUC) of all lines (Supplementary Figure S 1). Nlp20 treatment induces a generally weaker ROS burst in Col-0 plants and contrary to a previous report, production of ROS in *pad4* mutants was comparable to Col-0 (Pruitt et al. 2021). As expected, no ROS was produced in *rlp23* mutants since nlp20 is not recognized in the receptor mutant (Figure 8D). Surprisingly, the *rd19ac* double mutant showed a significantly higher ROS burst compared to Col-0 (Figure 8D). This ROS burst was dependent on PAD4, since the increased ROS burst was lost in the *rd19ac pad4* double mutant, which behaved comparable to *pad4* (Figure 8D). The statistical significance of the increase in ROS production in *rd19ac* was verified by measurement of the AUC (Supplementary Figure S 1).


A
flg22
FRK1
Relative quantification [to Col-0 mock]
a b a a a
Genotype
Col-0
fls2
pad4
rd19ac
rd19ac pad4
Experiment
A
B
C
nlp20
PAD3
b a ab b ab
rlp23


B
Col-0
fls2
rlp23
pad4
rd19ac
rd19ac pad4
mock
flg22
nlp20
kDa
pMPK6
pMPK3
α-p44/42
55 kDa
40 kDa
Ponceau

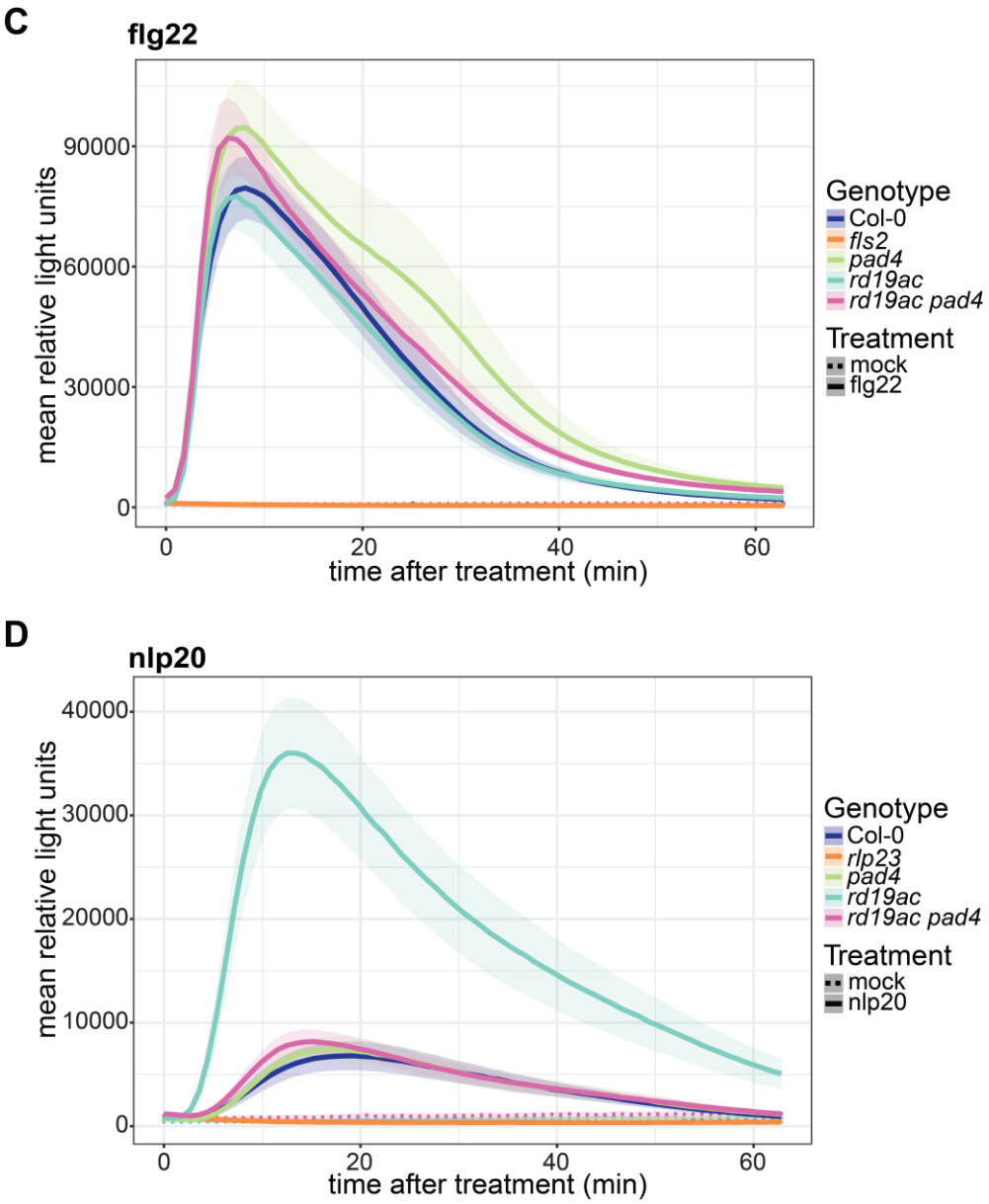


Figure 8: The role of RD19 in PTI following flg22 and nlp20 treatment. Col-0, *fls2*, *rlp23*, *pad4*, *rd19ac* and *rd19ac pad4* were used to analyze PTI hallmark outputs in 4.5-week-old plants. (**A**) Expression of *FRK1* and *PAD3* 3 h after elicitor treatment, determined by RT-qPCR. Relative quantification is represented in boxplots with dots of the same shape corresponding to technical replicates from one independent experiment. Data was normalized to Col-0 mock conditions in each biological replicate. UBI5 was used as a housekeeping gene. Genotypes sharing letters above boxplots do not show statistically significant differences (Kruskal-Wallis and Nemenyi-Test, $p < 0.05$, n=9). (**B**) MAPK activation was assessed by blotting with phospho-specific p44-p42 antibody. *fls2* and *rlp23* were used as negative controls for flg22 and nlp20 treatment, respectively. Samples were taken 15 minutes after infiltration. Pierce assay was performed to load equal amounts of protein and Ponceau-stained Rubisco served as a loading control. Similar MAPK activation was observed in 3 independent biological replicates. (**C**) and (**D**) ROS burst assay over 60 min of leaf discs treated with elicitor solutions. Shown are mean relative light units after (**C**) flg22 and (**D**) nlp20 treatment with standard errors shown by distribution around curves. n=24 (flg22 and nlp20) and n=6 (mock) leaf discs from three independent biological replicates.

Taken together, these results indicate that RD19 and PAD4 likely fulfill differing roles in PTI, with RD19 potentially acting as a negative regulator of ROS production.

2.4 Increased ROS burst in *rd19ac* is dependent on RBOHD

RBOHD is the major regulator of ROS produced during biotic stresses (Nühse et al. 2007; Qi et al. 2017; Torres and Dangl 2005; Torres et al. 2002). Therefore, the accumulation of the RBOHD protein in *rd19ac* lines was analyzed to understand whether an increased ROS burst may be caused by a change in accumulation/degradation of RBOHD (Figure 9A). Nlp20 treated Col-0 plants showed weak RBOHD accumulation at 0 min and 30 min after treatment but a stronger RBOHD accumulation at 15 min (Figure 9A). At approximately 15 min the peak in ROS production was observed (Figure 8C). *rd19ac* mutants showed more intense RBOHD protein accumulation in comparison to Col-0 at all tested timepoints, and was especially strong at 15 min (Figure 9A). *rbohd* mutants were used as control, and did not accumulate RBOHD protein (Figure 9A). No increased accumulation of RBOHD could be observed in flg22 triggered *rd19ac* (Supplementary Figure S 2A). To test whether this increase of RBOHD protein in *rd19ac* was dependent on transcriptional reprogramming, *RBOHD* gene expression was tested. Neither at the timepoints of the protein changes, nor at earlier timepoints preceding the changes at protein level, was an increase in *RBOHD* gene expression observed in *rd19ac* (Figure 9B; Supplementary Figure S 2B). We therefore concluded that any change in RBOHD accumulation would be the result of regulation at protein level.

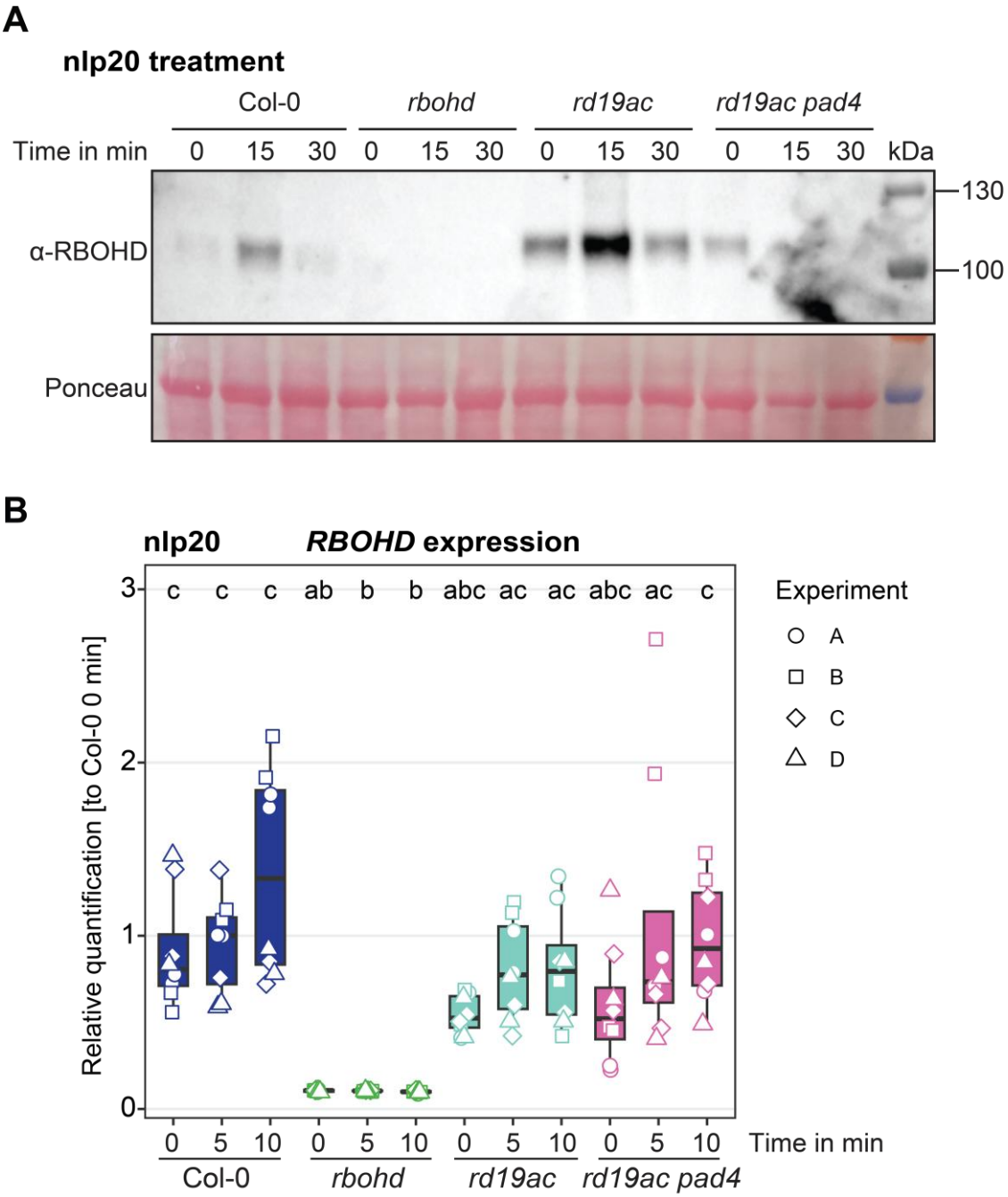


Figure 9: RBOHD protein and gene expression level following nlp20 treatment. (**A**) Protein levels of RBOHD and (**B**) *RBOHD* gene expression were analyzed in 4.5-week-old Col-0, *rbohd*, *rd19ac* and *rd19ac pad4*. (**A**) Protein levels were identified by immunoblotting with RBOHD antibody 0 min, 15 min and 30 min after nlp20 infiltration. Pierce assay was performed to load equal amounts of protein and Ponceau-stained Rubisco served as a loading control. Similar RBOHD protein levels were observed in three independent biological replicates. (**B**) *RBOHD* gene expression was detected 0 min, 5 min and 10 min after nlp20 infiltration. Relative quantification is represented in boxplots with dots of the same shape corresponding to technical replicates from one independent experiment. Data was normalized to Col-0 mock conditions in each biological replicate. UBI5 was used as a housekeeping gene. Genotypes sharing letters above boxplots do not show statistically significant differences (Kruskal-Wallis and Nemenyi-Test, $p < 0.05$, n=8).

Next, a cross of *rd19ac* and *rbohd* was generated and the resulting triple mutant was tested for both ROS burst and RBOHD protein accumulation following nlp20 treatment (Figure 10A and Figure 10B). In both experiments, *rd19ac rbohd* mutants behaved like *rbohd* single mutants, indicating that increased ROS burst of *rd19ac* was fully dependent on RBOHD (Figure 10A and Figure 10B).

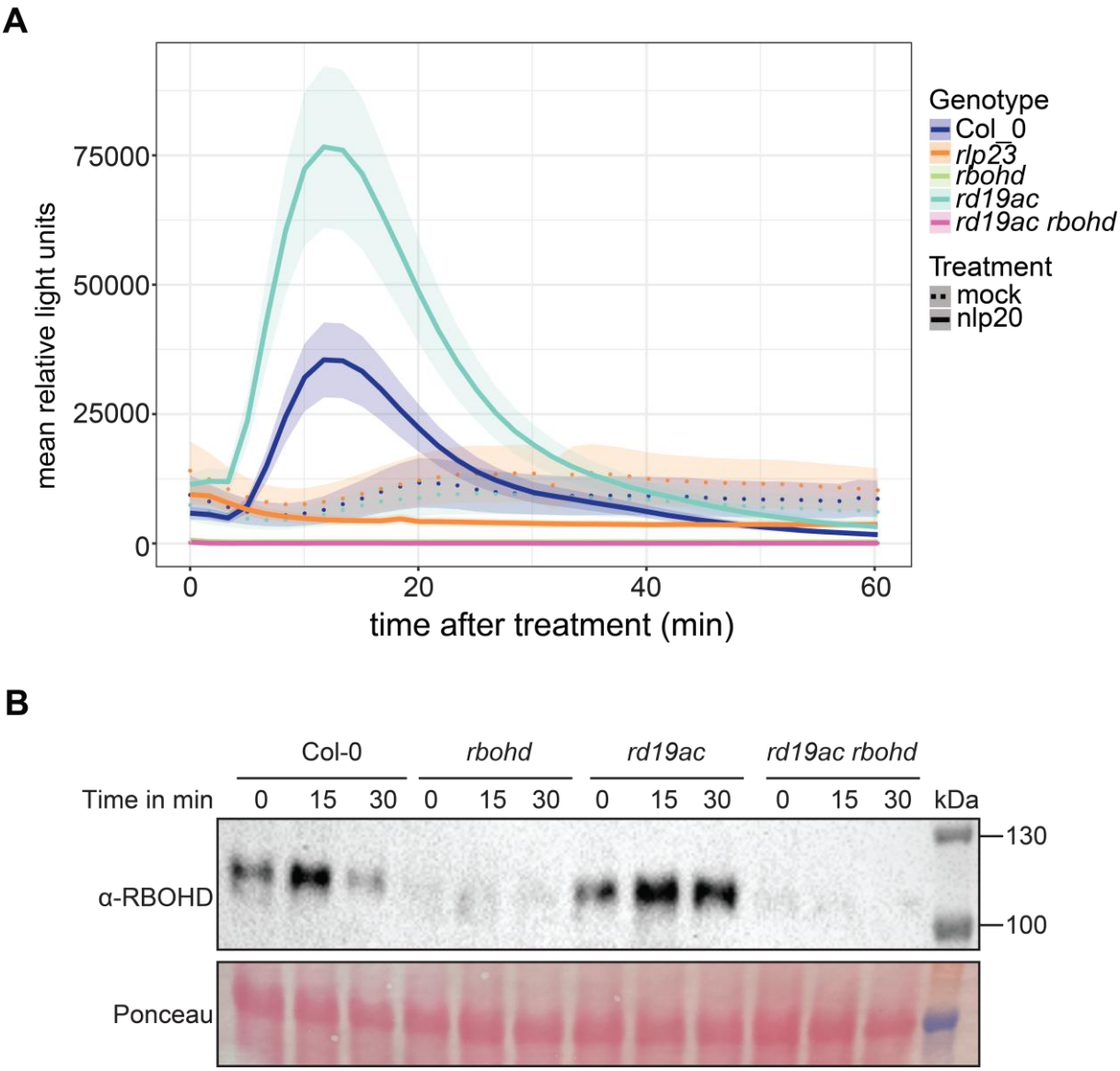


Figure 10: Response of *rd19ac rbohd* to nlp20 treatment. (**A**) ROS burst assay over 60 min of leaf discs treated with elicitor solutions. Shown are mean relative light units after nlp20 treatment with standard errors shown by distribution around curves. *rlp23* was included as additional control. n=24 (nlp20) and n=6 (mock) leaf discs from three independent biological replicates. (**B**) RBOHD protein levels were identified by immunoblotting with RBOHD antibody 0 min, 15 min and 30 min after nlp20 infiltration. Pierce assay was performed to load equal amounts of protein and Ponceau-stained Rubisco served as a loading control. Similar RBOHD protein levels were observed in three independent biological replicates.

Taken together, RBOHD protein accumulation in *rd19ac* is most likely regulated at protein and not transcriptional level and it is the putative driver for increased ROS burst observed in the *rd19ac* mutant lines.

2.5 RD19 is essential for nlp20-triggered priming against biotrophic and necrotrophic virulent pathogens

Pre-treatment with flg22 and nlp20 render *A. thaliana* Col-0 plants more resistant to a subsequent infection with a virulent pathogen such as *Pst* DC3000 by priming immune responses (Böhm et al. 2014; Zipfel et al. 2004). Since *rd19ac* mutants were not affected in resistance to *Pst* DC3000 (Figure 5B) but showed nlp20 specific increase of ROS burst, pre-treatment with nlp20 and flg22 were employed to investigate priming responses in these plants (Figure 11A). As expected, pre-treatment with both flg22 and nlp20 treatment in Col-0 plants lead to increased resistance to *Pst* DC3000 3 dpi compared to mock treatment (Figure 11B and Figure 11C). *fls2* and *rlp23* were used as negative controls and pre-treatments with flg22 or nlp20, respectively, did not restrict *Pst* DC3000 growth in comparison to mock treatments (Figure 11B and Figure 11C). Pretreating *rd19ac* with flg22 led to restricted growth of *Pst* DC3000, comparable to the effect observed in Col-0 (Figure 11B). On the other hand, resistance to *Pst* DC3000 was unchanged between a pre-treatment with nlp20 or mock in *rd19ac*, a phenotype reminiscent of *rlp23* or *pad4* mutants (Figure 11C; Pruitt et al. 2021).

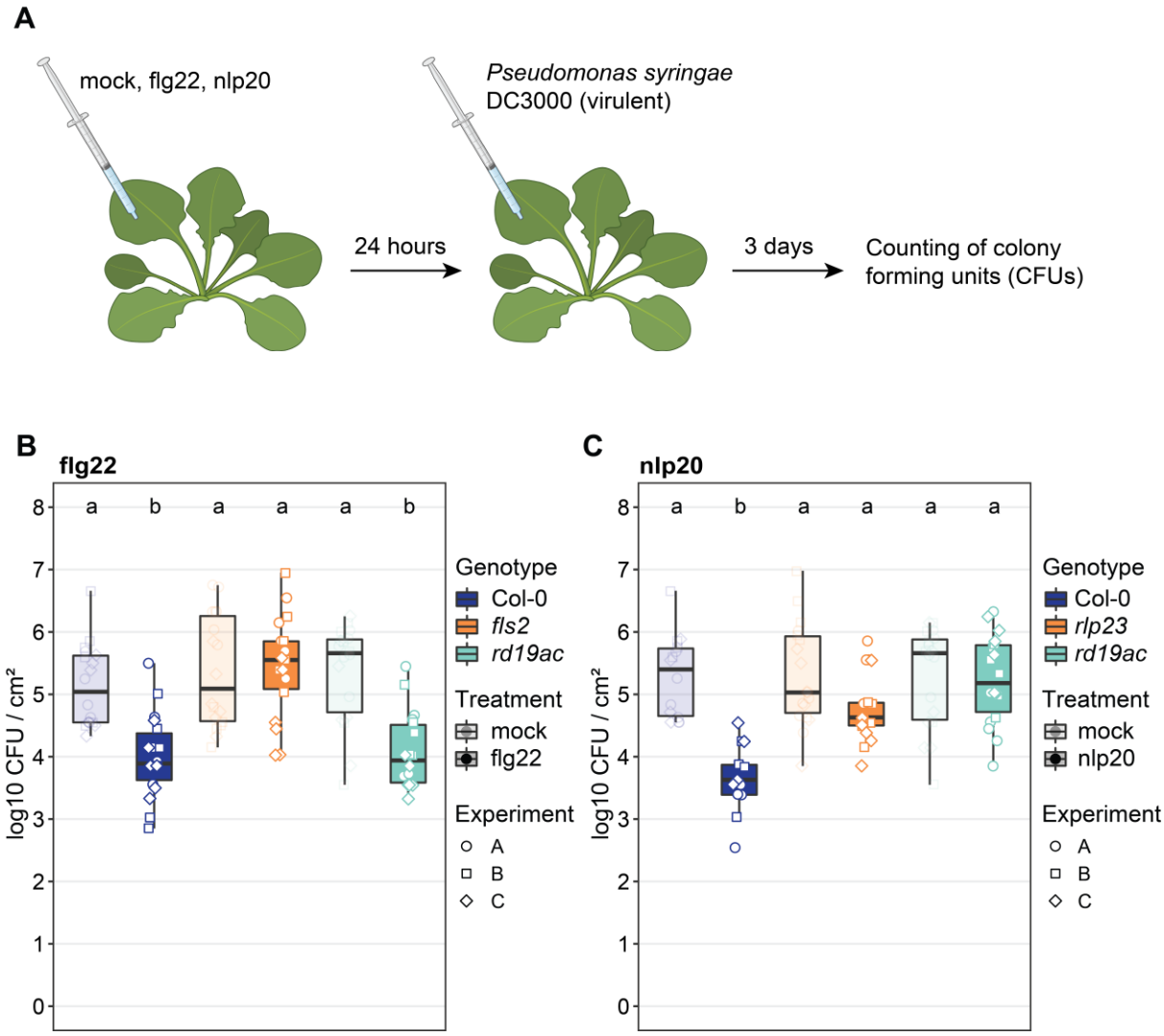


Figure 11: The role of RD19 in flg22- and nlp20-mediated priming responses to *Pst* DC3000. (**A**) Overview on experimental setup of priming responses in Col-0, *fls2*, *rlp23* and *rd19ac*. Cartoon was created using BioRender.com. (**B**) flg22 and (**C**) nlp20 were infiltrated to prime 4.5-week-old plants one day prior to syringe infiltration with *Pst* DC3000. Pre-treatment with a mock solution was used as control and is plotted in transparent colors. *fls2* and *rlp23* were used as controls for (**B**) flg22 and (**C**) nlp20 treatment, respectively. Boxplots show colony forming units (CFU)/cm^2 three days after infection, with dots of the same shape representing one biological replicate. Genotypes sharing letters above boxplots do not show statistically significant differences (ANOVA and Tukey HSD test, $p < 0.05$, n=18).

This primed resistance analysis was further extended to the necrotrophic fungus *B. cinerea*. Comparable to infections with *Pst* DC3000, a pre-treatment with flg22 or nlp20 increased resistance to *B. cinerea* in Col-0 plants (Figure 12A and Figure 12B). *fls2* and *rlp23* mutants were equally affected by *B. cinerea*, independent of mock or elicitor pre-treatment (Figure 12A and Figure 12B). Flg22 pre-treatment led to a slightly increased resistance to *B. cinerea* in *rd19ac*, though not significant and not to the same extent as observed in Col-0 (Figure 12A). Surprisingly, *rd19ac* was not only defective in nlp20-triggered priming but nlp20 pre-treatment even increased *rd19ac* susceptibility to *B. cinerea* (Figure 12B).

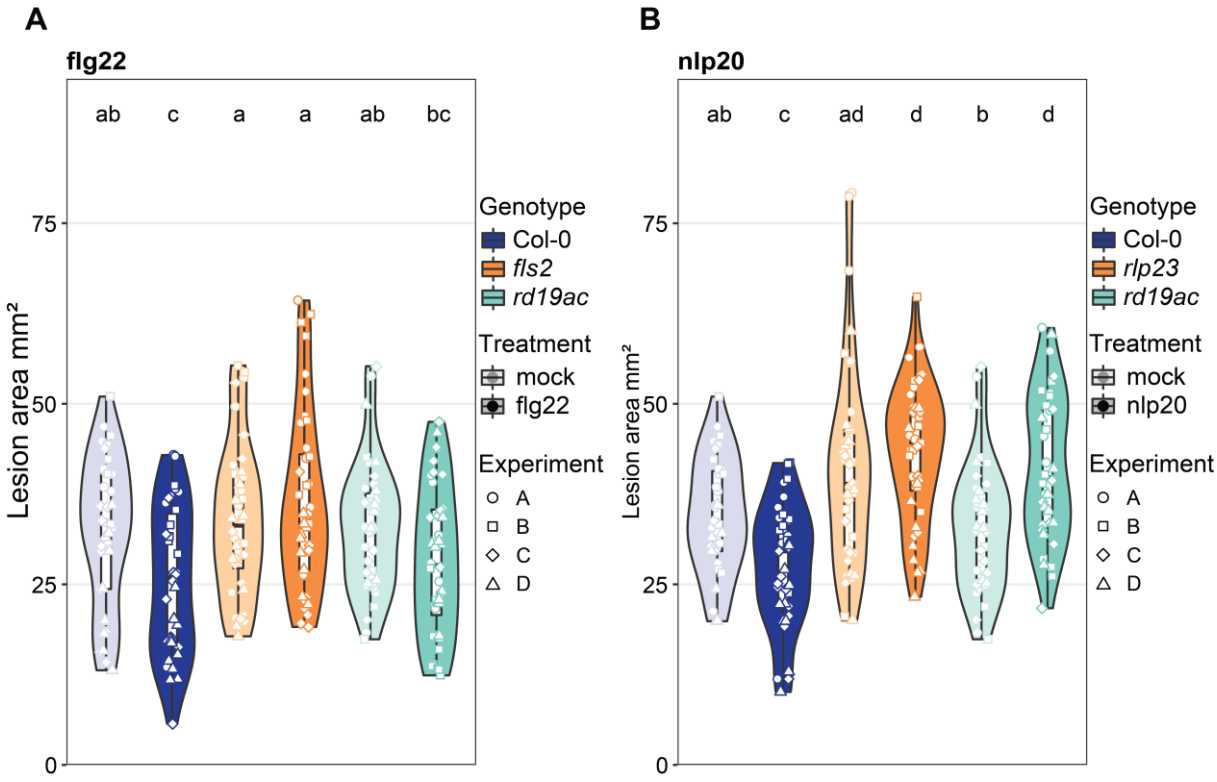


Figure 12: The role of RD19 in flg22- and nlp20-mediated priming responses to *Botrytis cinerea*. (**A**) flg22 and (**B**) nlp20 were sprayed to prime 4.5-week-old Col-0, *fls2*, *rlp23* and *rd19ac* plants one day prior to drop inoculations with *B. cinerea* and pathogen growth of lesion areas was measured 2 dpi using ImageJ. Pre-treatment with a mock solution was used as control and is plotted in transparent colors. *fls2* and *rlp23* were used as controls for (**A**) flg22 and (**B**) nlp20 treatment, respectively. Violin blots show lesion areas in mm^2, with dots of the same shape representing one biological replicate. Genotypes sharing letters above boxplots do not show statistically significant differences (Kruskal-Wallis and pairwise Wilcox-test, $p < 0.05$, n=35).

While *rd19ac* mutants are fully defective in nlp20-triggered priming responses to *Pst* DC3000 and *B. cinerea*, flg22 treatment fully primed *rd19ac* mutants to *Pst* DC3000 but only partially to *B. cinerea*.

2.6 *RD19* is expressed in guard cells but increased ROS burst in *rd19ac* does not lead to increased stomatal closure

To gain insight into different cell types that might require RD19 activity/function for immune responses, a recently published single-cell RNAseq dataset was used to screen for *RD19A* and *RD19C* expression 24 h and 40 h after infection with the biotrophic fungus *Colletotrichum higginsianum* (Figure 13A; Tang et al. 2023). *RD19A* expression was induced upon infection in almost all cell types in comparison to mock samples, including the epidermis and mesophyll cells (Figure 13A). Interestingly, strong upregulation of *RD19A* was also observed in cell types linked to (long-distance) transportation, such as the phloem, bundle sheath cells tightly surrounding the vasculature, and companion cells, a type of cell supporting sieve elements in phloem transportation (Figure 13A). Fungal infection also increased *RD19A* expression in

guard cells, the two cells forming stomata, and a potential direct entry point for the pathogen (Figure 13A).

While expression of *RD19A* extended to almost all infected cell types, *RD19C* was generally weaker expressed, mostly 24 h and 40 h after infection in the guard cells of stomata and 40 h after infection in companion cells (Figure 13A; Tang et al. 2023). Stomatal closure requires apoplastic ROS and is mediated mainly by RBOHF and RBOHD (Arnaud, Deeks, and Smirnoff 2023; Singh et al. 2017). Since both *RD19A* and *RD19C* showed increased expression in guard cells, it was tested whether increased ROS production in *rd19ac* after nlp20 treatment would affect the stomatal closure ability of *rd19ac* (Figure 8D). Epidermal peels of Col-0, *rbohd* and *rd19ac* placed for two hours in buffer solutions with the elicitors nlp20 or flg22, or in solution without any elicitor (mock treatment) were subsequently used for stomatal analysis by measuring the stomata aperture index (SAI; width/length of stomata) (Figure 13B). In Col-0, exposure to flg22 and nlp20 both induced closure of stomata in comparison to mock treatment, slightly weaker with nlp20 (Figure 13B). *rbohd* mutants did not respond to either of the elicitors, resulting in SAI comparable to mock treatment and full deficiency in stomatal closure (Figure 13B). Surprisingly, SAI of *rd19ac* showed increased closure under mock conditions (Figure 13B). While treatment with flg22 and nlp20 still induced a closure of stomata in comparison to *rd19ac* in mock conditions, the SAI was overall higher than those of flg22- and nlp20-treated Col-0 plants, suggesting reduced responsiveness of *rd19ac* to elicitors (Figure 13B).

To test whether the increased stomatal closure in mock conditions would affect *rd19ac* resistance, a *Pst* DC3000 strain lacking the phytohormone Coronatine (*Pst* ΔCor) was used in a resistance assay. Coronatine is typically used by *Pst* DC3000 to suppress plant stomatal closure and access the plant cells (Geng et al. 2012; Zheng et al. 2012), therefore *Pst* ΔCor is generally growing less on Col-0 than *Pst* DC3000 (Figure 5B; Figure 13C). While *pad4* and *rd19ac pad4* mutants were more susceptible to *Pst* ΔCor than Col-0, *rd19ac* mutants behaved like the wild type (Figure 13C). Therefore, even though *rd19ac* exhibited enhanced stomatal closure under mock conditions, no increased resistance was observed to *Pst* ΔCor, comparable to resistance to *Pst* DC3000 (Figure 5B; Figure 13C). It is therefore conceivable, that enhanced stomatal closure under mock conditions may not be linked to the disease resistance of *rd19ac* mutants.

Since stomatal closure might be only affected in immune responses when nlp20 is used as an elicitor, infection with *Pst* ΔCor was repeated with nlp20 pre-treatment. The expected priming effect between Col-0 mock and Col-0 nlp20 was not statistically significant, therefore the experiment should be repeated and considered as indicative preliminary result (Figure 13D). Nevertheless, the priming effect was fully lost in *rlp23* mutants and surprisingly, priming with

nlp20 led to increased susceptibility of *rd19ac*, reminiscent of the phenotype observed for *rd19ac* in *B. cinerea* infections with nlp20 pre-treatment (Figure 13D; Figure 12D).

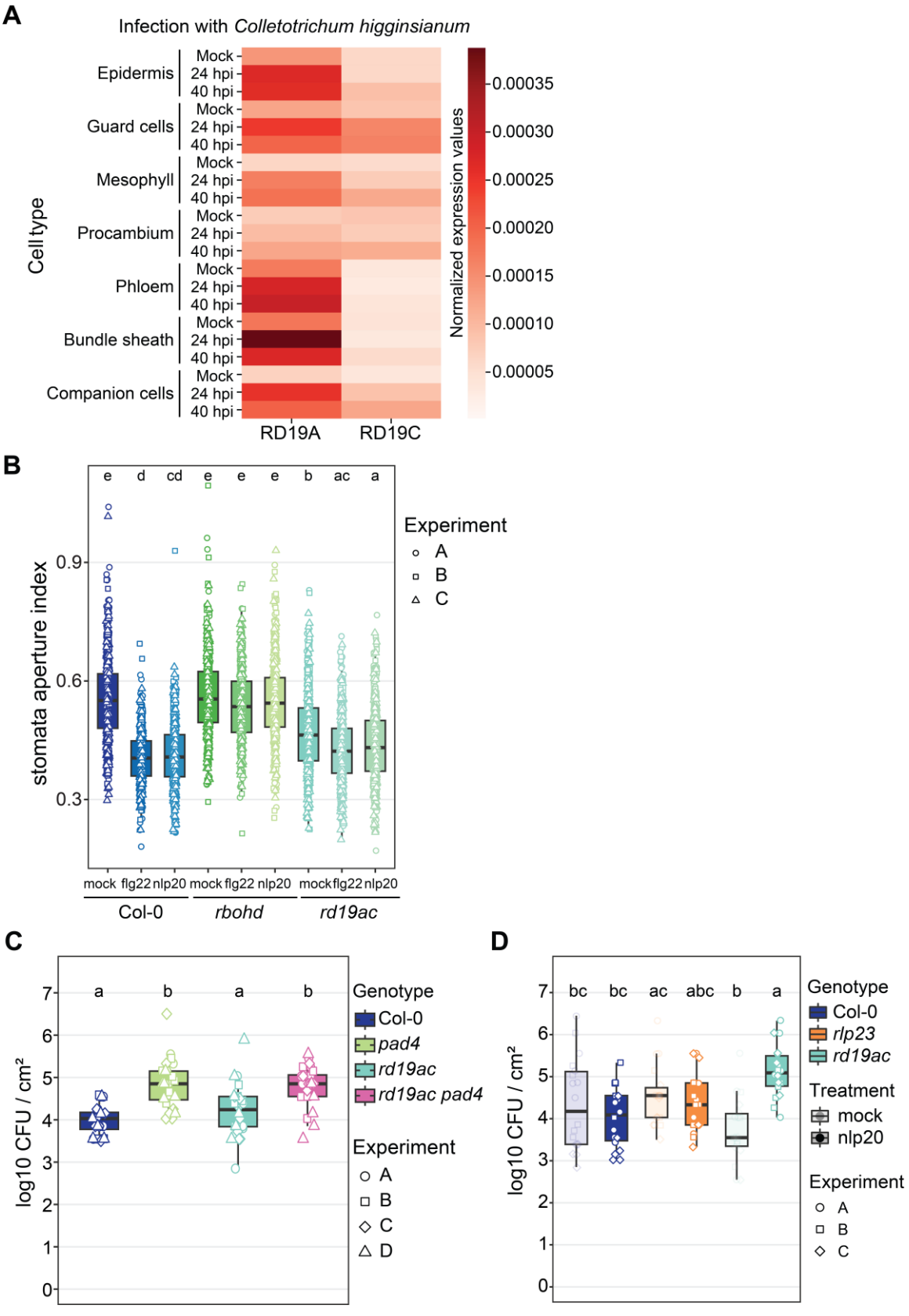


Figure 13: The role of RD19 in guard cell regulation. (**A**) Cell type specific expression analysis of *RD19A* and *RD19C* from publicly available single cell RNAseq dataset (Tang et al.

2023) following *A. thaliana* Col-0 infection with *Colletotrichum higginsianum* for 24 h and 40 h. Mock treatment was used as a control. Heatmap depicts normalized expression values and expression matrix was generated from monocle pipeline by aggregating expression of each gene in cells from the same cell type and normalize this by the cell number as size factor. (**B**) Boxplots of stomata aperture index (SAI) generated by calculating stomata width/length following Rhodamine R staining of epidermal peels from 4.5-week-old Col-0, *rbohd* and *rd19ac*, treated with mock, flg22 and nlp20 for 2 hours. (**C**) Infection of Col-0, *pad4*, *rd19ac* and *rd19ac pad4* with *Pst* ΔCor. Boxplots show colony forming units (CFU)/cm^2 three days after infection, with dots of the same shape representing one biological replicate. Genotypes sharing letters above boxplots do not show statistically significant differences (ANOVA and Tukey HSD test, $p < 0.05$, n=24). (**D**) nlp20 priming 24 h prior to infection with *Pst* ΔCor of Col-0, *rlp23* and *rd19ac*. Pre-treatment with a mock solution was used as control and is plotted in transparent colors. Boxplots show colony forming units (CFU)/cm^2 three days after infection, with dots of the same shape representing one biological replicate. Genotypes sharing letters above boxplots do not show statistically significant differences (ANOVA and Tukey HSD test, $p < 0.05$, n=18).

In summary, *RD19A* and *RD19C* gene expression was upregulated upon fungal infection in guard cells and stomatal closure was partially affected in *rd19ac* mutants both upon elicitor treatment and under mock conditions, though resistance in these lines was only impaired upon nlp20 pre-treatments (Figure 13). Therefore, the increased ROS burst did not lead to increased stomatal closure under nlp20 conditions (Figure 13B). Phenotypes of ROS burst, and stomatal closure might not be linked since increase in ROS was only observed with nlp20 but not flg22, while stomatal closure was affected under both conditions.

2.7 Overexpression of *RD19A* leads to nuclear and apoplastic localization

A nuclear co-localization of RD19A was proposed both with the effector PopP2 and with PAD4 (Bernoux et al. 2008; Zeng et al. 2024). All experiments showing a nuclear localization employed transient expression systems, such as *N. benthamiana* or *A. thaliana* protoplasts, therefore stable transgenic lines were used to identify RD19A protein expression patterns in different subcellular fractions. Overexpression of RD19A leads to an autoimmune phenotype, dependent on PAD4, EDS1 and the cysteine active sites (Zeng et al. 2024). Nuclei were extracted from previously published stable transgenic lines 35S::$RD19A^{WT}$-FLAG #1, 35S::$RD19A^{WT}$-FLAG #2, 35S::$RD19A^{C159A}$-FLAG #1, 35S::$RD19A^{C159A}$-FLAG #2, all in Col-0 background, and 35S::$RD19A^{WT}$-FLAG #2 in *pad4* (Zeng et al. 2024). Expression of RD19A in all lines was detected by α-FLAG immunoblotting, while extracted nuclei were detected with the histone H3 antibody α-H3 and cytosolic contaminations were detected by α-PEPC antibody as cytosolic marker (Figure 14). As previously described, two bands were detected for 35S::$RD19A^{WT}$-FLAG on western blots, most likely corresponding to full length RD19A (44 kDa) and proRD19A (41 kDa), while the mature form at 28 kDa was not detectable (Figure 14A; Zeng et al. 2024). Total extracts showed different accumulation intensities between lines, with RD19A accumulating strongly in *pad4* mutant background as full length and proRD19A

(44 kDa and 41 kDa) (Figure 14B). Moreover, the same two bands could be observed in 35S::RD19A^{WT} -FLAG #2 and with the lower band weakly visible, in 35S::RD19A^{WT}-FLAG #1 (Figure 14B). Both lines with mutation in the cysteine active site C159A only showed one band at approximately 41 kDa, likely corresponding to full length RD19A (Figure 14B). Antibodies α-H3 and α-PEPC confirmed total extraction, identifying bands of histone and cytosolic marker in all samples (Figure 14B). Nuclei depleted samples showed expression of RD19A in all tested lines, with intensities of expression and the bands observed in each line comparable to total extracts (Figure 14C). Nuclei depletion was verified by lack of H3 histone marker (Figure 14C). Surprisingly, α-PEPC antibody only presented very weak PEPC expression in these samples, but Ponceau staining confirmed the presence of cytosolic compounds (Figure 14C). Isolation of nuclei was successful, with increased accumulation of H3 histone in comparison to total extracts, no detection of PEPC and only weak Rubisco staining in the Ponceau (Figure 14D). RD19A expression was found in all lines tested besides 35S::RD19A^{C159A}-FLAG #1, which generally presented the weakest RD19A expression in all isolated compartments (Figure 14D). RD19A expression was overall weaker than in nuclei depleted samples or total extracts, but bands identified were comparable to expression in the other compartments (Figure 14).

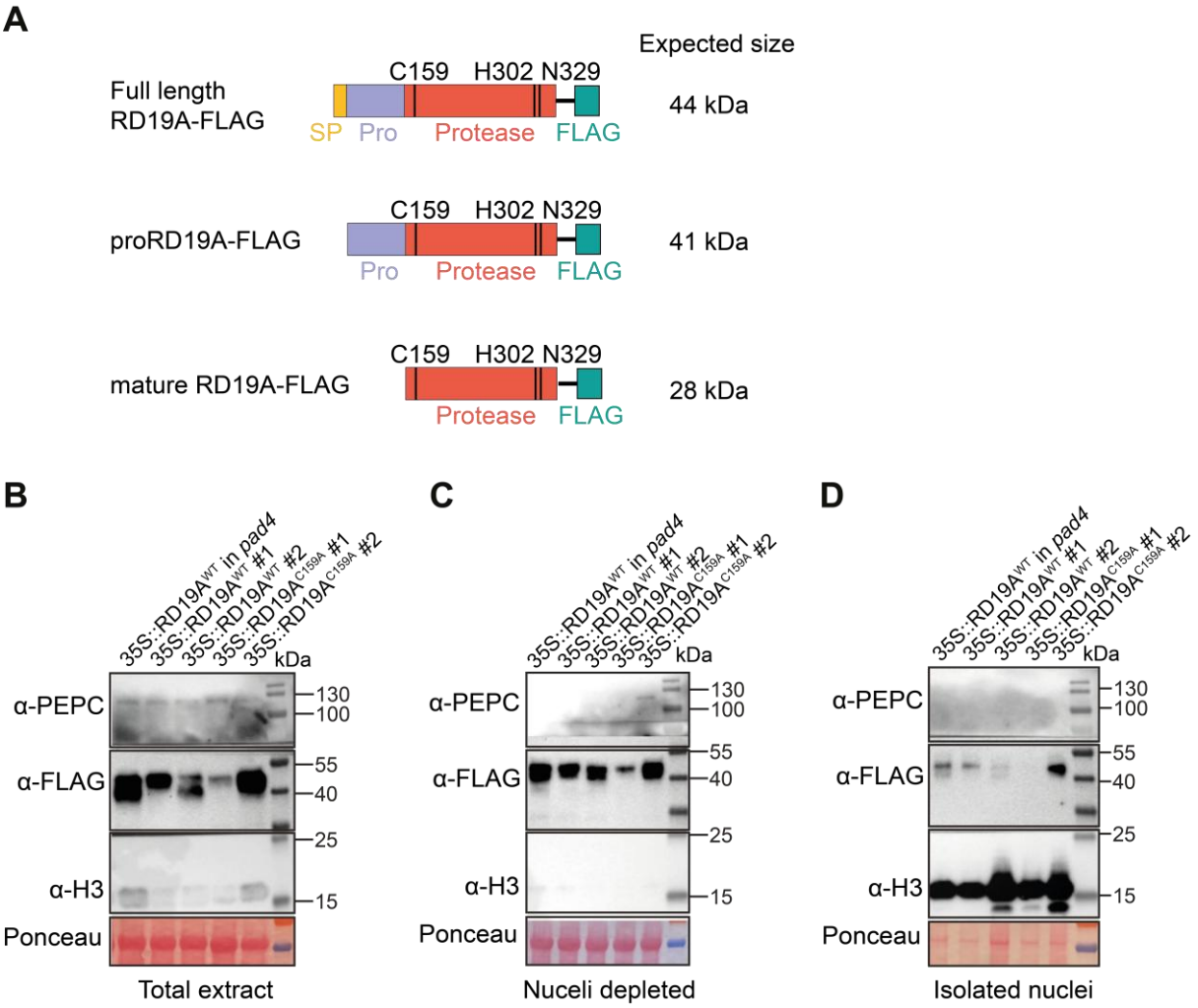


Figure 14: Isolation of subcellular compartments from 35S::RD19A-FLAG *A. thaliana* transgenic lines. (**A**) Overview on different maturation forms of RD19A found *in planta* and expected sizes of proteins with FLAG tag. (**B**) to (**D**) Western blotting using α-PEPC, α-FLAG and α-H3 for detection of proteins extracted from 35S:RD19A^{WT}-FLAG in *pad4*, 35S:RD19A^{WT}-FLAG #1 and #2 and 35S:RD19A^{C159A}-FLAG #1 and #2. (**B**) shows proteins in total extracts, (**C**) nuclei depleted samples and (**D**) isolated nuclei. Ponceau-stained Rubisco served as a loading control. Similar expression was observed in two independent biological replicates.

A variety of PLCP have been shown to be active in the apoplastic space, therefore RD19A localization in apoplastic fluids (AF) was tested by isolation of AF from stable transgenic lines overexpressing RD19A (Figure 15A). RD19A expression was detected in 35S::RD19A^{WT}-FLAG #2 in *pad4* background , 35S::RD19A^{WT}-FLAG #2 in *sag101*, 35S::RD19A^{WT}-FLAG #1 and 35S::RD19A^{C159A}-FLAG #2 (Figure 15A). Intriguingly, 35S::RD19A^{WT}-FLAG #2 in *pad4* showed increased accumulation of the lower band of RD19A (proRD19A) in comparison to observations in all other compartments (Figure 14A-C; Figure 15A). Unfortunately, AF isolation of *A. thaliana* turned out to give relatively strong cytosolic contaminations in Ponceau staining and by PEPC antibody, most likely due to damage of the delicate leaf material during isolation (Figure 15A).

Additionally, overexpressed RD19A likely localized to the apoplastic space in a transient expression assay in *N. benthamiana*. 35S::RD19A^{WT}-mCherry localization was comparable to 35S::*Nt*PR1a_RD19A^{WT}-mCherry, where the RD19A signal peptide was exchanged for *Nt*PR1a, a signal peptide highly effective in targeting proteins to the apoplast (Jin et al. 2023; Kobayashi et al. 2022; Kourelis et al. 2024) (Figure 15B). In addition to microscopical analysis, isolation of apoplastic fluids from *N. benthamiana* expressing 35S::RD19A^{WT}-mCherry or 35S::NtPR1a_RD19A^{WT}-mCherry verified presence of RD19A in the apoplast with bands at sizes of the three maturation forms (full length RD19A-mCherry = 67 kDa, proRD19A-mCherry = 65 kDa, mature RD19A-mCherry = 52 kDa) (Figure 15C). These results indicated that RD19A localization is not restricted to one subcellular compartment, but overexpression leads to localization in nuclei, cytosol and AF for all tested lines and ratio of full length RD19A to intermediate form of RD19A might depend on localization.

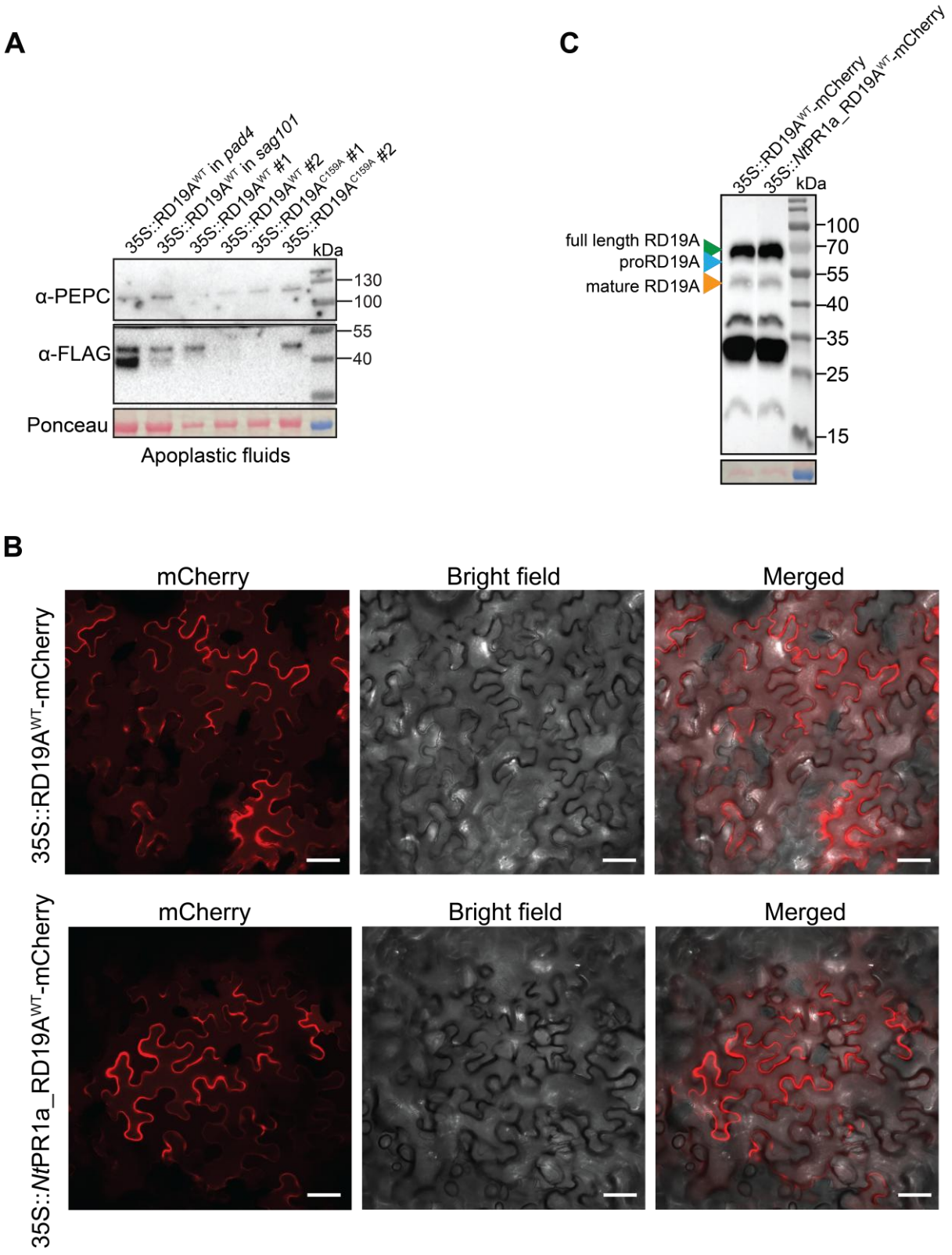


Figure 15: Investigation of apoplastic localization of 35S::RD19A. (**A**) Western blotting of apoplastic fluids from stable transgenic lines for detection of proteins extracted from 35S:RD19A^{WT}-FLAG in pad4, 35S:RD19A^{WT}-FLAG in sag101, 35S:RD19A^{WT}-FLAG #1 and #2 and 35S:RD19A^{C159A}-FLAG #1 and #2 using α-PEPC and α-FLAG. Ponceau-stained Rubisco served as a loading control. Similar expression was observed in two independent biological replicates. (**B**) Representative images of localization of 35S::RD19A^{WT}-mCherry and 35S::NtPR1a_RD19A^{WT}-mCherry using confocal microscopy. Scale bars = 50 µm.

Comparable localization patterns were observed in three independent N. benthamiana transformations. (**C**) Western blotting of apoplastic fluids isolated from N. benthamiana expressing 35S::RD19A^{WT}-mCherry and 35S::NtPR1a_RD19A^{WT}-mCherry. Detection of RD19A using α-mCherry antibodies. Ponceau-stained Rubisco served as a loading control. Green arrow indicates full length RD19A, blue arrow indicates proRD19A and orange arrow indicates mature RD19A. Similar expression was observed in two independent biological replicates.

While RD19A might be present in all subcellular compartments in overexpressed conditions, interaction with PAD4 could be restricted to specific localizations. To put this to a test, RD19A was co-expressed in wild type *N. benthamiana* in its active (wild type) and inactive form together with different versions of PAD4, which accumulate in different cellular localizations. PAD4 was expressed under native promoter in its wild-type form, with a nuclear localization signal (NLS), increasing PAD4 nuclear pool, and with a nuclear export signal (NES), promoting export of PAD4 from the nucleus and thereby increasing cytoplasmic PAD4 (Dongus PhD thesis, 2020). Site-directed mutagenesis (SDM) was used to mutate the predicted cysteine active site C159 to C159A but also a closely located cysteine C156 to C156A of 35S::RD19A^{WT}-mCherry, to remove any additional possible cysteine active site. Co-expressed proteins were extracted and YFP-tagged PAD4 used as a bait in co-IP (Figure 16). PAD4-YFP and PAD4_NLS-YFP were equally expressed in input samples, while PAD4_NES-YFP was only weakly expressed and not detected in input samples when co-expressed with 35S::RD19A^{WT}-mCherry (Figure 16). All PAD4 variants ran at approximately 100 kDa (Figure 16). In all combination RD19A-mCherry was well expressed in input samples, with 35S::RD19A^{WT}-mCherry showing two bands for the full length (70 kDa) and proRD19A form (68 kDa) and RD19A^{C156A_C159A} only containing full length RD19A (Figure 16). Immunoprecipitation (IP) of PAD4 and 35S::YFP increased protein accumulation in all samples, also in PAD4_NES-YFP, which was only partially detected in the input (Figure 16). Co-IP revealed the strongest interaction of wild type PAD4 with both maturation states of RD19A^{WT} and of full length 35S::RD19A^{C156A_C159A}-mCherry (Figure 16). Even though PAD4_NES-YFP was less abundant after IP, co-IP pulled down 35S::RD19A^{WT}-mCherry and 35S::RD19A^{C156A_C159A}-mCherry more strongly than PAD4_NLS-YFP (Figure 16). 35S::YFP was co-expressed with RD19A as a control for specific interaction and RD19A did not co-IP with 35S::YFP (Figure 16). Mature RD19A was not detected in Co-IP samples (Figure 14; Figure 15; Figure 16).

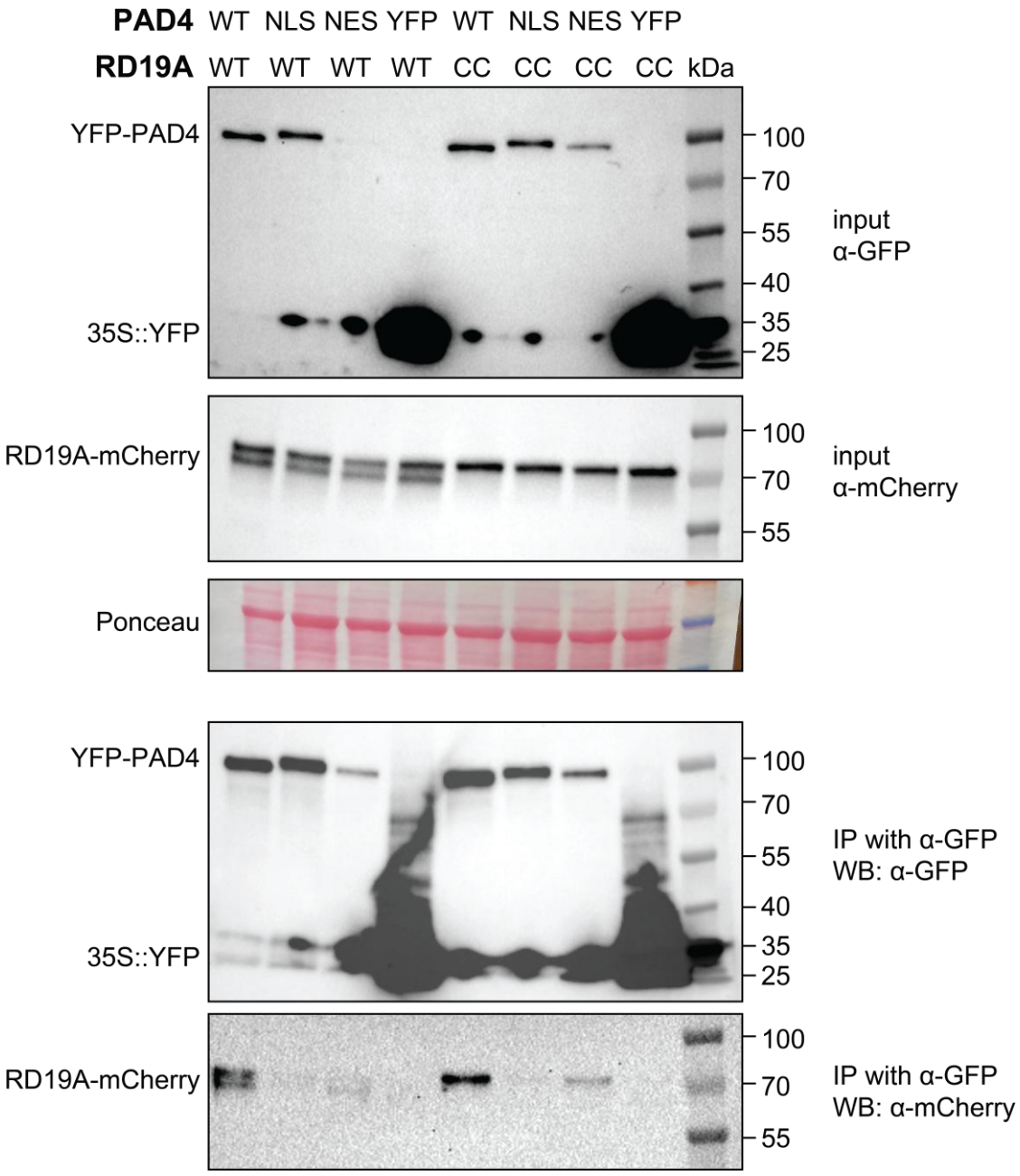


Figure 16: Interaction of 35S::RD19A with PAD4 targeted to different subcellular compartments. Western blotting of expression of RD19A and PAD4 in *N. benthamiana* followed by immunoprecipitation. WT corresponds to wild-type version of the protein, CC is indicating the catalytically mutated version C156A_C159A of RD19A (35S::RD19A^{C156A_C159A}), NES = nuclear export signal, NLS = nuclear localization signal. PAD4 was expressed under native promoter and YFP-tagged, RD19A was under 35S promoter and mCherry tagged. 35S::YFP was used as control instead of YFP-PAD4. IP was performed using α-GFP agarose beads. Proteins in input and IP samples were detected using GFP and mCherry antibodies. Ponceau-stained Rubisco served as a loading control. Similar expression was observed in two independent biological replicates.

The presented results support previous findings of a nuclear localization of RD19A, while also placing RD19A in the cytosol and apoplast (Figure 14; Figure 15; Figure 16). While mutation of cysteine active site(s) influenced self-processing of RD19A and therefore abolished presence of proRD19A, neither the tested protein abundance in subcellular compartments nor

the interaction with PAD4 were influenced by RD19A inactivity (Figure 14; Figure 15; Figure 16).

2.8 Activity-based protein profiling does not confirm RD19A activity in overexpressing RD19A^{WT} lines

An important tool in screening for protease activities is activity-based protein profiling (ABPP) (Morimoto and Van Der Hoorn 2016). For ABPP, the full leaf proteome or specific subcellular compartments can be extracted and subsequently incubated with a so-called activity-based probe (ABP). The choice of ABP depends on the family, the protease of interest belongs to, and consists of a binding site for the protease active site and a reporter (Morimoto and Van Der Hoorn 2016; Richau et al. 2012). For detection of RD19A activity, DCG-04 was used, an ABP with the PLCP activity inhibitor E64 linked to a biotin reporter, allowing for detection of active proteases by immunoblotting with α-Streptavidin antibody (Figure 17A). The ABP has only access to active PLCPs, since the active site would otherwise be blocked by an endogenous PLCP inhibitor present in the extracts or by the pro-domain of the PLCP, which is covering the active site (Morimoto and Van Der Hoorn 2016) (Supplementary Figure S 8). Since ABPs are always suitable for multiple PLCPs, all active PLCPs are labeled in ABPP (Morimoto and Van Der Hoorn 2016). To test RD19A activity, total proteome was extracted from leaves at pH 7.4 of Col-0*, rd19ac* and 35S::RD19A^{WT}-FLAG #2. The overexpression line #2 was chosen, because western blotting of these lines was previously reported to accumulate more RD19A (Zeng et al. 2024). Total leaf extracts of all lines were split into two probes, one additionally supplied with the PLCP inhibitor E64 as a negative control (Figure 17B; left panel). Active sites are blocked by the inhibitor and the ABP cannot bind, making all bands observed in these samples unspecific (Figure 17B; left panel). While ABPs are expected to label active, mature forms of proteases, sometimes also the intermediate pro-form might be labeled. This is possible if the pro-domain is only loosely covering the active site and the ABP can still enter (Supplementary Figure S 8). Immunoblotting analysis revealed a band most prominent in 35S::RD19A^{WT}-FLAG lines at approximately 38 kDa, which could correspond to proRD19A, since it is not found in samples with the E64 inhibitor (Figure 17B; left panel). Slightly above 25 kDa, a band could only be observed in Col-0 samples without E64, and the size may correspond to the mature RD19A (Figure 17B; left panel). These two candidate bands were not observed in *rd19ac* (Figure 17B; left panel). The no probe control (NPC), which is an equal mix of all used protein extracts but without any ABP added, reveals any unspecific bands, such as the band in all samples slightly below 35 kDa (Figure 17B; left panel). Equal expression of 35S::RD19A^{WT}-FLAG was verified by α-FLAG immunoblotting (Figure 17B; left panel).

The strong band observed in 35S::RD19A^{WT}-FLAG samples was a good candidate for showing RD19A activity, but the analysis was extended to actually confirm presence of RD19A in these

samples. In addition to the above described ABPP setup, chloroform-methanol precipitation of proteins was performed after adding the ABP, followed by a pulldown with α-Streptavidin agarose beads, to enrich for ABP-bound proteins in the sample (Figure 17C). By enriching ABP bound proteins, the goal was to also be able to detect potentially low abundant fully mature RD19A. In this experiment 35S::RD19A^{C159A}-FLAG #2 was included as a negative control, since none (or less) RD19A activity would be expected in these lines. Input samples before the pulldown with α-Streptavidin beads showed a band at size of proRD19A (~38 kDa) and mature RD19A (~25 kDa) more strongly in 35S::RD19A^{WT}-FLAG without E64 than in any of the other samples (Figure 17D). After pulldown, blotting of protein depleted samples revealed successful pulldown of biotin labeled samples with α-Streptavidin, since no proteins could be detected on the blot anymore (Figure 17D). Unfortunately, uneven pulldowns became visible on blots, either due to uneven loss of beads during washing steps or to adding uneven amounts of beads to the samples (Figure 17D). Nevertheless, the bands at size of proRD19A (~38 kDa) and mature RD19A (~25 kDa) were still detected in 35S::RD19A^{WT}-FLAG in replicates one, three and four, but also in 35S::RD19A^{C159A}-FLAG replicate three (Figure 17D). Surprisingly, the subsequent mass spectrometry analysis (performed by Anne Harzen and Dr. Sara Christina Stolze at Max-Planck-Institute for Plant Breeding Research) after on-bead digestion revealed identification of active RD19A in three out of the four replicates for 35S::RD19A^{C159A}-FLAG but only in one out of four replicates for 35S::RD19A^{WT}-FLAG (Figure 17E). No active RD19A was detected in the NPC and *rd19ac* (Figure 17E).

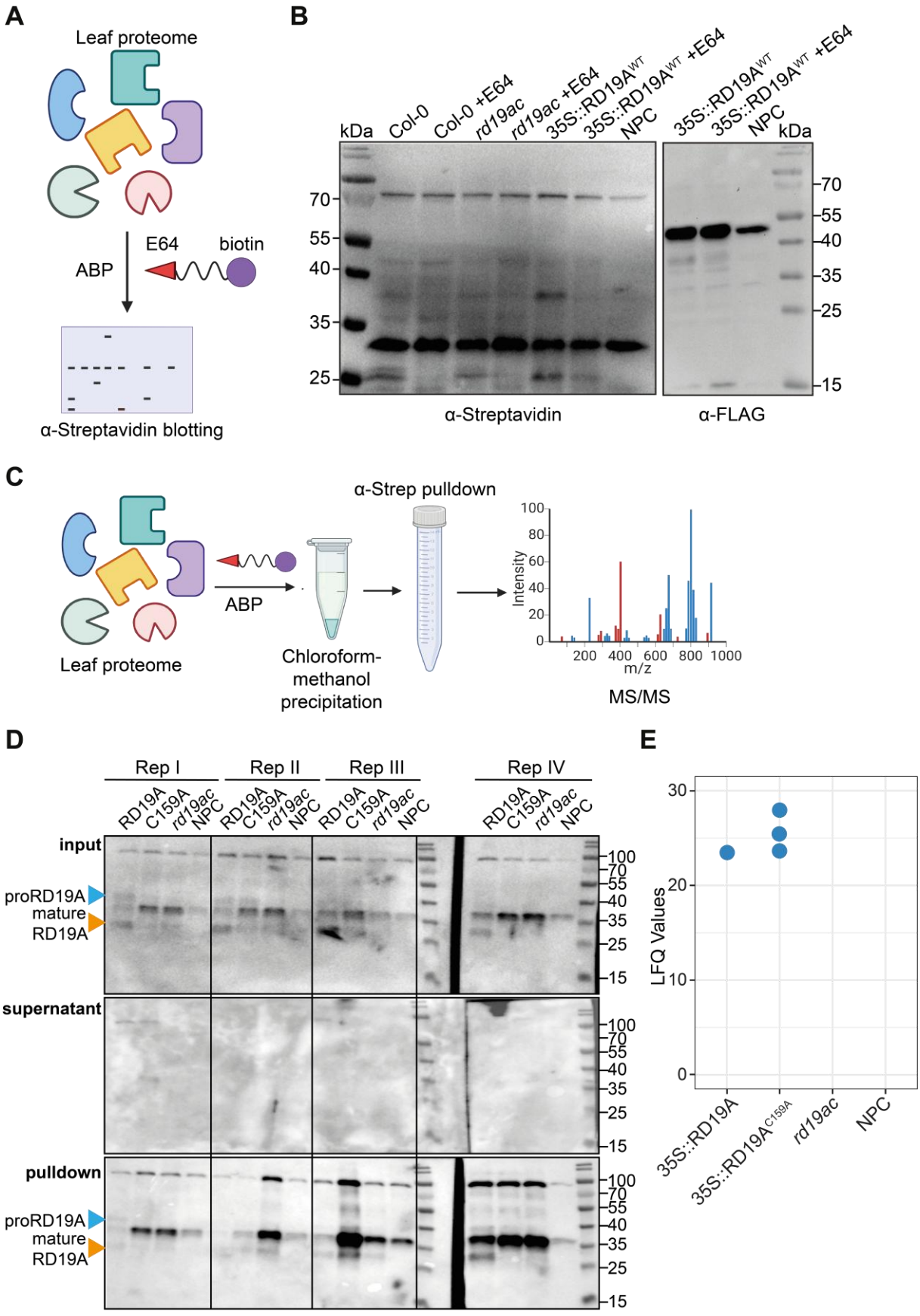


Figure 17: Activity-based protein profiling for detection of RD19A activity. (**A**) Schematic overview on ABPP workflow, created using BioRender.com. ABP = activity-based probe, E64 = PLCP inhibitor. (**B**) Immunoblotting of ABPP using Streptavidin specific antibody. Col-0,

rd19ac and 35S::RD19A^{WT}-FLAG were used for ABPP, NPC = no probe control, a mix of all protein extracts without addition of ABP. α-FLAG antibody was used as control for RD19A expression. (**C**) Schematic overview on ABPP linked to mass spectrometry analysis, created using BioRender.com. ABP = activity-based probe, MS/MS = tandem mass spectrometry. (**D**) Immunoblotting of different steps of ABPP followed by protein precipitation and pulldown with α-Streptavidin beads. RD19A are samples of transgenic 35S::RD19A^{WT}-FLAG are indicated as RD19A and samples 35S::RD19A^{C159A}-FLAG as C159A. NPC = no probe control. Input corresponds to total extracts prior to pulldown, supernatant was taken after protein pulldown with agarose beads and pulldown corresponds to washed beads after immunoprecipitation. Protein sizes potentially corresponding to proRD19A are indicated by blue arrow and those corresponding to mature RD19A by orange arrows. (**E**) MS/MS analysis following α-Streptavidin pulldown. Identification of RD19A from four biological replicates in 35S::RD19A^{WT}-FLAG, 35S::RD19A^{C159A}-FLAG, *rd19ac* and NPC (no probe control) is indicated by presence of blue circle at corresponding LFQ values. LFQ = label-free quantification.

No protease activity of RD19A in 35S::RD19A^{WT}-FLAG might be caused by experimental missteps or by the fact that the autoimmune phenotype of this line might negatively impact the analysis. Independent of the reason for this result, using the overexpression lines in further substrate analysis was considered too perilous and it was decided to instead establish transgenic lines of RD19A with native promoter, genomic DNA (gDNA) and in *rd19ac* background.

2.9 Generation of pRD19A::gRD19A stable transgenic lines in *rd19ac* mutant background

The cloning of pRD19A::gRD19A with mCherry, mYFP and HA tag was performed by infusion cloning. The selection of genomic *RD19*A and the upstream promoter region was chosen as previously described, selecting 1429 bp upstream of the *RD19A* start codon (Bernoux et al. 2008), while the stop codon was not included in amplification. SDM was used to generate the inactive form of RD19A, with C156A and C159A mutations (pRD19A::gRD19A^{C156A_C159A}). *A. thaliana rd19ac* mutants were transformed with constructs via floral dip. Following transformation, mCherry tagged plants showed only few successful transformants, of which none were proven for homozygous single copy insertion in T2, therefore only HA- and mYFP-tagged T3 and T4 single copy homozygous transgenic lines were used for further experiments. For all lines, complementation of *rd19ac* mutant phenotype by the pRD19A::gRD19A transgene was tested in ROS assays, using nlp20 as an elicitor. Since *rd19ac* mutants show increased ROS burst in response to nlp20, a successful complementation line was expected to show Col-0 like ROS burst levels. For lines complemented with pRD19A::gRD19A^{C156A_C159A}, ROS burst comparable to *rd19ac* mutants was expected, though Col-0 like ROS burst was conceivable, considering that RD19A protease activity might not be required for ROS regulation. For both pRD19A::gRD19A^{WT}-HA and pRD19A::gRD19A^{WT}-mYFP lines behaving like Col-0 could be identified: lines 4-4-3-2, 4-4-3-3 and 4-4-3-5 for HA-tagged RD19A, and 4-1-2 and 4-4-5 for mYFP-tagged RD19A (Figure 18A

and Figure 18C). All tested pRD19A::gRD19A^{C156A_C159A}-HA lines were complementing the *rd19ac* phenotype, showing Col-0 like or lower ROS bursts, while lines pRD19A::gRD19A^{C156A_C159A}-mYFP 4-4-3 and 4-4-4 showed ROS bursts higher than *rd19ac* (Figure 18B and Figure 18D).

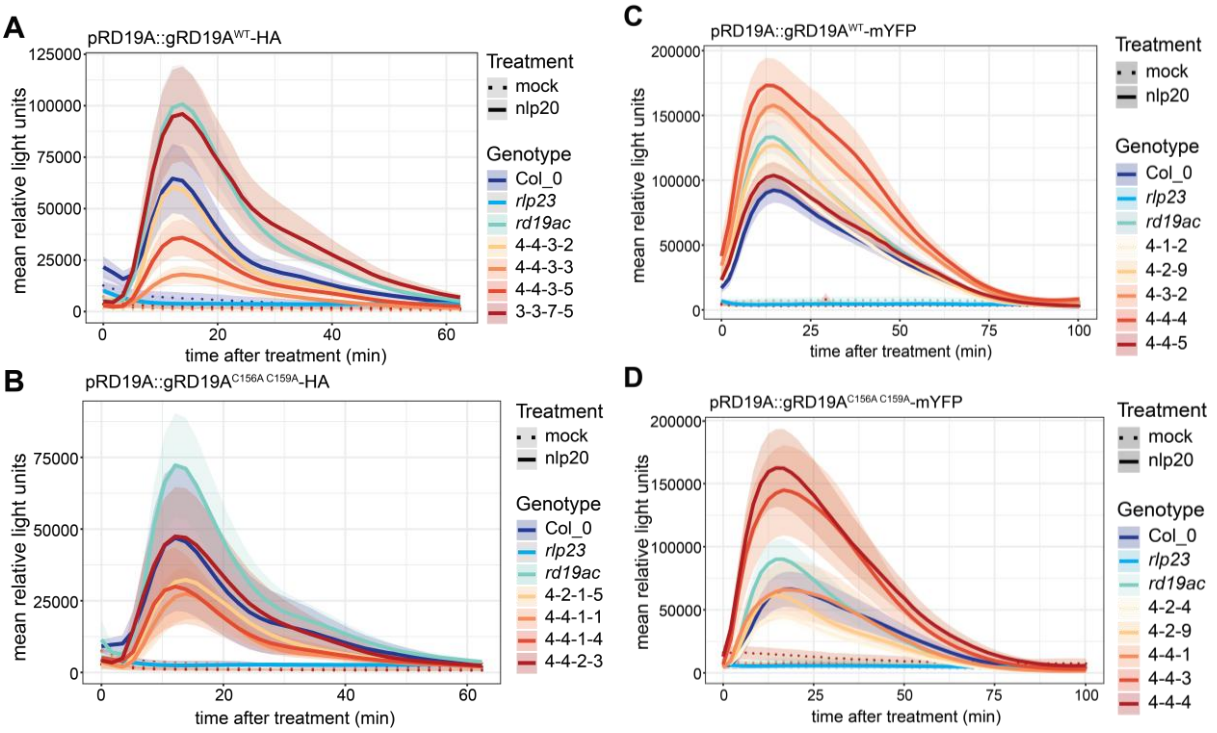


Figure 18: ROS assay of pRD19A::gRD19A stable transgenic lines in *rd19ac* following nlp20 elicitation. ROS burst assay over 60 min of leaf discs of (**A**) pRD19A::gRD19A^{WT}-HA, (**B**) pRD19A::gRD19A^{C156A_C159A}-HA, (**C**) pRD19A::gRD19A^{WT}-mYFP and (**D**) pRD19A::gRD19A^{C156A_C159A}-mYFP treated with elicitor solutions. Shown are mean relative light units after nlp20 treatment with standard errors shown by distribution around curves. *rlp23* was included as additional control. (**A**) and (**B**) n = 16 (nlp20) and n = 4 (mock) leaf discs from two independent biological replicates, (**C**) and (**D**) n = 24 (nlp20) and n = 6 (mock) leaf discs from three independent biological replicates.

Unfortunately, expression analysis of HA-tagged lines showed only very weak gene expression of *RD19A* 3 hours after nlp20 treatment in comparison to Col-0 and no detectable protein expression for any of the lines (Supplementary Figure S 4). Only an unspecific band also observed in Col-0 was detectable at ~35 kDa (Supplementary Figure S 4A). Out of mYFP-tagged lines, only line 4-2-9 showed increased *RD19A* gene expression levels 3 hours after nlp20 treatment, though not as high as in Col-0 (Supplementary Figure S 4A). Protein expression analysis revealed presence of one band at ~70 kDa for pRD19A::gRD19A^{WT}-mYFP lines 4-1-2, 4-2-9 and 4-4-5, and for pRD19A::gRD19A^{C156A_C159A}-mYFP 4-2-9, 4-4-3 and 4-4-4 (Supplementary Figure S 4B). This band was visible only after adding an enhanced chemiluminescence solution (Supplementary Figure S 4B). A subsequent immunoprecipitation of these lines after treatment with nlp20, using α-GFP agarose beads to increase RD19A-mYFP protein contents, indeed increased intensity of the band at ~70 kDa, specifically

in lines pRD19A::gRD19A^{WT}-mYFP 4-1-2 and 4-2-9, and pRD19A::gRD19A^{C156A_C159A}-mYFP 4-2-9 (Figure 19). This suggested that, indeed, the observed band is RD19A, most likely in its full-length form.

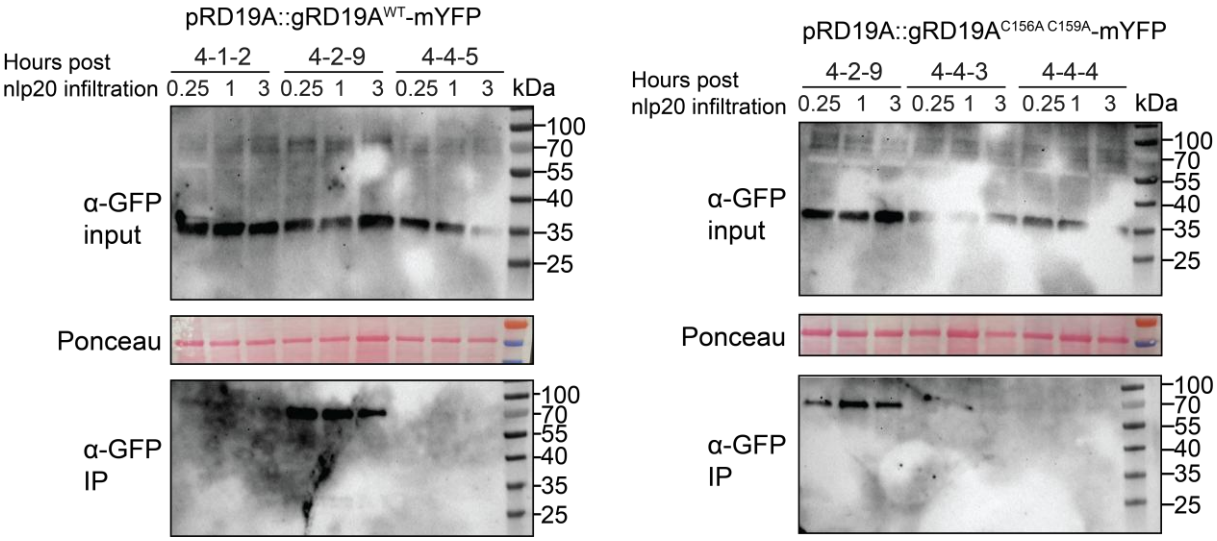


Figure 19: Protein expression of nlp20-treated pRD19A::gRD19A-mYFP stable transgenic lines in *rd19ac* following immunoprecipitation. Immunoprecipitation (IP) using α-GFP agarose beads was performed on pRD19A::gRD19A^{WT}-mYFP and pRD19A::gRD19A^{C156A_C159A}-mYFP to enrich protein levels. Proteins were detected using α-GFP antibodies in input (prior to pulldown) and IP samples. Ponceau-stained Rubisco served as a loading control.

Out of all tested transgenic lines, only one was proven to express pRD19A::gRD19A^{WT}-mYFP on a protein level and showed a complementation phenotype (Supplementary Table S 1). This was considered unsuitable for further analysis, as a minimum of two transgenic lines should be provided and substrate analysis were performed independent of these lines.

2.10 Proteomic Identification of Cleavage Sites (PICS) of RD19A reveals cleavage preference for non-polar amino acids

Since stable transgenic lines both with RD19A native promoter and 35S promoter were unsuitable for substrate analysis, an additional method was employed to gain insight into RD19A cleavage specificities, Proteomic Identification of Cleavage Sites (PICS). In PICS the protease of interest is incubated with a peptide library generated by a known protease, followed by mass spectrometry, to identify newly generated cleavage sites (Demir, Kuppusamy, et al. 2022; Schilling et al. 2011). Constructs of 35S::RD19A^{WT}-HA and 35S::RD19A^{C156A_C159A}-HA were generated and expressed in wild type *N. benthamiana*. From *N. benthamiana* leaves, AF were isolated, since overexpressed RD19A localized to the apoplastic space (Figure 15). RD19A expression in apoplastic fluids was furthermore tested by immunoblotting, using α-HA antibodies (Figure 20A). 35S::RD19A^{WT}-HA expression revealed three bands on the western blot, corresponding to full length RD19A, proRD19A and mature RD19A (Figure 20A). The

band of full length RD19A was only weakly visible in 35S::RD19A^{WT} samples, but the only band appearing in apoplastic fluids expressing 35S::RD19A^{C156A_C159A}-HA (Figure 20A). Bands were generally observed slightly higher than the predicted 44 kDa for full length RD19A-HA, 41 kDa for proRD19A-HA and 28 kDa for mature RD19A-HA (Figure 20A). Results verified that RD19A is self-processing and can therefore only maturate with a functional cysteine active site (Figure 20A). Next, AF were incubated with peptide libraries, generated by endopeptidases GluC, Trypsin and Legumain (Figure 20B). The inhibitor E64 added to wild-type RD19A was used as an additional control (Figure 20B). After incubation for 1 h and 16 h, E64 was added to stop the reaction and samples were submitted for tandem mass spectrometry analysis (MS/MS), performed by Melissa Mantz at the University of Freiburg. Peptide identification by MS allowed for subsequent peptide alignment and generation of ICE-Logos, which were provided by M. Mantz (Figure 20C). ICE-Logos of all libraries and incubation times were generated in the same manner. For example, incubation with the GluC library for 1 h resulted in a total number of 2225 peptides identified, of which 1900 peptides were found only in RD19A^{WT} samples and not in the two controls (Figure 20C). Of these, 70 peptides were identified by PINCIS (Pics N-/C-terminal Inferred Substrates perl Script), a script to filter the peptide list for cleavage sites by the GluC library, to leave only N- and C-terminal cleavage sites generated by the protease of interest (Schilling et al. 2011). The 70 peptides were used for generation of the ICE-Logos (Figure 20C). Incubation with GluC and Trypsin libraries resulted in a sufficient number of peptides identified by PINCIS (GluC 1 h 70 peptides, GluC 16 h 102 peptides, Trypsin 1 h 234 peptides, and Trypsin 16 h 164 peptides) (Figure 20C and Figure 20D). MS analysis of incubation with Legumain libraries resulted only in 16 identified peptides after 1 h and 24 peptides after 16 h, and the ICE-Logos were not included in identifying cleavage preferences (Supplementary Figure S 5). The x-axis of ICE-Logos shows the position, at which amino acids were found in relation to the cleavage site between P1 and P1', while the y-axis presents the likelihood of the identified amino acids and significance is indicated by the size of the letters (Figure 20C and Figure 20D). Besides amino acids at position P1, directly next to the cleavage site, position P2 was considered of high interest, since it has previously been described as crucial for PLCP activity (Paireder et al. 2016, 2017; Turk et al. 1995). Incubation with the GluC library for 1 h resulted in glycine, alanine and cysteine at position P1, and alanine, isoleucine and threonine at position P2. The 16 h timepoint resulted in rather different amino acids identified at position P1: leucine, glycine and methionine. Position P2 also showed high prominence of isoleucine and alanine, just as the 1 h incubation, but additionally lysine and phenylalanine (Figure 20C). The incubation with the trypsin library for both timepoints resulted in a higher number of amino acids identified for positions P1 and P2 in comparison to the GluC library (Figure 20D). After 1 h, leucine, methionine, tyrosine, glutamine, phenylalanine and histidine were found at position P1, while isoleucine, alanine, valine and

threonine were found at position P2 (Figure 20D). 16 h incubation resulted in methionine, leucine, alanine, tyrosine, phenylalanine and glutamine at position P1, and valine, alanine and isoleucine at P2 (Figure 20D). Therefore, amino acids identified with the trypsin library at position P1 and P2 were very similar between 1 h and 16 h incubation times (Figure 20D).

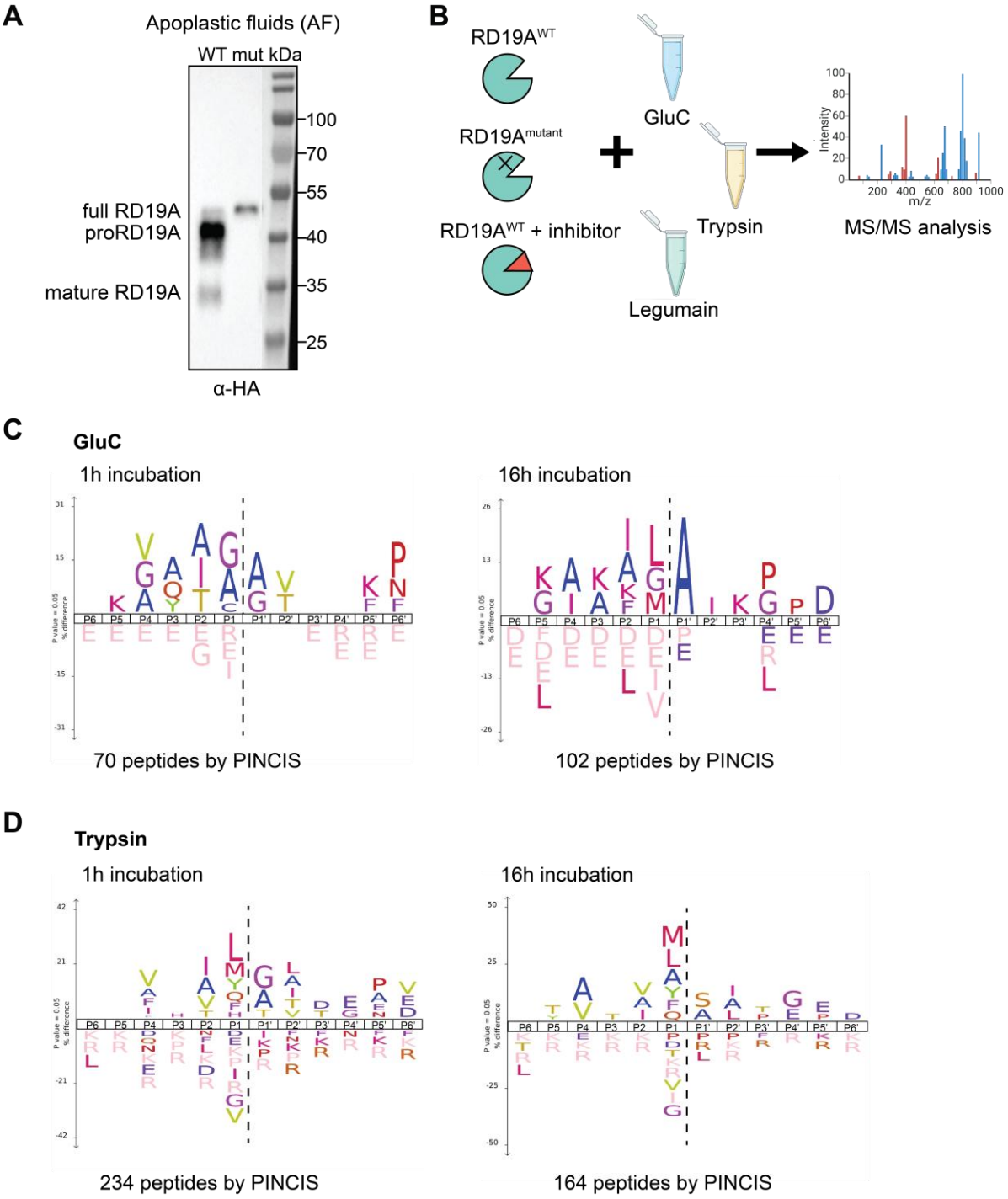


Figure 20: Identification of RD19A cleavage preferences by PICS assay. (**A**) Immunoblotting of apoplastic fluids (AF) from 35S::RD19A^{WT}-HA (=WT) and 35S::RD19A^{C156A_C159A}-HA (=mut; for catalytic mutant), using α-HA antibodies. Different maturation forms of RD19A are indicated next to the blot. (**B**) Schematic overview on PICS assay workflow, created using BioRender.com. RD19A^{WT} = 35S::RD19A^{WT}-HA and RD19A^{mutant} = 35S::RD19A^{C156A_C159A}-HA. The peptide libraries were made using

GluC/trypsin/legumain from an *E. coli* proteome and digested with 35S::RD19A^{WT}-HA, 35S::RD19A^{C156A_C159A}-HA and E64-inhibited 35S::RD19A^{WT}-HA. Following di-methylation, digested peptide libraries were analyzed using LC-MS/MS. MS/MS = tandem mass spectrometry. (**C**) and (**D**) Cleavage logos for RD19A with (**C**) GluC and (**D**) trypsin libraries. PINCIS-script was used to gain the prime and non-prime site specificity of proteases and sample size of peptides identified are indicated. Shown are amino acid residues only identified after incubation for 1 h and 16 h with active RD19A (35S::RD19A^{WT}-HA) relative to the cleavage bond, and their frequencies are indicated by font size. The x-axis corresponds to positions in relation to the cleavage site. Cleavage site is indicated by dotted line.

PICS analysis overall resulted in high prominence of non-polar amino acids throughout the profile and at important positions P1 and P2, helping to narrow down RD19 potential substrates in further analysis.

2.11 Proteomic analyses reveal potential RD19 substrates following nlp20-treatment

Following the identified RD19 cleavage preferences, proteomic approaches were used to determine potential RD19 targets. Substrate analysis of proteases remains a challenge since protease activities might induce subtle changes on the protein abundance, size or sequence of other proteins (Demir et al. 2018). Therefore, MS based proteomics are more and more described as appropriate methods to identify protease substrate (Demir et al. 2018). In this study, two different MS methods were exerted in collaboration with M. Mantz and P. Huesgen at the University of Freiburg. For these experiments, Col-0 and *rd19ac* plants were treated for 10 min and 3 h with nlp20 or remained untreated, as previous immune phenotypes were specific to nlp20 (Figure 8, Figure 9, Figure 11, Figure 12).

2.11.1 Shotgun proteomics verify increased presence of RBOHD in *rd19ac* mutants after nlp20 treatment

The first proteomic approach used was shotgun proteomics, a bottom-up analysis of in solution enzyme digested proteomes, to gain a general overview on protein abundances present in the plant (Demir et al. 2018). As an initial step, it was investigated whether treatment with nlp20 was successful, by checking the abundance of the RLP23-SOBIR1-BAK1 receptor complex responsible for initiating nlp20-triggered immunity in the raw intensities for each replicate (Figure 21A) RLP23 forms a complex with SOBIR1 already in resting state conditions and recruits BAK1 upon nlp20 recognition for initiation of immune signaling (Albert et al. 2015). Indeed, abundance of SOBIR1 and RLP23 did not undergo significant change in Col-0 plants after nlp20 treatment, while BAK1 abundance increased over time, verifying successful nlp20 treatment and activation of the receptor complex (Figure 21A).

Ratios of proteins in Col-0 versus *rd19ac* that were identified in 70 % valid values (i.e. in at least three out of the four replicates) were analyzed and plotted using Volcano plots (Figure 21B, Figure 21C, Figure 21D). Proteins enriched in Col-0 samples are shown in red, whereas

proteins less enriched in Col-0 or therefore more enriched in *rd19ac*, are shown in blue (Figure 21B, Figure 21C, Figure 21D). Overall, only few proteins were significantly enriched in Col-0 vs *rd19ac* and vice versa, suggesting that the proteome between lines was not majorly altered (Figure 21B, Figure 21C, Figure 21D). In untreated conditions, only one protein, VEGETATIVE STORAGE PROTEIN 2 (VSP2; AT5G24770) was significantly enriched in Col-0 (Figure 21B). At 10 min after nlp20 treatment, no protein was significantly enriched in Col-0, but significant enrichment of AT5G51010 was visible in *rd19ac* mutants (Figure 21C). AT5G51010 is a rubredoxin-like superfamily protein, with predicted localization in the chloroplast and ability to enable iron ion binding (Blum et al. 2021; McBride et al. 2017). After 3 h of nlp20 treatment, no significant change was observed between Col-0 and *rd19ac* (Figure 21D).

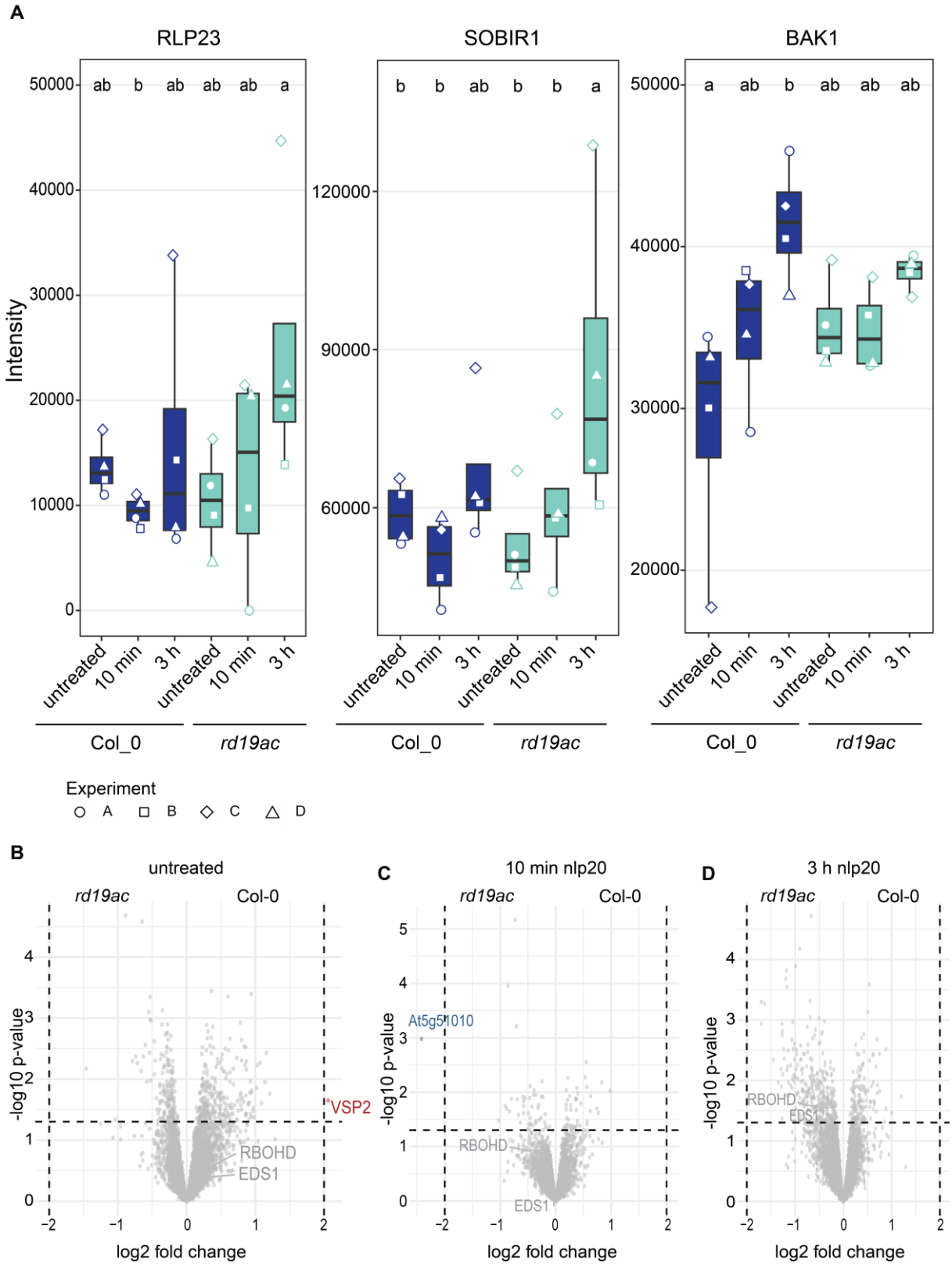


Figure 21: Shotgun proteomics reveals successful nlp20 treatment but only few proteomic changes based on Col-0 to *rd19ac* ratios. Col-0 and *rd19ac* were treated with nlp20 for 10 min or 3 h, or were left untreated, and subjected to shotgun tandem MS. (**A**) Unprocessed intensities of four individual replicates after tandem MS. RLP23, SOBIR1 and BAK1 proteomic changes were visualized in boxplots with dots of the same shape representing one biological replicate. Genotypes sharing letters above boxplots do not show statistically significant differences (ANOVA and Tukey HSD test, $p < 0.05$). (**B**) to (**D**) volcano blots of (**B**)

untreated, (**C**) 10 min nlp20 treatment and (**D**) 3 h nlp20 treatment for 70% valid values, enriched in Col-0 (red labels) or *rd19ac* (blue labels). Significance determined based on log2FC > 2/< -2 and p-value < 0.05, corresponding to -log10 p-value = 1.3025.

Though not significant, a shift of enrichment of EDS1 and RBOHD from Col-0 in untreated conditions to *rd19ac* mutants 3 h and for RBOHD also 10 min after nlp20 treatment could be observed (Figure 22). When analyzing RBOHD abundance using raw intensities of the four different replicates, an increase of RBOHD in *rd19ac* compared to Col-0 both 10 min and 3 h after nlp20 treatment was verified (Figure 22). Even though not significant, these findings were supportive of the observed increase of RBOHD protein levels in *rd19ac* mutants following nlp20 trigger (Figure 22).

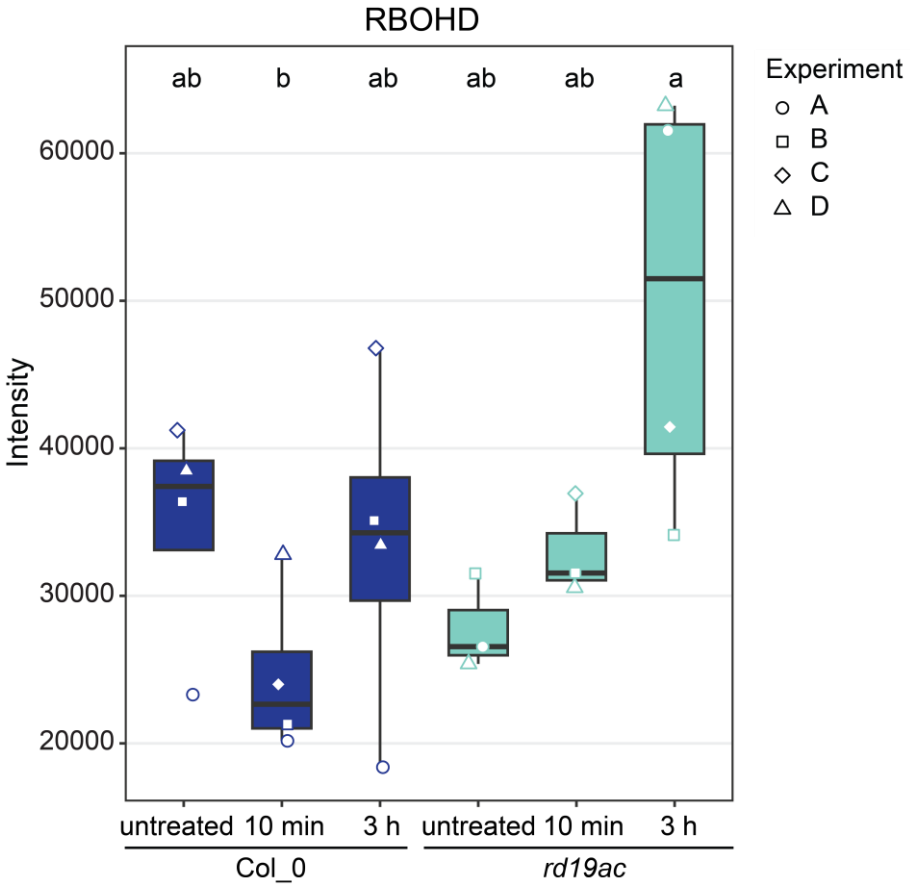


Figure 22: RBOHD intensities in four individual replicates of shotgun proteomics. Col-0 and *rd19ac* were treated with nlp20 for 10 min or 3 h, or were left untreated, and subjected to shotgun tandem MS. Graph shows unprocessed intensities of four individual replicates after tandem MS. RBOHD proteomic changes were visualized in boxplots with dots of the same shape representing one biological replicate. Genotypes sharing letters above boxplots do not show statistically significant differences (ANOVA and Tukey HSD test, $p < 0.05$).

In addition, candidates which were exclusively identified in Col-0 or *rd19ac*, independent of their significance, were analyzed (Figure 23). Venn diagrams of Col-0 at all timepoints revealed one protein identified in all three conditions, RD19A, while RD19C was only detected in untreated samples and 10 min after elicitor treatment (Figure 23A). Moreover, for each condition one specific protein was found: in untreated conditions, the mitochondrial LYR family

of Fe/S cluster biogenesis protein MAF19.16 (AT5G61220; also termed LYRM4) (Ivanova et al. 2019), 10 min after nlp20 treatment ELP5 (ELONGATOR COMPLEX PROTEIN 5; AT2G18410) and 3 h after nlp20 treatment, the ubiquitin carboxyl-terminal hydrolase-related protein AT3G47890 (Figure 23A). In *rd19ac* mutants, one protein was detected both in untreated conditions and after 10 min treatment, namely AT5G11330, belonging to the FAD/NAD(P)-binding oxidoreductase family, according to Interpro annotation (Blum et al. 2021) (Figure 23B). Furthermore, in untreated conditions HIGH MOBILITY GROUP B2 (HMGB2; AT1G20693) was identified and after 3 h the F-box protein AT1G15670 (KISS ME DEADLY 2; KELCH REPEAT F-BOX 1) (Figure 23B).

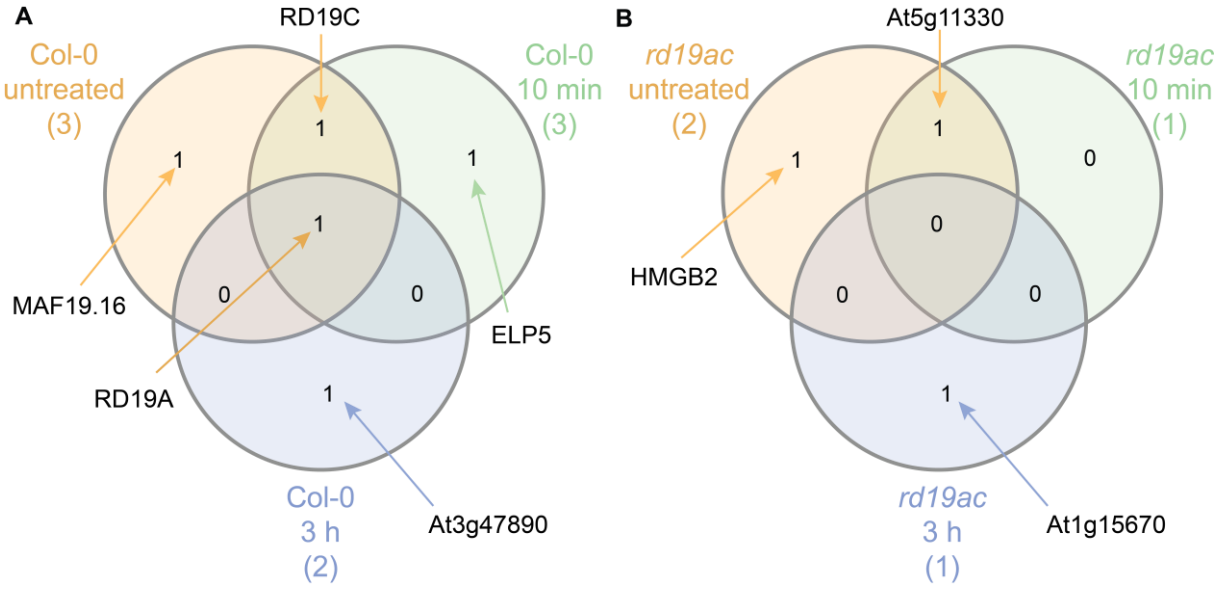


Figure 23: Analysis of shotgun proteomics based on proteins exclusively identified in Col-0 or *rd19ac* at 70 % valid values. Venn diagrams of (**A**) Col-0 and (**B**) *rd19ac* of proteins exclusively identified in Col-0 or *rd19ac* at all timepoints. Venn diagrams were generated using InteractiVenn.

Overall, shotgun proteomics revealed few changes between Col-0 and *rd19ac*, with none of the significantly enriched proteins being directly linked to plant immune activation. However, identification of intensities of the four individual replicates verified that nlp20 treatment was sufficient and reflected observed changes of RBOHD protein levels in *rd19ac*. The overview on proteomic changes by shotgun proteomics can be indicative but is not conclusive for identification of RD19 substrates.

2.11.2 N-terminomics method (HUNTER) allows identification of potential RD19 substrates

Following the results shown in the previous paragraph, a method specific for protease substrate identification was employed: High-efficiency Undecanal-based N Termini EnRichment (HUNTER) (Demir, Perrar, et al. 2022; Weng et al. 2019). Here, enrichment and labeling of endogenous N-termini (those generated for example by endopeptidases like RD19) is achieved by formaldehyde labeling and dimethylation, followed by LC-MS/MS based analysis coupled to data-independent acquisition (DIA). In these experiments, the same samples as for shotgun proteomics were used (Figure 21, Figure 22, Figure 23). The comparison was therefore between Col-0 plants, which still exhibit RD19A and RD19C protease activity, and *rd19ac* mutants, that lack this activity. LC-MS/MS peptide sequences were mapped to the *A. thaliana* Uniprot reference proteome UP000006548_3702 and further analyzed using a DIA HUNTER FragPipe pipeline. N-terminal peptide positions of different categories (P1, P2, SP, MT = mitochondrial transit peptide, CH = chloroplast transit peptide or “other” = non-canonical) and modification types (acetylated and dimethylated) were identified (Figure 24A). This resulted in a total of 18455 peptides identified after filtering for contamination (Figure 24A).

Following this analysis, 100% valid values (peptides appearing in all four biological replicates) for each condition (untreated, 10 min and 3 h) of dimethylated samples were plotted in volcano plots, comparing N-terminomic changes in Col-0 and *rd19ac* by using the ratio of Col-0 to *rd19ac* (Figure 24B, Figure 24C, Figure 24D). Positive values were therefore peptides stronger enriched in Col-0 samples or less enriched in *rd19ac* (shown in red), while negative values where more enriched in *rd19ac* or less enriched in Col-0 (shown in blue) (Figure 24B, Figure 24C, Figure 24D). A potential direct target of RD19 would be identified in Col-0 samples but identification of negatively enriched samples could potentially also suggest a link to RD19 activity. In untreated conditions, eight candidate peptides were enriched in Col-0 and 22 in *rd19ac* (Figure 24E and Figure 24F).

After 10 min, 6 peptides were enriched in Col-0 and 6 in *rd19ac*, while after 3 h, 15 peptides were enriched in Col-0 and only 5 in *rd19ac* (Figure 24E and Figure 24F). Since at 3 h after nlp20 treatment, more peptides enriched in Col-0 in comparison to *rd19ac* were identified compared to the other two timepoints, RD19 activity might be likely higher at 3 h following nlp20-triggered immunity (Figure 24E).

Overall, volcano blots showed only very few candidate peptides enriched in Col-0, out of which none showed predicted function in biotic stress responses according to GO term analysis but rather in photosynthetic pathways (Supplementary Figure S 6). Furthermore, GO term analysis

of cellular components revealed high presence of peptides from chloroplast compartments (Supplementary Figure S 6).

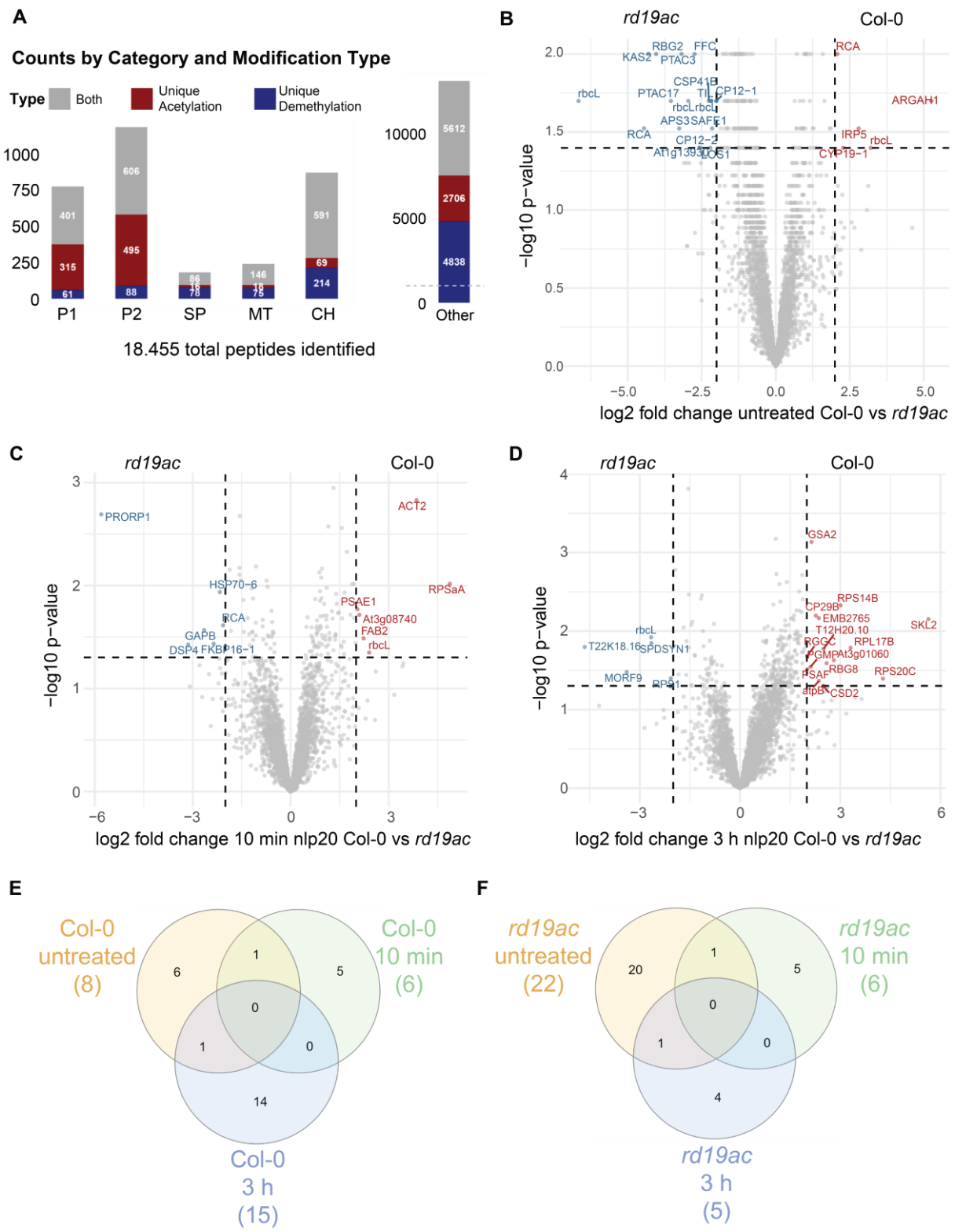


Figure 24: DIA HUNTER identified peptides. (**A**) Overview on identified counts of both unique acetylation and dimethylation. 18455 peptides were identified in total and categorized based on predicted positions. P1 = position 1, P2 = position 2, SP = signal peptide, MT = mitochondrial transit peptide, CH = chloroplast transit peptide, TH = thylakoid transit peptide, Others = non-canonical peptides (**B**) to (**D**) volcano plots of (**B**) untreated, (**C**) 10 min after

nlp20 treatment and (**D**) 3 h after nlp20 treatment for 100% valid values, enriched in Col-0 (red labels) or *rd19ac* (blue labels). Significance determined based on log2FC > 2/< -2 and p-value < 0.05, corresponding to -log10 p-value = 1.3025. (**E**) and (**F**) Venn diagrams of (**E**) Col-0 and (**F**) *rd19ac* significantly enriched proteins at all timepoints. Venn diagrams were generated using InteractiVenn.

Therefore, in the next step, analysis of dimethylated samples was extended to peptides that were only found in 100% valid values of Col-0 samples and not in any of the *rd19ac* mutant, independent of their significance in enrichment (Supplementary Table S 3). Venn diagrams revealed only 2 peptides commonly shared in Col-0 at all three treatments, RD19A and RD19C (Figure 25A). This verified that only Col-0 samples showed RD19A and RD19C cleavage and additionally suggested that already in untreated conditions, new N-termini of RD19A and RD19C were created and therefore the proteins potentially cleaved/processed. Low number of shared proteins also supported potential cleavage activities specific to nlp20-treatment (Figure 25A). Also, timepoints of 10 min and 3 h were relatively distinct, with only one protein identified in both, CA2 (BETA CARBONIC ANHYDRASE 2; AT5G14740) (Figure 25A), which encodes a beta carbonic anhydrase likely to be localized in the cytoplasm and that is an essential subunit of the respiratory chain NADH dehydrogenase complex (Zhang et al. 2018).

Between Col-0 untreated and Col-0 nlp20 10 min, also one protein was identified as common, GRP3 (GLYCINE RICH PROTEIN 3; AT2G05520), mutants of which have been shown to accumulate lower levels of ROS in response to *Xanthomonas citri* subsp. *citri* (*Xcc*) (Gottig et al. 2018). Venn diagrams of *rd19ac* at all timepoints revealed one overlap between untreated and treated conditions: TIP2-1 (DELTA TONOPLAST INTEGRAL PROTEIN; AT3G16240), which functions as water channel and ammonium transporter (Figure 25B) (Reinhardt et al. 2016). Surprisingly, more proteins were identified only in *rd19ac* but not in Col-0 at all timepoints (Figure 25B), suggesting that the loss of RD19A and RD19C could lead to activation of other processing enzymes (Supplementary Table S 3).

GO term annotations for Molecular Functions of peptides identified exclusively in Col-0 at 10 min and 3 h after nlp20-treatment revealed for both timepoints the GO term with most likelihood related to protease activity, since RD19A and RD19C were identified in these samples (Figure 25C and Figure 25D). At 3 h, salicylic acid binding was identified as enriched GO term with the gene GAPB (GLYCERALDEHYDE-3-PHOSPHATE DEHYDROGENASE B SUBUNIT; AT1G42970) (Figure 25D).

GO term analysis could not identify functions for all candidate peptides, and therefore potential functions were additionally manually curated for Col-0 and *rd19ac* 10 min and 3 h after treatment using information provided by TAIR (Supplementary Table S 4, Supplementary Table S 5, Supplementary Table S 6 and Supplementary Table S 7). Interestingly, this revealed that in *rd19ac* at 3 h, the cysteine protease RDL2 (AT3G19400) was identified, which has so

far not been described more in detail in the literature (Supplementary Table S 7). Furthermore, the cysteine protease inhibitor CYS3 (At2g40880) was found exclusively in *rd19ac* at 3 h (Supplementary Table S 7).

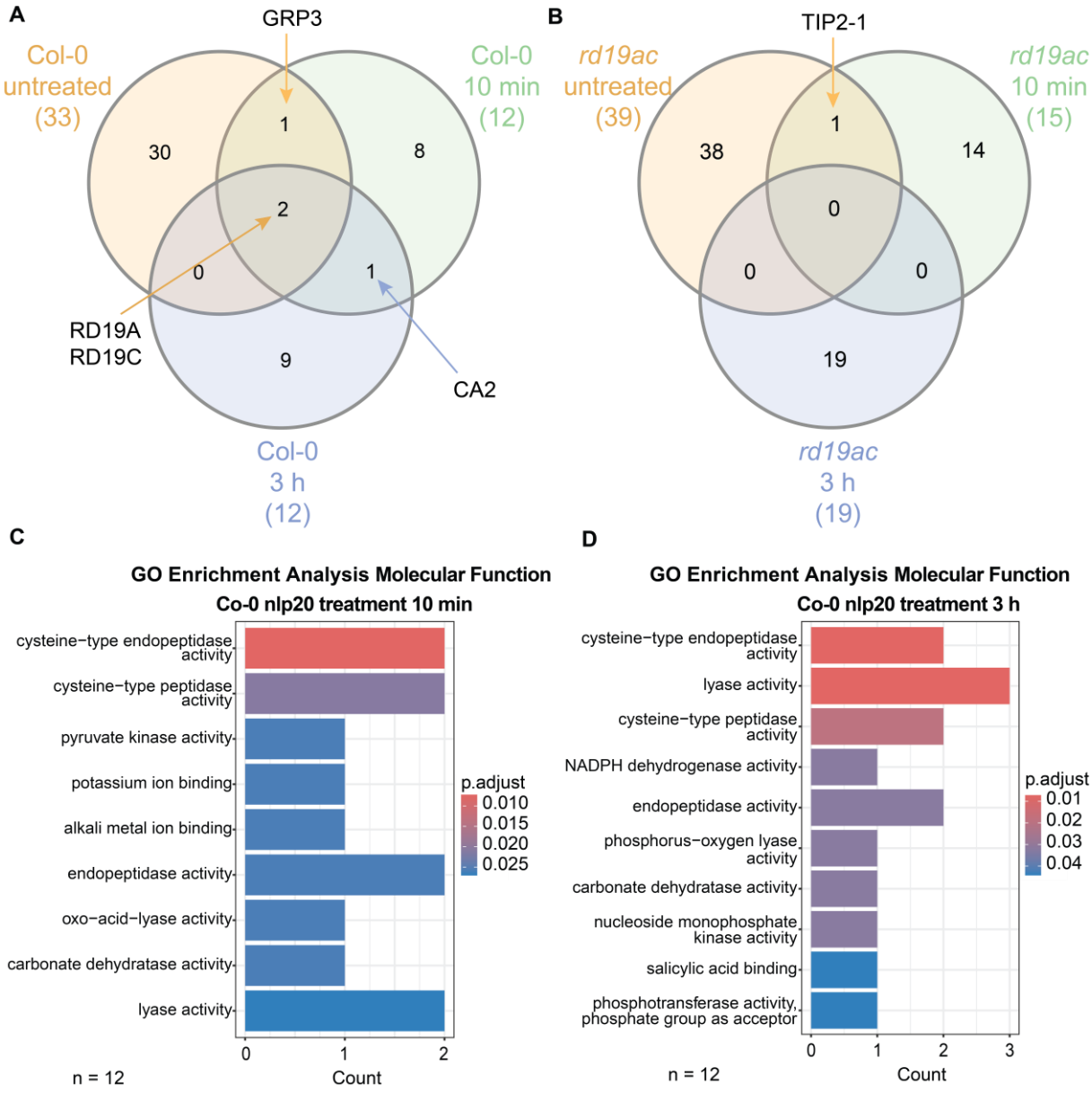


Figure 25: Results of peptides exclusively identified in Col-0 or *rd19ac* independent of significance. Venn diagrams of (**A**) Col-0 and (**B**) *rd19ac* of proteins exclusively identified in Col-0 or *rd19ac* at all timepoints. Venn diagrams were generated using InteractiVenn. (**C**) and (**D**) GO term Molecular Function prediction of peptides exclusively identified in Col-0 (**C**) 10 min or (**D**) 3 h after nlp20 treatment. Counts indicate number of peptides associated with one GO term. Significance is indicated by different colors based on $p < 0.05$. enrichGO function in R was used for determining GO terms.

Potential candidates identified in Col-0 10 min and 3 h after nlp20 treatment were further screened for the six amino acids preceding the cleavage site determined by HUNTER, to match potential candidates to the RD19 cleavage preference identified by PICS assay (Figure 20). Cleavage events preceded by Arginine (R) were excluded from evaluation, since these

were contamination of the trypsin digest performed prior to mass spectrometry (Supplementary Table S 9). Furthermore, only non-canonical peptides were considered in the analysis, excluding predicted chloroplast or mitochondrial transit peptides (Supplementary Table S 9).

As previously mentioned, PLCPs have a cleavage preference not only for position P1 but also P2, therefore both positions were examined for their match with PICS predictions (Table 1 and Table 2). Identified peptides were categorized for: both P1 and P2 fit with PICS prediction (green), only P1 fits with PICS prediction (orange) or only P2 fits with PICS prediction (blue) (Table 1 and Table 2). After 10 min, 1 peptide cleavage specific to Col-0 was aligning for P1 and P2 with the PICS prediction: AQUAPORIN INTERACTOR (AQI). Furthermore, three peptide cleavages were happening after a PICS predicted P1 site: AT5G56260, CA2 and GRP3 (Table 1). 3 h after nlp20 treatments, PHOSPHOENOLPYRUVATE CARBOXYLASE 2 (PPC2) showed overlap of P1 and P2 with PICS prediction, AT1G61730 (DNA-binding storekeeper protein) was identified with P1 overlap with PICS prediction (Table 2).

RD19A was the only protein identified in both conditions to only match the P2 prediction of the PICS assay, while RD19C was also identified in both conditions but cleavage was after R and therefore excluded from the dataset (Table 1 and Table 2).

Table 1: Cleavage sites identified only in Col-0 10 min after nlp20 treatment. Candidates were filtered for Arginine before cleavage site. aa = amino acid. Start and end give positions of cleavage window within the protein sequence.

Gene name	Start	End	First aa before sequence	First six aa before sequence	Cleavage window
RD19A	123	142	K	GFKLPK	GFKLPKDANKAP
RD19A	120	142	K	VRSGFK	VRSGFKLPKDAN
psbE	53	69	P	FGSPRP	FGSPRPNEYFTE
AT5G56260	34	55	M	HTESPM	HTESPMAAFATA
AT3G11930	18	34	K	TSAVEK	TSAVEKQPETTT
CA2	252	274	I	EDWVKI	EDWVKICLPAKS
GRP3	50	84	G	YGDNGG	YGDNGGNYNNGG
AQI	338	358	A	KQFLTA	KQFLTAADDSNP

Table 2: Cleavage sites identified only in Col-0 3 h after nlp20 treatment. Candidates were filtered for Arginine before cleavage site. aa = amino acid. Start and end give positions of cleavage window within the protein sequence.

Gene name	Start	End	First aa before sequence	First 6 aa before sequence	Cleavage window
RD19A	123	142	K	GFKLPK	GFKLPKDANKAP
RD19A	120	142	K	VRSGFK	VRSGFKLPKDAN
TIC56	127	153	V	FRASPV	FRASPVVQFMTR
PPC2	589	603	Q	RINGKQ	RINGKQEVMIGY
ISPF	166	179	I	LDATLI	LDATLILQRPKI
AT1G61730	126	141	G	PAMKSG	PAMKSGTKRPAS
CA2	95	126	D	LIEKDD	LIEKDDLKDVAA

Identification of cleavage events therefore narrowed down the list of potential candidates of RD19 substrates and in combination with prediction of function by GO term analysis and TAIR, the most interesting candidates were considered: AQI, CA2 and GRP3 at 10 min and PPC2, AT1G61730, CA2 and GAPB at 3 h after nlp20 infiltration.

3 Discussion

The results presented in this study provide a characterization of the cysteine protease RD19 in different types of immunity. In the beginning of this study, we hypothesized that RD19 as a PAD4-specific interaction partner might be required to support EDS1-PAD4-ADR1 in its unique function of connecting intracellular and surface triggered immunity. I approached this by testing the role of RD19 in different PAD4-dependent (and -independent) immune responses and identified that RD19 does not function as broadly as PAD4 and might have an opposing role in specific PTI responses. I furthermore tested, where RD19 might be expressed and aimed to show its activity in immunity. Nlp20-trigger induced strong ROS burst in *rd19ac* mutants, dependent on RBOHD. *RD19* overexpression led to presence of RD19 in all tested subcellular compartments, but activity analysis did not verify activity in overexpression lines. Lastly, in collaboration with Melissa Mantz and Pitter Huesgen at the University of Freiburg, I employed different proteomic approaches to identify potential targets of RD19, which were thought to be related to the potential role of RD19 in regulating ROS and immune priming (Figure 26).

3.1 The role of RD19 in PAD4-dependent immune responses

3.1.1 RD19 is not as broadly required for TNL-ETI and basal immune responses as PAD4

All studied TNLs in *A. thaliana* signal via the EDS1 family, with the EDS1-PAD4-ADR1 branch specifically leading to restriction of pathogen growth rather than induction of cell death (Bonardi et al. 2011; Lapin et al. 2019; Saile et al. 2020; Sun et al. 2021; Wu et al. 2019). The role of RD19 in immunity was therefore investigated in those immune responses in which an involvement of PAD4 had previously been described. While *rd19a*, *rd19c* and *rd19ac* were more susceptible to *Pst* DC3000 expressing the effector AvrRps4, RD19 was not required for resistance to *Hpa* Emwa1 (Zeng et al. 2024) (Figure 4C and Figure 4D). Though both pathogens activate PAD4-dependent TNL-ETI, their infection strategies and effector targets differ. While the hemi-biotrophic bacterial pathogen *Pst* enters plant cells via stomata and secretes effector molecules by a type-III-secretion system, *Hpa* is an oomycete with obligate biotrophic lifestyle and infects the plant by direct penetration of the cell wall, forming haustoria (Kamoun et al. 2015; Katagiri, Thilmony, and He 2002). Moreover, Emwa1 is recognized by the TNL receptor RPP4, while AvrRps4 is recognized by the receptor pair RRS1-RPS4 (Hinsch and Staskawicz 1996). Interestingly, the *Ralstonia solanacearum* effector PopP2, which has previously been described to target RD19A to the nucleus, is also recognized by RRS1-RPS4 (Bernoux et al. 2008). Similarly, out of the tested basal immune responses, loss of *RD19* only led to increased susceptibility to virulent powdery mildew *Golovinomyces cichoracearum* but not to virulent *Pst* DC3000 or *Hpa* Noco2 (Zeng et al. 2024) (Figure 5A and Figure 5B). While PAD4 is broadly utilized in immunity, a distinct requirement for immune components such as

RD19 might therefore be dependent on the infection strategy of the pathogen or could be determined downstream of effector recognition.

3.1.2 RD19 fulfills a distinct role in PTI responses by potentially regulating nlp20-triggered ROS burst

The EDS1-PAD4-ADR1 signaling branch was recently described as essential for PTI signaling specifically triggered by recognition of nlp20 by RLP23 but not for PTI activated by flg22 recognized by FLS2 (Pruitt et al. 2021). Comparable to PAD4, RD19 is exclusively required for nlp20- but not flg22-induced PTI responses, though analysis in this study shows that their functions most likely differ (Figure 8). While *pad4* mutants are impaired in *PAD3* gene expression, expression of this marker gene in *rd19ac* mutants was comparable to Col-0 wild type (Figure 8A). Previously published data of *pad4* shows a defect of the mutants in nlp20-mediated production of ROS, contrary to what was observed in the presented study (Pruitt et al. 2021) (Figure 8D; Supplementary Figure S 1). This is most likely due to variability in the experimental setup, since in an experiment that did not include the *rd19ac pad4* mutant - and was therefore not shown in this thesis - the previously reported nlp20-mediated *pad4* ROS phenotype was observed (Supplementary Figure S 7). Neither *pad4* nor *rd19ac* were defective in flg22- or nlp20- mediated MAPK activation, suggesting that machineries involved in very early PTI signaling are not severely affected by the lack of PAD4 and RD19 (Figure 8B) (Pruitt et al. 2021). Intriguingly, nlp20-mediated ROS burst was strongly induced in *rd19ac* mutants (Figure 8D; Supplementary Figure S 1). This phenotype was RBOHD-dependent (Figure 10A) and *rd19ac* mutants accumulated high levels of RBOHD protein (Figure 9A). These results suggest that the high ROS accumulation in *rd19ac* is due (at least in part) to lack of RBOHD degradation in the mutant (Figure 26). *rd19ac pad4* mutants generally behaved like *pad4* in all tested PTI outputs, suggesting that the increased nlp20-triggered ROS burst in *rd19ac* is additionally PAD4-dependent and/or that *rd19ac pad4* generally phenocopies the *pad4* mutant phenotype (Figure 8C and Figure 8D).

Unaltered ROS burst of *rd19ac* in response to flg22 was additionally reported in an independent study (Li et al. 2024). The authors furthermore demonstrated that overexpression of *RD19A* leads to increased ROS burst in response to flg22, comparable to what was observed for *rd19ac* in response to nlp20 in the present study (Figure 8C; Supplementary Figure S 1). Since the overexpression of RD19A leads to an autoimmune phenotype (Zeng et al. 2024), observed increase in ROS and also MAPK activation might solely be due to the overactivation of the immune system in these lines and not necessarily caused by a direct RD19 activity. The same study describes an interaction of RD19A and RD19C with the RLCK BRASSINOSTEROID-SIGNALING KINASE 1 (BSK1) (Li et al. 2024). BSK1 is one of the components shared between the development-associated brassinosteroid signaling pathway

and the immune activation pathway mediated by FLS2 (Lozano-Durán and Zipfel 2015; Shi et al. 2013). BSK1 and FLS2 interact in steady-state conditions and upon binding of flg22 by FLS2, BSK1 is released, positively regulating the ROS burst downstream of FLS2 (Lozano-Durán and Zipfel 2015; Shi et al. 2013; Tang et al. 2008). Interaction with BSK1 is therefore placing RD19 in close proximity to plasma membrane receptors (Li et al. 2024). In this thesis, RD19 was exclusively involved in nlp20-triggered immunity, which requires recognition of nlp20 by RLP23 receptor (Figure 8; Supplementary Figure S 1) (Albert et al. 2015; Böhm et al. 2014). The question therefore remains, why RD19 would interact with BSK1, which is required for FLS2- but not for RLP23-mediated signaling (Shi et al. 2013). Intriguingly, a recent pre-print was able to show a link between BSK1 and NLPs in *A. thaliana* and *Brassica napus* (Yalcin et al. 2023). They found that *A. thaliana bsk1* mutants respond significantly lower to the *B. cinerea* NLP BcNEP2 by inducing lower ROS burst and *bsk1* showed reduced resistance to *B. cincerea* (Yalcin et al. 2023). BSK1 might therefore not only be required for FLS2-activated signaling but also in RLP pathways, though it remains to be assessed whether *bsk1* mutants are also affected in nlp20-treatment. RD19 could thus potentially regulate BSK1 and contribute to signaling specificity downstream of PRRs.

3.1.3 RD19 is indispensable for nlp20-triggered priming in response to two distinct pathogens

While the use of elicitors such as flg22 and nlp20 provides a clean way to directly activate PTI signaling and test the role of proteins in these pathways, the full effect this perception has on disease resistance can only be evaluated through subsequent infection with a plant pathogen (Zipfel et al. 2004). For example, pre-treatment with flg22 or nlp20 primes Col-0 plants for subsequent infection with *Pst* DC3000 or *B. cinerea* (Figure 11 and Figure 12), however the precise molecular mechanism of priming establishment are not known, yet (Zipfel et al. 2004). While *rd19ac* showed Col-0 like phenotypes to infection with virulent *Pst* DC3000 (Figure 4C) or necrotrophic fungus *B. cinerea* (Figure 5 and Figure 6), pre-treatment with flg22 and nlp20 revealed a defect in nlp20-mediated priming responses to both pathogens in *rd19ac* mutants (Figure 11B and Figure 12B). This leads to the question of why *rd19ac* only shows altered resistance to pathogens when primed with nlp20, yet not during sole pathogen infection. It is possible that upon infections with only *Pst* DC3000 or *B. cinerea*, a requirement for RD19 in nlp20 signaling is not discernable because nlp20 is only one of many other PAMPs being recognized and resistance can be conferred, but when nlp20 is used in pre-treatments and signaling is not properly activated, no efficient additional barrier against the pathogen is established. A defect in *rd19ac* might therefore lie between direct immune activation and establishment of a long-lasting resistance. Here, the deficiency in priming might be guided by the increased ROS burst in *rd19ac* following nlp20 trigger (Figure 8D). Usually, if increased ROS production is observed during PTI elicitor treatment, the corresponding mutant lines also

display increased resistance to the pathogens tested, as exemplified with the receptor-like cytoplasmic kinase *pbl13* mutant (Lee et al. 2020). Nevertheless, a recent pre-print emphasized the requirement of a balanced ROS level in successful establishment of systemic immunity through control of SA signaling by post-translational modifications of transcription factors (Figure 26) (Cao et al. 2023). While high levels of ROS are known to be required to arrest pathogen growth, moderate levels of ROS are required for cell-to-cell signaling (Fichman et al. 2021; Wu et al. 2023). During priming with nlp20, the increased ROS burst might therefore lead to a disbalance of ROS required for establishing this spatiotemporal immune response, that is needed for resistance in the subsequent infection. One way to assess the effects of ROS levels on priming responses would be to use a line, such as the RBOHD overexpression line, producing high levels of ROS, and test it in a nlp20-mediated priming experiment. This would show whether the amount of ROS can determine a successful priming response and if too much ROS may inhibit rather than promote the boosted responsiveness of plant cells. It would furthermore be interesting to test whether *rd19ac* presents changes in Ca^{2+} levels or SA production. Both Ca^{2+} and SA have previously been linked to ROS production (Myers Jr et al. 2023; Oda et al. 2010; Ogasawara et al. 2008) and SA plays an important role in both priming and systemic immunity (Bernsdorff et al. 2016; Yildiz et al. 2021). Intriguingly, SA has been described to target the ROS-scavenging enzyme CATALASE 2 (CAT2), leading to H_2O_2 accumulation in SAR (Chen, Silva, and Klessig 1993; Conrath et al. 1995). While a role of RD19 in SAR remains to be determined, defect in nlp20-mediated priming in *rd19ac* could possibly and partially be caused by imbalance of ROS and SA levels.

In conclusion, though RD19 and PAD4 interact with each other, analysis of RD19 in PAD4-dependent immune responses showed distinct requirements for both proteins, only sharing a defect in nlp20-mediated priming responses. Therefore, the two proteins most likely do not (constitutively) work together in immunity, as additionally supported by their differential gene expression in response to different immune-related stresses (Figure 4A). Nevertheless, during priming responses, a requirement of the interaction for resistance might be possible.

3.1.4 RD19 shows increased expression at stomata and stomatal closure of *rd19ac* mutants is less responsive to elicitors

To better understand potential functions of RD19 in immunity, a single cell RNAseq dataset published by Tang et al. 2023 and generated at 24 and 40 hours after fungal infection with *Colletotrichum higginsianum*, was used to identify RD19 expression patterns (Figure 13A). Comparison with uninfected samples showed increased expression of *RD19A* in almost all cell types, and of *RD19C* especially in guard cells (Figure 13A). Since nlp20 induced an increased ROS burst in *rd19ac*, which was RBOHD dependent (Figure 10), and RBOHD together with RBOHF regulates ROS burst for stomatal closure in biotic stress responses, it was

hypothesized that the increased ROS burst could lead to increased stomatal closure in *rd19ac* (Dou and Zhou 2012; Melotto et al. 2006; Qi et al. 2017; Singh et al. 2017). Surprisingly, stomatal aperture index was decreased in mock conditions in *rd19ac* in comparison to Col-0 (Figure 13B). Regulation of stomatal opening and closing is important during drought conditions, to enable the plant to maintain water by reducing its loss through stomatal respiration. Since RD19 was initially identified as a factor required for response to dehydration (Koizumi et al. 1993), a potential increased stomatal closure in mock conditions might be linked to a role of this protein in abiotic stresses.

Contrary to the expected increase in stomatal closure upon nlp20 treatment, *rd19ac* mutants were less responsive to treatment with either flg22 or nlp20 (Figure 13B). This phenotype is reminiscent of autoimmune phenotypes in plants, where immune activity is already induced under mock conditions and plants do not respond to additional stimuli (Schulze et al. 2022; Wu et al. 2023). In preliminary results, resistance to *Pst* ΔCor was only affected when pre-treating plants with nlp20 but not to bacterial infection alone, alike what was observed for infection with *Pst* DC3000 and *B. cinerea* (Figure 13C and Figure 13D). While increased stomatal closure does therefore not positively affect resistance to the pathogen, potentially because a threshold of resistance is already achieved, nlp20 treatment induces less response in *rd19ac*, rendering them unprimed (Figure 11, Figure 12 and Figure 13B). RD19 was only required for nlp20-mediated priming responses but stomatal closure was affected in response to both flg22 and nlp20 (Figure 11, Figure 12 and Figure 13B). Intriguingly, EDS1-PAD4-ADR1 were previously shown to be required for stomatal closure in response to flg22, however, it remains to be assessed, whether this extends to nlp20 (Wang et al. 2024).

Single cell RNAseq also proposed *RD19* expression (especially of *RD19A*) in a variety of other cell types, such as those linked to the vasculature and long-distance transport (Figure 13A). In line with a role in priming responses, RD19A might be required in vasculature tissue during defense responses for signal propagation, potentially of ROS, to establish resistance in neighboring cells (Figure 8D, Figure 11, Figure 12, Figure 13A and Figure 26).

3.2 Localization and activity of RD19 and its link to PAD4

3.2.1 Subcellular localization of RD19A extends to all tested compartments in overexpression lines

All members of the EDS1 family have been shown to localize to the cytoplasm and the nucleus (Feys et al. 2001, 2005). A nuclear co-localization of RD19A and PAD4 was previously observed, with PAD4 promoting the nuclear localization of non-mature form of RD19 (proRD19), though this was achieved by expressing proRD19A (without signal peptide) transiently in *A. thaliana* protoplasts, and the lack of the signal peptide might influence the localization (Zeng et al. 2024). This study aimed to further identify localization of RD19A in both stable transgenic lines in *A. thaliana* and in transient expression in *N. benthamiana* and to test, where the interaction with PAD4 might take place. Overexpression lines of RD19A were used to study protein accumulations in different subcellular compartments, either in the RD19A wild-type form or the catalytically inactive version (C159A) in Col-0, *pad4* or *sag101* mutant background (Figure 14 and Figure 15A). Following fractionation of sub-cellular compartments, over-expressed RD19A protein was detected in all isolated cellular fractions, with a stronger signal accumulation in total extracts and nuclei depleted samples (Figure 14B and Figure 14C). Moreover, throughout all subcellular fractions, expression of RD19A was stronger in *pad4* mutant background, intriguingly with the ratio of full length RD19A to proRD19A shifting in AF, where a stronger band for proRD19A than full length RD19A was observed (Figure 15A). The previously published effect of the loss of PAD4 on maturation of RD19 in total extracts was not observed in this study but mutation of the cysteine active site abolished RD19 maturation independent of the cellular fraction (Figure 14 and Figure 15; (Zeng et al. 2024). Unfortunately, intensities of protein accumulations were difficult to evaluate between lines, due to non-normalized protein concentrations, uneven nuclei isolations among samples and different expression levels of RD19 in different lines, as shown in the total protein extracts (Figure 14B and Figure 14C). Additionally, isolation of AF from *A. thaliana* showed high cytosolic contamination by Ponceau staining, most likely due to the more delicate leaves of *A. thaliana* breaking easier than those of *N. benthamiana* (Figure 15A and Figure 15C). Therefore, apoplastic localization of RD19 was further verified by transient expression in *N. benthamiana*, using both fluorescence microscopy and western blotting of AF (Figure 15B and Figure 15C). In these western blots, all three forms of RD19 could be observed, independent of the signal peptide used (Figure 15C). Since mature RD19 was not observable in transgenic lines of RD19A, one possibility is that maturation and therefore activity of RD19 is only inhibited in the native *A. thaliana* background but not when expressed in *N. benthamiana*. Even though a RD19A-like protein was described in *N. benthamiana* (Grosse-Holz et al. 2018), Basic Local Alignment Search Tool (BLAST) search of the *At*RD19A protein sequence does not identify any RD19A-like protein from *N. benthamiana* in the top 5000 sequence alignment hits in the

search (blast.org; last accessed 03.10.2024). Therefore, it can be speculated that RD19A function is not shared between both species. Comparably, function of EDS1-PAD4-ADR1 is specific to *A. thaliana*, and the only role of this immune signaling branch described in *N. benthamiana* is in mediating stomatal closure (Wang et al. 2024). Therefore, in *N. benthamiana*, EDS1-SAG101-NRG1 fulfills both functions of pathogen restriction and activation of cell death (Lapin et al. 2019). Intriguingly, the recognition of nlp20 by RLP23 is also specific to *A. thaliana*, in line with the specific requirement of RD19 in nlp20-triggered immunity (Albert et al. 2015).

In conclusion, overexpression of RD19 led to detection of the protein in all tested subcellular compartments, however when testing for interaction with PAD4 with different localization sequences, RD19A in both inactive and active form interacted most strongly with the wild-type version of PAD4 (having a nucleocytoplasmic localization) (Figure 16). Moreover, interaction of both forms of RD19A was detected also with PAD4_NES, though to lesser extent than with PAD4_WT (Figure 16). Surprisingly, no mature RD19A was detected by western blotting, even though constructs used to express RD19A were the same as in the previous experiment (Figure 15C and Figure 16). It is plausible that mature RD19A in *N. benthamiana* rather locates to the apoplast, or that it is due to general higher expression level of RD19A when isolating AF, achieved using higher optical density in these experiments (Figure 15C and Figure 16). Alternatively, the presence of PAD4 could have influenced the maturation of RD19A, contrary to what was previously observed in *A. thaliana* (Zeng et al. 2024). Whether RD19A interacts preferentially with cytosolic PAD4 (PAD4_NES) than nuclear PAD4 (PAD4_NLS) should be tested under conditions with co-expressed EDS1 for full heterodimer function, and potentially also in immune-activated conditions. Data suggest that RD19A and PAD4 do not necessarily interact exclusively during RD19A activity (Figure 16). Comparably, previous reports of RD19 showed co-localization with the effector PopP2 in the nucleus but whether this mechanism is responsible for activation or inactivation of RD19, remains unclear (Bernoux et al. 2008). It is possible for RD19 to be active in untriggered tissues, where it localizes to vesicles and vacuolar associated compartments (Bernoux et al. 2008), and becomes inactivated during translocation to the nucleus. This would be supported by a previous report demonstrating RD19A and RD19C activity at acidic pH (pH 4–6.5), which is similar to vacuolar pH (Richau et al. 2012). Indeed, RD19A was described to contain two additional disulfide bonds, possibly increasing stability at extreme pH (Richau et al. 2012). A cytoplasmic localization of RD19 would be supported by its interaction with BSK1, a plasma-membrane anchored protein (Li et al. 2024). Alternatively, RD19 might have multiple localizations and active sites within the plant cell, possibly dependent on the cell type or also on the immune trigger used (Figure 26).

3.2.2 Activity-based protein profiling did not confirm RD19A protease activity in overexpression lines

To determine RD19A activity in overexpression lines, activity-based protein profiling (ABPP) was employed. The activity-based probe which consists of the PLCP inhibitor E64 linked to a biotin reporter, was incubated with total extracts at pH 7.4 and subsequently used for immunoblotting (Figure 17A). Even though RD19A and RD19C were shown to be active at pH 4-6.5 (Richau et al. 2012), the same pH as used when detecting RD19A in total extracts was chosen (pH 7.4), since here the strongest RD19A protein accumulation was observed (Figure 14B), and trials of ABPP from apoplastic fluids and isolated nuclei were not successful (data not shown).

Since overexpression lines of RD19A have a strong autoimmune phenotype, it was presumed that in these plants the immune system is already activated and no additional immune elicitation would be needed (Zeng et al. 2024). Western blots of ABPP showed one prominent band exclusively identified for the 35S::RD19A^{WT}-FLAG line, at the size of proRD19A (Figure 17B). The pro-form of a protease is not expected to show any activity, since the role of the pro-domain is to inhibit any unwanted functions of the protease by blocking its active site (Misas-Villamil et al. 2016). It might however be possible that the ABP gains access to the active site, if the pro-domain is only loosely covering the catalytic pocket (Supplementary Figure S 8). Another promising band was observed in Col-0 at size of mature RD19A (Figure 17B) but Col-0 was not included in the subsequent MS/MS analysis, because of sample size limitations and 35S::RD19A^{C159A}-FLAG was considered valuable as a control (Figure 17C and Figure 17D). Western blotting of input following the ABPP was promising, with bands the size of proRD19A and mature RD19A more strongly visible in 35S::RD19A^{WT}-FLAG than in any other line (Figure 17D). The fact that a band the size of mature RD19A was visible there but not before illustrates the potentially high variability of this assay, as it might appear with proteases that are more difficult to label than others (Richau et al. 2012). This emphasizes the requirement to - in the present case - verify activity-labeling by mass spectrometry and not solely rely on bands visible on western blots. Unfortunately, pulldown with α-Streptavidin agarose beads led to very uneven pulldown between different samples, either because uneven number of beads were added or because of unequal washing of the beads (Figure 17D).

Surprisingly, the subsequent MS/MS analysis revealed presence of active RD19A in only one out of four replicates for 35S::RD19A^{WT}-FLAG but in three out of four replicates of 35S::RD19A^{C159A}-FLAG (Figure 17E). Out of the identified peptide sequences, all replicates contained mapping to the pro-domain and protease domain, indeed showing that proRD19A was labeled as active in 35S::RD19A^{WT}-FLAG and 35S::RD19A^{C159A}-FLAG (Supplementary Table S 2). One explanation for the observed discrepancy of activity might be that in the

transgenic lines, 35S::RD19A does not actually render any activity or is inactivated by the plant, because too high levels of RD19A, potentially in all subcellular compartments (Figure 14 and Figure 15), would be toxic for the plant. This might be causing the autoimmune phenotype (Zeng et al. 2024). Indeed, on western blots of stable transgenic lines, mature RD19A was never detected (Figure 14 and Figure 15). The fact that 35S::RD19A^{C159A}-FLAG actually shows RD19A activity would mean that either RD19A activity of the Col-0 background was detected or that mutation of the predicted C159 active site was not sufficient to abolish protease activity. The first option appears more unlikely, because then activity should have also been detected in 35S::RD19A^{WT}-FLAG, unless the activation of cell death due to the autoimmune phenotype suppressed RD19A activity in Col-0. Lastly, since peptides mapping to the pro-domain of RD19A were detected in all samples, it remains plausible that ABPP was not precise enough in the labeling and that inactive RD19A was labeled in all samples (Supplementary Table S 2).

Since the overexpression lines were considered an unreliable tool to study RD19A activity and substrates, an alternative approach was to generate transgenic lines in the *rd19ac* mutant background, using constructs expressing *RD19A A. thaliana* endogenous promoter and genomic DNA. For catalytically inactive forms, the second cysteine C156 was additionally mutated for a more secured inactivation of protease activity. Lines were tested for complementation using nlp20-triggered ROS assay (Figure 18). Unfortunately, RD19A gene and protein expression was very weak in all lines, independent of the tag (HA or mYFP) or active or inactive RD19A (Supplementary Figure S 3 and Supplementary Figure S 4). Only immunoprecipitation allowed for protein detection of few of the mYFP-tagged lines (Figure 19). Interestingly, only at gene expression level an increase of RD19A expression was observed after nlp20 treatment, but not at protein level (Supplementary Figure S 3, Supplementary Figure S 4 and Figure 19). This is most likely due to the difference in sensitivity of the methods, and RT-qPCR can detect slight changes better than western blotting. Generally, expression levels of RD19A were very low, not only in transgenic lines but also in Col-0, with only three- to seven-fold increase after nlp20 treatment (Supplementary Figure S 3 and Supplementary Figure S 4). Earlier timepoints were chosen since RD19 appears to play a role in ROS signaling, as early as 15 to 30 minutes after trigger (Figure 8D). It is possible that timepoints chosen were too early to detect RD19A expression after nlp20 treatment, since expression in publicly available RNAseq datasets peaked at six hours after nlp20 treatment (Figure 7). Out of all tested lines, only one line was able to complement the ROS phenotype of *rd19ac* to Col-0 levels and additionally showed detectable gene and protein expression of RD19A (Supplementary Table S 1).

In the future, previous T2 generations should be further selected to test for RD19 expression and phenotype complementation, to employ at least two to three independent lines for

subsequent analysis. Additionally, the HA-tagged lines with promising complementation phenotypes (Figure 18) and slight RD19 gene expression levels (Supplementary Figure S 3) should be used for immunoprecipitation as performed with mYFP tagged lines, to increase chance of protein detection. Once two to three lines with detectable expression levels and complementation phenotype are selected, they should be subjected to ABPP, to verify RD19A activity.

3.3 Potential substrates of RD19 and their link to RD19 function in immunity

3.3.1 The loss of RD19 is interfering with RBOHD protein levels

The overarching question of the immune phenotyping and characterization of RD19A localization, was to identify molecular mechanisms, in which RD19 is functioning. Due to RD19 being a cysteine protease, the most likely hypothesis was that RD19s role in immunity is due to its role as cysteine protease, and therefore can be identified by its targets (Figure 26). ROS assays revealed an increased ROS burst in *rd19ac* following nlp20 trigger and this was dependent on RBOHD (Figure 8 and Figure 10). However, it is possible that *rd19ac rbohd* mutants simply phenocopied the *rbohd* phenotype because loss of RBOHD leads to loss of ROS generation independent of other proteins and pathways involved. The *rd19ac* phenotype might therefore not be fully dependent on RBOHD.

Moreover, RBOHD protein accumulated more in *rd19ac* mutants, already at timepoint zero but especially at 15 min after nlp20 treatment (Figure 9). Additionally, shotgun proteomics hinted to an increased presence, though not significant, of RBOHD in *rd19ac* mutants in comparison to Col-0 both 10 min and 3 h after nlp20 infiltration (Figure 22). Finally, gene expression analysis identified that regulation of RBOHD in *rd19ac* is executed on a protein and not gene expression level, as *RBOHD* induction was unchanged in comparison to Col-0 at all tested timepoints (Figure 9 and Supplementary Figure S 2). Therefore, a potential target of RD19 might be directly RBOHD or another protein regulating RBOHD accumulation in immune responses. Supporting the latter hypothesis, the requirement of RD19 for RBOHD degradation is specific to nlp20 and not flg22 (Figure 9, Figure 10 and Supplementary Figure S 2), suggesting that RD19 is not a universal regulator of RBOHD and might therefore rather target a positive regulator of RBOHD specific to nlp20 responses. Though, it might as well be that RD19 is indeed targeting RBOHD directly but that RD19 is activated by an unknown nlp20-specific upstream mechanism. A support of the hypothesis that RD19 is targeting RBOHD directly, would be the previously described vacuolar localization of RD19 (Bernoux et al. 2008) (Figure 26).

Indeed, a study recently showed RBOHD vacuolar degradation by the cysteine protease XCP1 (Liu et al. 2023). XCP1 is degrading RBOHD in resting state conditions, following a ubiquitination and phosphorylation that targets it to the vacuole, and under immune activation XCP1 is inhibited by CYS6, allowing RBOHD recycling to the plasma membrane (Lee et al. 2020; Liu et al. 2023). Authors therefore identified RBOHD as XCP1 target in untreated conditions, however the data shows an increased ROS burst in *xcp1* mutant lines following elf18 elicitation (Liu et al. 2023). Even though RBOHD protein levels in *xcp1* were not tested after elf18 trigger, the increased ROS burst after elicitor treatment is most likely due to the RBOHD accumulation (Liu et al. 2023). A comparable phenotype was observed for RD19 in this study, since RD19 appears to be important for regulating protein accumulation in nlp20-treated but also already in mock conditions (Figure 9). Furthermore, the effect observed in ROS burst assays with elf18 for *xcp1* is comparable to the increased nlp20 triggered ROS burst in *rd19ac* (Figure 8) (Liu et al. 2023). Intriguingly, these findings would suggest that a pool of RBOHD is permanently localized to the vacuole and the activation mechanism of RBOHD upon immune trigger is (partially) based on RBOHD recycling (Liu et al. 2023). In a different study, phosphatic acid (PA) was described to bind and stabilize RBOHD by suppressing its vacuolar degradation and therefore leading to enhanced ROS production upon chitin trigger (Qi et al. 2024). Moreover, PHAGOCYTOSIS OXIDASE/BEM1P (PB1) DOMAIN-CONTAINING PROTEIN (PB1CP) was shown to negatively regulate RBOHD by competing with BIK1 for RBOHD binding and promoting RBOHD endocytosis (Goto et al. 2024). Similar to *rd19ac* with nlp20, *pb1cp* mutants displayed higher ROS burst in response to elf18 and flg22, as well as chitin (Goto et al. 2024).

In this thesis, RBOHD protein accumulation and increased ROS burst were specific to nlp20, supporting a potential function of RD19 in relation to PAD4, and with it the EDS1-PAD4-ADR1 branch (Figure 8, Figure 9 and Supplementary Figure S 2). A possible scenario might therefore be that RBOHD is regulated independently upon different triggers and that already at resting state conditions, different regulatory mechanisms, such as proteases, might be available to act on RBOHD degradation in the vacuole. Whether RBOHD is a target of RD19, or RD19 is targeting an upstream component that activates RBOHD, remains to be elucidated (Figure 26).

3.3.2 Indicative overview of RD19-mediated proteomic changes by shotgun proteomics

In search for the molecular mechanism by which RD19 is acting in immunity, shotgun proteomics comparing Col-0 and *rd19ac* in untreated conditions and 10 min or 3 h after nlp20 treatment were performed. While nlp20 treatment was efficient, depictured by increased BAK1 protein levels upon nlp20 treatment, only few significant proteomic changes between Col-0 and *rd19ac* could be identified (Figure 21). In untreated conditions one protein, namely VSP2

was significantly enriched in Col-0 (Figure 21B). *VSP2* has previously been described as JA-responsive gene and therefore to be involved in insect herbivory responses but also to be required for OG or chitosan oligosaccharide induced resistance to *Pst* DC3000 (Howlader et al. 2020; Jia et al. 2018; Zhao et al. 2023). An enrichment of VSP2 in Col-0 could imply a decreased activation of JA responsive genes in *rd19ac* mutants, though exclusively in untriggered conditions. Even though priming responses have been mostly linked to SA, JA appears to also play a role in these responses (Howlader et al. 2020; Jia et al. 2018). Potentially less VSP2 already in untriggered conditions is creating a disbalance in *rd19ac*, which comes to light in nlp20 triggered priming responses (Figure 11 and Figure 12). Another explanation of identification of this protein in untriggered conditions would be that Col-0 plants were unknowingly subjected to higher insect pest when grown under controlled conditions in growth chambers. Though plant growth conditions were highly monitored, this cannot be fully excluded as a possibility for enrichment of an insect herbivory responsive protein.

10 min after nlp20 treatment, the rubredoxin-like superfamily protein AT5G51010 was enriched in *rd19ac*, but besides a function in iron ion binding, no role of this gene has been described in plant processes (Figure 21C) (Blum et al. 2021). Surprisingly, 3 hours after nlp20 treatment, no significantly enriched protein could be identified for Col-0 or *rd19ac* (Figure 21D). In the future it could be of interest to compare the two timepoints after treatment to the untreated condition of each line individually, to investigate proteomic changes and potential defects specific to *rd19ac*. However, though not significant, a difference in enrichment of immune components in response to nlp20 was visible between Col-0 and *rd19ac*, i.e. through RBOHD or EDS1 (Figure 21C and Figure 21D). It is possible that proteomic differences are very subtle and therefore not significant but still hold biological relevance.

Besides RD19A and RD19C, ELP5 and AT3G47890 were exclusively identified, independent of significance, in Col-0 10 min and 3 h after nlp20 treatment, respectively (Figure 23A). ELP5 has previously been described to localize to the cytosol and nucleus and be involved in tRNA modifications (Gaudet et al. 2009) and AT3G47890 is a ubiquitin carboxyl-terminal hydrolase-related protein (Blum et al. 2021) but neither protein has been reported in context of immune responses. Similarly, none of the detected proteins in *rd19ac* after nlp20 trigger were previously reported in immunity (Figure 23B). 10 min after nlp20 trigger AT5G11330, a FAD/NAD(P)-binding oxidoreductase family protein was detected (Blum et al. 2021) and at 3 h the F-box protein At1g15670 (KMD2 or KFB01) that mediates ubiquitination and degradation(Zhang, Gou, and Liu 2013).

Even though proteins exclusively identified in either Col-0 or *rd19ac*, or significantly enriched in one of the two lines, were very sparse and mostly not directly linked to immune responses, shotgun proteomics could support the previously observed increased accumulation of RBOHD

in *rd19ac* exclusively upon nlp20 trigger and furthermore verify the successful activation of nlp20-specific immune responses, which was invaluable to know for subsequent substrate analysis. Moreover, even though no direct link to immunity is known to date for the identified proteins, a possible, yet unknown role of these proteins cannot be excluded.

3.3.3 N-terminomic profiling using HUNTER revealed GRP3, CA2, GAPB and AQI as potential RD19 substrates

In this study, substrate identification using HUNTER was approached with two different analyses: based on 100% valid values, one analysis focused on cleavage sites of peptides enriched in Col-0 or *rd19ac* by generating ratios of Col-0 over *rd19ac*, while the other highlighted cleavage sites in peptides exclusively identified in Col-0 or in *rd19ac*, independent of their significance (Figure 24 and Figure 25). Analysis of Col-0 to *rd19ac* ratios presented only a small set of peptides that were enriched in Col-0 after nlp20 trigger and GO term analysis did not reveal any promising association of peptides to immune responses (Figure 24 and Supplementary Figure S 6). On the other hand, screening of exclusive peptides for Col-0 after treatment revealed more promising candidates. Here, one candidate was identified in both untreated conditions and 10 min after nlp20 treatment: GRP3 (Figure 25). GRP3 belongs to the GRP superfamily, which is characterized by the presence of variable semi-repetitive glycine-rich motifs and contains a putative SP that targets the protein to the apoplast (Gottig et al. 2018; Mangeon et al. 2016), where it interacts with the extracellular domain of WALL-ASSOCIATED KINASE 1 (WAK1) (Park et al. 2001). WAK1 was long thought to be an OG receptor (Brutus et al. 2010), though a recent BioRxiv refuted this claim by showing that WAK1 was dispensable in OG responses (Herold et al. 2024). GRP3 was furthermore identified to interact with the *Xanthomonas* type III secretion system pilus protein HrpE and *A. thaliana* mutants of GRP3 were more susceptible and accumulated lower levels of ROS in response to HrpE, possibly because GRP3 is required for the recognition of HrpE (Gottig et al. 2018). Though also identified in untreated conditions, GRP3 as a target of RD19 might positively regulate immune responses, potentially by regulating ROS balance or interaction with WAK1, though no role of WAK1 in nlp20-triggered immune signaling is known (Figure 26).

Exclusively found in Col-0 10 min and 3 h after nlp20 treatment was CA2 (Figure 25). CA2 constitutes a functional subunit of mitochondrial respiratory complex I, together with other four carbonic anhydrases (CA1, CA3, CAL1, and CAL2) and mutation of CA2 led to mitochondrial ROS production (Soto et al. 2015; Xu et al. 2023). However, CA2 localization was also identified in the cytosol (Fabre et al. 2007). Intriguingly, this cytoplasmic CA2 was described to undergo proteomic changes upon *Pst* AvrRpm1 trigger, suggesting posttranslational modifications (Jones, Mansfield, and Grant 2007) and mutants of *ca2* display increased drought tolerance (Xu et al. 2023). Possibly, RD19 cleavage could be defined as a

posttranslational modification, which might activate CA2. Indeed, the predicted cleavage site 10 min after nlp20 treatment was closely located to the C-terminus of the protein (Table 1). However, whether protease cleavage is necessary for CA2 activation remains to be determined (Figure 26).

At 3 h after nlp20 treatment in Col-0, GO term enrichment associates a SA binding function to GAPB, NADPH dehydrogenase activity to PROTOCHLOROPHYLLIDE OXIDOREDUCTASE C (PORC) and protein transmembrane transporter activity to TRANSLOCON AT THE INNER ENVELOPE MEMBRANE OF CHLOROPLASTS 56 (TIC56) (Figure 25). GAPB is a glyceraldehyde 3-phosphate dehydrogenase (GAPDH) with phosphorylating activity and characterized as chloroplastic photosynthetic GAPDH (Zaffagnini et al. 2013). Though sparsely described in plant immunity, one study identified downregulation of GAPB expression upon flg22 infiltration (Henry et al. 2015). ROS can induce GAPDH post-translational modifications and certain GAPDH knockout lines displayed increased production of ROS (Henry et al. 2015) (Figure 26). Compellingly, a recent pre-print showed the effect of chloroplast-derived ROS (cROS) on salicylic synthesis and consistently its requirement for immune priming responses (Roussin-Léveillée et al. 2024) (Figure 26). Both PORC and TIC56 are so far not described with a function in immune responses but predominantly involved in photosynthesis regulation (Gaudet et al. 2009; Oosawa et al. 2000).

Candidates identified by HUNTER were furthermore subjected to identification of cleavage sites previously predicted by PICS (Figure 20, Table 1 and Table 2). Out of potential substrates only identified in Col-0 after 10 min, one candidate displayed P1 and P2 sites as predicted by PICS: AQI (Table 1). AQI is an aquaporin interacting protein, belonging to the peptidase M20/M25/M40 family (Blum et al. 2021). Intriguingly, H_2O_2 crossing over plant plasma membranes is facilitated by aquaporins (Castro et al. 2021). Specifically, PLASMA MEMBRANE INTRINSIC PROTEIN 1;4 (PIP1;4) was found to be responsible to transport pathogen-induced apoplastic H_2O_2 to the cytoplasm of plant cells (Tian et al. 2016). Loss of PIP4;4 led to higher accumulation of H_2O_2 in the apoplast, without affecting H_2O_2 production directly, but altering the plants defense response to *Pst* DC3000 (Tian et al. 2016). Conversely, *rd19ac* displayed high levels of ROS but were affected in priming responses to *Pst* DC3000 and *B. cinerea* (Figure 11 and Figure 12). It is therefore tempting to hypothesize whether AQI functions as a link between RD19 and Aquaporin mediated membrane transfer of H_2O_2 (Figure 26).

Furthermore, after 10 min of nlp20 treatment, not only the beforementioned CA2 and GRP3, but also AT5G56260, a Ribonuclease E inhibitor RraA/Dimethylmenaquinone methyltransferase were identified with cleavage site P1 fitting PICS prediction (Table 1). While CA2 and GRP3 were considered interesting substrate candidates due to their previously

reported role in immunity, little is known about AT5G56260 besides a chloroplast localization and its ribonuclease activity (Blum et al. 2021; Gaudet et al. 2009).

3 h after nlp20 treatment, out of potential substrates only identified in Col-0, one protein exhibited PICS predicted P1 and P2 amino acid neighboring the cleavage sites, namely PPC2 (Table 2). The phosphoenolpyruvate carboxylase interacts with an E3 ligase in order to affect metabolite flux in carbon fixation, potentially leading to leaf senescence (Lan et al. 2022). Furthermore, a P1 position relative to PICS predicted cleavage sites was identified for AT1G61730 (Table 2). AT1G61730 is a DNA-binding storekeeper protein-related transcription factor with no further described function (B. Li et al. 2014).

Although RD19 specific cleavage would only be identified in Col-0, *rd19ac* specific peptides could hint to a role of RD19 in immunity. Intriguingly, while GO term analysis was not too promising, manually curated annotation of function using TAIR revealed two interesting peptides corresponding to the proteins RDL2 and CYS3 (Supplementary Table S 8). The protease RDL2 was so far not studied in immunity, only in a biochemical analysis where it was identified to be active at a variety of pHs (Richau et al. 2012). CYS3 (also termed CYSA) belongs to the group of cystatins, naturally occurring protease inhibitors of which some have been described in the context of plant immunity (van Wyk et al. 2016). The *Zea mays* CORN CYSTATIN 9 (CC9) for example, suppresses defense against *Ustilago maydis* by inhibiting apoplastic PLCPs (van der Linde et al. 2012). As mentioned before, XCP1 is inhibited by CYS6 in the vacuole (Liu et al. 2023), while for example CYS1 suppresses hypersensitive cell death (Belenghi et al. 2003). When overexpressing CYS3 in yeast it increased resistance to drought, high salt, cold and oxidative stress (Zhang, Liu, and Takano 2008) and CYS3 was furthermore found in *A. thaliana* as suppressor of VACUOLAR PROCESSING ENZYME γ (VPEγ), a cysteine protease induced during senescence (Rojo et al. 2004). A possibility would therefore be that CYS3 is inhibiting RD19 activity *in planta* upon nlp20 treatment and was therefore found as a cleaved substrate in *rd19ac* mutants (Supplementary Table S 8).

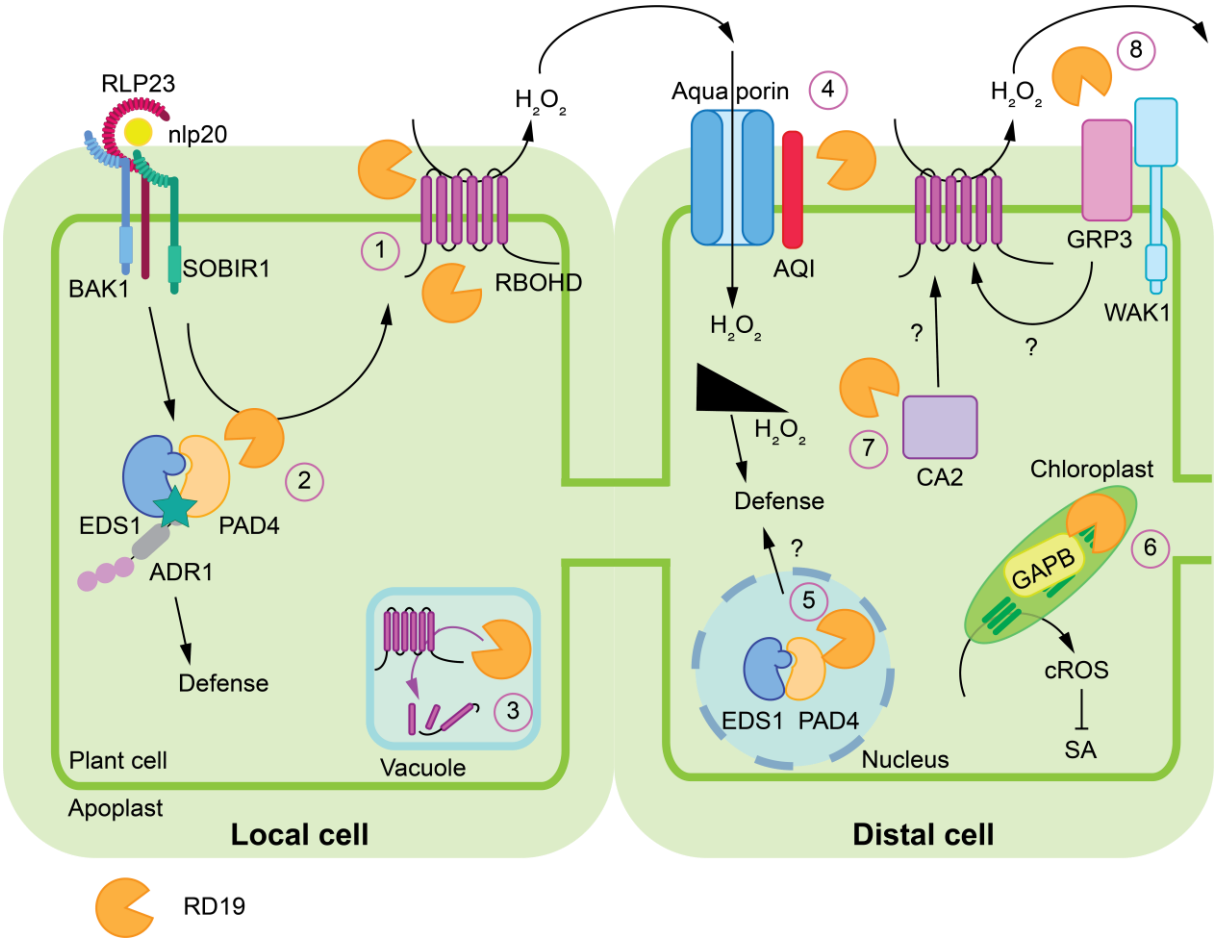


Figure 26: Working model on the potential role of RD19 in plant immunity. This study revealed a variety of potential substrates of RD19. All scenarios are depicted upon the perception of nlp20 by the receptor complex RLP23-SOBIR1-BAK1. RD19 = orange open circle. (1) RD19 might target RBOHD in the cytosol or apoplast and influences ROS production. (2) RD19 might interact with the EDS1-PAD4-ADR1 branch for influence of ROS production and establishment of priming responses. (3) RD19 might degrade RBOHD in the vacuole. (4) AQI might interact with aquaporin, mediating H_2O_2 transport into cell. AQI might be targeted by RD19. A specific gradient of H_2O_2 is required for defense activation and RD19 might be required to keep it in balance. (5) RD19 interacts with EDS1-PAD4 in the nucleus, potentially for defense activation. (6) RD19 might target GAPB in the chloroplast, influencing chloroplast-derived ROS (cROS) activation and inhibiting SA which negatively impairs priming. (7) RD19 might target CA2 in the cytosol, that could influence ROS production or (8) RD19 might target GRP3 apoplastically, controlling ROS production through GRP3 interaction with WAK1. Influence on ROS generation might impact the cell-to-cell signaling. Whether RD19 acts on targets in local or distal cells, remains to be determined.

In conclusion, even though genetic studies presented RBOHD as a valid candidate as substrate of RD19, and RBOHD intensities were increased in shotgun proteomics *rd19ac* compared to Col-0, RBOHD was not identified as a target in the HUNTER substrate analysis. Although HUNTER is a highly sensitive method, it also remains a possibility that not all RD19 substrates were identified in the analysis. Overall, out of peptides with cleavage sites exclusively identified in Col-0 but not *rd19ac* the most interesting candidates were GRP3, CA2, GAPB and AQI, while the role of peptides cleaved exclusively in *rd19ac* mutants should also be subject of further analysis (Figure 26).

3.4 Future perspectives

The presented study characterized the role of the PLCP RD19 in plant immune signaling and shed light on potential substrates of this protease, that could potentially link phenotypes observed in the *rd19ac* mutant to the molecular function of RD19 in immunity. Importantly, while the list of candidates was promising, since some of the proteins were previously described with a role in immunity, the cleavage by RD19 should be verified in an independent experiment. A relatively fast way of testing cleavage of those candidates, and potentially RBOHD, could be a co-expression assay in *N. benthamiana*, followed by visualization of potential changes in protein size by immunoblotting. Furthermore, *A. thaliana* knockout lines of candidate genes should be tested in immune assays, such as the nlp20-triggered ROS or priming assay, to identify whether the candidates are positive or negative regulators of plant immunity. Additionally, a cross of *rd19ac* and the candidate knockout lines should be generated to test for the complementation of phenotypes observed in *rd19ac*. Even though RBOHD was not identified as a potential substrate in the HUNTER assay, a potential vacuolar degradation of RBOHD by RD19 could be tested by checking RBOHD protein levels in *rd19ac* after addition of Concanamycin A (ConA). ConA is a well-established inhibitor of vacuolar degradation and RBOHD levels were previously shown to increase in Col-0 upon addition of ConA (Liu et al. 2023). If the stability of RBOHD in the *rd19ac* mutant remains unaffected by ConA, RD19 is most likely destabilizing RBOHD in the vacuole.

While identification and verification of RD19 substrates is great support in identifying the localization of RD19, identification of fluorescently tagged RD19 using microscopy would be the ideal verification of the subcellular localization. Here, the complementing stable transgenic lines with native RD19 promoter should be further selected, to establish two to three independent lines with detectable RD19 gene and protein expression and use microscopy to visualize RD19 localization.

This study was initiated with the hypothesis that RD19 and PAD4 interaction has an important function in plant immunity. However, phenotypes observed for *rd19ac* and *pad4* in this study were quite distinct, with both proteins only sharing a requirement for nlp20-mediated priming responses. It could be interesting to evaluate the interaction of RD19 and PAD4 specifically during this immune response. EDS1-PAD4 are known to promote SA levels, and an interaction of PAD4 and RD19 might be required for the interplay of ROS and SA in priming. Levels of SA, but also the Ca^{2+}-influx in *rd19ac* should be evaluated. Additionally, test of another *A. thaliana* line accumulating high levels of ROS, such as 35S::RBOHD, could support the search for a connection of the two phenotypes observed in *rd19ac*.

In conclusion, the presented study furthered our understanding of RD19 in immunity and paved the way for subsequent verifications and analysis to uncover the precise molecular mechanisms, by which this protease is acting in plant immunity.

4 Material and methods

4.1 Material

4.1.1 Oligonucleotides

The oligonucleotides used in this study were purchased from Sigma-Aldrich (Germany) and are listed in Table 3. Lyophilized primers were suspended in ddH_2O to a concentration of 100 µM, working solutions were diluted to a concentration of 10 µM.

Table 3: Oligonucleotides used in this study

ID	Sequence	Purpose	Orientation
nGH005	TGCCTGCAGGTCGACTCTAG CAGGTTTCATCCTTCTTGTAT AGG	InFusion cloning: fw primer pXCSG_OLE-RFP_MCS and pRD19-gRD19	fw
nGH006	CCTTGCTCACATGGGCGGTG GTTGAGAC	InFusion cloning: rv primer pRD19-gRD19 and mCherry	rv
nGH007	CACCGCCCATGTGAGCAAGG GCGAGGAGG	InFusion cloning: fw primer pRD19-gRD19 and mCherry	fw
nGH008	GGTACCCGGGGATCCTCTAG CTAGTTAATTAACTTGTACAG CTCG	InFusion cloning: rv primer mCherry and pXCSG_OLE-RFP_MCS	rv
nGH009	TGTAGTCCCCATGGGCGGTG GTTGAGAC	InFusion cloning: rv primer pRD19-gRD19 and 3xFLAG	rv
nGH010	CACCGCCCATGGGGACTACA AAGACCATGACGG	InFusion cloning: fw primer pRD19-gRD19 and 3xFLAG	fw
nGH011	GGTACCCGGGGATCCTCTAG CTACTTGTCATCGTCATCCTT GTAG	InFusion cloning: rv primer 3xFLAG and pXCSG_OLE-RFP_MCS	rv
nGH012	TCACCATCCCATGGGCGGTG GTTGAGAC	InFusion cloning: rv primer pRD19-gRD19 and mYFP	rv
nGH013	CACCGCCCATGGGATGGTGA GCAAGGGC	InFusion cloning: fw primer pRD19-gRD19 and mYFP	fw
nGH014	GGTACCCGGGGATCCTCTAG TTACTTGTACAGCTCGTCCAT GCC	InFusion cloning: rv primer mYFP and pXCSG_OLE-RFP_MCS	rv
nGH015	CGTATGGGTAATGGGCGGTG GTTGAGAC	InFusion cloning: rv primer pRD19-gRD19 and 3xHA-Strep	rv
nGH016	CACCGCCCATTACCCATACG ATGTTCCTGAC	InFusion cloning: fw primer pRD19-gRD19 and 3xHA-Strep	fw
nGH017	GGTACCCGGGGATCCTCTAG TTATTTTTCAAATTGAGGATG AGAC	InFusion cloning: rv primer 3xHA-Strep and pXCSG_OLE-RFP_MCS	rv
nGH018	ACTTTTGTTCATGGGCGGTG GTTGAGAC	InFusion cloning: rv primer pRD19-gRD19 and 3xMYC	rv
nGH019	CACCGCCCATGAACAAAAGT TGATTTCTGAAGAAG	InFusion cloning: fw primer pRD19-gRD19 and 3xMYC	fw
nGH020	GGTACCCGGGGATCCTCTAG TCTAGACTAGCTTTCCGTTCA AG	InFusion cloning: rv primer 3xMYC and pXCSG_OLE-RFP_MCS	rv

nGH021	AACCTCGTGATCACAGTCGAC	rd19a_LP; genotyping primer	LP
nGH022	AGACAACACGGCACTGCTAAC	rd19a_RP; genotyping primer	RP
nGH023	CTACTGATACTCAGACGGCGC	rd19c_LP; genotyping primer	LP
nGH024	ACAAAGATAATACCCCCAAGC	rd19c_RP; genotyping primer	RP
nGH105	CGTAAGAAGCACTTGGGGGT	qPCR_RD19A	fw
nGH106	GAGCCGCAAGATCCCTGATT	qPCR_RD19A	rv
nGH119	TGACTCGTTCTGAGTTTCGGAG	qPCR_RD19B	fw
nGH120	GCAAGAACCACAAGATCCCTGG	qPCR_RD19B	rv
nGH121	CGATTGTGATCAAGCGTGCG	qPCR_RD19D	fw
nGH122	TGCAATGGCCTCGTTTACCA	qPCR_RD19D	rv
nGH127	CGATGGTGAGCAAGGGCGA	in fusion_2082	fw
nGH128	TTGTATCGATAATTGTAAATGTAAT	in fusion_2082	rv
nGH129	CAATTATCGATACAAATGGATCGTCTTAAGCTTTATTTCT	in fusion_RD19+SP	fw
nGH130	CCTTGCTCACCATCGTTAATGGGCGGTGGTTGAGA	in fusion_RD19+SP	rv
nGH131	GCTTCTCTAGCTAGAGTCGATCGAC	in fusion_2537	fw
nGH132	CACCTGCACGGCAAGAGTG	in fusion_2537	rv
nGH133	CCACTCTTGCCGTGCAGGTGTCTGATGTCAACGACGGCG	in fusion_RD19-SP/mCherry	fw
nGH134	CCTTGCTCACATGGGCGGTGGTTGAGAC	in fusion_RD19-SP/mCherry	rv
nGH135	CACCGCCCATGTGAGCAAGGGCGAGGAGG	in fusion_mCherry	fw
nGH136	TCGACTCTAGCTAGAGAAGCCTAGTTAATTAACTTGTACAGCTCG	in fusion_mCherry	rv
nGH137	GGACCTCTAGCTATTGCTATC	qPCR_RD19C	fw
nGH138	CCAAATCCAACCAAGAGCACT	qPCR_RD19C	rv
nGH141	ACCTGCACGGCAAGAGTG	in fusion_2537_rv	rv
nGH142	CCCACTCTTGCCGTGCAGGTTCTGATGTCAACGACGGCG	in fusion_RD19-SP/mCherry_fw	fw
nGH143	TGTATCGATAATTGTAAATGTAATT	in fusion_2537_full RD19 insert	rv
nGH144	CATTTACAATTATCGATACAATGGATCGTCTTAAGCTTTATTTCT	in fusion_RD19+SP_in 2537	fw
nGH145	CAGGGATCTgcCGGCTCTgcCTGGAGTTTCAGCGCCACTG	SDM cDNA_RD19A_C156A_C159A	fw
nGH146	CAGTGGCGCTGAAACTCCAGgcAGAGCCGgcAGATCCCTG	SDM cDNA_RD19A_C156A_C159A	rv

nGH147	TCTGATGTCAACGACGGCGA	In fusion_2537_exchange NtPR1a with RD19SP	fw
nGH148	GTCGTTGACATCAGACGACG AAACCGAGACGATAAAGAAA GACAAAACGAAAACGGAGAA ATAAAGCTTAAGACGATCCAT TGTATCGATAATTGTAAATGT AATT	In fusion_2537_exchange NtPR1a with RD19SP	rv
nGH149	CCAGGAGGCTCAACCACGG	cDNA RD19-mCherry sequencing primer	fw
nGH150	ATGGGCGGTGGTTGAGAC	in fusion_2537 rv exchange of mCherry with 3xHA	rv
nGH151	TCAACCACCGCCCATTACCC ATACGATGTTCCTGAC	in fusion_3xHA fw_exchange of mCherry with 3xHA	fw
nGH152	TCTAGCTAGAGAAGCTTATTT TTCAAATTGAGGATGAGAC	in fusion_3xHA rv_exchange of mCherry with 3xHA	rv
nFL013	GTTAAGCTCGCTGTTCTTCAG T	qPCR_UBI5	fw
nFL014	TCAAGCTTCAACTCCTTCTTT C	qPCR_UBI5	rv
nFL085	CGAATGGCATCCTTTCTCAAT C	qPCR_RBOHD	fw
nFL086	GTCACCGAGAGTGCGGATAT G	qPCR_RBOHD	rv
nFL170	TCGCTGGCATAACACTATGG	qPCR_PAD3	fw
nFL171	TTGGGAGCAAGAGTGGAGT	qPCR_PAD3	rv
nFL005	TTAAACTCGACGATGCAACA	qPCR_FRK1	fw
nFL006	GATGGAAGTTTTCCCGTTTT	qPCR_FRK1	rv
AC434	GGATACTGATCATAGGCGTG GCTCCA	rbohd_genotyping	rv
AC435	GTCGCCAAAGGAGGCGCCG A	rbohd_genotyping	fw
AC436	CTTATTTCAGTAAGAGTGTGG GGTTTTGG	rbohd genotyping_dSPM detection	rv

4.1.2 Vectors

Vectors used and generated in this study are listed in Table 4.

Table 4: Vectors used in this study

ID	Vector	Purpose
pOJ155	pXCSG_OLE-RFP_MCS (pIF16)	For further cloning
pGH003	pIF16.1_gRD19_mCherry	For stable expression in *A. thaliana*
pGH004	pIF16.1_gRD19_mYFP	For stable expression in *A. thaliana*
pGH005	pIF16.1_gRD19_3xHA-Strep	For stable expression in *A. thaliana*
pGH006	pIF16.1_gRD19_3xMyc	For stable expression in *A. thaliana*
pGH007	pIF16.1_gRD19_3xFLAG	For stable expression in *A. thaliana*

pGH008	pRD19::gRD19A_C159A-mYFP	For stable expression in *A. thaliana*
pGH009	pRD19::gRD19A_H302A-mYFP	For stable expression in *A. thaliana*
pGH010	pRD19::gRD19A_C156A_C159A-mYFP	For stable expression in *A. thaliana*
pGH011	pRD19::gRD19A_C159A-HA	For stable expression in *A. thaliana*
pGH012	pRD19::gRD19A_N329-HA	For stable expression in *A. thaliana*
pGH013	pRD19::gRD19A_H302A-HA	For stable expression in *A. thaliana*
pGH014	pRD19::gRD19A_C156A_C159A-HA	For stable expression in *A. thaliana*
pGH015	pRD19::gRD19A_C159A-mCherry	For stable expression in *A. thaliana*
pGH016	pRD19::gRD19A_N329-mCherry	For stable expression in *A. thaliana*
pGH017	pRD19::gRD19A_C156A_C159A-mCherry	For stable expression in *A. thaliana*
pGH018	pRD19::gRD19A_C159A-FLAG	For stable expression in *A. thaliana*
pGH019	pRD19::gRD19A_N329-FLAG	For stable expression in *A. thaliana*
pGH020	pRD19::gRD19A_H302A-FLAG	For stable expression in *A. thaliana*
pGH021	pRD19::gRD19A_C159A-myc	For stable expression in *A. thaliana*
pGH022	pRD19::gRD19A_H302A-myc	For stable expression in *A. thaliana*
pGH023	2537_SPntpr1-Q10716 (provided by the group of G. Doehlemann)	For further cloning
pGH024	2537_NtPR1a_RD19A (-SP)-mCherry	For transient expression in *N. benthamiana*
pGH024	2537_NtPR1a_RD19A_C156A_C159A_ (-SP)-mCherry	For transient expression in *N. benthamiana*
pGH025	2537_full length RD19A-mCherry	For transient expression in *N. benthamiana*
pGH026	2537_full length RD19A_C156A_C159A_-mCherry	For transient expression in *N. benthamiana*
pGH027	2537_NtPR1a_RD19A (-SP)-HA	For transient expression in *N. benthamiana*
pGH028	2537_NtPR1a_RD19A_C156A_C159A_ (-SP)-HA	For transient expression in *N. benthamiana*
pGH029	2537_full length RD19A-HA	For transient expression in *N. benthamiana*
pGH030	2537_full length RD19A_C156A_C159A_-HA	For transient expression in *N. benthamiana*
pJW091	J2B-3xFLAG-GUS	For transient expression in *N. benthamiana*

Furthermore, DMSO stocks of *A. tumefaciens* described in Table 5 were used in this study.

Table 5: *A. tumefaciens* DMSO stocks used in this study

ID	Vector	Purpose
dGH011	pIF16.1_gRD19_mCherry	For stable expression in *A. thaliana*
dGH012	pIF16.1_gRD19_mYFP	For stable expression in *A. thaliana*
dGH013	pIF16.1_gRD19_3xHA-Strep	For stable expression in *A. thaliana*
dGH014	pIF16.1_gRD19_3xMyc	For stable expression in *A. thaliana*
dGH015	pIF16.1_gRD19_3xFLAG	For stable expression in *A. thaliana*
dGH018	J2B-3xFLAG-GUS	For transient expression in *N. benthamiana*
dGH020	p35S:EDS1-3xFLAG	For transient expression in *N. benthamiana*
dGH025	35S:YFP-stop-YFP	For transient expression in *N. benthamiana*
dGH070	pXCSG-cPAD4-3xFLAG	For transient expression in *N. benthamiana*
dGH112	pRD19::gRD19A_C156A_C159A-HA	For stable expression in *A. thaliana*
dGH119	pRD19::gRD19A_C156A_C159A-mCherry	For stable expression in *A. thaliana*
dGH135	pRD19::gRD19A_C156A_C159A-mYFP	For stable expression in *A. thaliana*
dGH138	2537_NtPR1a_RD19A (-SP)-mCherry	For transient expression in *N. benthamiana*
dGH140	2537_NtPR1a_RD19A_C156A_C159A_ (-SP)-mCherry	For transient expression in *N. benthamiana*
dGH142	2537_full length RD19A-mCherry	For transient expression in *N. benthamiana*
dGH144	2537_full length RD19A_C156A_C159A_-mCherry	For transient expression in *N. benthamiana*
dGH149	2537_NtPR1a_RD19A (-SP)-HA	For transient expression in *N. benthamiana*
dGH150	2537_NtPR1a_RD19A_C156A_C159A_ (-SP)-HA	For transient expression in *N. benthamiana*
dGH151	2537_full length RD19A-HA	For transient expression in *N. benthamiana*
dGH152	2537_full length RD19A_C156A_C159A_-HA	For transient expression in *N. benthamiana*
dJD143	YFP-gPAD4	For transient expression in *N. benthamiana*
dJD144	YFP-NLS-gPAD4	For transient expression in *N. benthamiana*
dJD146	YFP-NES-gPAD4	For transient expression in *N. benthamiana*

4.1.3 Plant material

The plant genotypes used and generated in this study are listed in Table 6.

Table 6: Plant lines used and generated in this study

Species	Genotype	Reference
Arabidopsis thaliana	Col_0	
Arabidopsis thaliana	Ws_2	
Arabidopsis thaliana	*eds1-12*	(Ordon et al. 2017)
Arabidopsis thaliana	*pad4-1*	(Glazebrook et al. 1997)
Arabidopsis thaliana	*fls2*	(Zipfel et al. 2004)
Arabidopsis thaliana	*rlp23*	(Pruitt et al. 2021)
Arabidopsis thaliana	*rbohd*	(Entila et al. 2024)
Arabidopsis thaliana	*rd19a*	(Zeng et al. 2024)
Arabidopsis thaliana	*rd19c*	(Zeng et al. 2024)
Arabidopsis thaliana	*rd19ac*	(Zeng et al. 2024)
Arabidopsis thaliana	*rd19ac pad4*	this study
Arabidopsis thaliana	*rd19ac rbohd*	this study
Arabidopsis thaliana	35S::RD19A-FLAG^{WT} #1	(Zeng et al. 2024)
Arabidopsis thaliana	35S::RD19A-FLAG^{WT} #2	(Zeng et al. 2024)
Arabidopsis thaliana	35S::RD19A-FLAG^{C159A} 2-10	(Zeng et al. 2024)
Arabidopsis thaliana	35S::RD19A-FLAG^{C159A} 6-19	(Zeng et al. 2024)
Arabidopsis thaliana	35S::RD19A-FLAG^{WT} in *pad4*	(Zeng et al. 2024)
Arabidopsis thaliana	35S::RD19A-FLAG^{WT} in *sag101*	(Zeng et al. 2024)
Nicotiana benthamiana	WT	MPIPZ, Cologne
Nicotiana benthamiana	*eds1 pad4 sag101a sag101b*	(Lapin et al. 2019)

4.1.4 Bacterial strains

The bacterial strains used and generated in this study are listed in Table 7.

Table 7: Bacterial strains used in this study

Species	Strain	Genotype
Escherichia coli	DH10B	F - mcrA Δ(mrr-hsdRMS-mcrBC) Φ80lacZΔM15 ΔlacX74 deoR recA1 endA1 araΔ139 Δ(ara, leu)7697 galU galK λ$^-$ rpsL (StrR) nupG
Agrobacterium tumefaciens	GV3101	pMP90RK (Koncz and Schell 1986)
Pseudomonas syringae	DC3000	pVSP61 EV (Hinsch and Staskawicz 1996)
Pseudomonas syringae	DC3000	pVSP61 AvrRps4 (Hinsch and Staskawicz 1996)
Pseudomonas syringae	DC3000	*Pst* ΔCor (Delta Coronatine) Provided by Renier van der Hoorn

4.1.5 Antibiotics

Antibiotics and their concentrations used for bacterial selections are listed in Table 8.

Table 8: Antibiotics used in this study

Name	Stock Concentration	Working Concentration	Solvent
Carbenicillin	100 mg/ml	50 mg/l	ddH_2O
Gentamycin	25 mg/ml	25 mg/l (*Pst*) or 15 mg/l (*Agrobacterium*)	ddH_2O
Kanamycin	50 mg/ml	25 mg/l	ddH_2O
Spectinomycin	100 mg/ml	100 mg/l	ddH_2O
Rifampicin	40 mg/ml	100 mg/l	DMSO

4.1.6 Antibodies

Antibodies used for immunoblotting analysis are listed in Table 9.

Table 9: Antibodies used in this study

Name	Source	Dilution	Type	Supplier
α-FLAG	Mouse M2 monoclonal	1:5000	primary	Sigma-Aldrich
α-GFP	mouse monoclonal	1:5000	primary	Roche
α-HA	rat monoclonal	1:5000	primary	Roche
α-mCherry	rabbit monoclonal	1:2500	primary	Agrisera
α-RBOHD	rabbit monoclonal	1:5000	primary	Agrisera
p-44/p-42	rabbit monoclonal	1:5000	primary	Cell Signaling
α-Streptavidin HRP	polymer conjugate	1:1000	conjugated	Merck
α-PEPC	rabbit monoclonal	1:10000	primary	Agrisera
α-H3.3	rabbit monoclonal	1:5000	primary	Abcam
α-mouse IgG HRP	rabbit monoclonal	1:5000	secondary	Cell Signaling
α-rabbit	goat monoclonal	1:5000	secondary	Cell Signaling
α-rat	goat monoclonal	1:5000	secondary	Sigma-Aldrich

4.1.7 Media

Media composition for cultivation of bacteria and fungi are listed in Table 10. For preparation of solid media, 1.5 % (w/v) agar was added to all media.

Table 10: Media composition for microbe cultivation

Name	Application	Composition
LB media	*E. coli* cultivation	Tryptone: 10.0 g/l Yeast Extract: 5.0 g/l NaCl: 5.0 g/l pH 7.0
YEB media	*A. tumefaciens* cultivation	Beef Extract: 5.0 g/l Yeast Extract: 1.0 g/l Peptone: 5.0 g/l Sucrose: 5.0 g/l 1 M MgSO4: 2.0 ml/l pH 7.2
NYGA media	*P. syringae* pv. *tomato* cultivation	Peptone: 5.0 g/l

		Yeast Extract: 3.0 g/l Glycerol: 20.0 ml/l pH 7.0
PG media	*Botrytis cinerea* cultivation	Potato Extract: 4.0 g/l Glucose: 20.0 g/l pH 5.6

4.1.8 Public RNAseq datasets

Publicly available RNAseq datasets used for gene expression analysis in this study were downloaded from the Sequence Read Archive (SRA) of NCBI and are listed in Table 11.

Table 11: Publicly available RNAseq datasets used in this study

SRA accession	Description	Reference
SRP201971	flg22, nlp20 or chitin infiltrated *A. thaliana* seedlings sampled at 0, 1, 6 and 24 hpi	(W. L. Wan, Fröhlich, et al. 2019)
SRP082532	flg22 infiltrated *A. thaliana* plants sampled at 0, 1 and 2 hpi	(Birkenbihl et al. 2017)
SRP151348	*Pst* DC3000 AvrRps4 infected *A. thaliana* plants sampled at 0, 8 and 24 hpi	(Bhandari et al. 2019)

Single cell RNAseq dataset of *A. thaliana* Col-0 infected with *Colletotrichum higginsianum* was used for cell-type specific gene expression analysis in this study. Data was downloaded from the ENA website under the project ID PRJEB61052 (Tang et al. 2023).

4.2 Methods

4.2.1 Biochemical methods

4.2.1.1 Total leaf protein extraction

For protein expression analysis, four 1 cm leaf discs of transiently transformed *N. benthamiana* or 2 full leaves of *A. thaliana* were harvested in Eppendorf tubes containing metal beads and immediately frozen in liquid nitrogen. The Qiagen TissueLyser II was used at 30 Hz for 1 min for grinding of plant material. Samples were resuspended in 2x Laemmli buffer (60 mM TRIS pH 6.8, 4 % (w/v) SDS, 200 mM DTT, 20 % (w/v) glycerol, 0.2 % (w/v) bromophenol blue), boiled at 95 °C for 10 min and centrifuged at 13,300 rpm for 1 min. Supernatant was either used for measurement of protein concentration or directly used in SDS-PAGE.

4.2.1.2 Measurement of protein concentration using Pierce 660 nm

Protein concentrations were measured using the Pierce 660 nm Protein-Assay-Kit (ThermoFisher) and a photometer (BioPhotometer plus, Eppendorf). Both the pre-diluted protein standards and protein samples were mixed with the Pierce Reagent at a ratio of 0.1 ml of sample to 1.5 ml of reagent. The standard curve was measured and values were used for calculation of the slope equation. Using this equation, protein samples were adjusted to a

protein concentration of 30 µg (MAPK assay) or 60 µg (all other assays) and diluted either with protein extraction buffer or 2x Laemmli buffer. In case of total protein extracts which were initially dissolved in 2x Laemmli buffer, Ionic Detergent Compatibility Reagent (IDCR, ThermoFisher) was added to the Pierce Reagent prior to assay performance.

4.2.1.3 Protein enrichment via immunoprecipitation (IP)

To enrich concentration of proteins or for study of protein interactions, tagged proteins were pulled down using immunoprecipitation (IP) or Co-IP. For this, four 1 cm leaf discs were cut from transfected *N. benthamiana* leaves, placed in tubes containing metal beads and immediately frozen in liquid nitrogen. The Qiagen TissueLyser II was used at 30 Hz for 1 min for grinding of plant material and ground tissue was resuspended in 1.9 ml of extraction buffer (10 % (v/v) glycerol, 100 mM TRIS-HCl pH 7.5, 5 mM MgCl2, 300 mM NaCl, 10 mM DTT, 0.5 % IGEPAL® CA-630, 1 x plant protease inhibitor, 2 % (w/v) Polyvinylpolypyrroliodone (PVPP)). After 10 min incubation on the inverting wheel at 4 °C, samples were centrifuged at 4,500 g at 4 °C for 35 min. Extracts were filtered through two layers Miracloth (475855, MilliporeSigma) and 50 µl aliquots of this filtered extract were taken as input samples. Co-IPs were conducted for 2 h with 20 µl α-GFP trap agarose beads (gta-20, Chromotek) or 20 µl α-HA trap agarose beads (11815016001, Roche) under constant rotation. Beads were collected by centrifugation at 800 x g for 5 min and washed 3 times in extraction buffer (without DTT and PVPP). All co-IP steps were performed at 4 °C. Beads and input samples were boiled at 95 °C in 2x Laemmli buffer (100 µl were added to beads) for 10 min.

4.2.1.4 SDS-PAGE

Separation of protein samples was performed by SDS-PAGE using the BioRad Mini-PROTEAN system. Samples dissolved in 2x Laemmli buffer were loaded on 7.5%, 10%, 12% or Any kD precast gels (BioRad) and run in 1x TRIS-Glycine-SDS running buffer (250 mM TRIS, 1.92 M Glycine, 1 % (w/v) SDS) at 200 V for 30 min to 45 min, depending on the gel used. PageRuler Prestained Protein Ladder (ThermoFisher) was used as size standard.

4.2.1.5 Immunoblot analysis

Following SDS-PAGE, separated proteins were transferred onto a BioRad 0.2 µm nitrocellulose membrane using the BioRad Mini Trans-Blot Turbo system. Gels were stacked onto wetted membranes (1x Transfer Buffer, BioRad) and transfer was carried out at 25 V for 15 min. Following the transfer, membranes were blocked for 1 h with 5 % (w/v) milk powder or 5 % (w/v) BSA (Bovine Serum Albumin) dissolved in TBS-T buffer (10 mM TRIS, 150 mM NaCl, 0.05 % (v/v) Tween-20, pH 7.5) at RT and afterwards incubated in primary antibody solution (in 2 % (w/v) milk powder or 2% (w/v) BSA solution in TBS-T) at 4 °C overnight. All antibody concentrations are indicated in Table 9. Membranes were washed three times for 10 min in TBS-T buffer at RT and afterwards incubated for 1.5 h with the secondary antibody

solution (in 2 % (w/v) milk powder or 2% (w/v) BSA solution in TBS-T). This was followed by three washes with TBS-T of 10 min and one wash with TBS for 2 min. All antibody concentrations are indicated in Table 9. For detection of HRP-labeled antibodies, membranes were covered in ~200 µl Clarity™ Western ECL Substrate (BioRad). Chemiluminescence was detected using a BioRad ChemiDoc™ XRS+ detection system.

4.2.2 Molecular Biological Methods

4.2.2.1 Plant gDNA extractions

Genomic DNA was extracted from A. thaliana seedlings by harvesting few mg of fresh leaf tissue in a Qiagen Collection tube with one metal bead. 200 µl of sucrose solution (50 mM TRIS-HCl pH 7.5, 300 mM NaCl, 300mM Sucrose) were added and samples were ground using the Qiagen TissueLyser II at 30 Hz for 1 min. After centrifugation at 1,000 rpm for 1 min, the tubes were placed in at 97 °C water bath for 15 min. Extracted gDNA was placed on ice for at least 30 min before use or stored at 4 °C for medium term storage.

4.2.2.2 Polymerase chain reaction (PCR)

For plant genotyping, the non-proofreading Phire HS II DNA Polymerase (ThermoFisher) was used in PCR reactions. The reaction mixture and PCR program are indicated in Table 12 and Table 13. For cloning purposes, the proofreading polymerases Phusion HS (NEB), PrimeStar HS or PrimeStar GXL (Takara Bio) were used. The reaction mixture and PCR program for cloning are indicated in Table 14 and Table 15.

Table 12: Reaction mixture of PCR used for genotyping

Reaction mix	Volume
Phire Green buffer (5x)	4.0 µl
dNTPs (10 mM)	0.4 µl
Primer fwd (10 mM)	1.0 µl
Primer rev (10 mM)	1.0 µl
Phire HS II Polymerase	0.2 µl
gDNA	1.0 µl
ddH_2O	ad 20.0 µl

Table 13: PCR cyler program used for genotyping

Step	Temperature	Time	Cycles
Initiation	98 °C	00:30	1x
Denaturation	98 °C	00:10	35 x
Annealing	60 °C	00:15	
Elongation	72 °C	00:15/kb	
Final Elongation	72 °C	05:00	1x
Storage	4 °C	∞	

Table 14: Reaction mixture of PCR used for cloning

Reaction mix	Volume
Phusion, GXL or PS buffer (5x)	4.0 µl
dNTPs (10 mM)	1.6 µl
Primer fwd (10 mM)	1.0 µl
Primer rev (10 mM)	1.0 µl
Phusion, PrimeStar or PrimeStar GXL Polymerase	0.6 µl
template	1.0 µl
ddH_2O	ad 20.0 µl

Table 15: PCR cycler program used for cloning

Step	Temperature	Time	Cycles
Initiation	98 °C	01:00	1x
Denaturation	98 °C	00:10	35 x
Annealing	60 °C	00:15	
Elongation	72 °C	00:15/kb Phusion 01:00/kb PrimeStar	
Final Elongation	72 °C	05:00	1x
Storage	4 °C	∞	

4.2.2.3 Agarose gel electrophoresis

Agarose gel electrophoresis was used for visualization of PCR products or digested vectors. Here, DNA was mixed with 6x DNA loading dye (ThermoFisher), if no pre-stained buffer had been used in PCR reaction, and samples were loaded on 1% (w/v) agarose gels in TAE buffer (40 mM TRIS, 20 mM acetic acid, 1 mM EDTA, pH 8.5), containing 0.2 mg/l ethidium bromide.

DNA separation was performed at 120-150 V for 30-45 min and bands were visualized using an UV trans-illuminator (Intas).

4.2.2.4 DNA purification from agarose gels

Bands confirmed via agarose gel electrophoresis were cut from gels and DNA was purified using the NucleoSpin® Gel and PCR Clean-up kit (Macherey-Nagel), following the manual instructions. 20-40 µl of ddH_2O were used to elute DNA from columns and samples were stored at -20 °C for further use.

4.2.2.5 Generation of In-Fusion expression vectors

In-Fusion seamless cloning (Takara Bio) was used in this study for generation of plant expression vectors. RD19A coding sequence (CDS) or RD19A genomic sequence with upstream predicted promoter region were amplified from Col-0 cDNA and gDNA, respectively. Primers generating overhangs for the different inserts (RD19A sequence, protein tags) were designed using the Takara Bio online design tool (https://www.takarabio.com/learning-centers/cloning/primer-design-and-other-tools) for all different constructs. Primers used for generation of In-Fusion constructs are listed in Table 3, vectors used and generated are listed in Table 4. All inserts were amplified using a proofreading polymerase as described in Table 14. After amplification, PCR products were run on agarose gels and purified as described before (4.2.2.4). For generation of pRD19A::gRD19A constructs, the pXCSG_OLE-RFP_MCS vector was linearized prior to In-Fusion reaction for 1 h at 37 °C using the restriction enzyme XbaI. Reaction mixture for plasmid digestion is described in Table 17.

Table 16: Reaction mixture for vector linearization

Reagent	Volume
DNA (~0.5 µg)	5.0 µl
XbaI	1.0 µl
CutSmart buffer	3.5 µl
ddH_2O	ad 10.0 µl

After plasmid linearization, a ratio of 2:1 (insert:vector), or in case of multiple inserts 2:2:1 (insert:insert:vector), were mixed with 0.5 µl of ddH_2O and 1 µl of In-Fusion enzyme (Takara Bio) and incubated for 15 min at 37 °C, followed by 15 min at 50 °C. 5 µl of the reaction mix was used for heat-shock transformation of 50 µl competent *E. coli* (DH10b) cells (4.2.4.1). Cells were plated on LB plates supplied with corresponding antibiotics and correct clones were tested using colony PCR followed by plasmid digestion (Table 17) and Sanger sequencing (4.2.2.7).

Table 17: Plasmid digestion reaction mix

Reaction mix	Volume
Plasmid DNA	200 – 500 ng
Buffer (10x)	1.0 µl
Restriction enzyme	0.3 µl
ddH_2O	ad 10.0 µl

4.2.2.6 Plasmid isolation and restriction enzyme digests

Plasmids generated in this study were isolated from *E. coli* (DH10b) cells using the NucleoSpin Plasmid kit (Macherey-Nagel), following the manual instructions. 50 µl of ddH_2O were used to elute DNA from columns and DNA concentrations were measured using the NanoDrop 1000 photo spectrometer (ThermoFisher). Restriction enzymes (NEB) were used as described in Table… for digestion and subsequent agarose gel analysis of the obtained vectors.

4.2.2.7 Sanger sequencing

Vectors generated in this study were sequenced by Eurofins Genomics using the Mix2Seq Kit, following the kit instructions.

4.2.2.8 Site-directed mutagenesis (SDM)

Mutations within active sites of RD19A were generated using site-directed mutagenesis (SDM). Vectors generated in 4.2.2.5 were used as templates in a mutagenizing PCR reaction, utilizing altered oligonucleotides, containing the desired mutations (Table…). A proofreading polymerase was used for PCR reaction with 10 ng of plasmid in a 40 µl reaction (otherwise following the reaction mix described in Table 14) using the PCR program as described in Table 15. DNA was digested by adding 1 µl of DpnI restriction enzyme (NEB) to the PCR mixes and mixes were incubated at 37 °C for 3 h. 5 µl of digestion mix were used for transformation of *E. coli* (DH10b) cells (4.2.4.1) and correct mutations were checked using Sanger sequencing (4.2.2.7).

Table 18: PCR cycler program for SDM

Step	Temperature	Time	Cycles
Initiation	98 °C	01:00	1x
Denaturation	98 °C	00:10	20 x
Annealing	55 °C (1 °C/s ramp)	00:15	
Elongation	72 °C	01:00/kb	
Final Elongation	72 °C	15:00	1x
Storage	4 °C	∞	

4.2.2.9 In silico sequence generation

SeqBuilder Pro 15 (DNASTAR) was used for *in silico* design of vector maps and planning of restriction digests. SeqMan Pro 15 (DNASTAR) was used for analysis of Sanger sequencing results.

4.2.2.10 RNA extraction and cDNA synthesis

Plant RNA extraction was performed using the my-Budget Plant RNA Kit (Bio-Budget) according to the kit's manual. RNA was eluted in 30 µl ddH_2O and concentrations were measured using the NanoDrop 1000 photo spectrometer (ThermoFisher). In a next step, RNA was diluted to 1 µg in 5 µl and treated with DNase I (ThermoFisher) for 1 h at 37 °C (reaction mix listed in Table 19) and DNase was inactivated by adding 1 µl 50mM EDTA to each reaction for 10 min at 65 °C. Next, 1 µl of oligodT (ThermoFisher) was added and the mix was incubated for 5 min at 65°C. Reverse transcription was performed using the RevertAid Minus cDNA synthesis kit (ThermoFisher), with components listed in Table 20. The reaction mix was incubated for 10 min at 25 °C, 60 min at 42 °C and 10 min at 70 °C. The cDNA was placed at 4 °C for short-term storage or at -20 °C for long term storage.

Table 19: DNase treatment of extracted RNA

Reaction mix	Volume
1 µg RNA	5.0 µl
DNase	1.0 µl
10x DNase buffer	1.0 µl
Ribolock	0.25 µl
ddH_2O	ad 10.0 µl

Table 20: Reverse transcription reaction mix

Reaction mix	Volume
5x reaction buffer	4.0 µl
Random primer	1.0 µl
dNTPs	2.0 µl
Ribolock	0.5 µl
Revert Aid	1 µl

4.2.2.11 RT-qPCR

Real time quantitative PCR was performed on cDNA using the iQ SYBR Green Supermix (BioRad) in a reaction mix as described in Table 21. Primers used for analysis of gene expression are indicated in Table 3. RT-qPCRs were run in the CFX Connect Real-Time PCR

Detection System (BioRad) with the program as described in Table 22. Cq values of runs were extracted from the program and used for calculation of the RQ (relative quantification) of different mutant lines.

Table 21: RT-qPCR reaction mix

Reaction mix	Volume
SYBR Green Supermix	5.0 µl
Primer fwd (10 mM)	0.5 µl
Primer rev (10 mM)	0.5 µl
cDNA (in a 1:5 dilution)	2.0 µl
ddH_2O	2.0 µl

Table 22: RT-qPCR cycler program

Step	Temperature	Time	Cycles
Initiation	95 °C	03:00	1x
Denaturation	95 °C	00:15	35 x
Annealing	55 °C	00:15	
Elongation	72 °C	00:15	
	+ Plate Read		
Melt Curve	55 °C to 95 °C; increment 0.5	00:05	1x
	+ Plate Read		

4.2.2.12 Measurement of ROS production

ROS assays were performed as previously described (Pruitt et al. 2021). Leaf discs of 0.5 cm were cut of 4-5-week-old *A. thaliana* plants and washed three times for 30 min in ddH_2O. One leaf disc per well was transferred to a 96-well plate containing 100 µl of ddH_2O and plates were incubated overnight at 22 °C, covered in aluminum foil. The next day, ddH_2O was removed and 100 µl of a solution of 20 µM L-012 (Wako Pure Chemical Industries), 2 µg/ml HRP (peroxidase) and 1 µM of elicitor was added to each well. Mock controls did not contain the elicitor. Luminescence was measured over 1 h using the Centro XS^3 LB 960 (Berthold Technologies).

4.2.2.13 MAPK activity assay

4-5-week-old *A. thaliana* leaves were infiltrated with 1 µM of elicitor solution and 2 leaves per sample were frozen with liquid nitrogen in a tube 15 min after infiltration. Proteins were extracted in 100-150 µl of MAPK extraction buffer (50 mM Tris-HCl pH 7.5, 200 mM NaCl,

1 mM EDTA, 10 mM NaF, 2 mM sodium orthovanadate, 1 mM sodium molybdate, 10 % (v/v) glycerol, 0.1 % (v/v) Tween, 1 mM AEBSF, 1 mM DTT, 1 x plant protease inhibitor) and samples were kept on ice for 10 min before centrifugation at 4 °C and 13,000 x g for 30 min. Supernatant was collected and protein concentrations were determined by Pierce 660 nm assay (as described in 4.2.1.2). Each sample was diluted with 2x Laemmli buffer to a protein concentration of 30 µg and separated by SDS-PAGE, as described in 4.2.1.4. Immunoblot analysis was performed as described in 4.2.1.5, using BSA in blocking and antibody solutions. MAPK activity was visualized by using the α-p44/42 primary antibody (Cell Signaling).

4.2.2.14 Isolation of apoplastic fluids from *N. benthamiana* and *A. thaliana*

For analysis of RD19A protein expression and further substrate analysis, 35S::RD19A with a 3xHA-Strep or mYFP tag were transiently expressed in WT *N. benthamiana* plants at an OD_{600} = 1 mediated by *A. tumefaciens*. 48h after infiltration, fully infiltrated leaves (depending on the leaf size between one and two), were cut from plants and placed in a 600 ml beaker filled with ddH_2O. For isolation of apoplastic fluids from *A. thaliana*, up to 15 full leaves of stably expressing 35S::RD19A-3xFLAG plants were used. Fabric nets were used to keep leaves under water and vacuum infiltration was applied at 60 mbar for 5 min. Vacuum was slowly released, ensuring infiltration of plant leaves. Leaves were then carefully rolled up and placed in a 20 ml syringe (without applicator) in a 50 ml falcon tube and centrifuged at 800 x g for 15 min. Apoplastic fluids (AF) were collected at the bottom of the tube and aliquot in 200 µl per tube. AF were used for further analysis in immunoblotting or PICS (Proteomic identification of cleavage sites).

4.2.2.15 Isolation of nuclei from *A. thaliana*

For isolation of nuclei from *A. thaliana*, 2 g of fresh leaf material was ground in a mortar with pestle using liquid nitrogen. 4 ml of Honda buffer (2.5 % Ficoll 400, 5 % Dextran T40, 0.4 M sucrose, 25 mM Tris-HCl, pH 7.4, 10 mM $MgCl_2$, 5 mM DTT, 1 x plant protease inhibitor cocktail) were added (DTT and protease inhibitor were always added to the buffer right before use) and plant extract was applied to a 62 µm filter in a falcon tube and filtered by slowly centrifuging for 3 min at 800 x g. Triton X-100 was added to a final concentration of 0.5 % and mixed slowly with the filtrate. 100 µl aliquot for total fraction was taken at this point. The solution was incubated on ice for 15 min, followed by centrifugation for 5 min at 1500 x g. 500 µl of supernatant were taken as the nuclei depleted sample, the rest of the supernatant was removed. The pellet was gently resuspended in 3 ml of Honda buffer with 0.1 % Triton X-100 by gently adding the buffer to the side of the falcon and swirling of the mixture. After centrifugation for 5 min at 1500 x g and discarding the supernatant, the pellet was resuspended in 3 ml of Honda buffer and transferred to Eppendorf tubes in 1 ml aliquots. Centrifugation at 100 x g for 5 min allowed for pelleting of starch and cell debris and the supernatant was

transferred to a fresh tube, centrifuged at 2000 x g for 5 min to pellet the nuclei. Nuclear pellets were resuspended in 100 µl of 2 x Laemmli buffer and proteins were denatured by boiling at 95 °C for 10 min. Nuclei extracts were used for further immunoblot analysis.

4.2.2.16 Guard cell aperature assay

Guard cell aperature assays were performed as previously described (Eisele et al. 2016). In brief, epidermal peels were obtained from 4-5-week-old *A. thaliana* plants by peeling off the abaxial side of rosette leaves using laboratory tape. Epidermal peels were placed in MES/KOH buffer (5 mM KCl, 50 µM $CaCl_2$, 10 mM MES pH 6.15) for two hours and then transferred for another two hours to fresh MES/KOH solutions containing 1 µM of the elicitors flg22 or nlp20, or ddH_2O for mock treatments. Peels were then stained and fixed in 4 % PFA solutions with 1 µM rhodamine 6G. Epidermal peels were imaged using the Zeiss LSM780 confocal microscope. Rhodamine 6G was imaged with λ_{Ex} = 514 nm, λ_{Em} = 535-580 nm. Fiji (Schindelin et al. 2012) was used for measurement of length and width of guard cells and the stomatal aperature index (SAI, width/length) was calculated.

4.2.3 Plant protease assays

4.2.3.1 Activity-based protein profiling

Activity-based protein profiling (ABPP) described in this study was performed in collaboration with PD Dr. Johana Misas-Villamil at the University of Cologne. ABPP was performed using plant total extracts, extracted at pH 7.4 using a Tris-HCl buffer. To the plant extracts, 50 mM Tris-HCl pH 7.4 buffer, 10 mM DTT and 1 µM activity-based probe DCG-04 (Greenbaum et al. 2000) were added. Samples with inhibitor control were additionally supplied with 20 µM E64, while the same amount of DMSO was added to other samples. DCG-04 contains the E64 warhead which covalently binds to active sites of PLCPs, and a biotin affinity tag for subsequent purification or detection. Labeling was performed for 4 h at room temperature and reaction was stopped by addition of 20 µM E64. Samples were either mixed with 2x Laemmli buffer for subsequent immunoblotting analysis or used for further purification analysis.

4.2.3.1.1 Protein purification and pulldown using biotin labeling

Protein purification using methanol-chloroform precipitation followed by streptavidin-agarose pulldown was performed as previously described (Melkonian et al. 2022). In short, protein precipitation was achieved by addition of methanol and then chloroform to ABPP extracts and protein were re-extracted in SDS-DTT-Tris buffer at pH 7.5 by ultrasonication. Active labeled proteases were pulled down by α-Streptavidin agarose beads (High Capacity Streptavidin Agarose beads, Thermo Fisher) overnight and beads were subsequently washed one time with wash buffer 1 (0.1 M phosphate, 0.15 M NaCl, 2% SDS, pH 7.2) and three times with wash buffer 2 (0.1 M phosphate, 0.15 M NaCl, pH 7.2) before further processing.

4.2.3.1.2 Tandem mass spectrometry for ABPP

Tandem mass spectrometry (MS/MS) analysis was performed in collaboration with Dr. Hirofumi Nakagami, Anne Harzen and Dr. Sara Christina Stolze at Max-Planck-Institute for Plant Breeding Research.

4.2.3.1.3 Sample preparation and LC-MS/MS data acquisition for ABPP

Enriched proteins of α-Streptavidin pulldown were submitted to on-bead digestion using trypsin. In brief, dry beads were re-dissolved in 25 µL digestion buffer 1 (50 mM Tris, pH 7.5, 2M urea, 1mM DTT, 5 ng/µL trypsin) and incubated for 30 min at 32 °C in a Thermomixer with 400 rpm. Next, beads were separated magnetically, and the supernatant was transferred to a fresh tube. 50 µL digestion buffer 2 (50 mM Tris, pH 7.5, 2M urea, 5 mM CAA) was added to the beads and mixed, beads were magnetically separated and the supernatant was collected and combined with the supernatant of the previous step. The combined supernatants were incubated overnight at 32 °C in a Thermomixer with 400 rpm. The digestion was stopped by adding 5 µL TFA (20%) and desalted with C18 Empore disk membranes according to the StageTip protocol (Rappsilber, Ishihama, and Mann 2003). Dried peptides were re-dissolved in 2% ACN, 0.1% TFA (10 µL) and samples were analyzed using an EASY-nLC 1200 (Thermo Fisher) coupled to a Q Exactive Plus mass spectrometer (Thermo Fisher). Peptides were separated on 16 cm frit-less silica emitters (New Objective, 75 µm inner diameter), packed in-house with reversed-phase ReproSil-Pur C18 AQ 1.9 µm resin (Dr. Maisch). Peptides were loaded on the column and eluted for 115 min using a segmented linear gradient of 5% to 95% solvent B (0 min : 5%B; 0-5 min -> 5%B; 5-65 min -> 20%B; 65-90 min ->35%B; 90-100 min -> 55%; 100-105 min ->95%, 105-115 min ->95%) (solvent A 0% ACN, 0.1% FA; solvent B 80% ACN, 0.1%FA) at a flow rate of 300 nL/min. Mass spectra were acquired in data-dependent acquisition mode with a TOP15 method. MS spectra were acquired in the Orbitrap analyzer with a mass range of 300–1750 m/z at a resolution of 70,000 FWHM and a target value of 3×10^6 ions. Precursors were selected with an isolation window of 1.3 m/z. HCD fragmentation was performed at a normalized collision energy of 25. MS/MS spectra were acquired with a target value of 10^5 ions at a resolution of 17,500 FWHM, a maximum injection time (max.) of 55 ms and a fixed first mass of m/z 100. Peptides with a charge of +1, greater than 6, or with unassigned charge state were excluded from fragmentation for MS^2, dynamic exclusion for 30s prevented repeated selection of precursors.

4.2.3.1.4 LC-MS/MS data analysis for ABPP

Raw data were processed using MaxQuant software (version 1.6.3.4, http://www.maxquant.org/) (Cox and Mann 2008) with label-free quantification (LFQ) and iBAQ enabled (Tyanova, Temu, and Cox 2016). MS/MS spectra were searched by the Andromeda search engine against the sequence of RD19. Trypsin specificity was required and a maximum

of two missed cleavages allowed. Minimal peptide length was set to seven amino acids. Carbamidomethylation of cysteine residues was set as fixed, oxidation of methionine and protein N-terminal acetylation as variable modifications. Peptide-spectrum-matches and proteins were retained if they were below a false discovery rate of 1%. The match-between runs option was disabled. Results were analyzed for the identification of RD19 in the individual conditions using the proteinGroups output, the peptides identified for RD19 were extracted from the modificationSpecificPeptides output of MaxQuant.

4.2.3.2 PICS assay

4.2.3.2.1 Sample preparation

Identification of RD19A specific cleavage pattern was performed by Proteomic Identification of Cleavage Sites (PICS) assay, in collaboration with Melissa Mantz and Pitter Huesgen, University of Freiburg. Active and inactive forms of RD19A were expressed in *N. benthamiana* plants as described in 4.2.5.3 and apoplastic fluids (AF) were isolated as described in 4.2.2.14. AF of active and inactive protease were incubated with GluC, legumain and trypsin peptide libraries (Demir, Kuppusamy, et al. 2022; Schilling et al. 2011). 2 µL of AF and 50 µL of peptide library were mixed with 10 mM $NaPO_4$, 150 mM NaCl, 1 mM EDTA, 0.5 mM DTT, 50 µM PepstatinA (Roth) and 50 µM 3,4-Dichlor-isocumarin (Sigma) and ddH_2O was added to a volume of 100 µl. As additional control, 100 µM E64 were added to part of the samples as negative control, while the same amount of DMSO was added to the remaining samples. After 1 h or 16 h incubation, 1 µl 10 mM E64 was added to all samples and the reaction was additionally stopped by freezing in liquid nitrogen. Samples were stored at -80 °C until further processing. N-termini were dimethyl labeled with different combinations of formaldehyde and cyanoborohydride (CH_2O + $NaBH_3CN$, CD_2O + $NaBH_3CN$, and $13CD_2O$ + $NaBD_3CN$) resulting in monoisotopic mass shifts.

4.2.3.2.2 MS measurement

PICS samples were measured with an Orbitrap Elite mass spectrometer instrument coupled to an UltiMate 3000 RSLCnano HPLC system (both Thermo Fisher Scientific). Peptides were separated on a two-column setup with a nanoEase™ M/Z Symmetry C18 precolumns (20 mm x 180 µm inner diameter; Waters) and a nanoEase™ M/Z HSS C18 T3 analytical column (250mm x 75 µm inner diameter; Waters) at a flow rate of 0.3 µl/min and column oven temperature of 40°C. Peptide elution was controlled by applying a binary solvent gradient. Solvent A consisted of 0.1% (v/v) formic acid (FA), while solvent B consisted of 0.1% (v/v) FA, 50% (v/v) methanol (MeOH), and 30% (v/v) acetonitrile (ACN). The elution gradient went from 7% to 65% solvent B over 30 minutes, followed by a 65% to 80% increase in 5 minutes, and finally held at 80% for 3 minutes. This system was interfaced online with the Nanospray Flex ion source featuring the PST-HV-NFU liquid junction (MS Wil) and fused silica emitters (EM-20-360; MicrOmics Technologies LLC). The following parameters were applied for MS1 scans:

mass range of m/z 370 - 1,700, a resolution of 120,000 (at m/z 400), a target value (AGC) of 1 x 10^6 ions, and a maximum injection time (IT) of 200 ms. For MS2 scans, up to 15 most intense precursor peptides with a charge ≥ 2 were selected for collision induced dissociation (CID) in the linear trap with a normalized collision energy of 35%, activation time 10 sec q-value = 0.25, an AGC of 5000 ions, a max. IT of 150 ms, and dynamic exclusion for 45 s.

4.2.3.2.3 Data analysis

Database searches for the PICS were performed using the software MaxQuant (version 2.4.2.0), with settings as described in Demir et al. 2022. Downstream analysis for creating iceLogos (Colaert et al. 2009) was also done as in Demir et al. by using the perl script PINCIS (version 12, downloaded from https://pincis.sourceforge.io).

4.2.3.3 N-terminomic profiling using High-efficiency Undecanal-based N-Termini EnRichment

4.2.3.3.1 Sample preparation

Ground frozen leaf material was suspended in guanidine protein extraction buffer containing Halt™ Protease-Inhibitor-Cocktail (Thermo Fisher Scientific) and processed according to the protocol of Demir, Perrar, et al. 2022: Protein concentration was determined using the Pierce™ Bicinchoninic Acid (BCA) Protein Assay (Thermo Fisher Scientific), after which cysteine residues in 200 µg of protein were reduced and alkylated. Proteins were labelled at the free primary amines including those of the n-termini with heavy formaldehyde (13CD2O) and cyanoborohydride as described in the protocol ('single-heavy label'). An aliquot of 50 µg of protein was separated beforehand for whole proteome analysis and therefore not labelled. The reaction was quenched by adding 100mM ammonium bicarbonate and incubating at 37°C for 30 minutes. Proteins were digested with Trypsin in a 1:100 protease:protein ratio over night at 37 °C. The enrichment for n-termini was performed as outlined in the protocol. In preparation for measurement, all samples were acidified and desalted by using self-packed SDB-RPS Stagetips.

4.2.3.3.2 MS measurement

HUNTER samples were measured with an Exploris 480 mass spectrometer coupled to an UltiMate 3000 RSLCnano HPLC system (both Thermo Fisher Scientific). Peptides were separated on a two-column setup with a µPAC™ C18 trapping column and a µPAC™ pillar array analytical column of 50cm length (both Thermo Fisher Scientific) at a flow rate of 0.5 µl/min and column oven temperature of 40°C. Peptide elution was controlled using a binary buffer system consisting of A (0.1% formic acid) and B (86% acetonitrile, 0.1% formic acid). The elution gradient went from 1% to 4% solvent B over 2 min, 4% to 25% solvent B over 24 min, followed by a 25% to 44% increase in 12 minutes, and a final flush held at 90% for 4 minutes. This system was interfaced online with the Nanospray Flex ion source (Thermo Fisher

Scientific) featuring the PST-HV-NFU liquid junction (MS Wil) and fused silica emitters (EM-20-360; MicrOmics Technologies LLC). MS measurements of the HUNTER samples were done in data independent acquisition (DIA) mode with one overview spectrum (RF lens of 40%, normalized AGC target of 300%, maximum injection time of 45 ms, m/z range of 350 to 1.400, resolution of 120.000, profile mode) and MS2 fragment spectra with 14 Da isolation windows at a precursor mass range of 361-450 m/z, 7 Da windows in a mass range of 450-800 m/z and 14 Da windows in a mass range of 800-1100 m/z each with a window overlap of 1 m/z and a resolution of 30000 and a maximum injection time (IT) of 54 ms.

4.2.3.3.3 Data Analysis

Searches of HUNTER samples were done with FragPipe (v. 22) as described in Stockert, Baeta, and Huesgen 2024, with enzyme specificity set to “semi-specific” ArgC and N-terminal demethylation as variable modification. LFQ and “Match between runs” was enabled. Spectra were matched against an UniProt reference proteome for *Arabidopsis thaliana* (accessed October 10, 2023).

Downstream analysis of proteome and HUNTER samples was performed using in-house R-Scripts. For comparative statistics the R-Package limma (Linear Models for Microarray Data) (Ritchie et al. 2015) was used. Limma is part of the Bioconductor package (Robinson, McCarthy, and Smyth 2010). R-Scripts were written and executed with RStudio (Racine 2012).

4.2.3.4 Shotgun proteomics

4.2.3.4.1 Sample preparation

Shotgun sample preparation was performed as described before for HUNTER sample preparation (4.2.3.3.1)

4.2.3.4.2 MS measurement

Proteome samples were measured on an UltiMateTM 3000 RSLCnano system was online coupled to a QExactive mass spectrometer (both Thermo Fisher Scientific). Peptides were separated on a PepMap C18 trapping column and an µPAC™ C18 pillar array column with 200 cm bed length (both Thermo Fisher Scientific) using a binary buffer system consisting of A (0.1% formic acid) and B (86% acetonitrile, 0.1% formic acid). For electrospray ionization of peptides, a Nanospray Flex ion source (Thermo Fisher Scientific) with a liquid Junction™ PST-HV-NFU (MS Wil) and a fused silica emitter (20 µm inner diameter, 360µm outer diameter, MicroOmics Technologies LLC) applying a source voltage of +1.800 V and an ion transfer tube temperature of 250 °C was used. Samples were measured in DIA mode with one overview spectrum (RF lens of 50%, normalized AGC target of 3e6, maximum injection time of 60 ms, m/z range of 385 to 1.050, resolution of 70.000 at 200m/z, profile mode) followed by MS2 fragment spectra generated by higher-energy collision-induced dissociation (HCD) at a normalized energy of 26% in a precursor *m/z* range from 400 to 1.000 in 50 windows of 12.5

m/z isolation width overlapping by 0.25 *m/z* and recorded at a resolution of 35.000 in profile mode.

4.2.3.4.3 Data analysis

Analysis of proteome samples was performed using FragPipe (v. 22) an open-source platform that combines several algorithms for peptide and protein identification and quantification. The spectral data was analyzed against an UniProt reference proteome for *Arabidopsis thaliana* (accessed October 10, 2023), using MSFragger. Standard search parameters were used, with trypsin as digestion enzyme with a maximum of two missed cleavages allowed. Carbamidomethylation of cysteines was set as fixed modification, while oxidation of methionine was set as variable modification. Identifications were filtered at a 1% False Discovery Rate (FDR) threshold using the Philosopher tool. Label-free Quantification (LFQ) was done with the integrated DIA-NN tool determining the peptide and protein abundance.

Downstream analysis of proteome was performed as described in 4.2.3.3.3.

4.2.4 Bacterial Methods

4.2.4.1 *E. coli* cultivation and transformation

Escherichia coli strain DH10b were grown in LB liquid medium or LB agar plates supplied with corresponding antibiotics (Table 8) at 37 °C. For transformation, 50 µl of chemically competent bacteria were thawed on ice and 5 µl plasmid or reaction mix were added. Bacteria and DNA were incubated on ice for 30 min and heat-shock transformation was performed in a water bath for 30 s at 42 °C. Bacteria were placed back on ice immediately and regenerated by adding 800 µl of pre-warmed LB media and shaken at 450 rpm for 1 h at 37 °C. Bacteria were pelleted at 11,000 rpm for 1 min, resuspended in 100 µl of LB and plated on LB plates containing corresponding antibiotics for selection of correctly transformed bacteria. Plates were incubated 1 day at 37 °C until colonies appeared and could be tested for correct transformation.

4.2.4.2 *A. tumefaciens* cultivation and transformation

Agrobacterium tumefaciens strain GV3101 pMP90RK was grown in in liquid YEB medium or on YEB agar plates supplied with Rifampicin, Gentamycin, Kanamycin and the antibiotics required for maintaining the plasmid (Table 8). For transformation, 50 µl of electrically competent *A. tumefaciens* cells were thawed on ice, 0.5 µl of plasmid were added, and the reaction mixture was incubated on ice for 10 min. Transformation was performed by adding the reaction to an electroporation cuvette (2 mm gap, Cell Projects) and electroporating with the BioRad Gene Pulser Xcell in the *Agrobacterium* pre-setting. For recovery, 800 µl of YEB medium were added to the cuvette, the mix was gently pipetted up and down and then transferred to a fresh tube. Bacteria were shaken for 2 h at 28 °C and 600 rpm. 50 µl of

transformed *A. tumefaciens* were plated onto YEB plates with corresponding antibiotics and incubated at 28 °C for 2 days until colonies appeared.

4.2.4.3 *P. syringae* cultivation

Pseudomonas syringae pv. *tomato* (*Pst*) DC3000 and *Pst AvrRps4* were grown in liquid NYGA medium or on NYGA agar plates supplied with Rifampicin and Kanamycin. *Pst* ΔCor was frown on NYGA plates supplied with Rifampicin, Kanamycin and Spectinomycin. Plates were grown at 28 °C for 2 days or until dense growth appeared on plates. Small amount of *Pst* from plates was used for inoculation of liquid cultures, incubating at 28 °C and 200 rpm overnight.

4.2.4.4 *B. cinerea* cultivation

Botrytis cinerea strain B05.10 was cultivated on PG plates for 20 days under light at room temperature until spores were harvested. Viability of spores was checked with a light microscope and spores were counted and spore concentration noted. Spores were stored for several weeks at 4 °C for continuous use in multiple experiments.

4.2.4.5 *H. arabidopsidis* (*Hpa*) cultivation

Hyaloperonospora arabidopsidis isolates Emwa1 and Noco2 were cultivated by spray inoculation on *A. thaliana* plants. Emwa1 is growing on Ws-2 plants, while Noco2 is especially growing on Col-0 plants. Spore solutions were generated from previously infected plants by cutting susceptible plants and placing them in a 50 ml falcon tube with 15 ml of ddH_2O, avoiding any contaminations with soil. Falcons were vortexed thoroughly and solutions were filtered through a miracloth into a new falcon tube. Spores were counted using a Neubauer chamber (Carl Roth) and spores were diluted with ddH_2O to a final concentration of 4×10^4 spores/ml. Spores were sprayed onto Col-0 and Ws-2 plants using an air brush. To ensure humidity on trays, a wet paper towel was placed at the bottom of the tray, they were covered with a plastic lid, closed with tape and placed into a plant growth chamber (22 °C, short day conditions). After 5 to 6 days, *Hpa* growth was strong enough to use plants for infection assays of mutant lines.

4.2.5 Plant Methods

4.2.5.1 Plant cultivation

A. thaliana seeds were sown on moist moist soil fertilized with 10 mg/l Confidor WG70 (Bayer) and treated with a nematode solution to prevent infestation. Trays were covered with lids, which were removed after small seedlings were grown. All assays were performed with *A. thaliana* grown in short day conditions (10 h light, 14 h dark) at ~150 µmol/m/s, 22 °C and 65 % humidity and at an age between three to 6 weeks, depending on the experiment. Propagation of plants was achieved by growth in “fast-breeding” chambers of 22 h light and 2 h dark (~150 µmol/m/s, 22 °C and 65 % humidity). For seed propagation, plants were bagged

when siliques appeared, and irrigation was stopped for siliques to dry completely. When plants were fully dry, seeds were harvested.

N. benthamiana was grown in the greenhouse with cycles of 16 h light and 8 h dark and used at the age of 4 to 5 weeks for transient expression experiments.

4.2.5.2 Stable transformation of *A. thaliana* (floral dip)

For the generation of stable transformants of *A. thaliana*, floral dip was performed as previously described (Logemann et al. 2006). Plants grown in fast-breeding conditions were fully cut once to increase the number of flowers in the re-growth and approximately 5-6-week-old plants were used for floral dip. Here, a solution of *A. tumefaciens* carrying the plasmid of choice at OD_{600} of 1.5 was mixed with 5 % sucrose and 0.01 % Silwet L-77 and poured into a small autoclave bag. Inflorescences were placed in the solution for 45 s to 1 min and dried off gently with a paper towel, to remove any excess bacteria. The plants were covered with plastic bags and placed in the dark for one day, followed by one day with the corners of the bags cut off. Finally, plants were placed back into the “fast breeding” chamber or the designated area in the greenhouse, until seeds were produced. Since a plant selection marker for red seed coat fluorescence was included in the vectors, successful transformants were identified by red fluorescence.

4.2.5.3 Transient protein expression in *N. benthamiana*

Proteins were transiently expressed in *N. benthamiana* by growing *A. tumefaciens* strains carrying the desired plasmids on YEB plates with respective antibiotics (Table 8) overnight at 28 °C and by resuspending bacteria in 3 ml of infiltration solution (10 mM MgCl2, 10 mM MES/KOH pH 5.6, 150 nM Acetosyringone) the next day. OD_{600} was measured using a photo spectrometer (BioPhotometer, Eppendorf) and adjusting the concentration to OD_{600} of 0.2, 0.5 or 1, depending on the experiment. Together with the strain of interest, in every experiment the *A. tumefaciens* strain carrying the helper plasmid p19, was expressed at OD_{600} of 0.1, as a suppressor of the plant gene silencing response (Voinnet, Pinto, and Baulcombe 1999). Leaves were infiltrated with needleless syringes and the infiltrated area was indicated, using a permanent marker. Plants were placed in a shadowy area of the laboratory.

4.2.5.4 *B. cinerea* growth assay in *A. thaliana*

B. cinerea growth assay was performed on 4-5-week-old *A. thaliana* plants. From stock solutions described in 4.2.4.4, a spore solution of $5x10^5$ was prepared for infection. A minimum of 10 leaves per sample (of 4 plants in one pot) were drop-inoculated on both sides of the middle veins with 10 µl of spore solution. Pots were placed on trays and irrigated with 1.5 l of lukewarm water and trays were closed with a lid and laboratory tape, to ensure high humidity. Trays were placed in a dark area at room temperature for 48 h, before the BioRad ChemiDoc™ XRS+ detection system was used for imaging. Lesion areas were measured on photos using

Fiji (Schindelin et al. 2012). In case of priming experiments, all leaves were sprayed with elicitor solutions (0.5 µM elicitor in ddH_2O) 24h before infection with *B. cinerea*. Plants were placed back into growth chambers until performing the infections the next day.

4.2.5.5 *Pst* growth assay in *A. thaliana*

Pst DC3000, *Pst* DC3000 *AvrRps4* and *Pst* ∆Cor were grown from DMSO stocks 48 h on NYGA plates with respective antibiotics (Table 8). 24 h before infection assays, strains were re-streaked on fresh NYGA plates with antibiotics, to ensure active growth of strains in the assays. For infections, strains were diluted with 10 mM $MgCl_2$ to a OD_{600} concentration of 0.0002 and infiltrated in full leaves of 4-5-week-old *A. thaliana* plants, using a needleless syringe. In case of spray inoculations, bacteria were diluted to a concentration of a OD_{600}=0.2, adding 0.04% of Silwet to the solution. Infiltrated leaves were marked with a permanent marker and leaves were dried for 4 h at room temperature. Three technical replicated with two leaf discs of 0.6 diameter were taken and placed in a tube with 1.5 ml of 10 mM $MgCl_2$ with 0.01% (v/v) Silwet. Tubes were shaken at 28 °C and 650 rpm for 1 h before plating bacterial solutions on NYGA plates with respective antibiotics and incubation for 2 days at 28 °C. Colonies were counted and colony forming units (CFUs) were calculated. Three days after infection, the same was repeated but taking 6 technical replicates and plating in dilution series up until dilution of 10^{-5}. In case of priming experiments, all leaves were infiltrated with elicitor solutions (0.5 µM elicitor in ddH_2O) using a needleless syringe, 24h before infection with *Pst*. Plants were placed back into growth chambers until performing the infections the next day.

4.2.5.6 *Hpa* Emwa1 and Noco2 growth assays in *A. thaliana*

Infection with *Hpa* Emwa1 and Noco2 was performed as described for maintenance of the strains in 4.2.4.5. 4 days after infection of lines of interest, plants treated with Emwa1 were stained using trypan blue for visualization of cell death and 5 days after infection, plants treated with Noco2 were used for spore counts to judge growth of the oomycete. Trypan blue assay was performed 4 days after spray inoculation and all experiments were performed under the hood. Trypan blue solution was mixed 1:1 with 100 % ethanol absolute and 2 ml were placed in plastic reagent tubes. One of the first two true leaves of ~12 independent plants was placed into the solution and boiled in a water bath until boiling and leaves were well stained. Tubes were removed from the water bath, and trypan blue solution was exchanged for 2 ml of Chloralhydrate, for de-staining of the leaves. Solution was refreshed once at the end of the day and de-stained overnight, turning on a rotor. The next day, Chloralhydrate solution was removed, and samples were stored until further use in 75% glycerol solutions. Before microscopy, leaves were placed on microscopy slides, using paint brushes. For spore counts after 5 to 6 days, three falcon tubes per sample (three technical replicates) were weighed before placing cut plant material inside. Full falcons were weighed, and fresh weight material

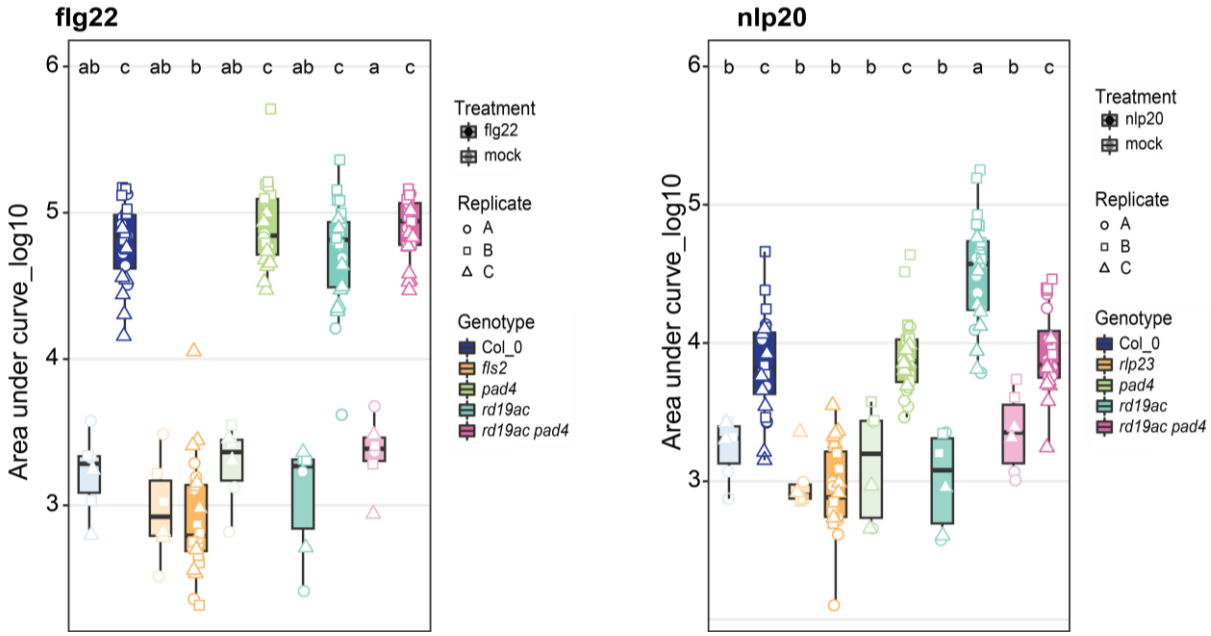
was calculated. 5 ml of ddH_2O were added to falcons and they were vortexed for 10 s each. 12 µl of spore solution was used for counting of spores in a Neubauer chamber (Carl Roth) and spores/g were calculated.

4.2.6 Microscopy

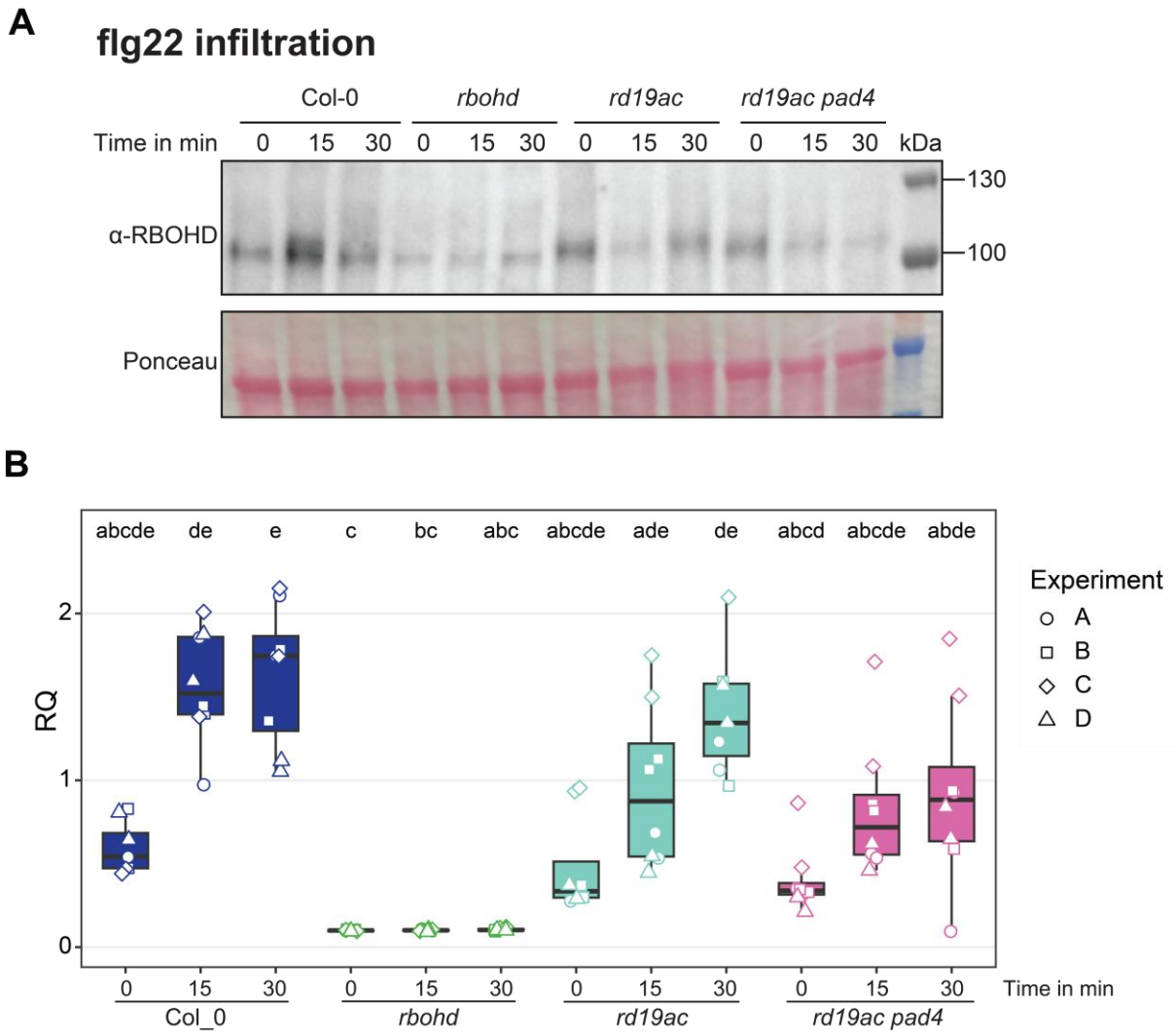
The light microscope Zeiss Axio Imager D2 together with the AxioCam camera was used for visualization of cell death and oomycete growth in *Hpa* Emwa1 infection assays (4.2.5.6). Protein localizations and stomata visualization was performed using the Zeiss LSM 780 confocal microscope.

5 Supplementary data

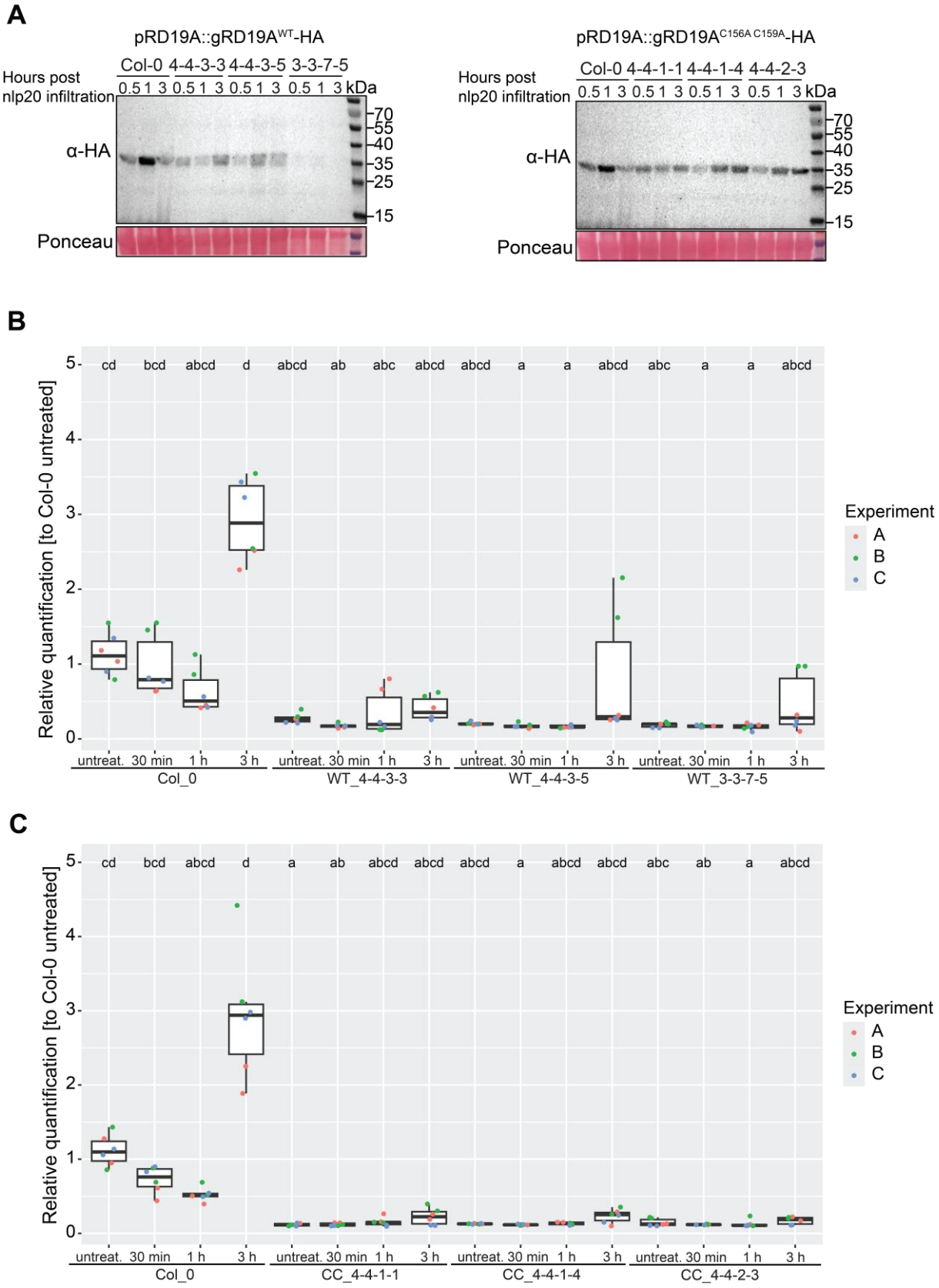
5.1 Supplementary figures



Supplementary Figure S 1: Area under curve of ROS bursts following elicitor treatment. Boxplots show log10 transformed values of area under curve (AUC) over 60 min ROS measurement with dots of the same shape representing one biological replicate. Genotypes sharing letters above boxplots do not show statistically significant differences (ANOVA and Tukey HSD test, $p < 0.05$, n=24 (flg22 and nlp20) and n=6 (mock) leaf discs from three independent biological replicates).

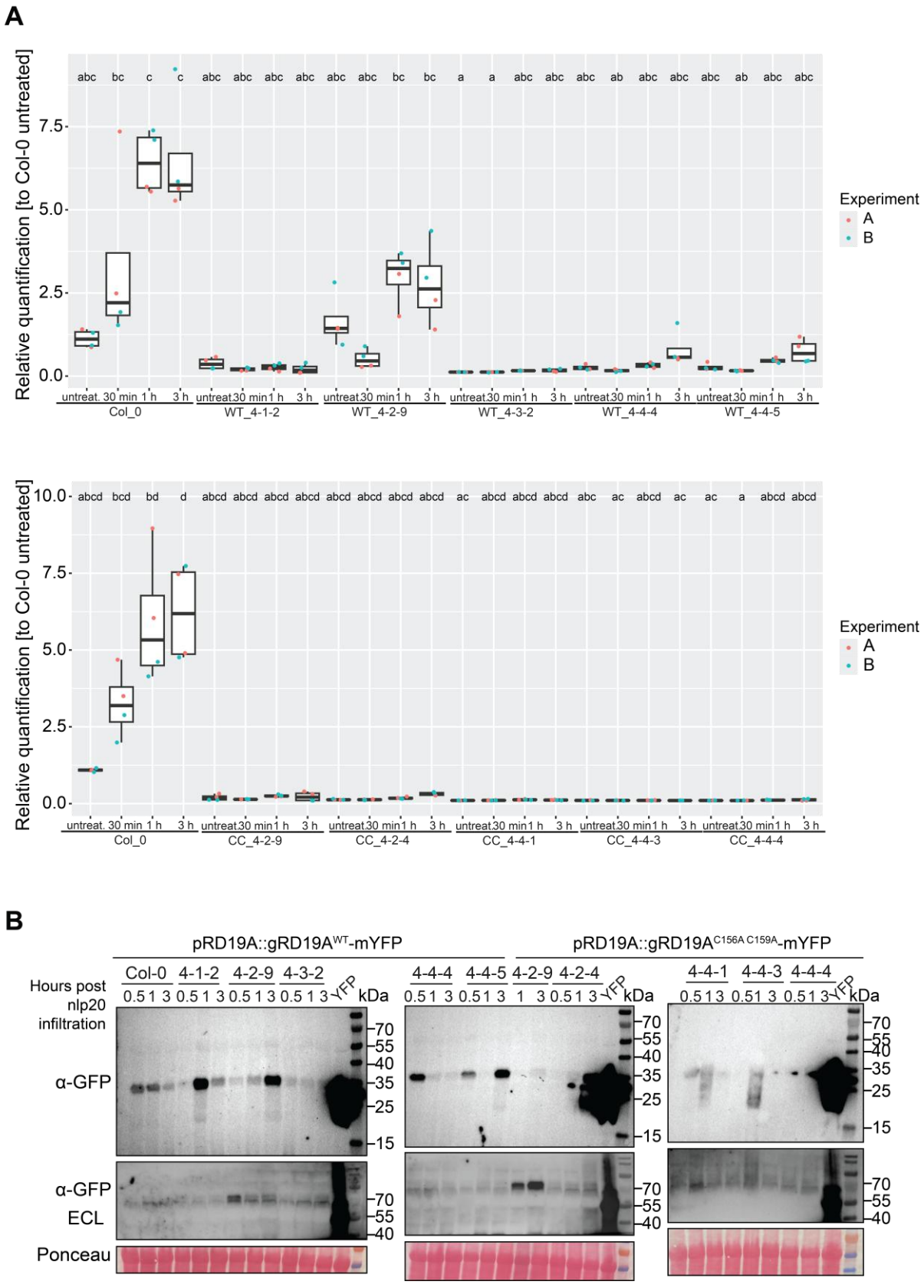


Supplementary Figure S 2: RBOHD protein levels following flg22 treatment and gene expression level following nlp20 treatment. (**A**) Protein levels of RBOHD after flg22 treatment and (**B**) *RBOHD* gene expression after nlp20 treatment were analyzed in Col-0, *rbohd*, *rd19ac* and *rd19ac pad4*. (**A**) Protein levels were identified by immunoblotting with RBOHD antibody 0 min, 15 min and 30 min after flg22 infiltration. Pierce assay was performed to load equal amounts of protein and Ponceau-stained Rubisco served as a loading control. Similar RBOHD protein levels were observed in two independent biological replicates. (**B**) *RBOHD* gene expression was detected 0 min, 15 min and 30 min after nlp20 infiltration. Relative quantification is represented in boxplots with dots of the same shape corresponding to technical replicates from one independent experiment. Data was normalized to Col-0 mock conditions in each biological replicate. Genotypes sharing letters above boxplots do not show statistically significant differences (Kruskal-Wallis and Nemenyi-Test, $p < 0.05$, n=8).



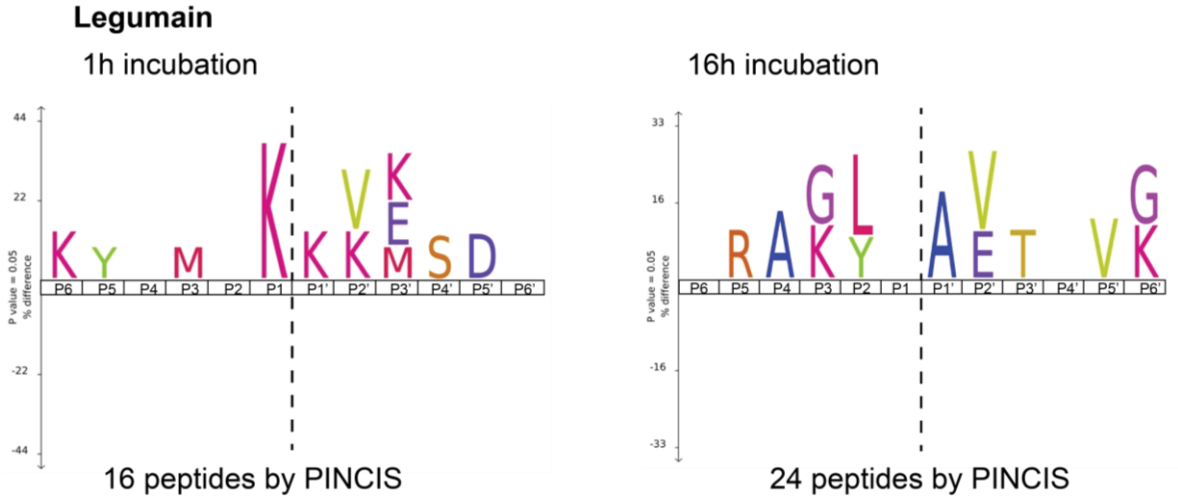
Supplementary Figure S 3: Expression levels of HA-tagged transgenic lines. (**A**) protein and (**B**) gene expression of pRD19A::gRD19A^{WT}-HA and pRD19A::gRD19A^{C156A_C159A}-HA transgenic lines 30 min, 1 h and 3 h after nlp20 infiltration, and in case of (**B**) in untreated conditions. (**A**) RD19A protein levels were identified by immunoblotting with HA antibodies. Ponceau-stained Rubisco served as a loading control. (**B**) *RD19A* gene expression analysis

shown as relative quantification to Col-0 untreated (Kruskal-Wallis and Nemenyi-Test, $p < 0.05$, n=6).

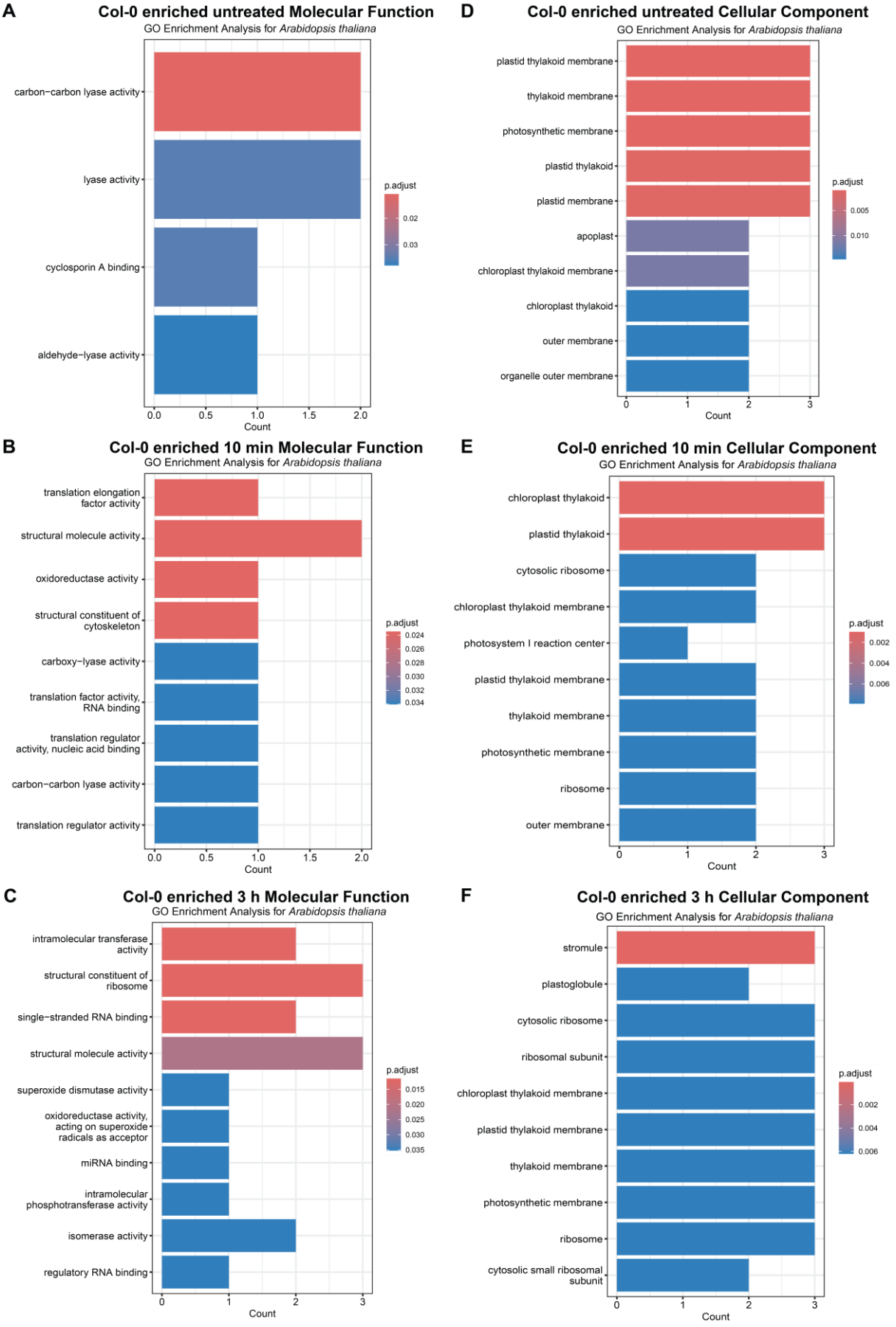


Supplementary Figure S 4:Expression levels of mYFP-tagged transgenic lines. (**A**) gene and (**B**) protein expression of pRD19A::gRD19A^{WT}-mYFP and pRD19A::gRD19A^{C156A_C159A}-mYFP transgenic lines 30 min, 1 h and 3 h after nlp20 infiltration, and in case of (**A**) in untreated

conditions. (A) *RD19A* gene expression analysis shown as relative quantification to Col-0 untreated (Kruskal-Wallis and Nemenyi-Test, $p < 0.05$, n=4). (**B**) RD19A protein levels were identified by immunoblotting with HA antibodies. Ponceau-stained Rubisco served as a loading control. ECL = enhanced chemiluminescence. Proteins extracted from 35S::YFP transiently transformed in *N. benthamiana* were used as YFP control.

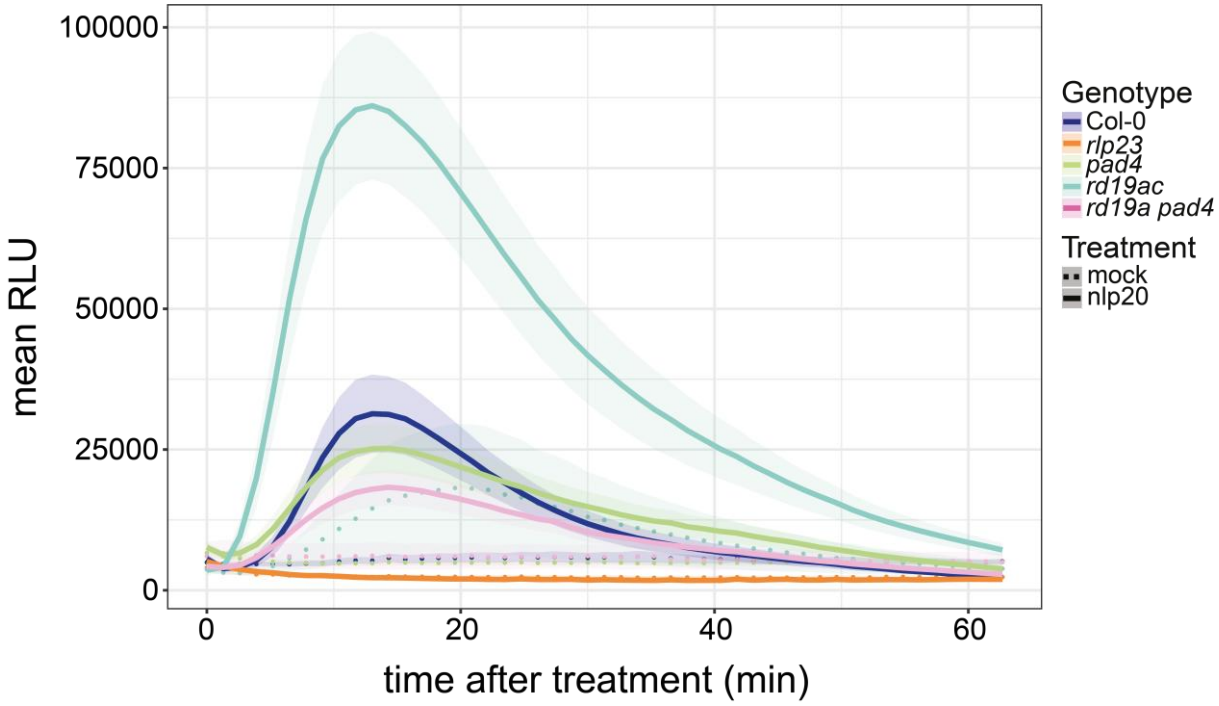


Supplementary Figure S 5: Cleavage logos of RD19A cleavage preferences by PICS assay using Legumain peptide library. PINCIS-script was used to gain the prime and non-prime site specificity of proteases and sample size of peptides identified are indicated. Shown are amino acid residues only identified after incubation for 1 h and 16 h with active RD19A (35S::RD19A^{WT}-HA) relative to the cleavage bond, and their frequencies are indicated by font size. The x-axis corresponds to positions in relation to the cleavage site. Sample size by PINCIS was considered too low and Logo was not included in analysis of amino acid preferences.

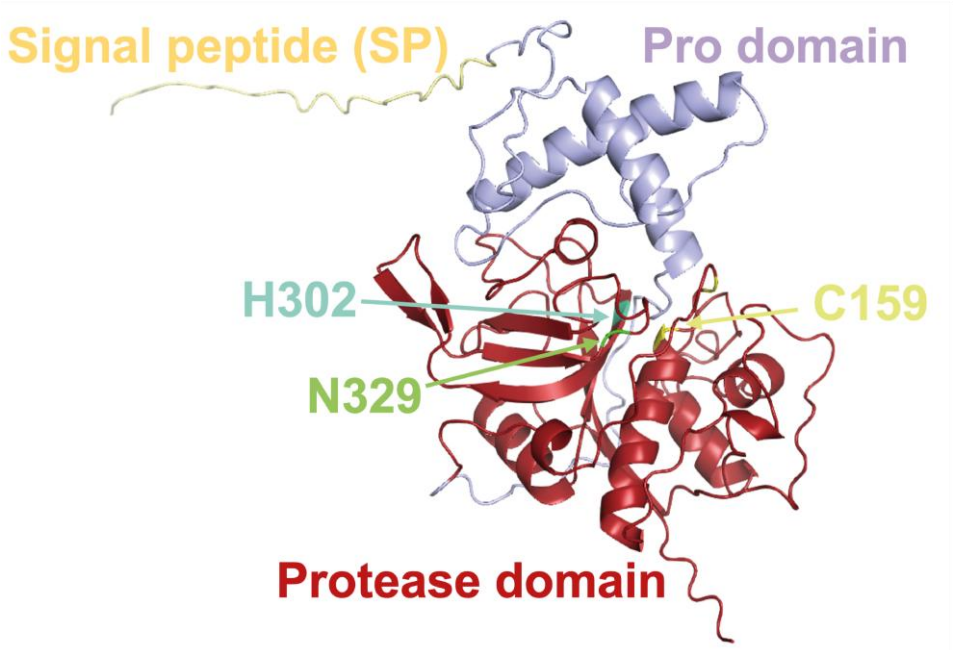


Supplementary Figure S 6: GO term analysis of peptides enriched in Col-0 samples. (**A**) to (**C**) Molecular Function and (**D**) to (**F**) Cellular Components predicted for Col-0 in (**A**) and

(**D**) untreated conditions, (**B**) and (**E**) 10 min after nlp20 trigger and (**C**) and (**F**) 3 h nlp20 treatment. Counts indicate number of peptides associated with one GO term. Significance is indicated by different colors based on $p < 0.05$. enrichGO function in R was used for determining GO terms.



Supplementary Figure S 7: RD19A and PAD4 in nlp20-triggered ROS burst assay. Col-0, *rlp23*, *pad4*, *rd19ac* and *rd19a pad4* in ROS burst assay over 60 min of leaf discs treated with elicitor solutions. Shown are mean relative light units after nlp20 treatment with standard errors shown by distribution around curves. n=24 (nlp20) and n=6 (mock) leaf discs from three independent biological replicates.



Supplementary Figure S 8: RD19A structure prediction using AlphaFold 2.0. Average pLDDT 86.39. Domains were colored according to the prediction. Active sites are highlighted and indicated by arrows.

5.2 Supplementary tables

Supplementary Table S 1: Stable transgenic lines expressing *RD19A* native promoter and genomic DNA in wild-type or catalytically mutated version. Summary table of complementation analysis, gene expression and protein expression levels

Tag	WT or mutant	Line	ROS phenotype	Gene expression	Protein expression
HA	WT	4-4-3-2	*rd19ac*		no
HA	WT	4-4-3-3	Col-0		no
HA	WT	4-4-3-5	Col-0	yes, weak	no
HA	WT	3-3-7-5	Col-0	yes, weak	no
HA	mut	4-2-1-5	Col-0		no
HA	mut	4-4-1-1	Col-0		no
HA	mut	4-4-1-4	Col-0		no
HA	mut	4-4-2-3	Col-0		no
mYFP	WT	4-1-2	Col-0		yes
mYFP	WT	4-2-9	*rd19ac*	yes, weak	yes
mYFP	WT	4-3-2	*rd19ac*		no
mYFP	WT	4-4-4	*rd19ac*		no
mYFP	WT	4-4-5	Col-0		no
mYFP	mut	4-2-4	Col-0		no
mYFP	mut	4-2-9	Col-0		yes
mYFP	mut	4-4-1	Col-0		no
mYFP	mut	4-4-3	*rd19ac*		no
mYFP	mut	4-4-4	*rd19ac*		no

Supplementary Table S 2: Peptide sequences identified by MS/MS analysis in samples following ABPP. Identification of RD19A from four biological replicates in 35S::RD19AWT-FLAG, 35S::RD19AC159A-FLAG, rd19ac and NPC (no probe control) is indicated by presence of blue circle at corresponding LFQ values. LFQ = label-free quantification.

		LFQ intensities				
Sample	**Peptide sequence**	**Replicate 1**	**Replicate 2**	**Replicate 3**	**Replicate 4**	**Domain**
35S::RD19A^{WT}-FLAG	DANKAPILPTENLPEDFDWRDHGAVTPVK	0	0	10929000	0	Pro-domain
35S::RD19A^{WT}-FLAG	LNHGVLLVGYGAAGYAPAR	0	0	2130800	0	Protease domain
35S::RD19A^{C159A}-FLAG	DANKAPILPTENLPEDFDWR	0	0	0	0	Pro-domain
35S::RD19A^{C159A}-FLAG	DANKAPILPTENLPEDFDWRDHGAVTPVK	0	284000000	51162000	0	Pro-domain
35S::RD19A^{C159A}-FLAG	EKPYWIIK	0	9590600	0	0	Protease domain
35S::RD19A^{C159A}-FLAG	FKEKPYWIIK	0	20570000	0	0	Protease domain
35S::RD19A^{C159A}-FLAG	LNHGVLLVGYGAAGYAPAR	0	46504000	11565000	0	Protease domain
35S::RD19A^{C159A}-FLAG	RLNHGVLLVGYGAAGYAPAR	0	83907000	0	0	Protease domain
35S::RD19A^{C159A}-FLAG	TGGLMKEEDYPYTGK	33616000	20990000	0	0	Protease domain
35S::RD19A^{C159A}-FLAG	TGGLMKEEDYPYTGKDGK	0	0	8256500	0	Protease domain

Supplementary Table S 3: Dimethylated samples significantly enriched in Col-0 in comparison to *rd19ac* 10 min and 3 h after nlp20 treatment, based on 100% valid values. Results of Go term analysis. MF = molecular function; CC = cellular component.

Up untreated_CC			
ID	**Description**	**geneID**	**Count**
GO:0055035	plastid thylakoid membrane	RBCL/CP33B/RCA	3
GO:0042651	thylakoid membrane	RBCL/CP33B/RCA	3
GO:0034357	photosynthetic membrane	RBCL/CP33B/RCA	3
GO:0031976	plastid thylakoid	RBCL/CP33B/RCA	3
GO:0042170	plastid membrane	RBCL/CP33B/RCA	3
GO:0048046	apoplast	RBCL/RCA	2
GO:0009535	chloroplast thylakoid membrane	RBCL/RCA	2
GO:0009534	chloroplast thylakoid	RBCL/RCA	2
GO:0019867	outer membrane	RBCL/RCA	2
GO:0031968	organelle outer membrane	RBCL/RCA	2
GO:0010319	stromule	RCA	1
GO:0098552	side of membrane	CP33B	1
Up untreated_MF			
ID	**Description**	**geneID**	**Count**
GO:0016830	carbon-carbon lyase activity	NA/RBCL	2
GO:0016829	lyase activity	NA/RBCL	2
GO:0016018	cyclosporin A binding	AtCYP19-1	1
GO:0016832	aldehyde-lyase activity	NA	1
Up 10 min_CC			
ID	**Description**	**geneID**	**Count**
GO:0009534	chloroplast thylakoid	RBCL/AtSSI2/PSAE-1	3
GO:0031976	plastid thylakoid	RBCL/AtSSI2/PSAE-1	3
GO:0022626	cytosolic ribosome	AP40/RBCL	2

GO:0009535	chloroplast thylakoid membrane	RBCL/PSAE-1	2
GO:0009538	photosystem I reaction center	PSAE-1	1
GO:0055035	plastid thylakoid membrane	RBCL/PSAE-1	2
GO:0042651	thylakoid membrane	RBCL/PSAE-1	2
GO:0034357	photosynthetic membrane	RBCL/PSAE-1	2
GO:0005840	ribosome	AP40/RBCL	2
GO:0019867	outer membrane	RBCL/PSAE-1	2
GO:0031968	organelle outer membrane	RBCL/PSAE-1	2
GO:0042170	plastid membrane	RBCL/PSAE-1	2
GO:0009522	photosystem I	PSAE-1	1
GO:0010287	plastoglobule	PSAE-1	1
GO:0009521	photosystem	PSAE-1	1
GO:0015629	actin cytoskeleton	ACT2	1
GO:0022627	cytosolic small ribosomal subunit	AP40	1
GO:0015935	small ribosomal subunit	AP40	1
Up 10 min_MF			
ID	**Description**	**geneID**	**Count**
GO:0003746 translation elongation factor activity		NA	1
GO:0005198 structural molecule activity		AP40/ACT2	2
GO:0016717 oxidoreductase activity, acting on paired donors, with oxidation of a pair of donors resulting in the reduction of molecular oxygen to two molecules of water		AtSSI2	1
GO:0005200 structural constituent of cytoskeleton		ACT2	1
GO:0016831 carboxy-lyase activity		RBCL	1
GO:0008135 translation factor activity, RNA binding		NA	1
GO:0090079 translation regulator activity, nucleic acid binding		NA	1

GO:0016830 carbon-carbon lyase activity		RBCL	1
GO:0045182 translation regulator activity		NA	1
Up 3 h_CC			
ID	**Description**	**geneID**	**Count**
GO:0010319	stromule	AthCF1beta/CP29B/ATPGMP	
GO:0010287	plastoglobule	AthCF1beta/PSAF	
GO:0022626	cytosolic ribosome	uS10z/uL22y/uS11y	
GO:0044391	ribosomal subunit	uS10z/uL22y/uS11y	
GO:0009535	chloroplast thylakoid membrane	AthCF1beta/CP29B/PSAF	
GO:0055035	plastid thylakoid membrane	AthCF1beta/CP29B/PSAF	
GO:0042651	thylakoid membrane	AthCF1beta/CP29B/PSAF	
GO:0034357	photosynthetic membrane	AthCF1beta/CP29B/PSAF	
GO:0005840	ribosome	uS10z/uL22y/uS11y	
GO:0022627	cytosolic small ribosomal subunit	uS10z/uS11y	
GO:0009534	chloroplast thylakoid	AthCF1beta/CP29B/PSAF	
GO:0031976	plastid thylakoid	AthCF1beta/CP29B/PSAF	
GO:0019867	outer membrane	AthCF1beta/CP29B/PSAF	
GO:0031968	organelle outer membrane	AthCF1beta/CP29B/PSAF	
GO:0042170	plastid membrane	AthCF1beta/CP29B/PSAF	
GO:0015935	small ribosomal subunit	uS10z/uS11y	
GO:0000275	mitochondrial proton-transporting ATP synthase complex, catalytic sector F(1)	AthCF1beta	
Up 3h_MF			
ID	**Description**	**geneID**	**Count**
GO:0016866	intramolecular transferase activity	GSA2/ATPGMP	2
GO:0003735	structural constituent of ribosome	uS10z/uL22y/uS11y	3
GO:0003727	single-stranded RNA binding	ATGRP8/CP29B	2
GO:0005198	structural molecule activity	uS10z/uL22y/uS11y	3
GO:0004784	superoxide dismutase activity	AtSOD2	1
GO:0016721	oxidoreductase activity, acting on superoxide radicals as acceptor	AtSOD2	1
GO:0035198	miRNA binding	ATGRP8	1
GO:0016868	intramolecular phosphotransferase activity	ATPGMP	1
GO:0016853	isomerase activity	GSA2/ATPGMP	2
GO:0061980	regulatory RNA binding	ATGRP8	1
GO:0016832	aldehyde-lyase activity	NA	1

GO:0046933	proton-transporting ATP synthase activity, rotational mechanism	AthCF1beta	1
GO:0008266	poly(U) RNA binding	CP29B	1
GO:0015252	proton channel activity	AthCF1beta	1
GO:0008187	poly-pyrimidine tract binding	CP29B	1
GO:0042625	ATPase-coupled ion transmembrane transporter activity	AthCF1beta	1
GO:0044769	ATPase activity, coupled to transmembrane movement of ions, rotational mechanism	AthCF1beta	1
GO:0046961	proton-transporting ATPase activity, rotational mechanism	AthCF1beta	1

Supplementary Table S 4: Dimethylated samples identified only in Col-0 or rd19ac, based on 100% valid values, independent of significance. ATG codes in table were used to perform GO term analysis.

Col-0 untreated		
Protein ID	**Gene name**	**ATG code**
A0A1I9LRK5	AT3G51140	AT3G51140
F4J3M2	PTAC3	AT3G04260
F4KF14	FTSHI4	AT5G64580
O80567-3	LARP6B	AT2G43970
O82240	AT2G47710	AT2G47710
P23321	PSBO1	AT5G66570
P43296	RD19A	AT4G39090
P43296	RD19A	AT4G39090
P43296	RD19A	AT4G39090
Q01667	LHCA1	AT3G54890
Q38867	CYP19-3	AT3G56070
Q56YA5	AGT1	AT2G13360
Q6ICZ8	AT5G13850	AT5G13850
Q84WZ8	AT2G28815	AT2G28815
Q94BS2	MET1	AT1G55480
Q96520	PER12	AT1G71695
Q9C5D0	CBSX2	AT4G34120
Q9FK35	ADK2	AT5G50370
Q9FMY5	U2AF35B	AT5G42820
Q9FY58	AT5G11070	AT5G11070
Q9LDZ0	HSP70-10	AT5G09590
Q9LF37	CLPB3	AT5G15450
Q9LS02	AOC2	AT3G25770
Q9LX31	GUN4	AT3G59400
Q9S762	HISN1A	AT1G58080
Q9S7M0	LHCB3	AT5G54270
Q9SAJ4	PGK3	AT1G79550
Q9SE83	DRP2A	AT1G10290
Q9SF45	F11F8_15	AT3G09580
Q9SJV5	TATC	AT2G01110
Q9SL15	GRP3	AT2G05520
Q9SRE0	COG0212	AT1G76730

Q9STW6	HSP70-6	AT4G24280
Q9SUL1	RD19C	AT4G16190
Q9ZNZ7-2	GLU1	AT5G04140
Col-0 10 min		
Protein ID	**Gene name**	**ATG code**
P43296	RD19A	AT4G39090
Q9SUL1	RD19C	AT4G16190
A0A1P8BCQ5	AT5G56260	AT5G56260
B9DG73	AT3G11930	AT3G11930
F4JTK8	AQI	AT4G38220
F4K875	CA2	AT5G14740
P10896	RCA	AT2G39730
P56779	psbE	ATCG00580
Q8LAP6	PAP12	AT1G51110/AT1G51115
Q9FLW9	PKP2	AT5G52920
Q9SHI1	AT1G17220	AT1G17220
Q9SL15	GRP3	AT2G05520
Col-0 3 h		
Protein ID	Gene name	ATG code
P43296	RD19A	AT4G39090
Q9SUL1	RD19C	AT4G16190
F4K875	CA2	AT5G14740
O48741	PORC	AT1G03630
P25857	GAPB	AT1G42970
Q0WW55-2	ZEU1	AT5G59440
Q5GM68	PPC2	AT2G42600
Q7Y1W1	TIC56	AT5G01590
Q8L606	AT3G53560	AT3G53560
Q9CAK8-2	ISPF	AT1G63970
Q9SSA5	CYP38	AT3G01480
Q9SYA9	AT1G61730	AT1G61730
***rd19ac* untreated**		
Protein ID	**Gene name**	**ATG code**
A0A1I9LSZ8	AT3G07195	AT3G07195
F4HTT6	CYP26-2	AT1G74070
F4J3Q8	GET3B	AT3G10350
F4K0E8-2	ISPG	AT5G60600
F4KGV2	GRF6	AT5G10450
O65581	FBA5	AT4G26530
O82487	T12H20.10	AT4G10750
P10896	RCA	AT2G39730
P11574	VHA-B1	AT1G76030
P11574	VHA-B1	AT1G76030
P29514	TUBB6	AT5G12250
P55228	APS1	AT5G48300
P59220	CAM7	AT3G43810

Q06738	RD29A	AT5G52310
Q41951	TIP2-1	AT3G16240
Q41951	TIP2-1	AT3G16240
Q42586	PYRE-F	AT3G54470
Q43127	GLN2	AT5G35630
Q8LB47	MGe2	AT4G26780
Q8VZP1	GPP2	AT5G57440
Q93W34	RBP45C	AT4G27000
Q94AG6	SAMC1	AT4G39460
Q96520	PER12	AT1G71695
Q9FEA2	OVA3	AT5G64050
Q9FIH8	SPP	AT5G42390
Q9FK35	ADK2	AT5G50370
Q9LF37	CLPB3	AT5G15450
Q9LI77	GATA	AT3G25660
Q9LIK9	APS1	AT3G22890
Q9LK61	RPS10	AT3G13120
Q9LPC5	BIG3	AT1G01960
Q9LPR4	IPMS1	AT1G18500
Q9LX65	VHA-H	AT3G42050
Q9LYN0	PRA1B1	AT3G56110
Q9MAB3	NOP5-2	AT3G05060
Q9S762	HISN1A	AT1G58080
Q9SHR7	LHCB2.1	AT2G05100
Q9SL15-4	GRP3	AT2G05520
Q9SUG3	ITPK3	AT4G08170
Q9SUR0	AT4G23670	AT4G23670
Q9ZQ78	AT2G03420	AT2G03420
Q9ZTZ7	KEA1	AT1G01790
***rd19ac* 10 min**		
Protein ID	**Gene name**	**ATG code**
Q41951	TIP2-1	AT3G16240
B9DGK2	AT2G35830	AT2G35830
F4J7A7-2	PPD7	AT3G05410
F4JFV6	GOX2	AT3G14415
F4JQJ7	AT4G36945	AT4G36945
P48523	CAD4	AT3G19450
P56799	rps4	ATCG00380
Q38814	THI1	AT5G54770
Q42064	RPL8C	AT4G36130
Q8H7F6	GRXS16	AT2G38270
Q8RWT4	AT2G42710	AT2G42710
Q8RWT4	AT2G42710	AT2G42710
Q8VYL1	AT5G35170	AT5G35170
Q9LD57	PGK1	AT3G12780

Q9LHP1	RPL7D	AT3G13580
Q9M2P7	PAP9	AT3G58010
***rd19ac* 3 h**		
Protein ID	**Gene name**	**ATG code**
O22218	ACA4	AT2G41560
O65390	APA1	AT1G11910
P05466	AT2G45300	AT2G45300
P14671	TSB1	AT5G54810
P31167	AAC1	AT3G08580
P38418	LOX2	AT3G45140
P92946	SULTR2;2	AT1G77990
Q0WMZ7	BCM2	AT4G17840
Q38997-1	KIN10	AT3G01090
Q41906	CYS3	AT2G40880
Q42290	MPPbeta	AT3G02090
Q56X76	RH39	AT4G09730
Q949X0	ADS3	AT3G15850
Q9LMK7	RANBP1A	AT1G07140
Q9LT77	RDL2	AT3G19400
Q9S7E4	FDH1	AT5G14780
Q9SCY3	PNSL4	AT4G39710
Q9STG6	DUT	AT3G46940
Q9SZJ5	SHM1	AT4G37930

Supplementary Table S 5: Dimethylated samples identified only in Col-0 10 min after nlp20 treatment, based on 100% valid values, independent of significance. Results of Go term analysis or if not available, TAIR search results.

Protein ID	Gene name	ATG code	Go term identified	Tair description for gene
P43296	RD19A	AT4G39090	GO:0004197: cysteine-type endopeptidase activity, GO:0008234: cysteine-type peptidase activity, GO:0004175: endopeptidase activity	
Q9SUL1	RD19C	AT4G16190	GO:0004197: cysteine-type endopeptidase activity, GO:0008234: cysteine-type peptidase activity, GO:0004175:	

			endopeptidase activity	
A0A1P8BCQ5	AT5G56260	AT5G56260		Ribonuclease E inhibitor RraA/Dimethylmenaquinone methyltransferase
B9DG73	AT3G11930	AT3G11930		Adenine nucleotide alpha hydrolases-like superfamily protein
F4JTK8	AQI	AT4G38220		AQUAPORIN INTERACTOR; Peptidase M20/M25/M40 family protein
F4K875	CA2	AT5G14740		CARBONIC ANHYDRASE 2; Encodes a beta carbonic anhydrase likely to be localized in the cytoplasm. Expression of its mRNA is seen in etiolated seedlings and points to a possible nonphotosynthetic role for this isoform
P10896	RCA	AT2G39730		RUBISCO ACTIVASE; Rubisco activase, a nuclear-encoded chloroplast protein that consists of two isoforms arising from alternative splicing in most plants. Required for the light activation of rubisco. Involved in jasmonate-induced leaf senescence.
P56779	psbE	ATCG00580		PHOTOSYSTEM II REACTION CENTER PROTEIN E; PSII cytochrome b559. There have been many speculations about the function of Cyt b559, but the most favored at present is that it plays a protective role by acting as an electron acceptor or electron donor under conditions when electron flow through PSII is not optimized
Q8LAP6	PAP12	AT1G51110		FIBRILLIN10; PAP/fibrillin (ECM1) localized to chloroplasts; involved in structural activity
Q9FLW9	PKP2	AT5G52920	GO:0004743: pyruvate kinase activity,	

			GO:0030955: potassium ion binding, GO:0031420: alkali metal ion binding	
Q9SHI1	AT1G17220	AT1G17220		FU-GAERI1; Encodes a chloroplast localized protein with similarity to translation initiation factor 2. Can complement loss of INFB in E.coli suggesting FUG1 does function as a translation initiation factor in vivo. Identified as a suppressor of the leaf variegation mutant var2-6. Suppression is only seen in hypomorphs as complete loss of function alleles are embryo lethal. The mRNA is cell-to-cell mobile.
Q9SL15	GRP3	AT2G05520		GLYCINE-RICH PROTEIN 3; Encodes a glycine-rich protein that is expressed mainly in stems and leaves. ATGRP3 functions in root size determination during development and in Al stress. mRNA levels are upregulated in response to ABA, salicylic acid and ethylene but downregulated in response to desiccation. The mRNA is cell-to-cell mobile.

Supplementary Table S 6: Dimethylated samples identified only in Col-0 3 h after nlp20 treatment, based on 100% valid values, independent of significance. Results of Go term analysis or if not available, TAIR search results.

Protein ID	Gene name	ATG code	Go term identified	Tair description for gene
P43296	RD19A	AT4G39090	GO:0004197: cysteine-type endopeptidase activity, GO:0008234: cysteine-type peptidase activity, GO:0004175: endopeptidase activity	
Q9SUL1	RD19C	AT4G16190	GO:0004197:	

			cysteine-type endopeptidase activity, GO:0008234: cysteine-type peptidase activity, GO:0004175: endopeptidase activity	
F4K875	CA2	AT5G14740	GO:0016829: lyase activity, GO:0004089: carbonate dehydratase activity,	
O48741	PORC	AT1G03630	GO:0003959: NADPH dehydrogenase activity, GO:0016628: oxidoreductase activity, acting on the CH-CH group of donors, NAD or NADP as acceptor,	
P25857	GAPB	AT1G42970	GO:1901149: salicylic acid binding, GO:0016620: oxidoreductase activity, acting on the aldehyde or oxo group of donors, NAD or NADP as acceptor, GO:0016903: oxidoreductase activity, acting on the aldehyde or oxo group of donors, GO:0033293: monocarboxylic acid binding, GO:0050661: NADP binding	
Q0WW55-2	ZEU1	AT5G59440	GO:0050145:	

			nucleoside monophosphate kinase activity, GO:0016776: phosphotransferase activity, phosphate group as acceptor, GO:0019205: nucleobase-containing compound kinase activity	
Q5GM68	PPC2	AT2G42600	GO:0016829: lyase activity, GO:0016831: carboxy-lyase activity	
Q7Y1W1	TIC56	AT5G01590	GO:0008320: protein transmembrane transporter activity, GO:0022884: macromolecule transmembrane transporter activity, GO:0140318: protein transporter activity	
Q8L606	AT3G53560	AT3G53560		Tetratricopeptide repeat (TPR)-like superfamily protein
Q9CAK8-2	ISPF	AT1G63970	GO:0016829: lyase activity, GO:0016849: phosphorus-oxygen lyase activity	
Q9SSA5	CYP38	AT3G01480	GO:0003755: peptidyl-prolyl cis-trans isomerase activity, GO:0016859: cis-trans isomerase activity	
Q9SYA9	AT1G61730	AT1G61730		DNA-binding storekeeper protein-related transcriptional regulator

Supplementary Table S 7: Dimethylated samples identified only in *rd19ac* 10 min after nlp20 treatment, based on 100% valid values, independent of significance. Results of Go term analysis or if not available, TAIR search results.

Protein ID	Gene name	ATG code	Go term identified	Tair description for gene

Q41951	TIP2-1	AT3G16240	GO:0015101: organic cation transmembrane transporter activity, GO:0005372: water transmembrane transporter activity, GO:0015250: water channel activity, GO:0042802: identical protein binding	
B9DGK2	AT2G35830	AT2G35830		ureidoglycolate hydrolase
F4J7A7-2	PPD7	AT3G05410		member of the thylakoid lumen proteome
F4JFV6	GOX2	AT3G14415	GO:0016614: oxidoreductase activity, acting on CH-OH group of donors, GO:0016899: oxidoreductase activity, acting on the CH-OH group of donors, oxygen as acceptor, GO:0010181: FMN binding	
F4JQJ7	AT4G36945	AT4G36945		PLC-like phosphodiesterases superfamily protein
P48523	CAD4	AT3G19450	GO:0016614: oxidoreductase activity, acting on CH-OH group of donors, GO:0052747: sinapyl alcohol dehydrogenase activity, GO:0045551: cinnamyl-alcohol dehydrogenase activity,	
P56799	rps4	ATCG00380	GO:0003735: structural constituent of ribosome, GO:0005198:	

			structural molecule activity	
Q38814	THI1	AT5G54770	GO:0042802: identical protein binding	
Q42064	RPL8C	AT4G36130		Ribosomal protein L2 family
Q8H7F6	GRXS16	AT2G38270		Encodes protein homologous to CXIP1. CXIP1 is a PICOT domain containing protein interacts with CAX1, a high capacity calcium transporter. However, CXP2 does not interact with CAX1 and only moderately activates another calcium transporter CAX4.
Q8RWT4	AT2G42710	AT2G42710	GO:0003735: structural constituent of ribosome, GO:0005198: structural molecule activity	
Q8RWT4	AT2G42710	AT2G42710		Key factor in mitochondrial unfolded protein response (UPRmt); regulates plant growth in a CORONATINE-INSENSITIVE1 (COI1)-dependent manner
Q8VYL1	AT5G35170	AT5G35170		adenylate kinase family protein
Q9LD57	PGK1	AT3G12780	GO:0016774: phosphotransferase activity, carboxyl group as acceptor, GO:0005524: ATP binding	
Q9LHP1	RPL7D	AT3G13580	GO:0003735: structural constituent of ribosome, GO:0005198: structural molecule activity	
Q9M2P7	PAP9	AT3G58010		plastoglobulin 34kD

Supplementary Table S 8: Dimethylated samples identified only in *rd19ac* 3 h after nlp20 treatment, based on 100% valid values, independent of significance. Results of Go term analysis or if not available, TAIR search results.

Protein ID	Gene name	ATG code	Go term identified	Tair description for gene
O22218	ACA4	AT2G41560		AUTOINHIBITED CA(2+)-ATPASE; Encodes a calmodulin-regulated Ca(2+)-ATPase that improves salt tolerance in yeast. Localized to the vacuole. Lesion mimic phenotype when mutation in the gene is combined with a mutation in ACA11. Lesion mimic phenotype of double knockout can be suppressed by nutritional supplements that increase anion levels (e.g. 15 mM Nitrate, Chloride, or Phosphate).ACA8 and ACA10, as well as ACA4 and ACA11, are critical in maintaining low resting cytosol Ca2+ level
O65390	APA1	AT1G11910	GO:0004175: endopeptidase activity	
P05466	AT2G45300	AT2G45300		encodes 3-phosphoshikimate 1-carboxyvinyltransferase / 5-enolpyruvylshikimate-3-phosphate / EPSP synthase involved in chorismate biosynthesis The mRNA is cell-to-cell mobile
P14671	TSB1	AT5G54810		A.thaliana tryptophan synthase beta subunit
P31167	AAC1	AT3G08580		mitochondrial ADP/ATP carrier
P38418	LOX2	AT3G45140		LIPOXYGENASE 2; Chloroplast lipoxygenase required for wound-induced jasmonic acid accumulation in Arabidopsis.Mutants are resistant to Staphylococcus aureus and accumulate salicylic acid upon infection. The mRNA is cell-to-cell mobile
P92946	SULTR2;2	AT1G77990		Encodes a low-affinity sulfate transporter.

Q0WMZ7	BCM2	AT4G17840	GO:0004175: endopeptidase activity, GO:0004222: metalloendopeptidase activity	BALANCE OF CHLOROPHYLL METABOLISM; CAAX protease self-immunity protein
Q38997-1	KIN10	AT3G01090		SNF1 KINASE HOMOLOG 10; Encodes a SNF1-related protein kinase that physically interacts with SCF subunit SKP1/ASK1 and 20S proteosome subunit PAD1. It can also interact with PRL1 DWD-containing protein. Based on in vitro degradation assays and cul4cs and prl1 mutants, there is evidence that AKIN10 is degraded in a proteasome-dependent manner, and that this depends on a CUL4-PRL1 E3 ligase
Q41906	CYS3	AT2G40880		Encodes a protein with cysteine proteinase inhibitor activity. Overexpression increases tolerance to abiotic stressors (i.e.salt,osmotic, cold stress). The mRNA is cell-to-cell mobile
Q42290	MPPbeta	AT3G02090	GO:0004175: endopeptidase activity, GO:0004222: metalloendopeptidase activity	
Q56X76	RH39	AT4G09730		Encodes RH39, a DEAD-box protein involved in the introduction of the hidden break into the 23S rRNA in the chloroplasts. Recombinant RH39 binds to the 23S rRNA in a segment adjacent to the stem-loop creating the hidden break target loop in a sequence-dependent manner. Has ATP-hydrolyzing activity at a Kcat of 5.3 /min in the presence of rRNA sequence. Mutants have

				drastically reduced level of level of ribulose 1,5-bisphosphate carboxylase/oxygenase. The mRNA is cell-to-cell mobile
Q949X0	ADS3	AT3G15850		Chloroplastic enzyme responsible for the synthesis of 16:1 fatty acids from galactolipids and sulpholipids. Uses ferredoxin as electron donor. The mRNA is cell-to-cell mobile
Q9LMK7	RANBP1A	AT1G07140		Encodes a putative Ran-binding protein (siRanBP)
Q9LT77	RDL2	AT3G19400	GO:0004175: endopeptidase activity	
Q9S7E4	FDH1	AT5G14780		Encodes a NAD-dependent formate dehydrogenase
Q9SCY3	PNSL4	AT4G39710		FK506-binding protein 16-2
Q9STG6	DUT	AT3g46940		DUTP-PYROPHOSPHATASE-LIKE 1
Q9SZJ5	SHM1	AT4g37930		Encodes a protein with mitochondrial serine hydroxymethyltransferase activity, which functions in the photorespiratory pathway, catalyzes the conversion of serine and tetrahydrofolate to glycine and 5,10-methylene tetrahydrofolate. Involved in controlling cell damage caused by abiotic stress, such as high light and salt and the hypersensitive defense response of plants

Supplementary Table S 9: Cleavage sites determined only in Col-0 or only in *rd19ac* in untreated conditions or 10 min and 3 h after nlp20 treatment, based on 100% valid values, independent of significance.

Valid_ comparison untreated	Valid_comparison 10 min	Valid_comparison 3 h	Gene	Before sequence	6_Amino_acids_before	Cleavage_ window
Col-0_ untreated	Col-0_ 10min	Col-0_ 3h	RD19C	R	KRRGFR	KRRGFRLP TDTQ

Col-0_ untreated	Col-0_ 10min	Col-0_ 3h	RD19A	K	GFKLPK	GFKLPKDA NKAP
Col-0_ untreated	Col-0_ 10min	Col-0_ 3h	RD19A	K	VRSGFK	VRSGFKLP KDAN
-	-	Col-0_ 3h	TIC56	V	FRASPV	FRASPVVQ FMTR
-	-	Col-0_ 3h	PORC	R	TTGLFR	TTGLFREHI PLF
-	-	Col-0_ 3h	GAPB	R	NGIALR	NGIALRVP TPNV
-	-	Col-0_ 3h	AT3G5 3560	R	LEEEER	LEEEERAL DEHL
-	-	Col-0_ 3h	CYP38	R	EDCVFR	EDCVFRIV LDGY
-	-	Col-0_ 3h	PPC2	Q	RINGKQ	RINGKQEV MIGY
-	-	Col-0_ 3h	ISPF	I	LDATLI	LDATLILQR PKI
-	-	Col-0_ 3h	AT1G6 1730	G	PAMKSG	PAMKSGTK RPAS
-	-	Col-0_ 3h	CA2	D	LIEKDD	LIEKDDLKD VAA
-	-	rd19ac_ 3h	GRP3	G	KPDQRG	KPDQRGY GDNGG
-	Col-0_ 10min	-	AT1G1 7220	R	VARVER	VARVERGL GVNT
-	Col-0_ 10min	-	PAP12	R	YPVPFR	YPVPFRLL GDEA
-	Col-0_ 10min	-	PKP2	R	TQPIWR	TQPIWRSQ STHN
-	Col-0_ 10min	-	psbE	P	FGSPRP	FGSPRPNE YFTE
-	Col-0_ 10min	-	AT5G5 6260	M	HTESPM	HTESPMAA FATA
-	Col-0_ 10min	-	AT3G1 1930	K	TSAVEK	TSAVEKQP ETTT
-	Col-0_ 10min	-	CA2	I	EDWVKI	EDWVKICL PAKS
-	Col-0_ 10min	-	GRP3	G	YGDNGG	YGDNGGN YNNGG
-	Col-0_ 10min	-	AQI	A	KQFLTA	KQFLTAAD DSNP
-	rd19ac_ 10min	-	AT1G1 7220	R	EIRLYR	EIRLYRVIY ELI
Col-0_ untreated	-	-	GRP3	Y	PDQRGY	PDQRGYG DNGGN
rd19ac_un treated	-	-	AT5G5 6260	R	VNGCVR	VNGCVRD VDEIN
rd19ac_un treated	-	-	PORC	R	HFLLSR	HFLLSRLLL DDL
rd19ac_un treated	-	-	CYP38	P	REVQKP	REVQKPLE DITD
rd19ac_un treated	-	-	GAPB	M	DSSLTM	DSSLTMVM GDDM

rd19ac_untreated	-	-	CA2	K	LPAKSK	LPAKSKVLAESE
rd19ac_untreated	-	-	GRP3	G	GYGDNG	GYGDNGGNYNNG
rd19ac_untreated	-	-	GRP3	G	GNYNNG	GNYNNGGGYQGG
rd19ac_untreated	-	-	GRP3	G	YGDNGG	YGDNGGNYNNGG

6 References

Albert, Isabell, Hannah Böhm, Markus Albert, Christina E. Feiler, Julia Imkampe, Niklas Wallmeroth, Caterina Brancato, Tom M. Raaymakers, Stan Oome, Heqiao Zhang, Elzbieta Krol, Christopher Grefen, Andrea A. Gust, Jijie Chai, Rainer Hedrich, Guido Van Den Ackerveken, and Thorsten Nürnberger. 2015. 'An RLP23-SOBIR1-BAK1 Complex Mediates NLP-Triggered Immunity'. *Nature Plants* 1.

Alvarez, María E., Roger I. Pennell, Per-Johan Meijer, Atsushi Ishikawa, Richard A. Dixon, and Chris Lamb. 1998. 'Reactive Oxygen Intermediates Mediate a Systemic Signal Network in the Establishment of Plant Immunity'. *Cell* 92(6):773–84.

Arnaud, Dominique, Michael J. Deeks, and Nicholas Smirnoff. 2023. 'RBOHF Activates Stomatal Immunity by Modulating Both Reactive Oxygen Species and Apoplastic PH Dynamics in Arabidopsis.' *The Plant Journal : For Cell and Molecular Biology* 116(2):404–15.

Baxter, Aaron, Ron Mittler, and Nobuhiro Suzuki. 2014. 'ROS as Key Players in Plant Stress Signalling'. *Journal of Experimental Botany* 65(5):1229–40.

Bayless, Adam M. and Marc T. Nishimura. 2020. 'Enzymatic Functions for Toll/Interleukin-1 Receptor Domain Proteins in the Plant Immune System '. *Frontiers in Genetics* 11.

Belenghi, Beatrice, Filippo Acconcia, Maurizio Trovato, Michele Perazzolli, Alessio Bocedi, Fabio Polticelli, Paolo Ascenzi, and Massimo Delledonne. 2003. 'AtCYS1, a Cystatin from Arabidopsis Thaliana, Suppresses Hypersensitive Cell Death'. *European Journal of Biochemistry* 270(12):2593–2604.

Bernoux, Maud, Ton Timmers, Alain Jauneau, Christian Brière, Pierre J. G. M. De Wit, Yves Marco, and Laurent Deslandesa. 2008. 'RD19, an Arabidopsis Cysteine Protease Required for RRS1-R-Mediated Resistance, Is Relocalized to the Nucleus by the Ralstonia Solanacearum PopP2 Effector'. *Plant Cell* 20(8):2252–64.

Bernsdorff, Friederike, Anne-Christin Döring, Katrin Gruner, Stefan Schuck, Andrea Bräutigam, and Jürgen Zeier. 2016. 'Pipecolic Acid Orchestrates Plant Systemic Acquired Resistance and Defense Priming via Salicylic Acid-Dependent and -Independent Pathways'. *The Plant Cell* 28(1):102–29.

Betsuyaku, Shigeyuki, Shinpei Katou, Yumiko Takebayashi, Hitoshi Sakakibara, Nobuhiko Nomura, and Hiroo Fukuda. 2018. 'Salicylic Acid and Jasmonic Acid Pathways Are Activated in Spatially Different Domains Around the Infection Site During Effector-Triggered Immunity in Arabidopsis Thaliana'. *Plant and Cell Physiology* 59(1):8–16.

Bhandari, Deepak D., Dmitry Lapin, Barbara Kracher, Patrick von Born, Jaqueline Bautor, Karsten Niefind, and Jane E. Parker. 2019. 'An EDS1 Heterodimer Signalling Surface Enforces Timely Reprogramming of Immunity Genes in Arabidopsis'. *Nature Communications* 10(1).

van der Biezen, Erik A., Cecilie T. Freddie, Katherine Kahn, Jane E. Parker, and Jonathan D. G. Jones. 2002. 'Arabidopsis RPP4 Is a Member of the RPP5 Multigene Family of TIR-NB-LRR Genes and Confers Downy Mildew Resistance through Multiple Signalling Components.' *The Plant Journal : For Cell and Molecular Biology* 29(4):439–51.

Birkenbihl, Rainer P., Barbara Kracher, Mario Roccaro, and Imre E. Somssich. 2017. 'Induced Genome-Wide Binding of Three Arabidopsis WRKY Transcription Factors during Early MAMP-Triggered Immunity.' *The Plant Cell* 29(1):20–38.

Bjornson, Marta and Cyril Zipfel. 2021. 'Plant Immunity: Crosstalk between Plant Immune

Receptors'. *Current Biology* 31(12):R796–98.

Blum, Matthias, Hsin-Yu Chang, Sara Chuguransky, Tiago Grego, Swaathi Kandasaamy, Alex Mitchell, Gift Nuka, Typhaine Paysan-Lafosse, Matloob Qureshi, Shriya Raj, Lorna Richardson, Gustavo A. Salazar, Lowri Williams, Peer Bork, Alan Bridge, Julian Gough, Daniel H. Haft, Ivica Letunic, Aron Marchler-Bauer, Huaiyu Mi, Darren A. Natale, Marco Necci, Christine A. Orengo, Arun P. Pandurangan, Catherine Rivoire, Christian J. A. Sigrist, Ian Sillitoe, Narmada Thanki, Paul D. Thomas, Silvio C. E. Tosatto, Cathy H. Wu, Alex Bateman, and Robert D. Finn. 2021. 'The InterPro Protein Families and Domains Database: 20 Years On.' *Nucleic Acids Research* 49(D1):D344–54.

Böhm, Hannah, Isabell Albert, Stan Oome, Tom M. Raaymakers, Guido Van den Ackerveken, and Thorsten Nürnberger. 2014. 'A Conserved Peptide Pattern from a Widespread Microbial Virulence Factor Triggers Pattern-Induced Immunity in Arabidopsis'. *PLoS Pathogens*.

Boller, Thomas and Georg Felix. 2009. 'A Renaissance of Elicitors: Perception of Microbe-Associated Molecular Patterns and Danger Signals by Pattern-Recognition Receptors.' *Annual Review of Plant Biology* 60:379–406.

Bonardi, Vera, Saijun Tang, Anna Stallmann, Melinda Roberts, Karen Cherkis, and Jeffery L. Dangl. 2011. 'Expanded Functions for a Family of Plant Intracellular Immune Receptors beyond Specific Recognition of Pathogen Effectors.' *Proceedings of the National Academy of Sciences of the United States of America* 108(39):16463–68.

Brutus, Alexandre, Francesca Sicilia, Alberto Macone, Felice Cervone, and Giulia De Lorenzo. 2010. 'A Domain Swap Approach Reveals a Role of the Plant Wall-Associated Kinase 1 (WAK1) as a Receptor of Oligogalacturonides'. *Proceedings of the National Academy of Sciences* 107(20):9452–57.

Cao, Lijun, Heejin Yoo, Tianyuan Chen, Musoki Mwimba, Xing Zhang, and Xinnian Dong. 2023. 'H₂O₂ Sulfenylates CHE Linking Local Infection to Establishment of Systemic Acquired Resistance'. *BioRxiv* 2023.07.27.550865.

Castel, Baptiste, Pok-Man Ngou, Volkan Cevik, Amey Redkar, Dae-Sung Kim, Ying Yang, Pingtao Ding, and Jonathan D. G. Jones. 2019. 'Diverse NLR Immune Receptors Activate Defence via the RPW8-NLR NRG1'. *New Phytologist* 222(2):966–80.

Castro, Bardo, Matteo Citterico, Sachie Kimura, Danielle M. Stevens, Michael Wrzaczek, and Gitta Coaker. 2021. 'Stress-Induced Reactive Oxygen Species Compartmentalization, Perception and Signalling'. *Nature Plants* 7(4):403–12.

Chen, Ying Lan, Fan Wei Lin, Kai Tan Cheng, Chi Hsin Chang, Sheng Chi Hung, Thomas Efferth, and Yet Ran Chen. 2023. 'XCP1 Cleaves Pathogenesis-Related Protein 1 into CAPE9 for Systemic Immunity in Arabidopsis'. *Nature Communications* 14(1).

Chen, Zhixiang, Herman Silva, and Daniel F. Klessig. 1993. 'Active Oxygen Species in the Induction of Plant Systemic Acquired Resistance by Salicylic Acid'. *Science* 262(5141):1883–86.

Cheval, Cecilia and Christine Faulkner. 2018. 'Plasmodesmal Regulation during Plant–Pathogen Interactions'. *New Phytologist* 217(1):62–67.

Chinchilla, Delphine, Cyril Zipfel, Silke Robatzek, Birgit Kemmerling, Thorsten Nürnberger, Jonathan D. G. Jones, Georg Felix, and Thomas Boller. 2007. 'A Flagellin-Induced Complex of the Receptor FLS2 and BAK1 Initiates Plant Defence'. *Nature* 448(7152):497–500.

Colaert, Niklaas, Kenny Helsens, Lennart Martens, Joël Vandekerckhove, and Kris Gevaert.

2009. ‘Improved Visualization of Protein Consensus Sequences by IceLogo’. *Nature Methods* 6(11):786–87.

Conrath, Uwe, Zhixiang Chen, Joseph R. Ricigliano, and Daniel F. Klessig. 1995. ‘Two Inducers of Plant Defense Responses, 2,6-Dichloroisonicotinec Acid and Salicylic Acid, Inhibit Catalase Activity in Tobacco’. *Proceedings of the National Academy of Sciences of the United States of America* 92(16):7143–47.

Couto, Daniel and Cyril Zipfel. 2016. ‘Regulation of Pattern Recognition Receptor Signalling in Plants’. *Nature Reviews Immunology* 16(9):537–52.

Cox, Jürgen and Matthias Mann. 2008. ‘MaxQuant Enables High Peptide Identification Rates, Individualized p.p.b.-Range Mass Accuracies and Proteome-Wide Protein Quantification’. *Nature Biotechnology* 26(12):1367–72.

Cui, Haitao, Enrico Gobbato, Barbara Kracher, Jingde Qiu, Jaqueline Bautor, and Jane E. Parker. 2017. ‘A Core Function of EDS1 with PAD4 Is to Protect the Salicylic Acid Defense Sector in Arabidopsis Immunity’. *New Phytologist* 213(4):1802–17.

Cui, Haitao, Jingde Qiu, Yue Zhou, Deepak D. Bhandari, Chunhui Zhao, Jaqueline Bautor, and Jane E. Parker. 2018. ‘Antagonism of Transcription Factor MYC2 by EDS1/PAD4 Complexes Bolsters Salicylic Acid Defense in Arabidopsis Effector-Triggered Immunity’. *Molecular Plant* 11(8):1053–66.

Dangl, J. L. and J. D. Jones. 2001. ‘Plant Pathogens and Integrated Defence Responses to Infection.’ *Nature* 411(6839):826–33.

Darino, Martin, Kostya Kanyuka, and Kim E. Hammond-Kosack. 2022. ‘Apoplastic and Vascular Defences’. *Essays in Biochemistry* 66(5):595–605.

Demir, Fatih, Maithreyan Kuppusamy, Andreas Perrar, and Pitter F. Huesgen. 2022. ‘Profiling Sequence Specificity of Proteolytic Activities Using Proteome-Derived Peptide Libraries.’ *Methods in Molecular Biology (Clifton, N.J.)* 2447:159–74.

Demir, Fatih, Stefan Niedermaier, Joji Grace Villamor, and Pitter Florian Huesgen. 2018. ‘Quantitative Proteomics in Plant Protease Substrate Identification’. *New Phytologist* 218(3):936–43.

Demir, Fatih, Andreas Perrar, Melissa Mantz, and Pitter F. Huesgen. 2022. ‘Sensitive Plant N-Terminome Profiling with HUNTER’. *Methods in Molecular Biology* 2447:139–58.

Dongus, Joram. n.d. *Structure-Function Analysis of the Central Defence Regulator PAD4 in Arabidopsis*.

Dongus, Joram A., Deepak D. Bhandari, Monika Patel, Lani Archer, Lucas Dijkgraaf, Laurent Deslandes, Jyoti Shah, and Jane E. Parker. 2020. ‘The Arabidopsis PAD4 Lipase-like Domain Is Sufficient for Resistance to Green Peach Aphid’. *Molecular Plant-Microbe Interactions* 33(2):328–35.

Dongus, Joram A., Deepak D. Bhandari, Eva Penner, Dmitry Lapin, Sara C. Stolze, Anne Harzen, Monika Patel, Lani Archer, Lucas Dijkgraaf, Jyoti Shah, Hirofumi Nakagami, and Jane E. Parker. 2022. ‘Cavity Surface Residues of PAD4 and SAG101 Contribute to EDS1 Dimer Signaling Specificity in Plant Immunity’. *Plant Journal* 110(5):1415–32.

Dou, Daolong and Jian-Min Zhou. 2012. ‘Phytopathogen Effectors Subverting Host Immunity: Different Foes, Similar Battleground’. *Cell Host & Microbe* 12(4):484–95.

Dubiella, Ullrich, Heike Seybold, Guido Durian, Eileen Komander, Roman Lassig, Claus-Peter Witte, Waltraud X. Schulze, and Tina Romeis. 2013. ‘Calcium-Dependent Protein Kinase/NADPH Oxidase Activation Circuit Is Required for Rapid Defense Signal Propagation’. *Proceedings of the National Academy of Sciences* 110(21):8744–49.

Duxbury, Zane, Shanshan Wang, Craig I. MacKenzie, Jeannette L. Tenthorey, Xiaoxiao Zhang, Sung Un Huh, Lanxi Hu, Lionel Hill, Pok Man Ngou, Pingtao Ding, Jian Chen, Yan Ma, Hailong Guo, Baptiste Castel, Panagiotis N. Moschou, Maud Bernoux, Peter N. Dodds, Russell E. Vance, and Jonathan D. G. Jones. 2020. 'Induced Proximity of a TIR Signaling Domain on a Plant-Mammalian NLR Chimera Activates Defense in Plants'. *Proceedings of the National Academy of Sciences of the United States of America* 117(31):18832–39.

Eisele, Jochen F., Florian Fäßler, Patrick F. Bürgel, and Christina Chaban. 2016. 'A Rapid and Simple Method for Microscopy-Based Stomata Analyses'. *PLoS ONE*.

Entila, Frederickson, Xiaowei Han, Akira Mine, Paul Schulze-Lefert, and Kenichi Tsuda. 2024. 'Commensal Lifestyle Regulated by a Negative Feedback Loop between Arabidopsis ROS and the Bacterial T2SS'. *Nature Communications* 15(1):456.

Essuman, Kow, Jeffrey Milbrandt, Jeffery L. Dangl, and Marc T. Nishimura. 2022. 'Shared TIR Enzymatic Functions Regulate Cell Death and Immunity across the Tree of Life'. *Science* 377(6605).

Fabre, Nicolas, Ilja M. Reiter, NOELLE BECUWE-LINKA, Bernard Genty, and Dominique Rumeau. 2007. 'Characterization and Expression Analysis of Genes Encoding α and β Carbonic Anhydrases in Arabidopsis'. *Plant, Cell & Environment* 30(5):617–29.

Farmer, Edward E., Yong-Qiang Gao, Gioia Lenzoni, Jean-Luc Wolfender, and Qian Wu. 2020. 'Wound- and Mechanostimulated Electrical Signals Control Hormone Responses'. *New Phytologist* 227(4):1037–50.

Feehan, Joanna M., Baptiste Castel, Adam R. Bentham, and Jonathan D. G. Jones. 2020. 'Plant NLRs Get by with a Little Help from Their Friends'. *Current Opinion in Plant Biology* 56:99–108.

Feehan, Joanna M., Junli Wang, Xinhua Sun, Jihyeon Choi, Hee-Kyung Ahn, Bruno Pok Man Ngou, Jane E. Parker, and Jonathan D. G. Jones. 2023. 'Oligomerization of a Plant Helper NLR Requires Cell-Surface and Intracellular Immune Receptor Activation'. *Proceedings of the National Academy of Sciences* 120(11):e2210406120.

Fernández-Fernández, Álvaro Daniel, Simon Stael, and Frank Van Breusegem. 2023. 'Mechanisms Controlling Plant Proteases and Their Substrates.' *Cell Death and Differentiation* 30(4):1047–58.

Feys, B. J., L. J. Moisan, M. A. Newman, and J. E. Parker. 2001. 'Direct Interaction between the Arabidopsis Disease Resistance Signaling Proteins, EDS1 and PAD4.' *The EMBO Journal* 20(19):5400–5411.

Feys, Bart J., Marcel Wiermer, Riyaz A. Bhat, Lisa J. Moisan, Nieves Medina-Escobar, Christina Neu, Adriana Cabral, and Jane E. Parker. 2005. 'Arabidopsis SENESCENCE-ASSOCIATED GENE101 Stabilizes and Signals within an ENHANCED DISEASE SUSCEPTIBILITY1 Complex in Plant Innate Immunity'. *Plant Cell* 17(9):2601–13.

Fichman, Yosef, Ronald J. Myers, Deana G. Grant, and Ron Mittler. 2021. *Plasmodesmata-Localized Proteins and ROS Orchestrate Light-Induced Rapid Systemic Signaling in Arabidopsis*. Vol. 14.

Förderer, Alexander, Ertong Li, Aaron W. Lawson, Ya-nan Deng, Yue Sun, Elke Logemann, Xiaoxiao Zhang, Jie Wen, Zhifu Han, Junbiao Chang, Yuhang Chen, Paul Schulze-Lefert, and Jijie Chai. 2022. 'A Wheat Resistosome Defines Common Principles of Immune Receptor Channels'. *Nature* 610(7932):532–39.

Fu, Zheng Qing and Xinnian Dong. 2013. 'Systemic Acquired Resistance: Turning Local Infection into Global Defense'. 64(Volume 64, 2013):839–63.

Gantner, Johannes, Jana Ordon, Carola Kretschmer, Raphaël Guerois, and Johannes Stuttmann. 2019. 'An EDS1-SAG101 Complex Is Essential for TNL-Mediated Immunity in Nicotiana Benthamiana'. *The Plant Cell* 31(10):2456–74.

García, Ana V., Servane Blanvillain-Baufumé, Robin P. Huibers, Marcel Wiermer, Guangyong Li, Enrico Gobbato, Steffen Rietz, and Jane E. Parker. 2010. 'Balanced Nuclear and Cytoplasmic Activities of EDS1 Are Required for a Complete Plant Innate Immune Response'. *PLOS Pathogens* 6(7):e1000970.

Gaudet, Pascale, Rex Chisholm, Tanya Berardini, Emily Dimmer, Stacia R. Engel, Petra Fey, David P. Hill, Doug Howe, James C. Hu, Rachael Huntley, Varsha K. Khodiyar, Ranjana Kishore, Donghui Li, Ruth C. Lovering, Fiona McCarthy, Li Ni, Victoria Petri, Deborah A. Siegele, Susan Tweedie, Kimberly Van Auken, Valerie Wood, Siddhartha Basu, Seth Carbon, Mary Dolan, Christopher J. Mungall, Kara Dolinski, Paul Thomas, Michael Ashburner, Judith A. Blake, J. Michael Cherry, and Suzanna E. Lewis. 2009. 'The Gene Ontology's Reference Genome Project: A Unified Framework for Functional Annotation across Species'. *PLoS Computational Biology*.

Geng, Xueqing, Jiye Cheng, Anju Gangadharan, and David Mackey. 2012. 'The Coronatine Toxin of Pseudomonas Syringae Is a Multifunctional Suppressor of Arabidopsis Defense '. *The Plant Cell* 24(11):4763–74.

Glazebrook, J., M. Zook, F. Mert, I. Kagan, E. E. Rogers, I. R. Crute, E. B. Holub, R. Hammerschmidt, and F. M. Ausubel. 1997. 'Phytoalexin-Deficient Mutants of Arabidopsis Reveal That PAD4 Encodes a Regulatory Factor and That Four PAD Genes Contribute to Downy Mildew Resistance.' *Genetics* 146(1):381–92.

Goto, Yukihisa, Noriko Maki, Jan Sklenar, Paul Derbyshire, Frank L. H. Menke, Cyril Zipfel, Yasuhiro Kadota, and Ken Shirasu. 2024. 'The Phagocytosis Oxidase/Bem1p Domain-Containing Protein PB1CP Negatively Regulates the NADPH Oxidase RBOHD in Plant Immunity'. *New Phytologist* 241(4):1763–79.

Gottig, Natalia, Cecilia V Vranych, Germán G. Sgro, Ainelén Piazza, and Jorgelina Ottado. 2018. 'HrpE, the Major Component of the Xanthomonas Type Three Protein Secretion Pilus, Elicits Plant Immunity Responses'. *Scientific Reports* 8(1):9842.

Greenbaum, D., K. F. Medzihradszky, A. Burlingame, and M. Bogyo. 2000. 'Epoxide Electrophiles as Activity-Dependent Cysteine Protease Profiling and Discovery Tools.' *Chemistry & Biology* 7(8):569–81.

Grosse-Holz, Friederike, Luisa Madeira, Muhammad Awais Zahid, Molly Songer, Jiorgos Kourelis, Mary Fesenko, Sabrina Ninck, Farnusch Kaschani, Markus Kaiser, and Renier A. L. van der Hoorn. 2018. 'Three Unrelated Protease Inhibitors Enhance Accumulation of Pharmaceutical Recombinant Proteins in Nicotiana Benthamiana'. *Plant Biotechnology Journal* 16(10):1797–1810.

Hander, Tim, Álvaro D. Fernández-Fernández, Robert P. Kumpf, Patrick Willems, Hendrik Schatowitz, Debbie Rombaut, An Staes, Jonah Nolf, Robin Pottie, Panfeng Yao, Amanda Gonçalves, Benjamin Pavie, Thomas Boller, Kris Gevaert, Frank Van Breusegem, Sebastian Bartels, and Simon Stael. 2019. 'Damage on Plants Activates Ca2+-Dependent Metacaspases for Release of Immunomodulatory Peptides'. *Science* 363(6433):eaar7486.

Hartmann, Michael and Jürgen Zeier. 2019. 'N-Hydroxypipecolic Acid and Salicylic Acid: A Metabolic Duo for Systemic Acquired Resistance'. *Current Opinion in Plant Biology* 50:44–57.

Hartmann, Michael, Tatyana Zeier, Friederike Bernsdorff, Vanessa Reichel-Deland, Denis Kim, Michele Hohmann, Nicola Scholten, Stefan Schuck, Andrea Bräutigam, Torsten Hölzel, Christian Ganter, and Jürgen Zeier. 2018. 'Flavin Monooxygenase-Generated N-

Hydroxypipecolic Acid Is a Critical Element of Plant Systemic Immunity.' *Cell* 173(2):456-469.e16.

He, Zuhua, Shanice Webster, and Sheng Yang He. 2022. 'Growth–Defense Trade-Offs in Plants'. *Current Biology* 32(12):R634–39.

Heese, Antje, Dagmar R. Hann, Selena Gimenez-Ibanez, Alexandra M. E. Jones, Kai He, Jia Li, Julian I. Schroeder, Scott C. Peck, and John P. Rathjen. 2007. 'The Receptor-like Kinase SERK3/BAK1 Is a Central Regulator of Innate Immunity in Plants'. *Proceedings of the National Academy of Sciences* 104(29):12217–22.

Henry, Elizabeth, Nicholas Fung, Jun Liu, Georgia Drakakaki, and Gitta Coaker. 2015. 'Beyond Glycolysis: GAPDHs Are Multi-Functional Enzymes Involved in Regulation of ROS, Autophagy, and Plant Immune Responses'. *PLoS Genetics*.

Herold, Laura, Chenlei Hua, Bruce Kohorn, Thorsten Nürnberger, Thomas DeFalco, and Cyril Zipfel. 2024. 'Arabidopsis WALL-ASSOCIATED KINASES Are Not Required for Oligogalacturonide-Induced Signaling and Immunity'. *BioRxiv* 2024.04.15.589471.

Hinsch, M. and B. Staskawicz. 1996. 'Identification of a New Arabidopsis Disease Resistance Locus, RPs4, and Cloning of the Corresponding Avirulence Gene, AvrRps4, from Pseudomonas Syringae Pv. Pisi.' *Molecular Plant-Microbe Interactions : MPMI* 9(1):55–61.

Van Der Hoorn, Renier A. L. 2008. 'Plant Proteases: From Phenotypes to Molecular Mechanisms'. *Annu. Rev. Plant Biol.* 59(1):191–223.

Horsefield, Shane, Hayden Burdett, Xiaoxiao Zhang, Mohammad K. Manik, Yun Shi, Jian Chen, Tiancong Qi, Jonathan Gilley, Jhih-Siang Lai, Maxwell X. Rank, Lachlan W. Casey, Weixi Gu, Daniel J. Ericsson, Gabriel Foley, Robert O. Hughes, Todd Bosanac, Mark von Itzstein, John P. Rathjen, Jeffrey D. Nanson, Mikael Boden, Ian B. Dry, Simon J. Williams, Brian J. Staskawicz, Michael P. Coleman, Thomas Ve, Peter N. Dodds, and Bostjan Kobe. 2019. 'NAD+ Cleavage Activity by Animal and Plant TIR Domains in Cell Death Pathways'. *Science* 365(6455):793–99.

Hou, Shuguo, Derui Liu, Shijia Huang, Dexian Luo, Zunyong Liu, Qingyuan Xiang, Ping Wang, Ruimin Mu, Zhifu Han, Sixue Chen, Jijie Chai, Libo Shan, and Ping He. 2021. 'The Arabidopsis MIK2 Receptor Elicits Immunity by Sensing a Conserved Signature from Phytocytokines and Microbes.' *Nature Communications* 12(1):5494.

Howlader, Prianka, Santosh Kumar Bose, Xiaochen Jia, Chunlai Zhang, Wenxia Wang, and Heng Yin. 2020. 'Oligogalacturonides Induce Resistance in Arabidopsis Thaliana by Triggering Salicylic Acid and Jasmonic Acid Pathways against Pst DC3000'. *International Journal of Biological Macromolecules* 164:4054–64.

Huang, Shijia, Aolin Jia, Shoucai Ma, Yue Sun, Xiaoyu Chang, Zhifu Han, and Jijie Chai. 2023. 'NLR Signaling in Plants: From Resistosomes to Second Messengers'. *Trends in Biochemical Sciences* 48(9):776–87.

Huang, Shijia, Aolin Jia, Wen Song, Giuliana Hessler, Yonggang Meng, Yue Sun, Lina Xu, Henriette Laessle, Jan Jirschitzka, Shoucai Ma, Yu Xiao, Dongli Yu, Jiao Hou, Ruiqi Liu, Huanhuan Sun, Xiaohui Liu, Zhifu Han, Junbiao Chang, Jane E. Parker, and Jijie Chai. 2022. 'Identification and Receptor Mechanism of TIR-Catalyzed Small Molecules in Plant Immunity'. *Science* 377(6605).

Ivanova, Aneta, Mabel Gill-Hille, Shaobai Huang, Rui M. Branca, Beata Kmiec, Pedro F. Teixeira, Janne Lehtiö, James Whelan, and Monika W. Murcha. 2019. 'A Mitochondrial LYR Protein Is Required for Complex I Assembly1 [OPEN]'. *Plant Physiology* 181(4):1632–50.

Jacob, Pierre, Junko Hige, and Jeffery L. Dangl. 2023. 'Is Localized Acquired Resistance the Mechanism for Effector-Triggered Disease Resistance in Plants?' *Nature Plants* 9(8):1184–90.

Jacob, Pierre, Hyun Kim, Feihua Wu, Farid El-Kasmi, William G. Walton, Oliver J. Furzer, Adam D. Lietzen, Sruthi Sunil, Korina Kempthorn, Matthew R. Redinbo, Zhen-Ming Pei, Li Wan, and Jeffery L. Dangl. n.d. 'The Plant Immune Receptors NRG1.1 and ADR1 Are Calcium Influx Channels'.

Jia, Aolin, Shijia Huang, Wen Song, Junli Wang, Yonggang Meng, Yue Sun, Lina Xu, Henriette Laessle, Jan Jirschitzka, Jiao Hou, Tiantian Zhang, Wenquan Yu, Giuliana Hessler, Ertong Li, Shoucai Ma, Dongli Yu, Jan Gebauer, Ulrich Baumann, Xiaohui Liu, Zhifu Han, Junbiao Chang, Jane E. Parker, and Jijie Chai. 2022. 'TIR-Catalyzed ADP-Ribosylation Reactions Produce Signaling Molecules for Plant Immunity'. *Science* 377(6605):eabq8180.

Jia, Xiaochen, Haihong Zeng, Wenxia Wang, Fuyun Zhang, and Heng Yin. 2018. 'Chitosan Oligosaccharide Induces Resistance to Pseudomonas Syringae Pv. Tomato DC3000 in Arabidopsis Thaliana by Activating Both Salicylic Acid– and Jasmonic Acid–Mediated Pathways'. *Molecular Plant-Microbe Interactions*® 31(12):1271–79.

Jin, Jing-Hao, Xue Zhou, Wang Liu, Zi-Hui Zhang, Shen-Xin Huang, Wen-Jing Zhao, and Xiao-Ren Chen. 2023. 'Influence of Affinity Tags and Tobacco PR1a Signal Peptide on Detection, Purification and Bioactivity Analyses of the Small Oomycete Apoplastic Effectors'. *Biotechnology Letters* 45(1):115–24.

Johanndrees, Oliver, Erin L. Baggs, Charles Uhlmann, Federica Locci, Henriette L. Läßle, Katharina Melkonian, Kiara Käufer, Joram A. Dongus, Hirofumi Nakagami, Ksenia V Krasileva, Jane E. Parker, and Dmitry Lapin. 2023. 'Variation in Plant Toll/Interleukin-1 Receptor Domain Protein Dependence on ENHANCED DISEASE SUSCEPTIBILITY 1'. *Plant Physiology* 191(1):626–42.

Jones, Alexandra Me, John Mansfield, and Murray Grant. 2007. 'Considerations on Post-Translational Modification and Protein Targeting in the Arabidopsis Defense Proteome.' *Plant Signaling & Behavior* 2(3):153–54.

Jones, Jonathan D. G. and Jeffery L. Dangl. 2006. 'The Plant Immune System'. *Nature* 444(7117):323–29.

Jones, Jonathan D. G., Brian J. Staskawicz, and Jeffery L. Dangl. 2024. 'The Plant Immune System: From Discovery to Deployment'. *Cell* 187(9):2095–2116.

Jones, Jonathan D. G., Russell E. Vance, and Jeffery L. Dangl. 2016. 'Intracellular Innate Immune Surveillance Devices in Plants and Animals'. *Science* 354(6316):aaf6395.

Kadota, Yasuhiro, Ken Shirasu, and Cyril Zipfel. 2015. 'Regulation of the NADPH Oxidase RBOHD During Plant Immunity'. *Plant and Cell Physiology* 56(8):1472–80.

Kadota, Yasuhiro, Jan Sklenar, Paul Derbyshire, Lena Stransfeld, Shuta Asai, Vardis Ntoukakis, Jonathan DG Jones, Ken Shirasu, Frank Menke, Alexandra Jones, and Cyril Zipfel. 2014. 'Direct Regulation of the NADPH Oxidase RBOHD by the PRR-Associated Kinase BIK1 during Plant Immunity'. *Molecular Cell* 54(1):43–55.

Kamoun, Sophien, Oliver Furzer, Jonathan D. G. Jones, Howard S. Judelson, Gul Shad Ali, Ronaldo J. D. Dalio, Sanjoy Guha Roy, Leonardo Schena, Antonios Zambounis, Franck Panabières, David Cahill, Michelina Ruocco, Andreia Figueiredo, Xiao-Ren Chen, Jon Hulvey, Remco Stam, Kurt Lamour, Mark Gijzen, Brett M. Tyler, Niklaus J. Grünwald, M. Shahid Mukhtar, Daniel F. A. Tomé, Mahmut Tör, Guido Van Den Ackerveken, John McDowell, Fouad Daayf, William E. Fry, Hannele Lindqvist-Kreuze, Harold J. G. Meijer, Benjamin Petre, Jean Ristaino, Kentaro Yoshida, Paul R. J. Birch, and Francine Govers.

2015. ‘The Top 10 Oomycete Pathogens in Molecular Plant Pathology’. *Molecular Plant Pathology* 16(4):413–34.

Katagiri, Fumiaki, Roger Thilmony, and Sheng Yang He. 2002. ‘The Arabidopsis Thaliana-Pseudomonas Syringae Interaction.’ *The Arabidopsis Book* 1:e0039.

Keogh, R. C., B. J. Deverall, and Stella McLeod. 1980. ‘Comparison of Histological and Physiological Responses to Phakopsora Pachyrhizi in Resistant and Susceptible Soybean’. *Transactions of the British Mycological Society* 74(2):329–33.

Kimura, Sachie, Kerri Hunter, Lauri Vaahtera, Huy Cuong Tran, Matteo Citterico, Aleksia Vaattovaara, Anne Rokka, Sara Christina Stolze, Anne Harzen, Lena Meißner, Maya Melina Tabea Wilkens, Thorsten Hamann, Masatsugu Toyota, Hirofumi Nakagami, and Michael Wrzaczek. 2020. ‘CRK2 and C-Terminal Phosphorylation of NADPH Oxidase RBOHD Regulate Reactive Oxygen Species Production in Arabidopsis’. *The Plant Cell* 32(4):1063–80.

Kobayashi, Michie, Hiroe Utsushi, Koki Fujisaki, Takumi Takeda, Tetsuro Yamashita, and Ryohei Terauchi. 2022. ‘A Jacalin-like Lectin Domain-Containing Protein of Sclerospora Graminicola Acts as an Apoplastic Virulence Effector in Plant-Oomycete Interactions.’ *Molecular Plant Pathology* 23(6):845–54.

Koizumi, Masahiro, Kazuko Yamaguchi-Shinozaki, Hideo Tsuji, and Kazuo Shinozaki. 1993. ‘Structure and Expression of Two Genes That Encode Distinct Drought-Inducible Cysteine Proteinases in Arabidopsis Thaliana’. *Gene* 129(2):175–82.

Koncz, Csaba and Jeff Schell. 1986. ‘The Promoter of TL-DNA Gene 5 Controls the Tissue-Specific Expression of Chimaeric Genes Carried by a Novel Type of Agrobacterium Binary Vector’. *Molecular and General Genetics MGG* 204(3):383–96.

Kourelis, Jiorgos, Mariana Schuster, Fatih Demir, Oliver Mattinson, Sonja Krauter, Parvinderdeep S. Kahlon, Ruby O’Grady, Samantha Royston, Ana Lucía Bravo-Cazar, Brian C. Mooney, Pitter F. Huesgen, Sophien Kamoun, and Renier A. L. van der Hoorn. 2024. ‘Bioengineering Secreted Proteases Converts Divergent Rcr3 Orthologs and Paralogs into Extracellular Immune Co-Receptors’. *The Plant Cell* 36(9):3260–76.

Krasileva, Ksenia V, Douglas Dahlbeck, and Brian J. Staskawicz. 2010. ‘Activation of an Arabidopsis Resistance Protein Is Specified by the in Planta Association of Its Leucine-Rich Repeat Domain with the Cognate Oomycete Effector ’. *The Plant Cell* 22(7):2444–58.

Krol, Elzbieta, Tobias Mentzel, Delphine Chinchilla, Thomas Boller, Georg Felix, Birgit Kemmerling, Sandra Postel, Michael Arents, Elena Jeworutzki, Khaled A. S. Al-Rasheid, Dirk Becker, and Rainer Hedrich. 2010. ‘Perception of the Arabidopsis Danger Signal Peptide 1 Involves the Pattern Recognition Receptor AtPEPR1 and Its Close Homologue AtPEPR2*’. *Journal of Biological Chemistry* 285(18):13471–79.

Lan, Wei, Weibo Ma, Shuai Zheng, Yuhao Qiu, Han Zhang, Haisen Lu, Yu Zhang, and Ying Miao. 2022. ‘Ubiquitome Profiling Reveals a Regulatory Pattern of UPL3 with UBP12 on Metabolic-Leaf Senescence’. *Life Science Alliance* 5(12):e202201492.

Lapin, Dmitry, Deepak D. Bhandari, and Jane E. Parker. 2020. ‘Origins and Immunity Networking Functions of EDS1 Family Proteins’. *Annual Review of Phytopathology* 58(1):1–24.

Lapin, Dmitry, Viera Kovacova, Xinhua Sun, Joram A. Dongus, Deepak Bhandari, Patrick Von Born, Jaqueline Bautor, Nina Guarneri, Jakub Rzemieniewski, Johannes Stuttmann, Andreas Beyer, and Jane E. Parker. 2019. ‘A Coevolved EDS1-SAG101-NRG1 Module Mediates Cell Death Signaling by TIR-Domain Immune Receptors’. *Plant Cell* 31(10):2430–55.

Lee, DongHyuk, Neeraj K. Lal, Zuh-Jyh Daniel Lin, Shisong Ma, Jun Liu, Bardo Castro, Tania Toruño, Savithramma P. Dinesh-Kumar, and Gitta Coaker. 2020. 'Regulation of Reactive Oxygen Species during Plant Immunity through Phosphorylation and Ubiquitination of RBOHD.' *Nature Communications* 11(1):1838.

Lee, Justin, Lennart Eschen-Lippold, Ines Lassowskat, Christoph Böttcher, and Dierk Scheel. 2015. 'Cellular Reprogramming through Mitogen-Activated Protein Kinases.' *Frontiers in Plant Science* 6:940.

Lee, Justin and Tina Romeis. 2022. 'An Epiphany for Plant Resistance Proteins and Its Impact on Calcium-Based Immune Signalling'. *New Phytologist* 234(3):769–72.

Li, Baohua, Allison Gaudinier, Michelle Tang, Mallorie Taylor-Teeples, Ngoc T. Nham, Cyrus Ghaffari, Darik Scott Benson, Margaret Steinmann, Jennifer A. Gray, Siobhan M. Brady, and Daniel J. Kliebenstein. 2014. 'Promoter-Based Integration in Plant Defense Regulation '. *Plant Physiology* 166(4):1803–20.

Li, Lei, Meng Li, Liping Yu, Zhaoyang Zhou, Xiangxiu Liang, Zixu Liu, Gaihong Cai, Liyan Gao, Xiaojuan Zhang, Yingchun Wang, She Chen, and Jian-Min Zhou. 2014. 'The FLS2-Associated Kinase BIK1 Directly Phosphorylates the NADPH Oxidase RbohD to Control Plant Immunity'. *Cell Host & Microbe* 15(3):329–38.

Li, Qiuyi, Jing Shao, Mingyu Luo, Desheng Chen, Dingzhong Tang, and Hua Shi. 2024. 'BRASSINOSTEROID-SIGNALING KINASE1 Associates with and Is Required for Cysteine Protease RESPONSE TO DEHYDRATION 19-Mediated Disease Resistance in Arabidopsis'. *Plant Science* 342:112033.

Li, Yujia, Jiao Xue, Feng Zhu Wang, Xiangjuan Huang, Ben Qiang Gong, Yuheng Tao, Wenzhong Shen, Kehan Tao, Nan Yao, Shi Xiao, Jian Min Zhou, and Jian Feng Li. 2022. 'Plasma Membrane-Nucleo-Cytoplasmic Coordination of a Receptor-like Cytoplasmic Kinase Promotes EDS1-Dependent Plant Immunity'. *Nature Plants 2022 8:7* 8(7):802–16.

Liang, Xiangxiu, Pingtao Ding, Kehui Lian, Jinlong Wang, Miaomiao Ma, Lin Li, Lei Li, Meng Li, Xiaojuan Zhang, She Chen, Yuelin Zhang, and Jian-Min Zhou. 2016. 'Arabidopsis Heterotrimeric G Proteins Regulate Immunity by Directly Coupling to the FLS2 Receptor' edited by T. Nürnberger. *ELife* 5:e13568.

Lin, Zuh-Jyh Daniel, Thomas W. H. Liebrand, Koste A. Yadeta, and Gitta Coaker. 2015. 'PBL13 Is a Serine/Threonine Protein Kinase That Negatively Regulates Arabidopsis Immune Responses '. *Plant Physiology* 169(4):2950–62.

van der Linde, Karina, Christoph Hemetsberger, Christine Kastner, Farnusch Kaschani, Renier A. L. van der Hoorn, Jochen Kumlehn, and Gunther Doehlemann. 2012. 'A Maize Cystatin Suppresses Host Immunity by Inhibiting Apoplastic Cysteine Proteases.' *The Plant Cell* 24(3):1285–1300.

Liu, Yanan, Edan Jackson, Xueru Liu, Xingchuan Huang, Renier A. L. van der Hoorn, Yuelin Zhang, and Xin Li. 2024. 'Proteolysis in Plant Immunity'. *The Plant Cell* koae142.

Liu, Yang, Tingting Gong, Xiangjiu Kong, Jiaqi Sun, and Lijing Liu. 2023. 'XYLEM CYSTEINE PEPTIDASE 1 and Its Inhibitor CYSTATIN 6 Regulate 2 Pattern-Triggered Immunity by Modulating the Stability of the NADPH Oxidase Short Title: XCP1 and CYS6 Control the Stability of RBOHD'.

Locci, Federica and Jane E. Parker. 2024. 'Plant NLR Immunity Activation and Execution: A Biochemical Perspective.' *Open Biology* 14(1):230387.

Locci, Federica, Junli Wang, and Jane E. Parker. 2023. 'TIR-Domain Enzymatic Activities at the Heart of Plant Immunity'. *Current Opinion in Plant Biology* 74.

Logemann, Elke, Rainer P. Birkenbihl, Bekir Ülker, and Imre E. Somssich. 2006. 'An Improved Method for Preparing Agrobacterium Cells That Simplifies the Arabidopsis Transformation Protocol.' *Plant Methods* 2:16.

Lozano-Durán, Rosa and Cyril Zipfel. 2015. 'Trade-off between Growth and Immunity: Role of Brassinosteroids'. *Trends in Plant Science* 20(1):12–19.

Ma, Shoucai, Dmitry Lapin, Li Liu, Yue Sun, Wen Song, Xiaoxiao Zhang, Elke Logemann, Dongli Yu, Jia Wang, Jan Jirschitzka, Zhifu Han, Paul Schulze-Lefert, Jane E. Parker, and Jijie Chai. 2020. 'Direct Pathogen-Induced Assembly of an NLR Immune Receptor Complex to Form a Holoenzyme'. *Science* 370(6521):eabe3069.

Mangeon, Amanda, Renan Pardal, Adriana Dias Menezes-Salgueiro, Guilherme Leitão Duarte, Ricardo de Seixas, Fernanda P. Cruz, Vanessa Cardeal, Claudia Magioli, Felipe Klein Ricachenevsky, Rogério Margis, and Gilberto Sachetto-Martins. 2016. 'AtGRP3 Is Implicated in Root Size and Aluminum Response Pathways in Arabidopsis.' *PloS One* 11(3):e0150583.

Martin, Raoul, Tiancong Qi, Haibo Zhang, Furong Liu, Miles King, Claire Toth, Eva Nogales, and Brian J. Staskawicz. 2020. 'Structure of the Activated ROQ1 Resistosome Directly Recognizing the Pathogen Effector XopQ.' *Science (New York, N.Y.)* 370(6521).

Martin, Raoul, Tiancong Qi, Haibo Zhang, Furong Liu, Miles King, Claire Toth, and Brian J. Staskawicz. n.d. 'Structure of the Activated Roq1 Resistosome Directly Recognizing the Pathogen Effector XopQ'.

Mazars, Christian, Patrice Thuleau, Olivier Lamotte, and Stéphane Bourque. 2010. 'Cross-Talk between ROS and Calcium in Regulation of Nuclear Activities'. *Molecular Plant* 3(4):706–18.

McBride, Zachary, Donglai Chen, Christy Reick, Jun Xie, and Daniel B. Szymanski. 2017. 'Global Analysis of Membrane-Associated Protein Oligomerization Using Protein Correlation Profiling*'. *Molecular & Cellular Proteomics* 16(11):1972–89.

Melkonian, Katharina, Sara Christina Stolze, Anne Harzen, and Hirofumi Nakagami. 2022. 'MiniTurbo-Based Interactomics of Two Plasma Membrane-Localized SNARE Proteins in Marchantia Polymorpha'. *New Phytologist* 235(2):786–800.

Melotto, Maeli, William Underwood, Jessica Koczan, Kinya Nomura, and Sheng Yang He. 2006. 'Plant Stomata Function in Innate Immunity against Bacterial Invasion'. *Cell* 126(5):969–80.

Miller, Gad, Karen Schlauch, Rachel Tam, Diego Cortes, Miguel A. Torres, Vladimir Shulaev, Jeffery L. Dangl, and Ron Mittler. 2009. 'The Plant NADPH Oxidase RBOHD Mediates Rapid Systemic Signaling in Response to Diverse Stimuli'. *Science Signaling* 2(84):ra45–ra45.

Misas-Villamil, Johana C., Renier A. L. van der Hoorn, and Gunther Doehlemann. 2016. 'Papain-like Cysteine Proteases as Hubs in Plant Immunity'. *New Phytologist* 212(4):902–7.

Monaghan, Jacqueline and Cyril Zipfel. 2012. 'Plant Pattern Recognition Receptor Complexes at the Plasma Membrane'. *Current Opinion in Plant Biology* 15(4):349–57.

Monson, Russell K., Amy M. Trowbridge, Richard L. Lindroth, and Manuel T. Lerdau. 2022. 'Coordinated Resource Allocation to Plant Growth–Defense Tradeoffs'. *New Phytologist* 233(3):1051–66.

Monteiro, Freddy and Marc T. Nishimura. 2018. 'Structural, Functional, and Genomic Diversity of Plant NLR Proteins: An Evolved Resource for Rational Engineering of Plant Immunity.' *Annual Review of Phytopathology* 56:243–67.

Morimoto, Kyoko and Renier A. L. Van Der Hoorn. 2016. 'The Increasing Impact of Activity-Based Protein Profiling in Plant Science'. *Plant and Cell Physiology* 57(3):446–61.

Mühlenbeck, Henning, Yuko Tsutsui, Mark A. Lemmon, Kyle W. Bender, and Cyril Zipfel. 2023. 'Allosteric Activation of the Co-Receptor BAK1 by the EFR Receptor Kinase Initiates Immune Signaling'.

Myers Jr, Ronald J., Yosef Fichman, Sara I. Zandalinas, and Ron Mittler. 2023. 'Jasmonic Acid and Salicylic Acid Modulate Systemic Reactive Oxygen Species Signaling during Stress Responses'. *Plant Physiology* 191(2):862–73.

Návarová, Hana, Friederike Bernsdorff, Anne-Christin Döring, and Jürgen Zeier. 2012. 'Pipecolic Acid, an Endogenous Mediator of Defense Amplification and Priming, Is a Critical Regulator of Inducible Plant Immunity'. *The Plant Cell* 24(12):5123–41.

Ngou, Bruno Pok Man, Hee Kyung Ahn, Pingtao Ding, and Jonathan D. G. Jones. 2021. 'Mutual Potentiation of Plant Immunity by Cell-Surface and Intracellular Receptors'. *Nature* 592(7852):110–15.

Ngou, Bruno Pok Man, Pingtao Ding, and Jonathan D. G. Jones. 2022. 'Thirty Years of Resistance: Zig-Zag through the Plant Immune System'. *The Plant Cell* 34(5):1447–78.

Nühse, Thomas S., Andrew R. Bottrill, Alexandra M. E. Jones, and Scott C. Peck. 2007. 'Quantitative Phosphoproteomic Analysis of Plasma Membrane Proteins Reveals Regulatory Mechanisms of Plant Innate Immune Responses'. *The Plant Journal* 51(5):931–40.

Oda, Takashi, Hiroshi Hashimoto, Naoyuki Kuwabara, Satoko Akashi, Kokoro Hayashi, Chojiro Kojima, Hann Ling Wong, Tsutomu Kawasaki, Ko Shimamoto, Mamoru Sato, and Toshiyuki Shimizu. 2010. 'Structure of the N-Terminal Regulatory Domain of a Plant NADPH Oxidase and Its Functional Implications * '. *Journal of Biological Chemistry* 285(2):1435–45.

Ogasawara, Yoko, Hidetaka Kaya, Goro Hiraoka, Fumiaki Yumoto, Sachie Kimura, Yasuhiro Kadota, Haruka Hishinuma, Eriko Senzaki, Satoshi Yamagoe, Koji Nagata, Masayuki Nara, Kazuo Suzuki, Masaru Tanokura, and Kazuyuki Kuchitsu. 2008. 'Synergistic Activation of the Arabidopsis NADPH Oxidase AtrbohD by Ca2+ and Phosphorylation.' *The Journal of Biological Chemistry* 283(14):8885–92.

Ono, Erika, Kazuyuki Mise, and Yoshitaka Takano. 2020. 'RLP23 Is Required for Arabidopsis Immunity against the Grey Mould Pathogen Botrytis Cinerea'. *Scientific Reports* 10(1):13798.

Oosawa, Naoki, Tatsuru Masuda, Koichiro Awai, Naoki Fusada, Hiroshi Shimada, Hiroyuki Ohta, and Ken-ichiro Takamiya. 2000. 'Identification and Light-Induced Expression of a Novel Gene of NADPH-Protochlorophyllide Oxidoreductase Isoform in Arabidopsis Thaliana'. *FEBS Letters* 474(2–3):133–36.

Ordon, Jana, Johannes Gantner, Jan Kemna, Lennart Schwalgun, Maik Reschke, Jana Streubel, Jens Boch, and Johannes Stuttmann. 2017. 'Generation of Chromosomal Deletions in Dicotyledonous Plants Employing a User-Friendly Genome Editing Toolkit'. *The Plant Journal* 89(1):155–68.

Orosa, Beatriz, Gary Yates, Vivek Verma, Anjil K. Srivastava, Moumita Srivastava, Alberto Campanaro, Daniel De Vega, Alanna Fernandes, Cunjin Zhang, Jack Lee, Malcolm J. Bennett, and Ari Sadanandom. 2018. 'SUMO Conjugation to the Pattern Recognition Receptor FLS2 Triggers Intracellular Signalling in Plant Innate Immunity'. *Nature Communications* 9(1):5185.

Paireder, Melanie, Ulrich Mehofer, Stefan Tholen, Andreas Porodko, Philipp Schähs, Daniel

Maresch, Martin L. Biniossek, Renier A. L. van der Hoorn, Brigita Lenarcic, Marko Novinec, Oliver Schilling, and Lukas Mach. 2016. 'The Death Enzyme CP14 Is a Unique Papain-like Cysteine Proteinase with a Pronounced S2 Subsite Selectivity'. *Archives of Biochemistry and Biophysics* 603:110–17.

Paireder, Melanie, Stefan Tholen, Andreas Porodko, Martin L. Biniossek, Bettina Mayer, Marko Novinec, Oliver Schilling, and Lukas Mach. 2017. 'The Papain-like Cysteine Proteinases NbCysP6 and NbCysP7 Are Highly Processive Enzymes with Substrate Specificities Complementary to Nicotiana Benthamiana Cathepsin B'. *Biochimica et Biophysica Acta (BBA)-Proteins and Proteomics* 1865(4):444–52.

Park, Ae Ran, Somi K. Cho, Ui Jeong Yun, Mi Young Jin, Seoung Hyun Lee, Gilberto Sachetto-Martins, and Ohkmae K. Park. 2001. 'Interaction of the Arabidopsis Receptor Protein Kinase Wak1 with a Glycine-Rich Protein, AtGRP-3*'. *Journal of Biological Chemistry* 276(28):26688–93.

Parker, J. E., E. B. Holub, L. N. Frost, A. Falk, N. D. Gunn, and M. J. Daniels. 1996. 'Characterization of Eds1, a Mutation in Arabidopsis Suppressing Resistance to Peronospora Parasitica Specified by Several Different RPP Genes.' *The Plant Cell* 8(11):2033–46.

Parker, Jane E., Giuliana Hessler, and Haitao Cui. 2021. 'A New Biochemistry Connecting Pathogen Detection to Induced Defense in Plants'. *New Phytologist* n/a(n/a).

Paulus, Judith K. and Renier A. L. Van der Hoorn. 2019. 'Do Proteolytic Cascades Exist in Plants?' *Journal of Experimental Botany* 70(7):1997–2002.

Paulus, Judith K., Jiorgos Kourelis, Selva Ramasubramanian, Felix Homma, Alice Godson, Anja C. Hörger, Tram Ngoc Hong, Daniel Krahn, Laura Ossorio Carballo, Shuaishuai Wang, Joe Win, Matthew Smoker, Sophien Kamoun, Suomeng Dong, and Renier A. L. van der Hoorn. 2020. 'Extracellular Proteolytic Cascade in Tomato Activates Immune Protease Rcr3'. *Proceedings of the National Academy of Sciences* 117(29):17409–17.

Pruitt, Rory N., Federica Locci, Friederike Wanke, Lisha Zhang, Svenja C. Saile, Anna Joe, Darya Karelina, Chenlei Hua, Katja Fröhlich, Wei-Lin Wan, Meijuan Hu, Shaofei Rao, Sara C. Stolze, Anne Harzen, Andrea A. Gust, Klaus Harter, Matthieu H. A. J. Joosten, Bart P. H. J. Thomma, Jian-Min Zhou, Jeffery L. Dangl, Detlef Weigel, Hirofumi Nakagami, Claudia Oecking, Farid El Kasmi, Jane E. Parker, and Thorsten Nürnberger. 2021. 'The EDS1–PAD4–ADR1 Node Mediates Arabidopsis Pattern-Triggered Immunity'. *Nature* 598(7881):495–99.

Qi, Fan, Jianwei Li, Yingfei Ai, Keke Shangguan, Ping Li, Fucheng Lin, and Yan Liang. 2024. 'DGK5β-Derived Phosphatidic Acid Regulates ROS Production in Plant Immunity by Stabilizing NADPH Oxidase'. *Cell Host & Microbe* 32(3):425-440.e7.

Qi, Junsheng, Jinlong Wang, Zhizhong Gong, and Jian-Min Zhou. 2017. 'Apoplastic ROS Signaling in Plant Immunity'. *Current Opinion in Plant Biology* 38:92–100.

Qi, Tiancong, Kyungyong Seong, Daniela P. T. Thomazella, Joonyoung Ryan Kim, Julie Pham, Eunyoung Seo, Myeong-Je Cho, Alex Schultink, and Brian J. Staskawicz. 2018. 'NRG1 Functions Downstream of EDS1 to Regulate TIR-NLR-Mediated Plant Immunity in Nicotiana Benthamiana.' *Proceedings of the National Academy of Sciences of the United States of America* 115(46):E10979–87.

Racine, Jeffrey S. 2012. 'RStudio: A Platform-Independent IDE for R and Sweave'. *Journal of Applied Econometrics* 27(1):167–72.

Rappsilber, Juri, Yasushi Ishihama, and Matthias Mann. 2003. 'Stop and Go Extraction Tips for Matrix-Assisted Laser Desorption/Ionization, Nanoelectrospray, and LC/MS Sample Pretreatment in Proteomics'. *Analytical Chemistry* 75(3):663–70.

Rawlings, Neil D., Alan J. Barrett, Paul D. Thomas, Xiaosong Huang, Alex Bateman, and Robert D. Finn. 2018. 'The MEROPS Database of Proteolytic Enzymes, Their Substrates and Inhibitors in 2017 and a Comparison with Peptidases in the PANTHER Database'. *Nucleic Acids Research* 46(D1):D624–32.

Reinhardt, Hagen, Charles Hachez, Manuela Désirée Bienert, Azeez Beebo, Kamal Swarup, Ute Voß, Karim Bouhidel, Lorenzo Frigerio, Jan K. Schjoerring, Malcolm J. Bennett, and Francois Chaumont. 2016. 'Tonoplast Aquaporins Facilitate Lateral Root Emergence '. *Plant Physiology* 170(3):1640–54.

Rhodes, Jack, Huanjie Yang, Steven Moussu, Freddy Boutrot, Julia Santiago, and Cyril Zipfel. 2021. 'Perception of a Divergent Family of Phytocytokines by the Arabidopsis Receptor Kinase MIK2'. *Nature Communications* 12(1):705.

Richau, Kerstin H., Farnusch Kaschani, Martijn Verdoes, Twinkal C. Pansuriya, Sherry Niessen, Kurt Stüber, Tom Colby, Hermen S. Overkleeft, Matthew Bogyo, and Renier A. L. van der Hoorn. 2012. 'Subclassification and Biochemical Analysis of Plant Papain-like Cysteine Proteases Displays Subfamily-Specific Characteristics'. *Plant Physiology* 158(4):1583–99.

Rietz, Steffen, Anika Stamm, Stefan Malonek, Stephan Wagner, Dieter Becker, Nieves Medina-Escobar, A. Corina Vlot, Bart J. Feys, Karsten Niefind, and Jane E. Parker. 2011. 'Different Roles of Enhanced Disease Susceptibility1 (EDS1) Bound to and Dissociated from Phytoalexin Deficient4 (PAD4) in Arabidopsis Immunity.' *The New Phytologist* 191(1):107–19.

Ritchie, Matthew E., Belinda Phipson, Di Wu, Yifang Hu, Charity W. Law, Wei Shi, and Gordon K. Smyth. 2015. 'Limma Powers Differential Expression Analyses for RNA-Sequencing and Microarray Studies.' *Nucleic Acids Research* 43(7):e47.

Robinson, Mark D., Davis J. McCarthy, and Gordon K. Smyth. 2010. 'EdgeR: A Bioconductor Package for Differential Expression Analysis of Digital Gene Expression Data'. *Bioinformatics* 26(1):139–40.

Rojo, Enrique, Raquel Martín, Clay Carter, Jan Zouhar, Songqin Pan, Julia Plotnikova, Hailing Jin, Manuel Paneque, José Juan Sánchez-Serrano, Barbara Baker, Frederick M. Ausubel, and Natasha V Raikhel. 2004. 'VPEγ Exhibits a Caspase-like Activity That Contributes to Defense against Pathogens'. *Current Biology* 14(21):1897–1906.

Roussin-Léveillée, Charles, Méliane St-Amand, Philippe Desbiens-Fortin, Rosaëlle Perreault, Antoine Pelletier, Sabrina Gauthier, Faye Gaudreault-Lafleur, Isabelle Laforest-Lapointe, and Peter Moffett. 2024. 'Chloroplastic ROS Bursts Initiate Salicylic Acid Biosynthesis in Plant Immunity'. *BioRxiv* 2024.08.26.609370.

Rzemieniewski, Jakub and Martin Stegmann. 2022. 'Regulation of Pattern-Triggered Immunity and Growth by Phytocytokines'. *Current Opinion in Plant Biology* 68:102230.

Saile, Svenja C., Frank M. Ackermann, Sruthi Sunil, Jutta Keicher, Adam Bayless, Vera Bonardi, Li Wan, Mehdi Doumane, Eva Stöbbe, Yvon Jaillais, Marie Cécile Caillaud, Jeffery L. Dangl, Marc T. Nishimura, Claudia Oecking, and Farid El Kasmi. 2021. 'Arabidopsis ADR1 Helper NLR Immune Receptors Localize and Function at the Plasma Membrane in a Phospholipid Dependent Manner'. *New Phytologist* 232(6):2440–56.

Saile, Svenja C., Pierre Jacob, Baptiste Castel, Lance M. Jubic, Isai Salas-Gonzáles, Marcel Bäcker, Jonathan D. G. Jones, Jeffery L. Dangl, and Farid El Kasmi. 2020. 'Two Unequally Redundant "Helper" Immune Receptor Families Mediate Arabidopsis Thaliana Intracellular "Sensor" Immune Receptor Functions'. *PLoS Biology* 18(9).

Schilling, Oliver, Pitter F. Huesgen, Olivier Barré, Ulrich auf dem Keller, and Christopher M. Overall. 2011. 'Characterization of the Prime and Non-Prime Active Site Specificities of

Proteases by Proteome-Derived Peptide Libraries and Tandem Mass Spectrometry'. *Nature Protocols* 6(1):111–20.

Schindelin, Johannes, Ignacio Arganda-Carreras, Erwin Frise, Verena Kaynig, Mark Longair, Tobias Pietzsch, Stephan Preibisch, Curtis Rueden, Stephan Saalfeld, Benjamin Schmid, Jean-Yves Tinevez, Daniel James White, Volker Hartenstein, Kevin Eliceiri, Pavel Tomancak, and Albert Cardona. 2012. 'Fiji: An Open-Source Platform for Biological-Image Analysis.' *Nature Methods* 9(7):676–82.

Schnake, Anika, Michael Hartmann, Stefan Schreiber, Jana Malik, Lisa Brahmann, Ipek Yildiz, Janina von Dahlen, Laura E. Rose, Ulrich Schaffrath, and Jürgen Zeier. 2020. 'Inducible Biosynthesis and Immune Function of the Systemic Acquired Resistance Inducer N-Hydroxypipecolic Acid in Monocotyledonous and Dicotyledonous Plants'. *Journal of Experimental Botany* 71(20):6444–59.

Schultink, Alex, Tiancong Qi, Arielle Lee, Adam D. Steinbrenner, and Brian Staskawicz. 2017. 'Roq1 Mediates Recognition of the Xanthomonas and Pseudomonas Effector Proteins XopQ and HopQ1.' *The Plant Journal : For Cell and Molecular Biology* 92(5):787–95.

Schulze, Sarina, Liping Yu, Chenlei Hua, Lisha Zhang, Dagmar Kolb, Hannah Weber, Alexandra Ehinger, Svenja C. Saile, Mark Stahl, Mirita Franz-Wachtel, Lei Li, Farid El Kasmi, Thorsten Nürnberger, Volkan Cevik, and Birgit Kemmerling. 2022. 'The Arabidopsis TIR-NBS-LRR Protein CSA1 Guards BAK1-BIR3 Homeostasis and Mediates Convergence of Pattern- and Effector-Induced Immune Responses.' *Cell Host & Microbe* 30(12):1717-1731.e6.

Seybold, Heike, Fabian Trempel, Stefanie Ranf, Dierk Scheel, Tina Romeis, and Justin Lee. 2014. 'Ca2+ Signalling in Plant Immune Response: From Pattern Recognition Receptors to Ca2+ Decoding Mechanisms.' *The New Phytologist* 204(4):782–90.

Shi, Hua, Qiujing Shen, Yiping Qi, Haojie Yan, Haozhen Nie, Yongfang Chen, Ting Zhao, Fumiaki Katagiri, and Dingzhong Tang. 2013. 'BR-SIGNALING KINASE1 Physically Associates with FLAGELLIN SENSING2 and Regulates Plant Innate Immunity in Arabidopsis.' *The Plant Cell* 25(3):1143–57.

Singh, Archana, Amit Kumar, Sunita Yadav, and Indrakant Kumar Singh. 2019. 'Reactive Oxygen Species-Mediated Signaling during Abiotic Stress'. *Plant Gene* 18:100173.

Singh, Rachana, Parul Parihar, Samiksha Singh, Rohit Kumar Mishra, Vijay Pratap Singh, and Sheo Mohan Prasad. 2017. 'Reactive Oxygen Species Signaling and Stomatal Movement: Current Updates and Future Perspectives'. *Redox Biology* 11:213–18.

Soto, Débora, Juan Pablo Córdoba, Fernando Villarreal, Carlos Bartoli, Jessica Schmitz, Veronica G. Maurino, Hans Peter Braun, Gabriela C. Pagnussat, and Eduardo Zabaleta. 2015. 'Functional Characterization of Mutants Affected in the Carbonic Anhydrase Domain of the Respiratory Complex I in Rabidopsis Thaliana'. *The Plant Journal* 83(5):831–44.

Spoel, Steven H. and Xinnian Dong. 2008. 'Making Sense of Hormone Crosstalk during Plant Immune Responses'. *Cell Host & Microbe* 3(6):348–51.

Stockert, Fabian, Henrique Baeta, and Pitter F. B. T. Methods in Enzymology Huesgen. 2024. 'Analysis of Mitochondrial Targeting Signal Cleavage and Protein Processing by Mass Spectrometry'. Academic Press.

Sun, Xinhua, Dmitry Lapin, Joanna M. Feehan, Sara C. Stolze, Katharina Kramer, Joram A. Dongus, Jakub Rzemieniewski, Servane Blanvillain-Baufumé, Anne Harzen, Jaqueline Bautor, Paul Derbyshire, Frank L. H. Menke, Iris Finkemeier, Hirofumi Nakagami, Jonathan D. G. Jones, and Jane E. Parker. 2021. 'Pathogen Effector Recognition-

Dependent Association of NRG1 with EDS1 and SAG101 in TNL Receptor Immunity'. *Nature Communications* 12(1).

Sun, Yadong, Zhifu Han, Jiao Tang, Zehan Hu, Chengliang Chai, Bin Zhou, and Jijie Chai. 2013. 'Structure Reveals That BAK1 as a Co-Receptor Recognizes the BRI1-Bound Brassinolide'. *Cell Research* 23(11):1326–29.

Suzuki, Nobuhiro, Gad Miller, Jorge Morales, Vladimir Shulaev, Miguel Angel Torres, and Ron Mittler. 2011. 'Respiratory Burst Oxidases: The Engines of ROS Signaling'. *Current Opinion in Plant Biology* 14(6):691–99.

Tamborski, Janina and Ksenia V Krasileva. 2020. 'Evolution of Plant NLRs: From Natural History to Precise Modifications.' *Annual Review of Plant Biology* 71:355–78.

Tang, Bozeng, Li Feng, Michelle T. Hulin, Pingtao Ding, and Wenbo Ma. 2023. 'Cell-Type-Specific Responses to Fungal Infection in Plants Revealed by Single-Cell Transcriptomics'. *Cell Host & Microbe* 31(10):1732-1747.e5.

Tang, Wenqiang, Tae-Wuk Kim, Juan A. Oses-Prieto, Yu Sun, Zhiping Deng, Shengwei Zhu, Ruiju Wang, Alma L. Burlingame, and Zhi-Yong Wang. 2008. 'BSKs Mediate Signal Transduction from the Receptor Kinase BRI1 in Arabidopsis'. *Science* 321(5888):557–60.

Tian, Hainan, Zhongshou Wu, Siyu Chen, Kevin Ao, Weijie Huang, Hoda Yaghmaiean, Tongjun Sun, Fang Xu, Yanjun Zhang, Shucai Wang, Xin Li, and Yuelin Zhang. 2021. 'Activation of TIR Signalling Boosts Pattern-Triggered Immunity'. *Nature* 598(7881):500–503.

Tian, Shan, Xiaobing Wang, Ping Li, Hao Wang, Hongtao Ji, Junyi Xie, Qinglei Qiu, Dan Shen, and Hansong Dong. 2016. 'Plant Aquaporin AtPIP1;4 Links Apoplastic H2O2 Induction to Disease Immunity Pathways.' *Plant Physiology* 171(3):1635–50.

Torres, Miguel Angel and Jeffery L. Dangl. 2005. 'Functions of the Respiratory Burst Oxidase in Biotic Interactions, Abiotic Stress and Development'. *Current Opinion in Plant Biology* 8(4):397–403.

Torres, Miguel Angel, Jeffery L. Dangl, and Jonathan D. G. Jones. 2002. 'Arabidopsis Gp91phox Homologues Atrbohd and Atrbohf Are Required for Accumulation of Reactive Oxygen Intermediates in the Plant Defense Response'. *Proceedings of the National Academy of Sciences of the United States of America* 99(1):517–22.

Torres, Miguel Angel, Jonathan D. G. Jones, and Jeffery L. Dangl. 2005. 'Pathogen-Induced, NADPH Oxidase–Derived Reactive Oxygen Intermediates Suppress Spread of Cell Death in Arabidopsis Thaliana'. *Nature Genetics* 37(10):1130–34.

Turk, D., M. Podobnik, T. Popovic, N. Katunuma, W. Bode, R. Huber, and V. Turk. 1995. 'Crystal Structure of Cathepsin B Inhibited with CA030 at 2.0-.ANG. Resolution: A Basis for the Design of Specific Epoxysuccinyl Inhibitors'. *Biochemistry* 34(14):4791–97.

Tyanova, Stefka, Tikira Temu, and Juergen Cox. 2016. 'The MaxQuant Computational Platform for Mass Spectrometry-Based Shotgun Proteomics'. *Nature Protocols* 11(12):2301–19.

Vercammen, Dominique, Brigitte van de Cotte, Geert De Jaeger, Dominique Eeckhout, Peter Casteels, Klaas Vandepoele, Isabel Vandenberghe, Jozef Van Beeumen, Dirk Inzé, and Frank Van Breusegem. 2004. 'Type II Metacaspases Atmc4 and Atmc9 of Arabidopsis Thaliana</Em> Cleave Substrates after Arginine and Lysine *'. *Journal of Biological Chemistry* 279(44):45329–36.

Voinnet, Olivier, Yvonne M. Pinto, and David C. Baulcombe. 1999. 'Suppression of Gene Silencing: A General Strategy Used by Diverse DNA and RNA Viruses of Plants'.

Proceedings of the National Academy of Sciences 96(24):14147–52.

Wagner, Stephan, Johannes Stuttmann, Steffen Rietz, Raphael Guerois, Elena Brunstein, Jaqueline Bautor, Karsten Niefind, and Jane E. Parker. 2013. 'Structural Basis for Signaling by Exclusive EDS1 Heteromeric Complexes with SAG101 or PAD4 in Plant Innate Immunity'. *Cell Host and Microbe* 14(6):619–30.

Wan, Li, Kow Essuman, Ryan G. Anderson, Yo Sasaki, Freddy Monteiro, Eui-Hwan Chung, Erin Osborne Nishimura, Aaron DiAntonio, Jeffrey Milbrandt, Jeffery L. Dangl, and Marc T. Nishimura. 2019. *TIR Domains of Plant Immune Receptors Are NAD +-Cleaving Enzymes That Promote Cell Death*.

Wan, Wei Lin, Katja Fröhlich, Rory N. Pruitt, Thorsten Nürnberger, and Lisha Zhang. 2019. 'Plant Cell Surface Immune Receptor Complex Signaling'. *Current Opinion in Plant Biology* 50:18–28.

Wan, Wei Lin, Lisha Zhang, Rory Pruitt, Maricris Zaidem, Rik Brugman, Xiyu Ma, Elzbieta Krol, Artemis Perraki, Joachim Kilian, Guido Grossmann, Mark Stahl, Libo Shan, Cyril Zipfel, Jan A. L. van Kan, Rainer Hedrich, Detlef Weigel, Andrea A. Gust, and Thorsten Nürnberger. 2019. 'Comparing Arabidopsis Receptor Kinase and Receptor Protein-Mediated Immune Signaling Reveals BIK1-Dependent Differences'. *New Phytologist* 221(4):2080–95.

Wang, Chao and Sheng Luan. 2024. 'Calcium Homeostasis and Signaling in Plant Immunity'. *Current Opinion in Plant Biology* 77:102485.

Wang, Hanling, Susheng Song, Shang Gao, Qiangsheng Yu, Haibo Zhang, Xiulin Cui, Jun Fan, Xiufang Xin, Yule Liu, Brian Staskawicz, and Tiancong Qi. 2024. 'The NLR Immune Receptor ADR1 and Lipase-like Proteins EDS1 and PAD4 Mediate Stomatal Immunity in Nicotiana Benthamiana and Arabidopsis'. *The Plant Cell* 36(2):427–46.

Wang, Jizong, Meijuan Hu, Jia Wang, Jinfeng Qi, Zhifu Han, Guoxun Wang, Yijun Qi, Hong-Wei Wang, Jian-Min Zhou, and Jijie Chai. 2019. 'Reconstitution and Structure of a Plant NLR Resistosome Conferring Immunity'. *Science* 364(6435):eaav5870.

Wang, Jizong, Jia Wang, Meijuan Hu, Shan Wu, Jinfeng Qi, Guoxun Wang, Zhifu Han, Yijun Qi, Ning Gao, Hong-Wei Wang, Jian-Min Zhou, and Jijie Chai. 2019. 'Ligand-Triggered Allosteric ADP Release Primes a Plant NLR Complex'. *Science* 364(6435):eaav5868.

Wang, Yiming, Ruben Garrido-Oter, Jingni Wu, Thomas M. Winkelmüller, Matthew Agler, Thomas Colby, Tatsuya Nobori, Eric Kemen, and Kenichi Tsuda. 2019. 'Site-Specific Cleavage of Bacterial MucD by Secreted Proteases Mediates Antibacterial Resistance in Arabidopsis'. *Nature Communications* 10(1):2853.

Wang, Zaiqing, Xiaoxiao Liu, Jie Yu, Shuining Yin, Wenjuan Cai, Nak Hyun Kim, Farid El Kasmi, Jeffery L. Dangl, and Li Wan. 2023. 'Plasma Membrane Association and Resistosome Formation of Plant Helper Immune Receptors'. *Proceedings of the National Academy of Sciences* 120(32):e2222036120.

Weng, Samuel S. H., Fatih Demir, Enes K. Ergin, Sabrina Dirnberger, Anuli Uzozie, Domenic Tuscher, Lorenz Nierves, Janice Tsui, Pitter F. Huesgen, and Philipp F. Lange. 2019. 'Sensitive Determination of Proteolytic Proteoforms in Limited Microscale Proteome Samples *'. *Molecular & Cellular Proteomics* 18(11):2335–47.

Wu, Binyan, Fan Qi, and Yan Liang. 2023. 'Fuels for ROS Signaling in Plant Immunity'. *Trends in Plant Science* 28(10):1124–31.

Wu, Zhongshou, Meng Li, Oliver Xiaoou Dong, Shitou Xia, Wanwan Liang, Yongkang Bao, Geoffrey Wasteneys, and Xin Li. 2019. 'Differential Regulation of TNL-Mediated Immune Signaling by Redundant Helper CNLs'. *New Phytologist* 222(2):938–53.

van Wyk, Stefan G., Karl J. Kunert, Christopher A. Cullis, Priyen Pillay, Matome E. Makgopa, Urte Schlüter, and Barend J. Vorster. 2016. 'Review: The Future of Cystatin Engineering'. *Plant Science* 246:119–27.

Xu, Duorong, Qian Tang, Ping Xu, Anton R. Schäffner, Dario Leister, and Tatjana Kleine. 2023. 'Response of the Organellar and Nuclear (Post)Transcriptomes of Arabidopsis to Drought'. *Frontiers in Plant Science* 14.

Yalcin, Hicret Asli, Ricardo Humberto Ramirez-Gonzalez, Catherine N. Jacott, Burkhard Steuernagel, Gurpinder Singh Sidhu, Rachel Kirby, Emma Verbeek, Henk-jan Schoonbeek, Christopher J. Ridout, and Rachel Wells. 2023. 'Recognition of Necrosis and Ethylene-Inducing like Peptides Confers Disease Resistance in <Em>Brassica Napus</Em> and Is Modulated by <Em>BSK1</Em> in Arabidopsis'. *BioRxiv* 2023.08.01.551450.

Yamada, Kohji, Misuzu Yamashita-Yamada, Taishi Hirase, Tadashi Fujiwara, Kenichi Tsuda, Kei Hiruma, and Yusuke Saijo. 2016. 'Danger Peptide Receptor Signaling in Plants Ensures Basal Immunity upon Pathogen‐Induced Depletion of BAK1'. *The EMBO Journal* 35(1):46–61.

Yamaguchi, Yube, Alisa Huffaker, Anthony C. Bryan, Frans E. Tax, and Clarence A. Ryan. 2010. 'PEPR2 Is a Second Receptor for the Pep1 and Pep2 Peptides and Contributes to Defense Responses in Arabidopsis '. *The Plant Cell* 22(2):508–22.

Yang, Huanjie, Xeniya Kim, Jan Skłenar, Sébastien Aubourg, Gloria Sancho-Andrés, Elia Stahl, Marie-Charlotte Guillou, Nora Gigli-Bisceglia, Loup Tran Van Canh, Kyle W. Bender, Annick Stintzi, Philippe Reymond, Clara Sánchez-Rodríguez, Christa Testerink, Jean-Pierre Renou, Frank L. H. Menke, Andreas Schaller, Jack Rhodes, and Cyril Zipfel. 2023. 'Subtilase-Mediated Biogenesis of the Expanded Family of SERINE RICH ENDOGENOUS PEPTIDES'. *Nature Plants* 9(12):2085–94.

Yildiz, Ipek, Melissa Mantz, Michael Hartmann, Tatyana Zeier, Jana Kessel, Corinna Thurow, Christiane Gatz, Patrick Petzsch, Karl Köhrer, and Jürgen Zeier. 2021. 'The Mobile SAR Signal N-Hydroxypipecolic Acid Induces NPR1-Dependent Transcriptional Reprogramming and Immune Priming'. *Plant Physiology* 186(3):1679–1705.

Yuan, Minhang, Zeyu Jiang, Guozhi Bi, Kinya Nomura, Menghui Liu, Yiping Wang, Boying Cai, Jian Min Zhou, Sheng Yang He, and Xiu Fang Xin. 2021. 'Pattern-Recognition Receptors Are Required for NLR-Mediated Plant Immunity'. *Nature* 592(7852):105–9.

Yuan, Minhang, Bruno Pok Man Ngou, Pingtao Ding, and Xiu-Fang Xin. 2021. 'PTI-ETI Crosstalk: An Integrative View of Plant Immunity'. *Current Opinion in Plant Biology* 62:102030.

Zaffagnini, Mirko, Simona Fermani, Alex Costa, Stéphane D. Lemaire, and Paolo Trost. 2013. 'Plant Cytoplasmic GAPDH: Redox Post-Translational Modifications and Moonlighting Properties'. *Frontiers in Plant Science* 4.

Zavaliev, Raul and Xinnian Dong. 2024. 'NPR1, a Key Immune Regulator for Plant Survival under Biotic and Abiotic Stresses'. *Molecular Cell* 84(1):131–41.

Zeier, Jürgen. 2021. 'Metabolic Regulation of Systemic Acquired Resistance'. *Current Opinion in Plant Biology* 62:102050.

Zeng, Yanhong, Zichao Zheng, Giuliana Hessler, Ke Zou, Junchen Leng, Jaqueline Bautor, Johannes Stuttmann, Li Xue, Jane E. Parker, and Haitao Cui. 2024. 'Arabidopsis PHYTOALEXIN DEFICIENT 4 Promotes the Maturation and Nuclear Accumulation of Immune-Related Cysteine Protease RD19'. *Journal of Experimental Botany* 75(5):1530–46.

Zhang, Hui, Ting Ting Zhang, Hui Liu, De Ying Shi, Meng Wang, Xiao Min Bie, Xing Guo Li, and Xian Sheng Zhang. 2018. 'Thioredoxin-Mediated ROS Homeostasis Explains Natural Variation in Plant Regeneration '. *Plant Physiology* 176(3):2231–50.

Zhang, Jie, Wei Li, Tingting Xiang, Zixu Liu, Kristin Laluk, Xiaojun Ding, Yan Zou, Minghui Gao, Xiaojuan Zhang, She Chen, Tesfaye Mengiste, Yuelin Zhang, and Jian-Min Zhou. 2010. 'Receptor-like Cytoplasmic Kinases Integrate Signaling from Multiple Plant Immune Receptors and Are Targeted by a Pseudomonas Syringae Effector'. *Cell Host & Microbe* 7(4):290–301.

Zhang, Xinxin, Shenkui Liu, and Tetsuo Takano. 2008. 'Two Cysteine Proteinase Inhibitors from Arabidopsis Thaliana, AtCYSa and AtCYSb, Increasing the Salt, Drought, Oxidation and Cold Tolerance'. *Plant Molecular Biology* 68(1):131–43.

Zhang, Xuebin, Mingyue Gou, and Chang-Jun Liu. 2013. 'Arabidopsis Kelch Repeat F-Box Proteins Regulate Phenylpropanoid Biosynthesis via Controlling the Turnover of Phenylalanine Ammonia-Lyase '. *The Plant Cell* 25(12):4994–5010.

Zhao, Qian, Fang Liu, Cong Song, Tingting Zhai, Ziwei He, Limei Ma, Xuemeng Zhao, Zhenhua Jia, and Shuishan Song. 2023. 'Diffusible Signal Factor Primes Plant Immunity against Xanthomonas Campestris Pv. Campestris (Xcc) via JA Signaling in Arabidopsis and Brassica Oleracea'. *Frontiers in Cellular and Infection Microbiology* 13.

Zheng, Xiao-yu, Natalie Weaver Spivey, Weiqing Zeng, Po-Pu Liu, Zheng Qing Fu, Daniel F. Klessig, Sheng Yang He, and Xinnian Dong. 2012. 'Coronatine Promotes Pseudomonas Syringae</Em> Virulence in Plants by Activating a Signaling Cascade That Inhibits Salicylic Acid Accumulation'. *Cell Host & Microbe* 11(6):587–96.

Zhou, Jinggeng, Ping Wang, Lucas A. N. Claus, Daniel V. Savatin, Guangyuan Xu, Shujing Wu, Xiangzong Meng, Eugenia Russinova, Ping He, and Libo Shan. 2019. 'Proteolytic Processing of SERK3/BAK1 Regulates Plant Immunity, Development, and Cell Death'. *Plant Physiology* 180(1):543.

Ziemann, Sebastian, Karina van der Linde, Urs Lahrmann, Beyda Acar, Farnusch Kaschani, Tom Colby, Markus Kaiser, Yezhang Ding, Eric Schmelz, Alisa Huffaker, Nicholas Holton, Cyril Zipfel, and Gunther Doehlemann. 2018. 'An Apoplastic Peptide Activates Salicylic Acid Signalling in Maize'. *Nature Plants* 4(3):172–80.

Zipfel, Cyril, Gernot Kunze, Delphine Chinchilla, Anne Caniard, Jonathan D. G. Jones, Thomas Boller, and Georg Felix. 2006. 'Perception of the Bacterial PAMP EF-Tu by the Receptor EFR Restricts Agrobacterium-Mediated Transformation'. *Cell* 125(4):749–60.

Zipfel, Cyril, Silke Robatzek, Lionel Navarro, Edward J. Oakeley, Jonathan D. G. Jones, Georg Felix, and Thomas Boller. 2004. 'Bacterial Disease Resistance in Arabidopsis through Flagellin Perception'. *Nature* 428(6984):764–67.